https://doi.org/10.35662/unine-thesis-3241

unine
Université de Neuchâtel

# Magnetron Sputtered Quantized Nanolaminates: Development of Industrial Processes for Complex Optical Interference Filters

---

**Submitted to:**
Université de Neuchâtel
Faculty of Science

**For the Degree of:**
Doctor of Science

**By the Author:**
Manuel Ilias Bärtschi

**Presented in:**
December 2025

**To the Jury of:**

| | | |
|---|---|---|
| Prof. Dr. Thomas Südmeyer | UniNE | Director |
| Dr. Valentin Wittwer | UniNE | Examiner |
| Dr. Silvia Schwyn Thöny | Evatec | Examiner |
| Dr. Matthias Golling | RhySearch | Examiner |

unine
Université de Neuchâtel
Faculté des sciences

Rue Emile-Argand 11
CH-2000 Neuchâtel
doctorat.sciences@unine.ch

# IMPRIMATUR POUR THESE DE DOCTORAT

**La Faculté des sciences de l'Université de Neuchâtel autorise l'impression de la présente thèse soutenue par**

## Monsieur Manuel BÄRTSCHI

Titre :

## "Magnetron Sputtered Quantized Nanolaminates: Development of Industrial Processes for Complex Optical Interference Filters"

**sur le rapport des membres du jury composé comme suit :**

- **Prof. Thomas Südmeyer,** directeur de thèse, Université de Neuchâtel, Suisse
- **Dr Valentin Wittwer,** Université de Neuchâtel, Suisse
- **Dr Matthias Golling,** RhySearch, Suisse
- **Dr Silvia Schwyn Thöny,** Evatec AG, Suisse

Neuchâtel, le 3 février 2026

Le Doyen, Prof. P. Brunner

# Abstract

The vast majority of this dissertation was carried out within two research and development projects and is based on the insights obtained there. The first project focused on testing and optimizing the Clusterline 200 BPM magnetron sputtering tool from Evatec. Numerous processes were developed, mainly based on $Ta_2O_5$ and $SiO_2$, and several subsystems such as the optical monitoring system (GSM) were tested and further improved. Towards the end of the project, two processes for the deposition of quantized nanolaminates (QNL) were successfully developed and patented.
Quantized nanolaminates are optical multilayer systems in which periodically alternating, ultrathin layers restrict the mobility of valence electrons in the high index material and thereby shifting the absorption edge of the system. The promising perspectives of the patent in this still relatively young field motivated a second continuing project devoted almost exclusively to the QNL topic.
The thesis first introduces the fundamentals of optical physics, including wave propagation in optical media, the refractive index, extinction coefficient, and absorption. The behavior of electromagnetic waves at interfaces, thin-film interference, and the design and calculation of multilayer systems and common optical filters are then discussed. A substantial part is devoted to metrology, which presents the key instruments and methods used in the projects, their accessible physical quantities, and the limitations of the underlying models. This is followed by a general introduction to magnetron sputtering and a description of the sputtering system and its main subsystems, which provides the basis for the subsequent chapters on QNL fabrication, characterization, and interpretation.
A dedicated theory chapter then addresses QNL in more detail. The chapter introduces the calculation of the effective refractive index of laminate stacks, the description of band edge shifts using a simple finite potential well model based on the Schrödinger equation, and the limiting influence of tunneling. The different regions of the absorption curve and the determination of the band edge via Tauc plots are discussed, establishing the theoretical framework for interpreting the experimental results.
The experimental part begins with a description of the configuration of the sputtering system and the evaluation methods used. A central element is the participation in the 2024 SPIE Laser Damage Competition in San Ramon (CA), which focused on the development of mirrors with optimized femtosecond laser damage thresholds at $1030\,nm$. Various QNL variations were fabricated, characterized, and used to design and produce the corresponding mirrors, which were then tested in the competition. The results and insights gained are presented and discussed. As the project is not finished, there are still open questions and topics, where the most important topics are discussed and explained in the end.



## Keywords

Quantized Nanolaminates, Magnetron Sputtering, Optical Interference Coating, Thin Film Deposition, Laser Induced Damage Threshold

# Résumé

Une grande partie de cette thèse a été réalisée dans le cadre de deux projets de recherche et développement et s'appuie sur les résultats obtenus dans ce contexte. Le premier projet était consacré aux tests et à l'optimisation du système de pulvérisation cathodique magnétron BPM 200 Clusterline d'Evatec. De nombreux procédés ont été développés, principalement à base de $Ta_2O_5$ et de $SiO_2$, et plusieurs sous-systèmes, tels que le système de surveillance optique (GSM), ont été testés et améliorés. Vers la fin de ce projet, deux procédés de dépôt de nanostructures laminaires quantifiées (QNL) ont été développés avec succès et brevetés.
Les nanostructures laminaires quantifiées sont des systèmes optiques multicouches dans lesquels des couches ultraminces, disposées périodiquement en alternance, limitent la mobilité des électrons de valence dans le matériau à fort indice et déplacent ainsi le bord d'absorption du système. Les perspectives prometteuses offertes par le brevet dans ce domaine encore relativement jeune ont motivé un deuxième projet de développement consacré presque exclusivement à la thématique des QNL.
La thèse commence par une présentation des bases de la physique optique, notamment la propagation des ondes dans les milieux optiques, l'indice de réfraction, le coefficient d'extinction et l'absorption. Le comportement des ondes électromagnétiques aux interfaces, les interférences dans les couches minces, ainsi que la conception et le calcul de systèmes multicouches et de filtres optiques courants sont ensuite discutés. Une partie substantielle est consacrée à la métrologie, présentant les principaux instruments et méthodes utilisés dans les projets, les grandeurs physiques accessibles et les limites des modèles sous-jacents. Cette partie est suivie d'une introduction générale à la pulvérisation cathodique magnétron et d'une description du système de dépôt et de ses principaux sous-systèmes, qui fournit la base des chapitres suivants consacrés à la fabrication, à la caractérisation et à l'interprétation des QNL.
Un chapitre théorique dédié traite ensuite plus en détail des QNL. Il présente le calcul de l'indice de réfraction effectif de piles laminaires, la description des décalages de bord de bande à l'aide d'un modèle simple de puits de potentiel fini basé sur l'équation de Schrödinger, ainsi que l'influence limitante de l'effet tunnel. Les différentes régions de la courbe d'absorption et la détermination du bord de bande au moyen de tracés de Tauc y sont discutées, établissant ainsi le cadre théorique pour l'interprétation des résultats expérimentaux.
La partie expérimentale commence par la description de la configuration du système de pulvérisation et des méthodes d'évaluation utilisées. Un élément central est la participation à la compétition « SPIE Laser Damage 2024 » à San Ramon (CA), axée sur le développement de miroirs présentant des seuils de dommage laser optimisés dans le régime femtoseconde à $1030\,nm$. Plusieurs variantes de QNL ont été fabriquées, caractérisées, puis utilisées pour concevoir et produire les miroirs correspondants, qui ont ensuite été testés lors de la compétition. Les résultats obtenus et les enseignements tirés sont présentés et discutés. Le projet n'étant pas encore achevé, plusieurs questions et thématiques restent ouvertes ; les plus importantes sont discutées et explicitées en conclusion.



## Mots-Clés

Nanostructures laminaires quantifiées, Pulvérisation cathodique magnétron, Revêtement interférentiel optique, Dépôt de couches minces, Seuil de dommage induit par le laser

# Contents

# 1 Introduction

This dissertation is as mentioned largely based on the insights and results obtained during two research projects funded by Innosuisse. The first project named "Magnificoat" was carried out with RhySearch as the main research partner, where I was employed shortly after the start of the project. Soon after the beginning, I enrolled as PhD student at the University of Neuchâtel at the Institute for physics under the supervision of Thomas Südmeyer.
In addition to RhySearch, the project involved the "University of Applied Science" NTB as an associated research partner, providing support with various measurement techniques, and Evatec as an industrial partner and coating device manufacturer. The core of the project was the Clusterline 200 BPM magnetron sputtering tool from Evatec. The aim was to test and improve this prototype tool and at the same time to gain more detailed insight into magnetron sputtering processes. The focus during the project was on complex optical interference coatings based on $Ta_2O_5$ and $SiO_2$.
My own work focuses on the development of coating processes. I was able to characterize, evaluate, and analyze these processes directly using a wide range of measurement equipment provided by Evatec and RhySearch. This required close collaboration with specialists from Evatec as well as NTB. As I spent most of my time near the coating system, and therefore at Evatec, I constantly took on more organizational responsibilities within the project. During the three and a half year project duration, a large number of experiments was carried out. Among other results, we developed a process for coating alternating periodic ultra thin layers, the QNL already mentioned, which could then be patented. Because this process allowed an extremely fast deposition of reproducible and highly precise fabrication of QNL, a second project focusing on these layers was proposed.
The following project "Quintessence" is conducted on the same coating tool and also again with and at Evatec. Now I had the opportunity to attend this project from the beginning as the project leader. For this project, "Swiss Federal Laboratories for Materials Science and Technology" EMPA in Thun joined as an additional research partner, supporting us with more complex and elaborate characterization methods such as transmission electron microscopy (TEM), Nanoindentation and X-ray reflectometry (XRR).
This second project therefore investigates these ultrathin layers in even greater depth and allows me to work with a high tech coating tool, to make use of an extensive "playground" of measurement instruments, and to interact and exchange ideas with a large number of experts from all partner institutes and companies.
The situation outlined above has led to a variety of interesting experiments, discussions, and insights over the past five years. In this thesis, I present what I consider the most important and interesting results and explain both their derivation and the conclusions that can be drawn from them.
The work is divided into several chapters.

It begins with the **Fundamentals**. I go back to Maxwell's equations and show that with very few assumptions, virtually everything used in the work can be derived and explained. First, the general behavior of electromagnetic waves is discussed, followed by an explanation of how they behave in matter. This allows us to explain well known and important quantities such as refractive index and absorption behavior.

From the behavior at interfaces, **Layer Design** takes over. By taking into account the potential phase shift at interfaces and the geometric arrangement of different materials, targeted interference effects and thus optical interference filters can be created. This section shows how such effects can be calculated in principle and how some simple ones can be produced.

After the theoretical background about electromagnetic waves and optical designs the measurement devices used in the projects are presented in the chapter **Metrology**. This is important in order to understand how they work, where their limitations lie, and how models can be understood.

Since the core of my work in the projects is operating the Clusterline 200 BPM coating system, the following chapter **Experimental Setup** briefly describes and explains magnetron sputtering in general, as well as the specific system used together with additional devices.

Up to this point, I would describe this section as the classical part. Next comes the part of the work based on experiments relating to QNL. To begin with, a **Theoretical Description of**

**Quantized Nanolaminates** is introduced, explaining what it is and how it can be understood.

The following short chapter **Evaluation in Practice** links the previous two chapters and uses the equipment used to illustrate why it is so well suited to producing this QNL. Furthermore, a real series is used to show how it is evaluated and what we can learn from the measurements.

One of the most important parts of this work was participating in the **Laser Damage competition** in San Ramon CA in 2024. This involved designing and coating highly reflective filters, which were then used to compare the laser resistance of all participants. We took the opportunity to participate in this competition with our QNL, and in this chapter I explain how we prepared for it, how we went about creating and selecting the designs, and what the outcome of our participation was.

Even though we were satisfied with the results achieved in the competition, there were still some open issues where we suspected that the QNL had greater potential for laser resistance. We made a second attempt for **Design Optimization** and carried out a second series of measurements. In this chapter, I will explain the approach taken in the second series, the results obtained and how these values can be interpreted.

Towards the end, there are still some **Open Topics** that are still being worked on at the time of writing or are still in the planning stage. I would like to mention these, as I believe they are important issues that will likely continue to occupy me in the coming months.

At the end, there is a **Conclusion** in which I summarize the work presented and the results achieved

The end of the thesis then presents a summary of my further **Scientific Contributions**. Here I list the peer review publications I participated with brief explanations of what they are about, as well as the patent we have filed and the posters and presentations I have given at conferences.

I hope that the work is interesting for the respective reader and that it leads to one insight or another as a result.
Have fun (:

# 2 Fundamentals of optical physics

Optical interference coating is mostly about depositing a number of very thin optically transparent materials on a substrate so that incident light can be influenced as desired by using interference effects. So, simplified the theory behind this science is about the description of properties of light and materials and how they interact with each other. As most of the people know, light is an electromagnetic wave, but what that means and how to describe such a wave is explained in this section. Also, what happens if light transmits through material and why a part of it get absorbed within or reflected by the surface or interface. The idea behind this chapter is to explain most of the theory behind the optical properties

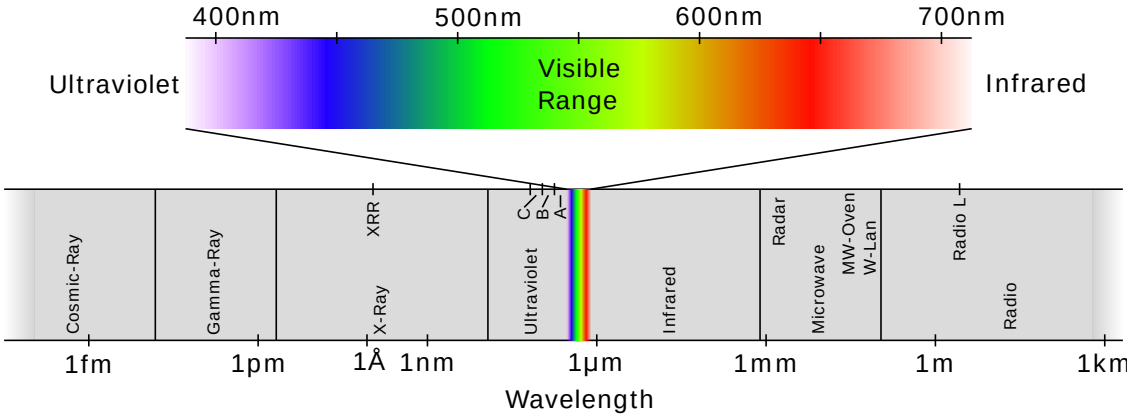


Figure 1: The visible part of the electromagnetic spectrum is only a small part and covers a wavelength range of approximately $400 - 700\,nm$. Below starts the ultra violet and above the infrared region. But also microwave, radar and radio waves are part of the same spectrum.

of materials and to show that only a few basic assumptions are needed to explain a big part of it. The chapter begins with a description of electromagnetic waves and then moves on to their interaction with matter, introducing the basic concepts of optical physics, such as refractive index, absorption, Snell's law and how to get there with the said few assumptions.

## 2.1 Electromagnetic Waves in General

The fundamentals of optical physics can be found in probably all textbooks on the subject and are generally structured in a similar way. For this chapter, I followed mainly the two books 2 and 3 of the series "Experimentalphysik" by Wolfgang Demtröder [1], [2] and also "Electrodynamics of Solids" [3] from Dressel and Grüner, as I find them easy to understand and added a few explanations and additions where necessary.
We begin this chapter with Maxwell's equations to demonstrate that virtually everything we will do later can be derived relatively directly from this solid foundation and, in general, with only very few assumptions.

### 2.1.1 Periodic Waves

Maxwell's equations consist of four parts [1] (P.140):

$$\vec{\nabla} \cdot \vec{E} = \frac{\rho}{\epsilon_0} : \quad \textbf{Gauss's} \quad \textbf{Law} \tag{1}$$

With:

$\vec{\nabla} = \begin{pmatrix} \frac{\partial}{\partial x} \\ \frac{\partial}{\partial y} \\ \frac{\partial}{\partial z} \end{pmatrix}$ ... as the Nabla operator

$\vec{E}$ $[\frac{V}{m}]$ ... the electric field

$\rho$ $[\frac{A \cdot s}{m^3}]$ ... the charge density

$\epsilon_0 \approx 8.8542...$ $[\frac{A \cdot s}{V \cdot m}]$ ... the permittivity of free space

**Gauss's law** describes the relation of charges or charge densities ($\rho$) and the electric field ($\vec{E}$). The charge is the source of the electric field lines, which diverge and point away from positive charges and towards negative ones. The surface integral over an area is always proportional to the charge that is locked in, given by the permittivity of free space ($\epsilon_0$).

$$\vec{\nabla} \cdot \vec{B} = 0 : \quad \textbf{Gauss's Law for magnetism} \tag{2}$$

With:

$\vec{B}$ $[T]$ ... the magnetic field

**Gauss's law for magnetism** states that the magnetic field lines do not diverge compared to the electric field lines. They are always closed and therefore there are no magnetic monopoles.

$$\vec{\nabla} \times \vec{E} = -\frac{\partial \vec{B}}{\partial t} : \quad \textbf{Faraday's Law for induction} \tag{3}$$

**Faraday's law for induction** states that a change in magnetic flux density over time leads to an electric vortex field.

$$\vec{\nabla} \times \vec{B} = \mu_0 \vec{j} + \frac{1}{c^2} \cdot \frac{\partial \vec{E}}{\partial t} : \quad \textbf{Maxwell's addition to Ampere's law} \tag{4}$$

With:

$\mu_0 = 4\pi \cdot 10^{-7}$ $[\frac{N}{A^2}]$ ... the vacuum permeability

$\vec{j}$ $[\frac{A}{m^2}]$ ... the current density

$c \approx 2.998... \cdot 10^8$ $[\frac{m}{s}]$ ... the speed of light in vacuum

**Maxwell's addition to Ampère's law** states that the electrical current and also the displacement current induce a magnetic vortex field.
For $\mu_0$ applies: $\frac{1}{c^2} = \epsilon_0 \cdot \mu_0$.
The next few steps are there to show that we can use a simple wave function as an expression for the electric field.
If we take Maxwell's equation for an electromagnetic wave in a charge- and current free vacuum ($\rho = 0$, $\vec{j} = \mathbf{0}$), we can reduce the equations to the non-vanishing terms left [1] (P.196):

$$\begin{aligned} \vec{\nabla} \times \vec{E} &= -\frac{\partial \vec{B}}{\partial t} \\ \vec{\nabla} \times \vec{B} &= \frac{1}{c^2} \frac{\partial \vec{E}}{\partial t} \end{aligned} \tag{5}$$

with some math, we can put together both terms and get:

$$\triangle \vec{E} = \frac{1}{c^2} \frac{\partial^2 \vec{E}}{\partial t^2} \tag{6}$$

Where:

$\triangle = \vec{\nabla}^2$ ... describes the Laplace operator.

This expression is a wave equation that describes the propagation of an electric field wave in space with the speed of light. This equation can be written in cartesian coordinates for better understanding of the following steps as:

$$\begin{pmatrix} \frac{\partial^2 E_x}{\partial x^2} + \frac{\partial^2 E_x}{\partial y^2} + \frac{\partial^2 E_x}{\partial z^2} \\ \frac{\partial^2 E_y}{\partial x^2} + \frac{\partial^2 E_y}{\partial y^2} + \frac{\partial^2 E_y}{\partial z^2} \\ \frac{\partial^2 E_z}{\partial x^2} + \frac{\partial^2 E_z}{\partial y^2} + \frac{\partial^2 E_z}{\partial z^2} \end{pmatrix} = \frac{1}{c^2} \frac{\partial^2}{\partial t^2} \begin{pmatrix} E_x \\ E_y \\ E_z \end{pmatrix} \tag{7}$$

This expression is also universally valid, which means that we can rotate our coordinate system so that the propagation direction is the same as the z-axis. This means that $\frac{\partial \vec{E}}{\partial x} = \frac{\partial \vec{E}}{\partial y} = \mathbf{0}$ and, therefore:

$$\frac{\partial^2 \vec{E}}{\partial z^2} = \frac{1}{c^2} \frac{\partial^2 \vec{E}}{\partial t^2} \tag{8}$$

because we have no charges, we can use Gauss's law $\nabla \cdot \vec{E} = 0$ which leads to $\frac{\partial E_z}{\partial z} = 0$ and we are left with a wave function which has only entries of $E_x$- and $E_y$-terms.

$$\vec{E} = \begin{pmatrix} E_x \\ E_y \\ 0 \end{pmatrix} \tag{9}$$

This means that we have a transverse wave where the field vector is perpendicular to the propagation direction $\vec{E} \perp \hat{e}_z$.
We assume that we have a spatially periodic wave, which means that, after a certain distance $\lambda$, the wave function $f(z,t) = f(z+\lambda,t)$ has the same value again, which leads to the expression for this wave of:

$$\vec{E}(z,t) = \vec{E}_0 \cdot \sin k(z - ct) \tag{10}$$

The periodicity condition now follows $k \cdot \lambda = 2\pi \Rightarrow k = \frac{2\pi}{\lambda}$ and by writing the speed of light as the combination of its wavelength and frequency $c = \nu\lambda$
Where:

$\vec{E}_0$ $[\frac{V}{m}]$ ... is the amplitude vector of the wave function

$k$ $[\frac{1}{m}]$ ... describes the wave number

$\lambda$ $[m]$ ... is called the wavelength

$\nu$ $[\frac{1}{s}]$ ... describes the frequency of the wavefunction

$\omega = 2\pi\nu$ $[\frac{rad}{s}]$ ...as the angular frequency

This means we can write the wave function as:

$$\vec{E}(z,t) = \vec{E}_0 \cdot \sin(kz - \omega t) \tag{11}$$

Such a simple wave is shown in fig. 2.
The following part is to show that the magnetic and the electric wave behave pretty similar, so we can later use the electric wave for calculations or explanations.

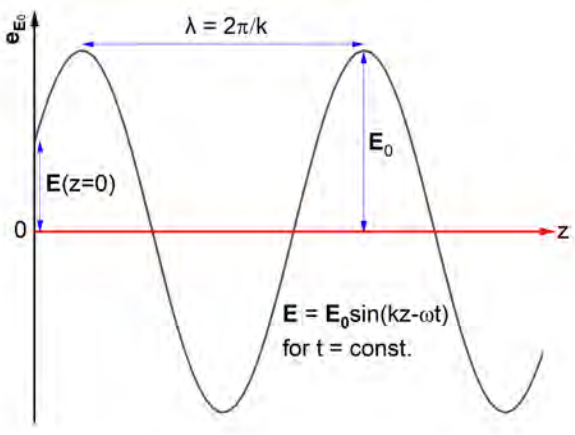


Figure 2: A harmonic electric field wave at a constant time. While the wave propagates into z-direction, the E-field stands perpendicular to it.

It is possible to write $kz$ as the product of a wave vector $\vec{k} = \begin{pmatrix} k_x \\ k_y \\ k_z \end{pmatrix}$ with the same length $\mathbf{k} = |\vec{k}| = \frac{2\pi}{\lambda}$ and the position of the wave $\vec{r}$ as $\vec{k} \cdot \vec{r} = kz$. This is possible because $\vec{k} \cdot \vec{r} = const.$ for all points on the same phase front $\perp \vec{k}$. This wave function can also be written in an exponential expression while omit the complex conjugated part because we can assume that $\vec{E}$ is a real vector as [1] (P.199):

$$\vec{E}(\vec{r}, t) = \vec{E}_0 \cdot \mathbf{e}^{i(\vec{k} \cdot \vec{r} - \omega t)} \tag{12}$$

With Faraday's Law for induction

$$\frac{\partial \vec{B}}{\partial t} = -(\nabla \times \vec{E}) \tag{13}$$

with a simultaneous calculation path we can determine the magnetic field for the wave as:

$$\vec{B} = \frac{1}{\omega}(\vec{k} \times \vec{E}) \tag{14}$$

This shows that the magnitude of the electric and magnetic parts are locked as:

$$|\vec{B}| = \frac{1}{c}|\vec{E}| \tag{15}$$

but also that $\vec{B}$ stands perpendicular to $\vec{k}$ and $\vec{E}$: $\rightarrow \vec{B} \perp \vec{E} \perp \vec{k}$, $\quad \vec{B} \perp \vec{k}$. Summarized, $\vec{k}$ points always towards the propagation direction of the light wave, and the magnetic and electric waves each stand not just perpendicular to $\vec{k}$ but also always to each other. The relation is shown in fig. 3.

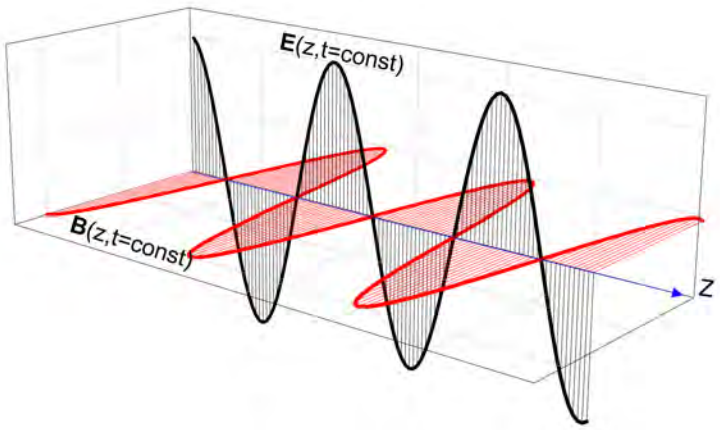


Figure 3: Displayed is the propagation of an electromagnetic wave in z-direction at a fixed time $\vec{E}(z, t = const.)$, $\vec{B}(z, t = const.)$. The E-field stands always perpendicular on the B-field and both are perpendicular on the propagation direction

### 2.1.2 Polarization of Waves

As mentioned previously, we can limit our consideration only to the electric part as the magnetic behaves the same.
An important property of the wave is its **polarisation**, which is given by the direction of the electric field vector $\vec{E}$. Roughly explained that is the direction in which the field swings while propagating. The most simple is the linearly polarized wave. If the vector $\vec{E}_0$ always points in the same direction $\perp \vec{e}_z$, it is linearly polarized. This means:

$$\vec{E}(z, t)_{linear} = \begin{pmatrix} E_{0x} \cdot \cos(kz - \omega t) \\ E_{0y} \cdot \cos(kz - \omega t) \end{pmatrix} = \begin{pmatrix} E_{0x} \\ E_{0y} \end{pmatrix} \cdot \cos(kz - \omega t) \tag{16}$$

so both components swing in phase, which is visualized in fig. 4. If the absolute values of $E_{0x}$ and

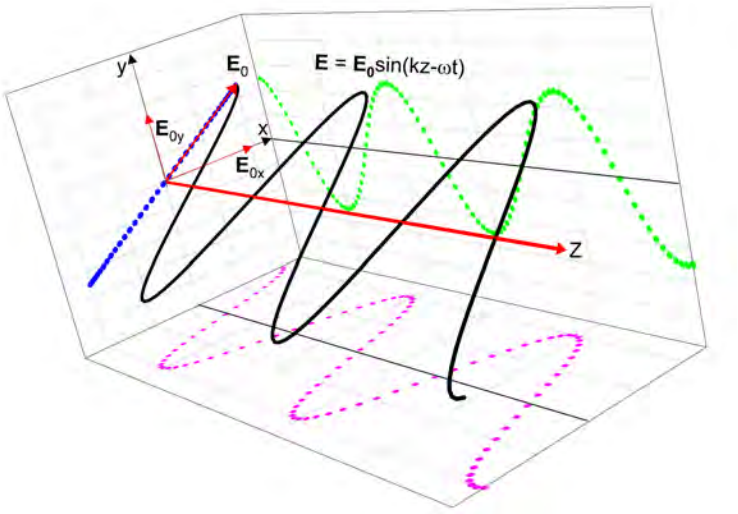


Figure 4: This shows a linearly polarized wave with the vector $\vec{E}_0(z, t = const.)$ pointing in a constant x,y-direction.

$E_{0y}$ are the same, so $E_{0x} = E_{0y} = E_0$ but their phase is shifted by 90° (or $\pi/2$), the wave is circularly polarized.

$$\vec{E}(z,t)_{circular} = \begin{pmatrix} E_0 \cdot \cos(kz - \omega t) \\ E_0 \cdot \sin(kz - \omega t) \end{pmatrix} = E_0 \begin{pmatrix} \cos(kz - \omega t) \\ \sin(kz - \omega t) \end{pmatrix} \tag{17}$$

So in the origin of the function $\vec{E}(z = 0, t)$ the deflection of the vector $\vec{E}_0$ is given by the angle $\phi(t)$ and the connection of $E_{0y} = |E_0| \sin(\phi)$ and $E_{0y} = |E_0| \cos(\phi)$, which leads to:

$$\vec{E}(z = 0, t) = E_0 \begin{pmatrix} \cos(\omega t) \\ \pm \sin(\omega t) \end{pmatrix} \tag{18}$$

The "±" at the y-term gives the direction of rotation. The vector of the wave in the x-y-plane now describes a circle with the circular frequency of $\omega = \frac{d\phi}{dt} \rightarrow \phi = \omega \cdot t$. The circularly polarized electric wave is shown in fig. 5.

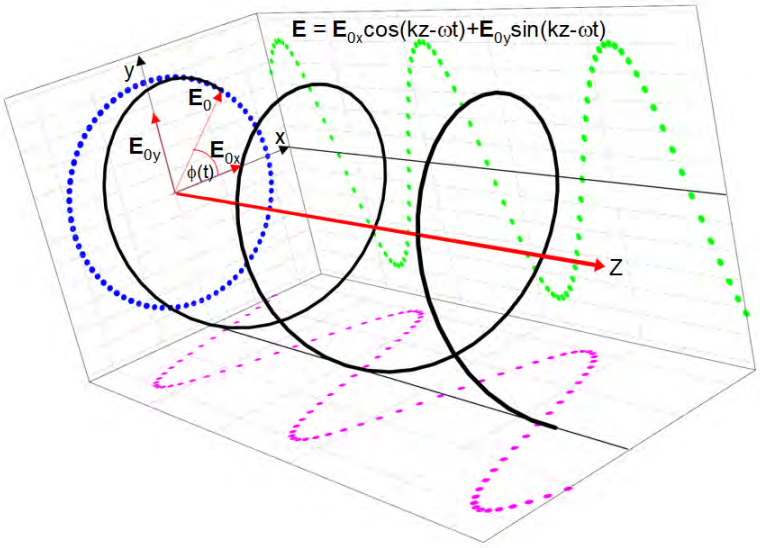


Figure 5: This shows a circularly polarized wave with $\vec{E}(z,t) = \vec{E}_{0x} \cdot \cos(kz - \omega t) + \vec{E}_{0y} \cdot \sin(kz - \omega t)$ and $|\vec{E}_{0x}| = |\vec{E}_{0y}|$

The circular polarized wave is a special case of the more general elliptic polarized wave, where $E_{0x} \neq E_{0y}$ or the phase shift of $\delta\phi$ of both components is not 90°. In this case, the vector $\vec{E}_0(t, z = 0)$ does not describe a circle but an ellipse in the x-y-plane.
The "normal" everyday-light that one comes in contact with, such as from the sun or from a light bulb, consists of light waves which are unpolarized because they are a superposition of many different waves. This means that the vector $\vec{E}_0$ shows no constant direction and also no periodically elliptic or circular function.

## 2.2 Electromagnetic Waves in Materials

In the previous subsection, we described plane electromagnetic waves in vacuum; we now consider their interaction with matter. This is important to understand where important material properties such as the refractive index or extinction coefficient come from.

### 2.2.1 Simplified Refractive Index

We start with the introduction of an important physical quantity, the dimensionless **refractive index** $n$. It can be simplified as the ratio factor that links the speed of light in a material with the speed of light in vacuum.
For explanation we need the **phase speed** $v_{ph}$ which describes the propagation speed of the same phase of a monochromatic wave. In vacuum, the phase speed is the same as the speed of light in vacuum $c$ with $n_{vac} = 1$. If this electromagnetic wave travels through a transparent medium, the propagation speed of this phase is reduced within the material by the factor $n$, while this factor depends on the wavelength. So, the phase speed in the material is [1] (P.223):

$$v_{ph}(\lambda) = \frac{c}{n(\lambda)} = \frac{\omega}{k(\lambda)} \tag{19}$$

With:

$\nu_{ph}$ $[\frac{m}{s}]$ ... describes the phase speed of the wave

$n$ ... the dimensionless refractive index already mentioned

In the material the circular frequency $\omega$ of the light remains constant, but with the lower phase speed the wavelength changes to $\lambda(n) = \lambda_0/n$. The behavior of the wave passing a material and the influence on the wavelength can be seen in fig. 6. The wave within the medium can be described similar to the wave in vacuum by using the correlation $k = \omega/v_{ph}$ which leads to the expression for a plane wave of:

$$\vec{E}(z,t) = \vec{E}_0 \cdot \mathbf{e}^{i(\omega t - kz)} = \vec{E}_0 \cdot \mathbf{e}^{i\omega(t - z/v_{ph})} = \vec{E}_0 \cdot \mathbf{e}^{i\omega(t - zn/c)} \tag{20}$$

### 2.2.2 Optically Thin Material

To avoid confusion, it needs to be said that the term "optically thin material" refers to a low optical density with a refractive index close to 1 and does not imply a physical thickness.
To explain why the electric wave moves slower in a medium than in vacuum, we have to take a look at the interaction of the light with the material. In the material, it needs the additional time of $\Delta t = (n-1) \cdot \Delta z/c$. This delay can be described with the refractive index $n$. To pass a material of thickness $\Delta z$, the wave would need to pass in vacuum the time of $t = \Delta z/c$. So, the wave after passing the material can be written as:

$$\vec{E}(z,t) = \vec{E}_0 \mathbf{e}^{i\omega[t-(n-1)\Delta z/c - z/c]} = \vec{E}_0 \mathbf{e}^{i\omega(t-z/c)} \cdot \underbrace{\mathbf{e}^{-i\omega(n-1)\Delta z/c}}_{=\mathbf{e}^{-i\phi}} \tag{21}$$

For a medium with a low optical density $n - 1 << 1$ such as a gas, the phase shift of the wave is small and therefore the expression $\mathbf{e}^{-i\phi}$ can be written as $\mathbf{e}^{-i\phi} \simeq 1 - i\phi$ [1] (P.224). So, this leads to the expression for the total electric field of:

$$\vec{E}(z,t)_{thin} = \underbrace{\vec{E}_0 \mathbf{e}^{i\omega(t-\frac{z}{c})}}_{\vec{E}_P} \underbrace{- \vec{E}_0 \mathbf{e}^{i\omega(t-\frac{z}{c})} \cdot i\omega(n-1)\frac{\Delta z}{c}}_{\sum \vec{E}_S = \vec{E}_{med}} \tag{22}$$

However, the used expressions are:

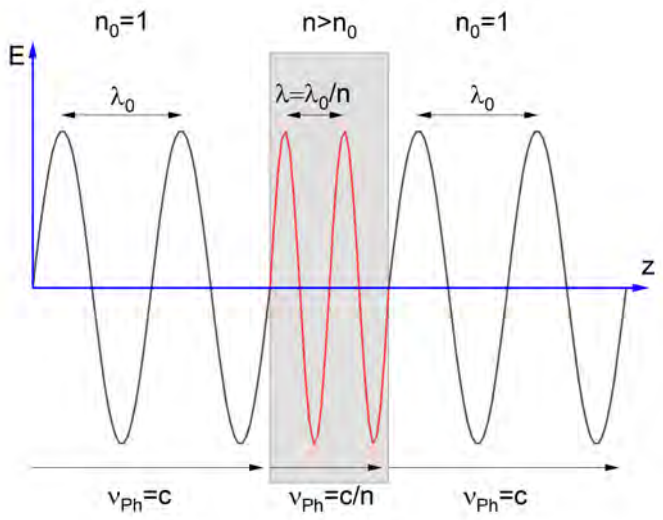


Figure 6: This shows the behavior of an electric wave passing a material. The phase speed and also the wavelength changes in dependence of the refractive index $n$. The circular frequency $\omega$ stays constant.

$\vec{E}_P \quad [\frac{V}{m}]$ ... stands for the primary/ incoming wave

$\sum \vec{E}_S = \vec{E}_{med}\ [\frac{V}{m}]$ ... the secondary waves summed up over all dipoles

As an explanation, in the material the electrons are excited by the external primary electric field with the frequency $\omega$. In return, these represent an oscillating dipole, radiating a wave with the same frequency $\omega$ but with a delayed phase relative to the exciting wave due to the forced oscillation, the secondary wave. Those secondary waves $\vec{E}_S$ sum up to $\vec{E}_{med}$ over the layers of atoms passed, superimpose with the primary wave $\vec{E}_P$ and form a delayed total wave field $\vec{E}(z,t)_{thin}$.
To understand how these secondary electric fields sum up to the final total wave function we have to take a look at the single excited electron, which behaves like a driven oscillator due to the electric force induced by the primary electric field with $\vec{F} = -e \cdot \vec{E}$ which we can write with a general expression as [1] (P224):

$$m\ddot{x}(t) + b\dot{x}(t) + Dx(t) = -eE_0\mathbf{e}^{i(\omega t - kz)} \tag{23}$$

For this equation, we can use some solution approaches where we chose:

$$\omega_0^2 = D/m \ \ ; \qquad \gamma = b/m \ \ ; \qquad m = m_e \tag{24}$$

Where:

$e \approx 1.602... \cdot 10^{-19}\ [C]$ ... stands for the elementary or electron charge

$\omega_0\ [\frac{1}{s}]$ ... describes the resonance frequency of the electron

$\gamma\ [\frac{1}{s}]$ ... describes the damping factor and

$m_e \approx 9.11... \cdot 10^{-31}\ [kg]$ ... stands for the mass of the electron

and the approach of using $x(t) = x_0 \cdot \mathbf{e}^{i\omega t}$ as the description of the deflection of the oscillator, we can use the general expression:

$$x_0 = -\frac{eE_0/m_e}{(\omega_0^2 - \omega^2) + i\gamma\omega} \tag{25}$$

and expand the fraction by $[(\omega_0^2 - \omega^2) - i\gamma\omega]$ and get:

$$x_0 = -\frac{(\omega_0^2 - \omega^2 - i\gamma\omega)e/m_e}{(\omega_0^2 - \omega^2)^2 + (\gamma\omega)^2}E_0 \rightarrow x = -\frac{e/m_e}{\sqrt{(\omega_0^2 - \omega^2)^2 + (\gamma\omega)^2}}E_0\mathbf{e}^{i(\omega t + \phi)} \tag{26}$$

There we can see that the amplitude of the forced oscillation depends not only on $E_0$ but also on the difference in the frequency of the primary electric wave and the resonant frequency of the atomic electrons and the damping factor $\gamma$. Those electrons form together with the positive atomic nucleus an oscillating dipole which also generates an electric wave. The field of the dipole on the z-axis at the point $r >> x_0$ is according to [1] (P.225):

$$E_{dipole}(r,\theta) = -\frac{e\omega^2 x_0 \sin\theta}{4\pi\epsilon_0 c^2 r}\mathbf{e}^{i\omega(t-r/c)} \tag{27}$$

$\theta$ describes the angle between the dipole axis and the direction from the dipole to the point considered, while $r$ describes the distance to the dipole.
We do not have just one dipole but a density $N$ of dipoles in the whole surface area $dA = 2\pi\rho d\rho$, the primary electric wave from a light source meets through the whole material with the thickness $\Delta z$. This leads to the total number of dipoles of $\Delta z \int N dA$. Because we are only interested in the field on the z-axis where all the dipole movements are mostly perpendicular, we can set $\sin(\theta) \simeq 1$ [1] (P.226). So we get the expression on the z-axis:

$$E(z) = -\frac{e\omega^2 x_0 \mathbf{e}^{i\omega t}}{4\pi\epsilon_0 c^2}\Delta z \int_0^\infty N\frac{\mathbf{e}^{-i\omega r/c}}{r} 2\pi\rho d\rho \tag{28}$$

Because $N$ is constant, we can remove it from the integral. In addition, we can write $r^2 = z^2 + \rho^2 \rightarrow r \cdot dr = \rho \cdot d\rho$ because $z$ is constant in the z-plane. So we can write the integral part as:

$$\int_0^\infty N\frac{\mathbf{e}^{-i\omega r/c}}{r} 2\pi\rho d\rho = N \cdot 2\pi \cdot \int_{r=z}^\infty \mathbf{e}^{-i\omega r/c} dr = -\frac{2\pi N c}{i\omega}\left[\mathbf{e}^{-i\omega r/c}\right]_z^\infty \tag{29}$$

Because outside of the area the wave meets the material, the dipoles do not get excited, and therefore we can ignore the upper limit and get

$$E(z) = \frac{i\omega e x_0 N}{2\epsilon_0 c}\mathbf{e}^{i\omega(t-z/c)} \cdot \Delta z \tag{30}$$

if we set this back in equation 26 we get:

$$E(z) = -i\omega\frac{\Delta z}{c} \cdot \frac{Ne^2}{2\epsilon_0 m[(\omega_0^2 - \omega^2) + i\omega\gamma]} \cdot E_0 \mathbf{e}^{i\omega(t-z/c)} \tag{31}$$

If we compare this to the equation 22 we can express the refractive index as:

$$\tilde{n} = 1 + \frac{Ne^2}{2\epsilon_0 m[(\omega_0^2 - \omega^2) + i\omega\gamma]} \tag{32}$$

This shows that the total refractive index has an imaginary component and can be written as $\tilde{n} = n_{real} - i\kappa$. With the new unit

$\kappa$ ... as the extinction coefficient.

Often, when the refractive index is mentioned, only the real part is meant. Most of the time it does not make a difference as the imaginary part is negligibly small. The extinction coefficient is often represented with a "k", but as it is already used here for the wave number, the extinction coefficient is changed to "$\kappa$".
This equation is only valid for optical thin materials with $(n-1) << 1$ like most gasses. We can also see that the refractive index depends on the atomic density of the medium and also on the frequency difference $\Delta\omega = \omega_0 - \omega$ of the incoming primary wave frequency $\omega$ and the resonance frequency of the oscillating atomic electrons $\omega_0 = \sqrt{D/m_e}$ where $F_r = -D \cdot x$ describes the restoring force of the electrons to their rest position.

### 2.2.3 Optically Thick Material

As said, the previous derivation works only for optical thin materials where the incoming primary wave and the secondary driven wave have only a small phase shift. If we have an optical thicker material, like transparent glass, optical coatings, and so on, we need another approach. For this we first need to look at the dielectric polarization [1] (P.25). The dielectric material describes an electrical insulator with charge carriers that are not freely moving. For atoms with no external electric field, the electrons form a cloud around the atomic nucleus so that the charge center of gravity of both sits at the same position. Therefore, the positive charges from the nucleus and the negative charge from the electron cloud form no electric field which can be seen from outside the cloud. If an external electric field is added, the electrons move against the external field, leading to a difference in the charge center of gravity for the electrons $S^-$ and the nucleus $S^+$. This leads to an electric field, induced by the charges and the distance $\vec{d}$ between $S^-$ and $S^+$, which points in a direction opposite to the external field. The induced dipole moment $\vec{p}$ can be described by the distance between the two charge centers and the charge as:

$$\vec{p} = q \cdot \vec{d} \tag{33}$$

The sum of all dipole moments on all polarized atoms $N$ in a unit of volume $V$ is called polarization $\vec{P}$.

$$\vec{P} = \frac{1}{V} \sum_i \vec{p}_i \tag{34}$$

Because all the dipoles point in the same direction if we neglect any further external influences, we can write $\vec{P} = N \cdot q \cdot \vec{d} = N \cdot \vec{p}$. The external force acting on charges is $\vec{F} = q \cdot \vec{E}$ and holds the displacement of the electrons compared to the nucleus against their electrical attraction force in equilibrium. Because the displacement $\vec{d}$ is small compared to the size of the atoms, the back driving force $-\vec{F}$ of the two separated charges is proportional to their displacement, so $\vec{d} \propto \vec{E}$ and therefore:

$$\vec{p} = \boldsymbol{\alpha} \vec{E} \tag{35}$$

The proportionality constant $\boldsymbol{\alpha}$ is called polarizability and describes the restoring force in the atom due to the displacement of the charges and depends on the direction.
Due to the charge shift of the dielectric material, charges appear on the surface $A$ of the medium that are called polarization charges $Q_{pol}$. Their surface charge density $\sigma_{pol}$ is:

$$\sigma_{pol} = \frac{Q_{pol}}{A} = \frac{n \cdot q \cdot d \cdot A}{A} = P \tag{36}$$

In a dielectric, the external electric field $\vec{E}_{vac} = \sigma_{vac}/\epsilon_0$ overlays the opposing polarization field $\vec{E}_{pol} = \sigma_{pol}/\epsilon_0$, resulting in the total dielectric electric field:

$$\vec{E}_{diel} = \frac{\sigma_{vac} - \sigma_{pol}}{\epsilon_0} \hat{e} = \vec{E}_{vac} - \frac{\vec{P}}{\epsilon_0} \tag{37}$$

For a homogeneous external electric field, within the medium the positive and negative charges cancel each other out, and the total charge density is 0. For inhomogeneous fields the polarization is not the same at every place in the medium, and therefore the excess charge $\Delta Q_{pol}$ is formed, which can be described by the spatial polarization charge density $\rho_{pol}$ over the whole volume.

$$\Delta Q_{pol} = -\int_V \rho_{pol} dV \tag{38}$$

However, it can also be described by the charge displacement over the surface $A$ of the medium by:

$$\Delta Q_{pol} = \int_A \sigma_{pol} d\vec{A} \tag{39}$$

This leads with Gauss's Law to the equation:

$$-\int_V \rho_{pol} dV = \int_A \sigma_{pol} d\vec{A} = \int_A \vec{P} d\vec{A} = \int_V (\vec{\nabla} \cdot \vec{P}) dV \tag{40}$$

and leads to the equation:

$$\vec{\nabla} \cdot \vec{P} = -\rho_{pol} \tag{41}$$

This means that we can expand the first of Maxwell's equations in a dielectric medium with:

$$\vec{\nabla} \cdot \vec{E}_{diel} = \vec{\nabla} \cdot (\vec{E}_{vac} - \vec{P}/\epsilon_0) = \frac{\rho_{vac} + \rho_{pol}}{\epsilon_0} \tag{42}$$

The dielectric displacement field describes the density of electric field waves in an area and combines the polarization field and an electric field to an auxiliary field which is defined as:

$$\vec{D} \equiv \epsilon_0 \vec{E}_{diel} + \vec{P} = \epsilon \cdot \epsilon_0 \vec{E}_{diel} \tag{43}$$

which leads to:

$$\vec{\nabla} \cdot \vec{D} = \rho \tag{44}$$

With this excursion to the polarization of dielectric media, we can use Maxwell's equation to describe the refractive index of thicker optical materials by expanding the equations 1-4 with:

$$\begin{aligned} \vec{\nabla} \cdot \vec{D} = \rho, \quad \vec{\nabla} \times \vec{E} = -\frac{\partial \vec{B}}{\partial t} \\ \vec{\nabla} \cdot \vec{B} = 0, \quad \vec{\nabla} \times \vec{B} = \mu\mu_0 \left( \vec{j} + \frac{\partial \vec{D}}{\partial t} \right) \end{aligned} \tag{45}$$

In an uncharged insulator there are no currents $\vec{j} = 0$ and also no free charges $\rho = 0$. Therefore, while continuing in 2.2.2 we get:

$$\triangle \vec{E} = \mu\mu_0\epsilon\epsilon_0 \frac{\partial^2 \vec{E}}{\partial t^2} = \frac{1}{v_{ph}^2} \frac{\partial^2 \vec{E}}{\partial t^2} \tag{46}$$

with the propagation speed of the wave in a medium of:

$$v_{ph} = \frac{1}{\sqrt{\mu\mu_0\epsilon\epsilon_0}} = \frac{c}{\sqrt{\mu\epsilon}} \tag{47}$$

With $v_{ph} = \frac{c}{n} \rightarrow n = \frac{c}{v_{ph}}$ follows:

$$n = \frac{c}{v_{ph}} = \sqrt{\mu\epsilon} \tag{48}$$

This equation can be reduced if we assume for a non-magnetic medium $\mu \approx 1$ [1] (P.231). If we set $\vec{D} = \epsilon_0 \vec{E} + \vec{P}$ in the extended Maxwell's equation with $\mu \approx 1$ we get:

$$\triangle \vec{E} = \mu_0\epsilon_0 \frac{\partial^2 \vec{E}}{\partial t^2} + \mu_0 \frac{\partial^2 \vec{P}}{\partial t^2} = \frac{1}{c^2} \frac{\partial^2 \vec{E}}{\partial t^2} + \frac{1}{\epsilon_0 c^2} \frac{\partial^2 \vec{P}}{\partial t^2} \tag{49}$$

From our equation $\vec{B} = 1/\omega(\vec{k} \times \vec{E})$ follows with $\vec{k} = n\vec{k}_0$, $|\vec{k}|/\omega = 1/c$ and $\hat{\vec{k}}_0 = \vec{k}_0/|\vec{k}_0|$:

$$\vec{B} = \frac{n}{c}(\hat{\vec{k}}_0 \times \vec{E}) = \frac{|n|}{c}(\hat{\vec{k}}_0 \times \vec{E})\mathbf{e}^{i\phi_n} \tag{50}$$

with the complex refractive index $n = n_r - i\kappa$ as:

$$n = |n| \cdot \mathbf{e}^{i\phi_n}, \quad \tan\phi_n = -\frac{\kappa}{n_r} \tag{51}$$

We can see for absorbing material that the electric and magnetic fields are no longer in phase.
As written before, we can write $\vec{P}$ for an electric wave of $\vec{E} = \vec{E}_0 \cdot \mathbf{e}^{i(\omega t - kz)}$ as:

$$\vec{P} = N \cdot \vec{p} = N\boldsymbol{\alpha}\vec{E}_0\mathbf{e}^{i(\omega t - kz)} \tag{52}$$

and set this back in equation 49 which gives:

$$\begin{aligned}
\triangle \vec{E}_0 \mathbf{e}^{i(\omega t - kz)} &= \frac{1}{c^2} \frac{\partial^2 \vec{E}_0 \mathbf{e}^{i(\omega t - kz)}}{\partial t^2} + \frac{1}{\epsilon_0 c^2} \frac{\partial^2 \boldsymbol{\alpha} N \vec{E}_0 \mathbf{e}^{i(\omega t - kz)}}{\partial t^2} \\
\Rightarrow -k^2 \vec{E}_0 \mathbf{e}^{i(\omega t - kz)} &= -\frac{\omega^2}{c^2} \vec{E}_0 \mathbf{e}^{i(\omega t - kz)} - \frac{\omega^2 N \boldsymbol{\alpha}}{\epsilon_0 c^2} \vec{E}_0 \mathbf{e}^{i(\omega t - kz)} \\
\Rightarrow k^2 &= \frac{\omega^2}{c^2} \left(1 + \frac{\boldsymbol{\alpha} N}{\epsilon_0}\right)
\end{aligned} \tag{53}$$

this leads with: $n = c \cdot k/\omega$ to:

$$n^2 = 1 + \boldsymbol{\alpha} N \epsilon_0 \tag{54}$$

This equation describes the connection of the refractive index and the polarizability of the atoms in the medium. If we look back to the induced dipole moment $p = -e\vec{d}$ by the external electric field $\vec{E}$ with the equation for a driven oscillator 25 we can express the dipole moment as:

$$\vec{p} = \frac{e^2 \vec{E}}{m(\omega_0^2 - \omega^2 + i\gamma\omega)} \tag{55}$$

and get with the relation of $\vec{p} = \boldsymbol{\alpha}\vec{E}$ a detailed expression for $\boldsymbol{\alpha}$:

$$\boldsymbol{\alpha} = \frac{e^2}{m_e(\omega_0^2 - \omega^2 + i\gamma\omega)} \tag{56}$$

So we are finally able to write the refractive index as:

$$n^2 = 1 + \frac{e^2 N}{\epsilon_0 m_e(\omega_0^2 - \omega^2 + i\gamma\omega)} \tag{57}$$

Now we can compare this with the refractive index for optically thin materials $(n-1) << 1$ with $(n^2 - 1) \approx (n-1) \cdot 2$ and see that it leads to the same result as in equation 32.
In equation 57 is shown that the refractive index depends on the frequency or wavelength of the light. To give an example, the refractive index for red light is lower than it is for blue light in an optically transparent medium. This effect is called "dispersion".

### 2.2.4 Multi Oscillator Model

In a realistic material, there is not only one type of electron-atom binding but there are several resonant frequencies. This leads to a sum of $k$ different oscillators, each having its own resonant frequency $\omega_k$ and its damping factor $\gamma_k$, which gives the expression for a refractive index with several oscillators [4](31.3), [5] (P.25):

$$\epsilon(\omega) = n^2(\omega) = 1 + \frac{e^2}{\epsilon_0 m} \sum_k \frac{N_k}{(\omega_k^2 - \omega^2) + i\omega\gamma_k} = 1 + \sum_k \frac{\omega_{P,k}^2}{(\omega_k^2 - \omega^2) + i\omega\gamma_k} \tag{58}$$

Where:

$\omega_{P,k} = \sqrt{\frac{e^2 N_k}{\epsilon_0 m}}$ $[\frac{1}{s}]$ ... Is called the plasma frequency

This model shows and describes that the real refractive index and the extinction coefficient also have multiple peaks over a certain range. It also shows that there are ranges in which the refractive index can be obtained $n < 1$.
This happens close to a resonant frequency, where $\omega > \omega_k$ the frequency is higher as a close resonant frequency. This does not mean that the light in the medium is higher than the speed of light in vacuum but that its phase speed is [1](P.230). In figure 7 a simple multi oscillator model is shown to fit the measured spectra of $SiO_2$, data from [6] provided by the free online database "*refractiveindex.info*" [7]. Since this is only an illustration to show the behavior of the oscillators using a realistic example, one must overlook the fact that it only reflects reality to a very limited extent.
To keep the illustration simple, I took only three oscilators. One was placed in the UV below the

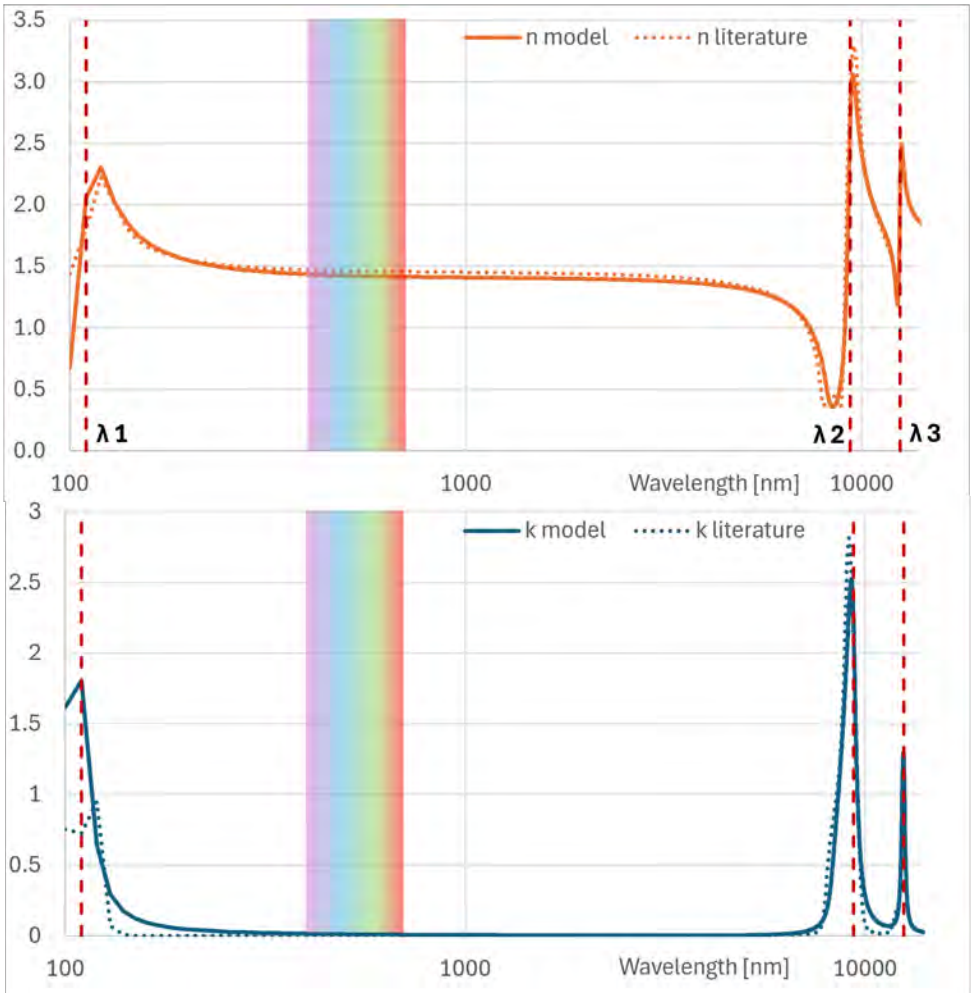


Figure 7: The figure is an approach to visualize realistic n and k for $SiO_2$. Three oscillators were summed up and plotted against measurement data from [6]. The visible range is highlighted and shows for the refractive index good agreement.

visible range and two phononic in the IR-range and optimized the values by hand.
To explain the graph, the resonance frequencies describe where each oscillator is located with $\omega_1 \approx 9.1 \cdot 10^{-3}\, nm^{-1} \rightarrow \lambda_1 = 110\, nm$, $\omega_2 \approx 1.07 \cdot 10^{-4}\, nm^{-1} \rightarrow \lambda_2 \approx 9.3 \cdot 10^{3}\, nm$ and $\omega_3 \approx 8 \cdot 10^{-5}\, nm^{-1} \rightarrow \lambda_3 = 1.25 \cdot 10^{4}\, nm$. The damping term describes how "fast" the oscillation loses energy, so the smaller $\gamma$, the sharper the peak. The damping constants are chosen here as $\gamma_1 = 1.2 \cdot 10^{-3}\, nm^{-1}$, $\gamma_2 = 5 \cdot 10^{-6}\, nm^{-1}$ and $\gamma_3 = 1.5 \cdot 10^{-6}\, nm^{-1}$. The plasma frequency describes the amplitude of the oscillator. Here with $\omega_{P,1} = 9 \cdot 10^{-3}\, nm^{-1}$, $\omega_{P,2} = 8 \cdot 10^{-5}\, nm^{-1}$ and $\omega_{P,3} = 2.5 \cdot 10^{-5}\, nm^{-1}$.

### 2.2.5 Absorption Coefficient

As light propagates through a material, it interacts with the electrons and atoms within it [2] (P.233), transferring part of its energy to them. This process, known as absorption, can occur through various mechanisms, such as the excitation of valence electrons, phonon excitation, or interactions with free charge carriers. To describe the effect of absorption, we begin by once again considering an electromagnetic wave propagating through an optical material.

$$\vec{E}(z,t) = \vec{E}_0 \cdot \mathbf{e}^{i(\tilde{k}z - \omega t)} \tag{59}$$

Here, $k$ denotes the complex wave number. It can be expressed using the complex refractive index $\tilde{n} = n - i\kappa$ as $k = \frac{2\pi}{\lambda}\tilde{n} = \frac{2\pi}{\lambda}(n - i\kappa)$. This leads to the expression for the electric field

$$\vec{E}(z,t) = \vec{E}_0 \cdot \mathbf{e}^{i(\omega t - \tilde{k}z)} = \vec{E}_0 \cdot \mathbf{e}^{i(\omega t - \frac{2\pi}{\lambda}(n - i\kappa)z)} = \vec{E}_0 \cdot \mathbf{e}^{-\frac{2\pi}{\lambda}\kappa z}\mathbf{e}^{i(\omega t - \frac{2\pi n}{\lambda}z)} \tag{60}$$

This leaves us with a real amplitude term, where we obtain a real wave number $k = \frac{2\pi n}{\lambda}$, and a damping term $\mathbf{e}^{-\frac{2\pi\kappa}{\lambda}z}$ that reduces the amplitude as a function of the distance traveled within the material.
The intensity of an electromagnetic wave describes its power density per unit area and can be expressed as [2] (P.78):

$$I_0 = \frac{1}{2}\epsilon_0 c|\vec{E}_0|^2 = \frac{c}{\mu_0}|\vec{B}_0|^2 \tag{61}$$

If we use the previously derived expression for the electric field in matter, we can express the position-dependent intensity within the material as:

$$I(z) = \frac{1}{2}\epsilon_0 c|\vec{E(z)}|^2 = \frac{1}{2}\epsilon_0 c|\vec{E}_0 \cdot \mathbf{e}^{-\frac{2\pi}{\lambda}\kappa z}\mathbf{e}^{i(\omega t - kz)}|^2 = I_0\mathbf{e}^{-\frac{4\pi}{\lambda}\kappa z} = I_0\mathbf{e}^{-\tilde{\alpha}z} \tag{62}$$

This formula shows the decrease in the intensity of the wave in a medium as a function of the distance traveled. The expression $\tilde{\alpha} = \frac{4\pi\kappa}{\lambda} = \frac{2\omega\kappa}{c}$ is called the absorption coefficient and depends on the material and the wavelength [1] (P.227).
Normally, the absorption coefficient is written only as $\alpha$ instead of $\tilde{\alpha}$, but as we already use alpha as the polarizability and also as angles, I chose to add a wave for better differentiation.

## 2.3 Electromagnetic Waves at Interfaces

To describe what happens to an electromagnetic wave when it moves from one material to another, we need to look at the interfaces of the materials. For a wave that leaves medium 1 and enters medium 2 we can decompose the vectors for the electromagnetic field in a parallel (tangential) and perpendicular (normal) part as $\vec{E} = \vec{E}_{pa} + \vec{E}_n$ and $\vec{B} = \vec{B}_{pa} + \vec{B}_n$ related to the surface. At the transition of the wave from one medium into another, the tangential part of the electric- and perpendicular part of the magnetic- waves have to be continuous, which follows with some extra work from Maxwell's Law 45. This means $\vec{E}_{1pa} = \vec{E}_{2pa}$ and $\vec{B}_{1n} = \vec{B}_{2n}$ at the interface.
Although the parallel component of the electric field stays constant in both materials, the electric field strength decreases in a dielectric medium by the relative dielectric constant $\epsilon$, which can be traced back to the normal component of the electric field [1] (P.235):

$$E_{1pa} = E_{2pa}, \quad \frac{E_{1n}}{E_{2n}} = \frac{\epsilon_2}{\epsilon_1} = \frac{n_2^2}{n_1^2} \tag{63}$$

For the magnetic part of the wave the perpendicular stays the same which means in the same relation that the parallel part has to change relative to the permeability:

$$B_{1n} = B_{2n}, \quad \frac{B_{1pa}}{B_{2pa}} = \frac{\mu_1}{\mu_2} \tag{64}$$

However, for non magnetic materials $\mu_{1,2} \approx 1$, which means $B_{1pa} \approx B_{2pa}$.
If a plane wave meets the boundary between two materials under an angle $\alpha$ we get a reflecting and a transmitting wave and we can describe the three waves in general as:

$$\begin{aligned} \vec{E}_i &= \vec{A}_i \cdot \mathbf{e}^{i(\omega_i t - \vec{k}_i\vec{r})} \\ \vec{E}_r &= \vec{A}_r \cdot \mathbf{e}^{i(\omega_r t - \vec{k}_r\vec{r})} \\ \vec{E}_t &= \vec{A}_t \cdot \mathbf{e}^{i(\omega_t t - \vec{k}_t\vec{r})} \end{aligned} \tag{65}$$

Also, with three waves, the principle of continuity needs to be fulfilled at the surface as $E_{ipa} = E_{rpa} = E_{tpa}$. We can set our coordinate system so that the incoming wave lies completely in the x-y plane, while the interface of the two materials is described by the x-axis and the point of the wave meeting the second material is at the origin of the coordinate system. This situation is shown in fig. 8. With the continuous condition for the tangential part of the electric wave that is valid for all times $t$ at the interface of the two materials at the origin of the coordinate system $r = 0$, we can conclude that all the waves have the same frequency $\omega = \omega_i = \omega_r = \omega_t$. This means that on transit, from medium 1 to medium 2 with different phase frequencies $\nu_{ph}$, only the wavelength can change.

$$\nu_{ph1} = \frac{c}{n_1} = \frac{\omega \cdot \lambda_1}{2\pi} \neq \nu_{ph2} = \frac{c}{n_2} = \frac{\omega \cdot \lambda_2}{2\pi} \tag{66}$$

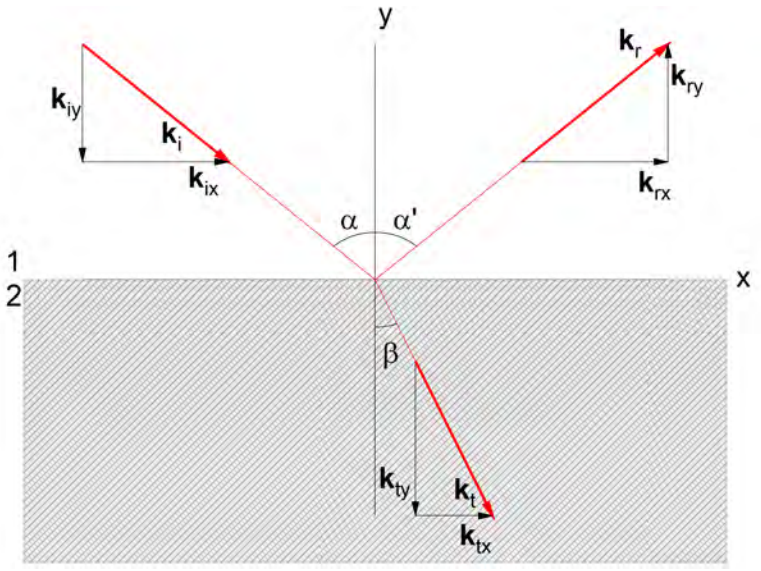


Figure 8: The propagation angles from an electromagnetic wave traveling from one material into another with the wave vectors for the incoming, transmitting and reflecting wave parts are shown.

We can develop the continuous condition for all the points at the interface of the two materials with $\vec{k}_i \cdot \vec{r} = \vec{k}_r \cdot \vec{r} = \vec{k}_t \cdot \vec{r}$. Because the interface lies in the x-z plane, the vectors $\vec{r}$ and $\vec{k}$ can be written as:

$$\vec{r} = x\vec{e}_x + z\vec{e}_z, \quad \vec{k}_i = k_{ix}\vec{e}_x + k_{iy}\vec{e}_y \tag{67}$$

From those equations we can see, with the previous condition, that $k_{ix} = k_{rx} = k_{tx}$ and $k_{iz} = k_{rz} = k_{tz}$, which means that also the reflected and transmitted waves have to move completely in the x-y plane and have no z-part. Together with the angles of incidence $\alpha$, $\alpha'$ and $\beta$, we can express the wave number as:

$$k_{ix} = k_i \cdot \sin(\alpha), \quad k_{rx} = k_r \cdot \sin(\alpha'), \quad k_{tx} = k_t \cdot \sin(\beta) \tag{68}$$

With the equation for the wave number $k = \frac{\omega \cdot n}{c}$ and the condition $k_{ix} = k_{rx} = k_{tx}$ this leads to:

$$n_1 sin(\alpha) = n_1 sin(\alpha') = n_2 sin(\beta) \tag{69}$$

With the same material for the incoming and also reflected wave, we can see that the angles for both waves are the same $\alpha = \alpha'$, and with some transforming we get Snell's Law [1] (P.237):

$$\frac{\sin(\alpha)}{\sin(\beta)} = \frac{n_2}{n_1} \tag{70}$$

For a brief explanation, in the English literature, the german acronyms "S" and "P" are commonly used for perpendicular and parallel components. For overview reasons I chose the symbols $\perp$ and $\parallel$ instead for identical terms.
Now we only looked at the wave vector and how it leads to the angle of the waves in dependence on the refractive indices. However, electric and magnetic fields can have components in all directions perpendicular to $\vec{k}$. So we can split the amplitude $\vec{A} = A_x, A_y, A_z$ of the waves in a parallel part relative to the x-y plane $\vec{A}_\parallel = A_x, A_y, 0$ and a vertical part relative to the x-y plane, namely, in the z-direction $\vec{A}_\perp = 0, 0, A_z$. Because of the continuous condition for parallel electric field components at the surface works also in this notation we can set $A_{i\perp} + A_{r\perp} = A_{t\perp}$. For non magnetic materials with $\mu \approx 1$ we can write for the magnetic part with $\vec{B} = 1/\omega(\vec{k} \times \vec{E})$:

$$(\vec{k}_i \times \vec{E}_i)\vec{e}_x + (\vec{k}_r \times \vec{E}_r)\vec{e}_x = (\vec{k}_t \times \vec{E}_t)\vec{e}_x \tag{71}$$

So we can write the equation:

$$k_{iy}A_{i\perp} + k_{ry}A_{r\perp} = k_{ty}A_{t\perp} \tag{72}$$

Together with $k_{ry} = -k_{iy}$ this leads to the expressions:

$$\begin{aligned} A_{i\perp} - A_{r\perp} &= \frac{k_{ty}}{k_{iy}} A_{t\perp} \\ \Rightarrow A_{t\perp} &= \frac{2}{1 + \frac{k_{ty}}{k_{iy}}} A_{i\perp} \\ \Rightarrow A_{r\perp} &= \frac{1 - \frac{k_{ty}}{k_{iy}}}{1 + \frac{k_{ty}}{k_{iy}}} A_{i\perp} \end{aligned} \tag{73}$$

For the parallel part of the electric field, also because of the continuous condition, we can write:

$$A_{i\parallel} \cos\alpha - A_{r\parallel} \cos\alpha = A_{t\parallel} \cos\beta \tag{74}$$

From the continuous condition for the parallel magnetic field in a non ferromagnetic material with $\nu_1 \approx \nu_2 \approx 1$ follows:

$$\begin{aligned} \frac{n_1}{c} A_{i\parallel} + \frac{n_1}{c} A_{r\parallel} &= \frac{n_2}{c} A_{t\parallel} \\ \Rightarrow A_{i\parallel} \cos\alpha - A_{r\parallel} \cos\alpha &= \frac{n_1}{n_2} A_{i\parallel} \cos\beta \\ \frac{A_{r\parallel}}{A_{i\parallel}} &= \frac{\cos\alpha - n_1/n_2 \cos\beta}{\cos\alpha + n_1/n_2 \cos\beta} \end{aligned} \tag{75}$$

Now with the relation of the angles $\frac{k_{iy}}{k_i} = \cos\alpha$, $\frac{k_{ty}}{k_t} = \cos\beta$ and the expression $k_t = (n_2/n_1)k_i$ we get the Fresnel Equations:

$$\begin{aligned} \rho_\perp = \frac{A_{r\perp}}{A_{i\perp}} &= \frac{n_1 \cos\alpha - n_2 \cos\beta}{n_1 \cos\alpha + n_2 \cos\beta} = -\frac{\sin(\alpha - \beta)}{\sin(\alpha + \beta)} \\ \rho_\parallel = \frac{A_{r\parallel}}{A_{i\parallel}} &= \frac{n_2 \cos\alpha - n_1 \cos\beta}{n_2 \cos\alpha + n_1 \cos\beta} = \frac{\tan(\alpha - \beta)}{\tan(\alpha + \beta)} \\ \tau_\perp = \frac{A_{t\perp}}{A_{i\perp}} &= \frac{2n_1 \cos\alpha}{n_1 \cos\alpha + n_2 \cos\beta} = \frac{2\sin\beta\cos\alpha}{\sin(\alpha + \beta)} \\ \tau_\parallel = \frac{A_{t\parallel}}{A_{i\parallel}} &= \frac{2n_1 \cos\alpha}{n_2 \cos\alpha + n_1 \cos\beta} = \frac{2\sin\beta\cos\alpha}{\sin(\alpha + \beta)\cos(\alpha - \beta)} \end{aligned} \tag{76}$$

Where $\rho_\perp$, $\rho_\parallel$ are called reflection coefficients in the perpendicular and parallel direction and $\tau_\perp$, $\tau_\parallel$ are called transmission coefficients also in the vertical and parallel direction and in sum they are called Fresnel coefficients. From this point we can calculate the reflectance $R$ and transmittance $T$ using the time averaged intensity $\bar{I}$ of an electromagnetic wave:

$$\begin{aligned} \bar{I}_i &= \epsilon_0 \epsilon_1 \frac{c}{n_1} \overline{E^2}_i = \epsilon_0 \epsilon_1 \frac{c}{n_1} \frac{1}{2} A_i^2 \\ \bar{I}_r &= \epsilon_0 \epsilon_1 \frac{c}{n_1} \overline{E^2}_r = \epsilon_0 \epsilon_1 \frac{c}{n_1} \frac{1}{2} A_r^2 \\ \bar{I}_t &= \epsilon_0 \epsilon_2 \frac{c}{n_2} \overline{E^2}_t = \epsilon_0 \epsilon_2 \frac{c}{n_2} \frac{1}{2} A_t^2 \end{aligned} \tag{77}$$

where $A_{i/r/t} = \sqrt{A_{i/r/t,\perp}^2 + A_{i/r/t,\parallel}^2}$ and $\bar{I}_{i,r,t} = \epsilon_0 \epsilon_{1,2} \frac{n_{1,2}}{c} \bar{E^2}_{i,r,t} = \frac{1}{2} \epsilon_0 \epsilon_{1,2} \frac{n_{1,2}}{c} A_{i,r,t}^2$. So we can describe $R$ and $T$ as:

$$\begin{aligned} R &= \frac{\bar{I}_r}{\bar{I}_i} = \frac{A_r^2}{A_i^2} \\ T &= \frac{\bar{I}_t \cos\beta}{\bar{I}_i \cos\alpha} = \frac{n_2 \cos\beta A_t^2}{n_1 \cos\alpha A_i^2} \end{aligned} \tag{78}$$

Because the parallel and perpendicular parts of the reflection- and transmission coefficient can be different we can see that the reflectance and transmittance depend not just on the angle of the incoming wave but also on the polarization which leads to the polarization dependent reflectance and transmittance of:

$$\begin{aligned}
R_\perp &= \frac{A_{r\perp}^2}{A_{i\perp}^2} = \left(\frac{n_1\cos\alpha - n_2\cos\beta}{n_1\cos\alpha + n_2\cos\beta}\right)^2 = \left(\frac{\sin(\alpha-\beta)}{\sin(\alpha+\beta)}\right)^2 \\
R_\parallel &= \frac{A_{r\parallel}^2}{A_{i\parallel}^2} = \left(\frac{n_2\cos\alpha - n_1\cos\beta}{n_2\cos\alpha + n_1\cos\beta}\right)^2 = \left(\frac{\tan(\alpha-\beta)}{\tan(\alpha+\beta)}\right)^2 \\
T_\perp &= \frac{n_2\cos\beta}{n_1\cos\alpha}\frac{A_{t\perp}^2}{A_{i\perp}^2} = \frac{n_2\cos\beta}{n_1\cos\alpha}\left(\frac{2n_1\cos\alpha}{n_1\cos\alpha + n_2\cos\beta}\right)^2 = \frac{n_2\cos\beta}{n_1\cos\alpha}\left(\frac{2\sin\beta\cos\alpha}{\sin(\alpha+\beta)}\right)^2 \\
T_\parallel &= \frac{n_2\cos\beta}{n_1\cos\alpha}\frac{A_{t\parallel}^2}{A_{i\parallel}^2} = \frac{n_2\cos\beta}{n_1\cos\alpha}\left(\frac{2n_1\cos\alpha}{n_2\cos\alpha + n_1\cos\beta}\right)^2 = \frac{n_2\cos\beta}{n_1\cos\alpha}\left(\frac{2\sin\beta\cos\alpha}{\sin(\alpha+\beta)\cos(\alpha-\beta)}\right)^2
\end{aligned} \tag{79}$$

Without absorption, the following equations have to apply:

$$\begin{aligned}
T_\parallel + R_\parallel &= 1 \\
T_\perp + R_\perp &= 1 \\
T + R &= 1
\end{aligned} \tag{80}$$

An example in which a light wave coming from air with $n_1 = 1$ meets a $Ta_2O_5$ layer with refractive index of $n_2 = 2.1$ is shown in figure 9. As you can see in a condition where $\alpha + \beta = 90°$, the parallel component of the reflection coefficient gets zero $\rho_\parallel = 0$ and therefore the parallel reflectance gets also zero $R_\parallel = 0$ where 100% of the parallel polarized light gets transmitted $T_\parallel = 1$. This angle is called the Brewster angle $\alpha_B$ and can be calculated by [1] (P.240):

$$\tan(\alpha_B) = \frac{n_2}{n_1} \tag{81}$$

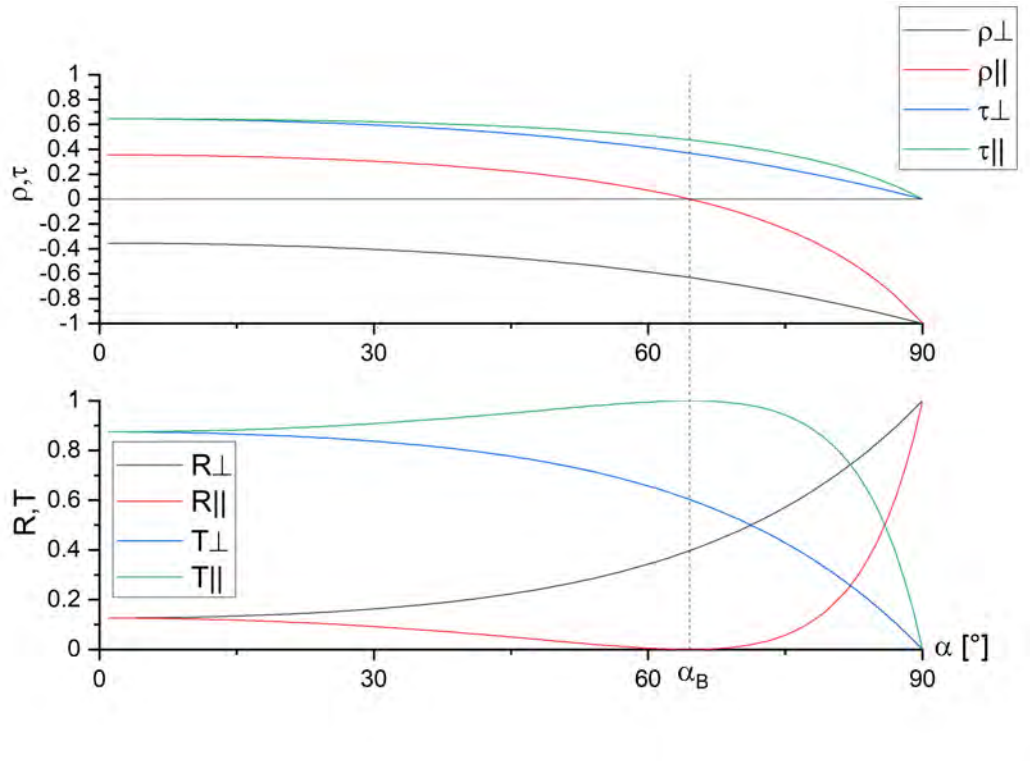


Figure 9: The graph shows the reflectance and transmittance with the reflection and transmission coefficient in dependence of the angle $\alpha$ for air $n_1 = 1$ and $Ta_2O_5$ with $n_2 = 2.1$ at $550\,nm$. With the Brewster angle $\alpha_B$.

# 3 Layer Design

While the previous chapter described the behavior of electromagnetic waves at interfaces and as they pass through materials, the focus now shifts to how we can make use of wave interference to design layer systems that manipulate light in a controlled and intended manner. In doing so, we make use of the fact that at each transition between two materials, light is partially reflected and partially transmitted. This results in a set of overlapping waves with different phase shifts.
This chapter first explains how this superposition can be calculated in general terms and then presents some practical examples using realistic filter designs.

## 3.1 Interference Effect at two Interfaces

If we consider equation from 79, we can see that the parallel and perpendicular components of reflection and transmission at the interface between two media can be calculated as functions of the angle of incidence and the refractive indices of the two materials.

### 3.1.1 Phase Shift with Backside Reflection

It is important to note that light is reflected not only at the front surface of an optically transparent material but also at its backside. The light reflected at the rear surface travels once more through the material and can again be reflected or transmitted at the front surface. If the beam reflected on the back side is transmitted to the front, it generates a beam ($R_2$) that propagates in the same direction as the one directly reflected ($R_1$), which can be seen in figure 10. The light reflected directly

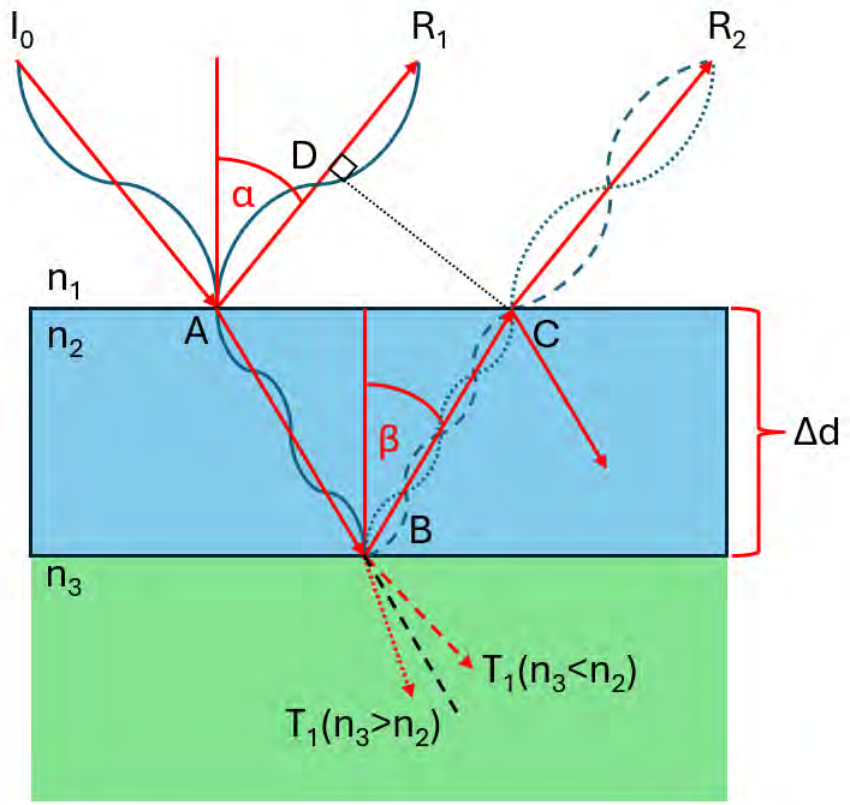


Figure 10: The figure shows a light beam entering a transparent material with a specific thickness and a split of the light beam at every interface into transmitting or reflecting parts. After exiting the material it can have a phase shift due to optical path difference compared to the other light beams in the same direction leading to interference effects.

on the surface exhibits an optical path difference of $A \rightarrow D$ compared to the light reflected on the

back surface, which follows the path $A \to B \to C$, until both beams are again parallel and propagate in the same direction. This optical path difference determines the interference effects that occur [1] (P.313), [8] (P.651).

$$\triangle s = n_2 \cdot \left[ |\vec{AB}| + |\vec{BC}| \right] - n_1 \cdot |\vec{AD}| \tag{82}$$

Using the fact that $|\vec{AB}| = |\vec{BC}| = \frac{\triangle d}{\cos\beta}$, $|\vec{AD}| = |\vec{AC}| \cdot \sin\alpha$, and $|\vec{AC}| = 2\triangle d \tan\beta$ we can express the equation as:

$$\triangle s = \frac{2n_2 \triangle d}{\cos\beta} - 2n_1 \triangle d \tan\beta \sin\alpha \tag{83}$$

Using Snell's Law 70 we can transform it to:

$$\begin{aligned} \triangle s &= \frac{2n_2 \triangle d}{\cos\beta} - 2n_1 \triangle d \underbrace{\tan\beta}_{\frac{sin\beta}{\cos\beta}} \sin\alpha \\ \triangle s &= \frac{2n_2 \triangle d}{\cos\beta} \left[ 1 - \underbrace{\frac{n_1}{n_2} \sin\beta \sin\alpha}_{\sin^2\beta} \right] = 2n_2 \triangle d \cos\beta \end{aligned} \tag{84}$$

We can thus calculate the optical path difference between the two waves.
However, we must consider the possibility of phase shifts at transitions.
When light is reflected at the boundary of a material with a refractive index higher than the medium from which it originates, a phase jump of 180° (or $\pi$) occurs. In our scenario, we assume that incident light comes from air or vacuum ($n_1 = 1$), and the optical material used $n_2$ has a higher refractive index ($n_2 > n_1$), meaning that the directly reflected light $R_1$ will undergo a phase jump. However, the question is what lies behind the optical layer. If the substrate or underlying material $n_3$ has an even higher refractive index ($n_3 > n_2$), then a phase jump will also occur there (dotted wave). If it is air, vacuum or another material with a refractive index lower than $n_2$ ($n_3 < n_2$), no phase jump will occur at that interface (dashed wave). This also leads to the situation where we have to distinguish between the two cases for the resulting phase difference of $\triangle\phi$ for
$n_3 < n_2$:

$$\triangle\phi = \frac{2\pi}{\lambda_1} \triangle s = \frac{2\pi}{\lambda_1} 2n_2 \triangle d \cos\beta \tag{85}$$

and with $n_3 > n_2$:

$$\triangle\phi = \frac{2\pi}{\lambda_1} \triangle s + \underbrace{\pi}_{phase\ jump} = \frac{4\pi n_2 \triangle d}{\lambda_1} \cos\beta + \pi \tag{86}$$

We can also consider two special cases: constructive and destructive interference. Constructive interference occurs when the total phase difference is an integer multiple $m$ of $2\pi m$, that is,

$$\triangle\phi_{constructive} = 2\pi \left[ \underbrace{\frac{\triangle s}{\lambda_1} + \overbrace{(\pi\ or\ 0)}^{potential\ phase\ jump}}_{=m\in\mathbb{Z}} \right] = 2\pi m \quad ; m \in \mathbb{Z} \tag{87}$$

Destructive interference occurs when the total phase difference is an integer multiple $m$ of $2\pi(m+1)$, that is,

$$\triangle\phi_{destructive} = 2\pi \left[ \underbrace{\frac{\triangle s}{\lambda_1} + \overbrace{(\pi\ or\ 0)}^{potential\ phase\ jump} + 1}_{=m\in\mathbb{Z}} \right] = 2\pi m + 1 \quad ; m \in \mathbb{Z} \tag{88}$$

Therefore, it is possible to calculate the phase difference between the two reflected beams $R_1$ and $R_2$. However, it must be noted that the example shown is a strong simplification. At point $B$ in the diagram, it can be seen that part of the beam is transmitted into the medium 3. This portion is again partially reflected and partially transmitted on the back side of the material and therefore can return to the interface between materials 2 and 3, where it can also contribute to interference

effects influencing the reflected beams $R1$ and $R_2$. Furthermore, at point $C$, one can see that even at the interface from material 2 back to material 1, a portion of the beam that forms $R_2$ is again reflected toward material 3 where it would again separate into a reflecting and transmitting part, causing possible interference effects with $T_1$. This results in a quasi-infinite series of beam divisions into reflected and transmitted components between the layers, all of which contribute to the total reflected and transmitted intensities and interfering with each other. However, since the components $T1$ as well as $R_1$ and $R_2$ represent the dominant contributions, it is common to neglect the higher order components for the sake of simplification for this scenario where we focus on the interference behavior of two waves from two reflecting transition zones of the same layer.

### 3.1.2 Internal Multi Reflection

After the previous section explained how to calculate the phase difference of waves reflected at different interfaces, the intensity ratios of the individual waves still need to be known in order to determine the resulting interference behavior. In Equation 62, the absorption coefficient $\alpha$ was introduced. It describes the decrease in the amplitude of a wave's intensity as it propagates through a material. Together with the splitting of the light beam at each interface, we can calculate this intensity in order to subsequently determine the completely reflected and transmitted components, taking into account all interference effects and absorption. In Figure 11, we see a light beam with intensity $I_0$ incident

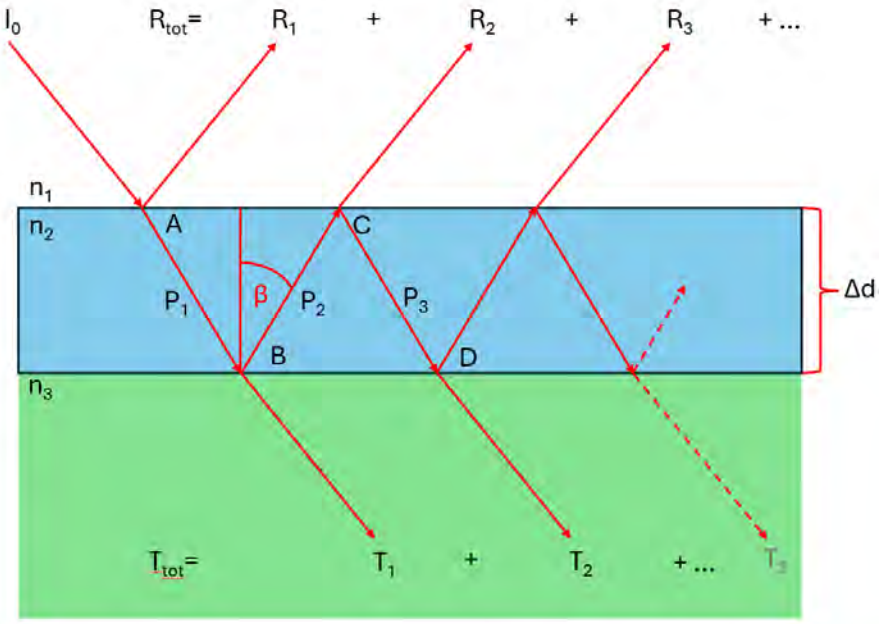


Figure 11: This Figure shows how the total reflection and total Transmission on an optical thin film sums up. It also shows the influence of absorption in those paths.

on a thin layer at the point "$A$". Depending on the refractive indices of the materials $n_1$ and $n_2$, as well as the angle and polarization, a portion is directly reflected as a beam $R_1 = R_{FS}$. This value can be calculated directly from Equation 79 and in this case is simply referred to as $R_{FS}$ (Frontside) for simplicity. Another portion passes through the material at this point as beam $P_1$ for (passing), traveling toward the point "$B$". For simplicity, the distance traveled will henceforth be denoted as $l = d/\cos\beta$. When the beam reaches point "$B$", its intensity has been reduced due to absorption. This decrease can be described according to 62 by the factor $A_1 = \mathbf{e}^{-\alpha l}$. At point "$B$", the beam $P_1$ is again split into two partial beams: one reflected at the backside back into the medium as beam $P_2$, and one transmitted out of the material as beam $T_1$. This ratio, $R_{BS}$, again depends on the two refractive indices and may differ from $R_{FS}$ depending on what is present on the backside of the film.

We can therefore write $T_1$, the first order transmitted beam as:

$$T_1 = I_0 \left[ (1 - R_{FS}) \cdot \underbrace{\mathbf{e}^{-\alpha l}}_{=A_1} \cdot (1 - R_{BS}) \right] \tag{89}$$

However, from point "$B$", another portion of the wave propagates as "$P_2$" towards "$C$". This component undergoes the same absorption as "$P_2$", given by $A_1 = A_2 = \mathbf{e}^{-\alpha l} = \mathbf{e}^{-\alpha \frac{d}{cos\beta}} = A$. At point "$C$", this wave is again split into two components: The part transmitted at the front surface, "$R_2$", and a reflected component, "$P_3$". We can then express "$R_2$" as follows:

$$R_2 = I_0 \left[ (1 - R_{FS})^2 \cdot \underbrace{\mathbf{e}^{-2\alpha l}}_{=A_1} \cdot (R_{BS}) \right] \tag{90}$$

Following the same principle, we can find expressions for the next transmitting and also reflecting beam parts as:

$$T_2 = I_0 \left[ (1 - R_{FS})(1 - R_{BS}) \cdot A^3 \cdot R_{FS} \cdot R_{BS} \right] \tag{91}$$

and

$$R_3 = I_0 \left[ (1 - R_{FS}) \cdot A^4 \cdot R_{FS} \cdot R_{BS}^2 \right] \tag{92}$$

which shows a pattern we can express as

$$\frac{T_n}{I_0} = (1 - R_{FS})(1 - R_{BS}) \cdot A^{2n-1} \cdot R_{FS}^{n-1} \cdot R_{BS}^{n-1} : \forall n \in \mathbb{N} \tag{93}$$

and

$$\frac{R_n}{I_0} = (1 - R_{FS})^2 \cdot A^{2(n-1)} \cdot R_{BS}^{n-1} \cdot R_{FS}^{n-2} : \forall n \in \mathbb{N} \backslash \{1\} \tag{94}$$

where $\frac{R_1}{I_0} = R_{FS}$. So, if we want to express the total reflected $R_{tot} = \sum_{n=1}^{\infty} R_n$ and total transmitted part of the light $T_{tot} = \sum_{n=1}^{\infty} T_n$ we can calculate them using the geometric series with $\sum_{k=0}^{\infty} q^k = \frac{1}{1-q}$ if $|q| < 1$ as [1] (P.319):

$$\begin{aligned} T_{tot} &= (1 - R_{FS})(1 - R_{BS}) \cdot A \sum_{m=0}^{\infty} A^{2m} R_{FS}^m R_{BS}^m = \frac{A(1 - R_{FS})(1 - R_{BS})}{1 - A^2 R_{FS} R_{BS}} \\ R_{tot} &= R_{FS} + (1 - R_{FS})^2 A^2 R_{BS} \sum_{m=0}^{\infty} A^{2m} R_{FS}^m R_{BS}^m = R_{FS} + \frac{A^2 R_{BS}(1 - R_{FS})^2}{(1 - A^2 R_{FS} R_{BS})} \end{aligned} \tag{95}$$

To illustrate the different influences on the reflectivity of a single layer, these effects are shown in figure 12. The calculation is based on a $100\,nm$ thick $Ta_2O_5$ layer at an incidence angle of $0°$, using material parameters obtained from a measurement within the scope of this project, which will also be used for subsequent calculations. First, the influence of the front-surface reflection due to the refractive index difference between air and the coating layer is shown (green), this corresponds to $R_{FS} = R_1$ in equation 95. It is calculated using the formula 79, as we only calculate with $0°$ there is no difference for the parallel and perpendicular polarized field and the formula reduces to $R = \left[ \frac{n_2 - n_1}{n_2 + n_1} \right]^2$.
To simplify the calculation, it is assumed that it is a standalone film without any substrate behind to obtain the same refractive index ($n_{Air/Vac} = 1$) in front as behind the $Ta_2O_5$ film. Combined with the back-surface reflection (blue), it becomes clear that the total reflectivity does not simply double even if $R_{FS} = R_{BS}$. This is because the portion of the beam reaching the back surface no longer carries the full intensity of the initial wave, as part of it has already been reflected at the front. In addition, in the case of the solid line, part of the light is also absorbed by the layer. The difference between the calculation with and without absorption is particularly evident in the short wavelength region on the left side of the figure. At $200\,nm$, the absorption of the layer is so strong that nearly the entire reflectivity arises from the front surface, rendering the contribution from the back surface negligible.
The interference effects resulting from phase shifts were then taken into account (red). Again, the solid line represents the calculation including absorption, whereas the dashed line shows the result without absorption. It is clearly visible where constructive and destructive interference occurs. In the short

wavelength region, the impact of absorption is also evident, highlighting how significantly it influences the interference pattern.
Note that this is a purely theoretical calculation that cannot be exactly reproduced in practice, as it is very difficult to fabricate a layer this thin without a substrate. However, for the purposes of the calculation, it represents the simplest and most comprehensible way to illustrate the relevant effects.

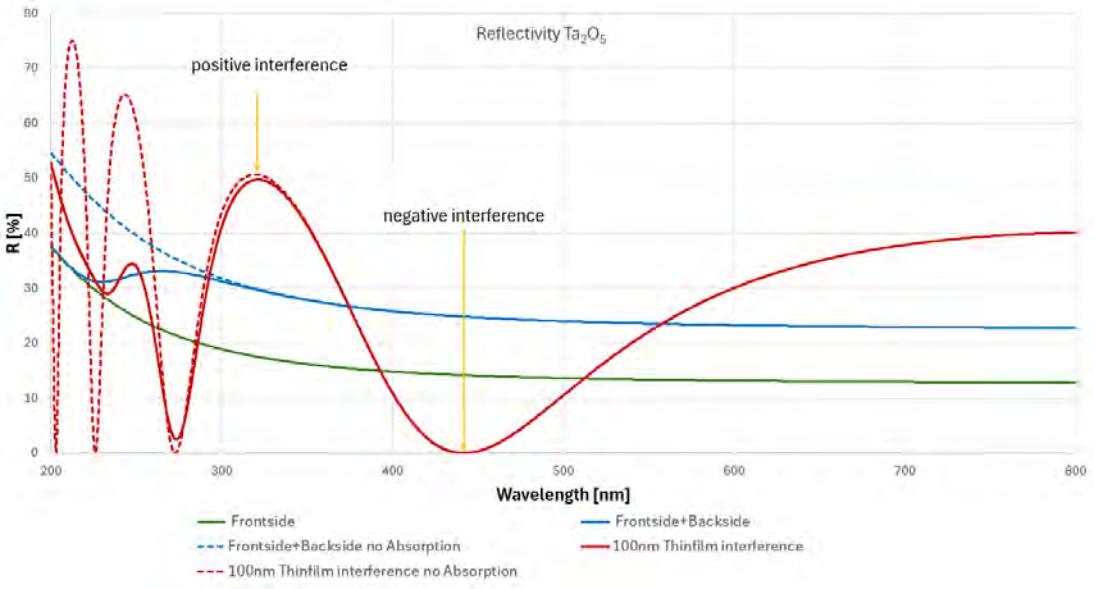


Figure 12: The figure shows the different reflection effects at a $100\,nm$ thick $Ta_2O_5$ layer under an angle of 0°. On the one hand, there is the simple reflection at the front surface due to the refractive index difference (green) which would correspond to $R_{FS} = R_1$ in 95. For comparison, the front-surface reflection combined with the back-surface reflection is shown (blue), calculated as in 95, both with absorption (solid line) and without absorption (dashed line). Additionally, the interference effect as a function of wavelength is shown (red), also both with (solid) and without absorption (dashed).

## 3.2 Calculation of Complex Filters

In the previous chapter, we demonstrated how to calculate the interference and propagation of waves in a single-layer system. The same principle can be extended to multilayer structures. However, this approach presents a significant challenge: at each interface between two layers, part of the incident wave is reflected, while another part is transmitted. As the number of layers increases, the number of resulting optical paths grows rapidly, making it impractical to analytically derive the individual contributions by hand. To address this complexity and enable the analysis of more advanced designs, the transfer matrix method is used [9], [10], [11](P.41/51). We now consider a system consisting of a number $N$ of optically plane-parallel layers with refractive indices $n_j \in n_1, n_2, ..n_{N+1}$ where the layers $n_1$ to $n_N$ have a finite thickness $d_j \in d_1, d_2, ..d_N$. $n_0$ and $n_{N+1}$ represent the refractive indices of the surrounding media, assumed $n_0 = n_{N+1} = 1$ to be air or vacuum with semi infinite thickness.
The electric wave in layer $j$ can be considered as a superposition of a forward and backward propagating wave, given by:

$$E_j(z) = A_j \mathbf{e}^{ik_{j,z}z} + B_j \mathbf{e}^{-ik_{j,z}z} \tag{96}$$

while $k_{j,z} = \frac{2\pi n_j}{\lambda} \cos\theta_j$ describes the wavenumber of the respective layer.
The phase shift within the path $l_j = d_j \cdot \cos\theta_j$, compared to the equation 86, can be described as:

$$\delta_j = k_j l_j = \frac{2\pi n_j d_j \cos\theta_j}{\lambda} \tag{97}$$

and use it in a matrix to describe the phase shift for both ways in each specific layer as:

$$\mathbf{P}_j = \begin{pmatrix} e^{i\delta_j} & 0 \\ 0 & e^{-i\delta_j} \end{pmatrix} \tag{98}$$

So far, no absorption has been taken into account. However, it becomes relevant at this point. As shown in 62, the real refractive index can be replaced by a complex one. The calculation then formally remains unchanged, but a damping term arises that describes the absorption and becomes part of the variable $\delta_j \to \tilde{\delta}_j = \frac{2\pi\tilde{n}_j l}{\lambda} = \frac{2\pi(n_j - i\kappa_j)l}{\lambda}$, making it complex.
To describe the behavior at the interface of two layers, we need to express it with an interface matrix

$$\mathbf{I}^{\perp,\parallel}_{j,j+1} = \frac{1}{\tau^{\perp,\parallel}_j} \begin{pmatrix} 1 & \rho^{\perp,\parallel}_j \\ \rho^{\perp,\parallel}_j & 1 \end{pmatrix} \tag{99}$$

while:

$$\begin{aligned} \rho^{\perp,\parallel}_j &= \frac{\eta^{\perp,\parallel}_j - \eta^{\perp,\parallel}_{j+1}}{\eta^{\perp,\parallel}_j + \eta^{\perp,\parallel}_{j+1}} \\ \tau^{\perp,\parallel}_j &= \frac{2\eta^{\perp,\parallel}_j}{\eta^{\perp,\parallel}_j + \eta^{\perp,\parallel}_{j+1}} \end{aligned} \tag{100}$$

with [11] (P.37):

$$\begin{aligned} \eta^{\perp}_j &= -i\sqrt{\tilde{n}_0^2 \sin^2\theta_0 - \tilde{n}_j^2} \\ \eta^{\parallel}_j &= +i\frac{\tilde{n}_j^2}{\sqrt{\tilde{n}_0^2 \sin^2\theta_0 - \tilde{n}_j^2}} \end{aligned} \tag{101}$$

This gives us with Snells law 70 the same expression for $\rho^{\perp,\parallel}_j$ and $\tau^{\perp,\parallel}_j$, as described with the Fresnel coefficients of equation 76 for each individual layer. To express the whole system, we can use the system transfer matrix [9]:

$$\mathbf{M}^{\perp,\parallel} = \mathbf{I}^{\perp,\parallel}_{0,1} \cdot \mathbf{P}_1 \cdot \mathbf{I}^{\perp,\parallel}_{1,2} \cdot \mathbf{P}_2 \cdot \mathbf{I}^{\perp,\parallel}_{2,3} \cdot \cdot ... \cdot \mathbf{I}^{\perp,\parallel}_{N-1,N} \cdot \mathbf{P}_N \cdot \mathbf{I}^{\perp,\parallel}_{N,N+1} \tag{102}$$

We then insert these into a system in which $A_0$ represents the incident wave and $B_0$ the reflected wave on the front side of the substrate, while $A_{N+1}$ denotes the transmitted wave that exits the multilayer system. There is no backward wave on the semi infinite substrate, therefore $B_{N+1} = 0$.

$$\begin{pmatrix} A_0 \\ B_0 \end{pmatrix} = \mathbf{M}^{\perp,\parallel} \begin{pmatrix} A_{N+1} \\ \underbrace{B_{N+1}}_{=0} \end{pmatrix} = A_{N+1} \begin{pmatrix} M_{11} \\ M_{21} \end{pmatrix} \tag{103}$$

From this, the reflection and transmission values can be calculated analogously to equation 79 using:

$$\begin{aligned} R^{\perp,\parallel}_{tot} &= |r|^2 = |\frac{B_0}{A_0}|^2 = |\frac{M_{21}}{M_{11}}|^2 \\ T^{\perp,\parallel}_{tot} &= |t|^2 \cdot \Re\left(\frac{\eta^{\perp,\parallel}_{N+1}}{\eta^{\perp,\parallel}_0}\right) = |\frac{A_{N+1}}{A_0}|^2 \cdot \Re\left(\frac{\eta^{\perp,\parallel}_{N+1}}{\eta^{\perp,\parallel}_0}\right) = |\frac{1}{M_{11}}|^2 \cdot \Re\left(\frac{\eta^{\perp,\parallel}_{N+1}}{\eta^{\perp,\parallel}_0}\right) \end{aligned} \tag{104}$$

The part: $\Re\left(\frac{\eta^{\perp,\parallel}_{N+1}}{\eta^{\perp,\parallel}_0}\right)$ comes from the energy flux in the system and is caused by the loss within the layer [11] (P.30),[9]. This system is typically used in design software to calculate complex multilayer systems. However, it must be noted that this requires plane-parallel and homogeneous layers without scattering losses and also plane waves [10].
This type of transfer matrix method (TMM) can be used for many different calculations and is discussed in more detail in section 10.3 where it is used to calculate possible quantum states in a series of potential wells.

## 3.3 Standard Multilayer Systems

We have discussed in detail how to calculate the resulting reflections and transmissions for both a single layer and an entire multilayer system. Depending on the materials used, their thicknesses, and the angles of incidence, various optical effects can occur that can be deliberately exploited for specific applications.
As the whole topic becomes much more complicated and complex, all designs are in a normal incidence.

### 3.3.1 AR-Coatings

One of the most widespread applications of optical interference coatings is anti-reflection (AR) coating. The objective in this case is to achieve minimal reflection at a substrate surface. In simple cases, this can be tailored for a single wavelength or a narrow spectral band, as is often required in laser applications where sharply defined frequencies are used. However, AR coatings can also be designed for broadband performance, which is essential in everyday applications such as eyeglasses, display screens, watches or optical windows [11] (P.96). The fundamental idea is based on destructive interference, in which secondary reflections cancel out the primary reflection, as can already be inferred from Figure 12. The simplest implementation of this principle is a single quarter-wave anti-reflection (AR) coating. In this case, a single layer with a physical thickness of $d_{phy} = \frac{\lambda_0}{4n_{layer}}$ is deposited onto the substrate, while $\lambda_0$ is the design wavelength, the desired wavelength for the AR-coating, and $n_{layer}$ is the refractive index of the coated layer, which as an additional condition needs to have the value $n_{layer} = \sqrt{n_{Air} \cdot n_{Sub}}$ while $n_{Sub}$ is the refractive index of the substrate [8] (P.696). As simple as it sounds, the condition to have a specific refractive index for the layer is often not that easy to match. This is why it is often necessary to extend the coating by a second layer, resulting in a high refractive index material $n_H$ on the substrate and on top of that a low refractive index material $n_L$, the so called V-coating [11] (P.105). If both layers have one so called quarter wave optical thickness (QWOT):

$$d_H^{phy} = \underbrace{\frac{\lambda_0}{4n_H}}_{QWOT_H}, \qquad d_L^{phy} = \underbrace{\frac{\lambda_0}{4n_L}}_{QWOT_L} \tag{105}$$

It is possible to design an anti-reflection coating with two layers of each a quarter wave thickness which in theory reaches a reflection of $R = 0$ if the condition is satisfied.

$$\left(\frac{n_H}{n_L}\right)^2 = \frac{n_{sub}}{n_0} \tag{106}$$

is met [8] (P.696), [11] (P.105) Where:

$n_{sub}$ ... is the refractive index of the substrate at the design wavelength

$n_0$ ... is the refractive index of the surrounding medium, most often air or vacuum with $n_0 = 1$

This gives an additional degree of freedom because we don't need a specific refractive index anymore for a given substrate but only a ratio in refractive indices of the two used materials.
In reality it is again not that easy to find a combination of materials which fits the condition perfectly, so it is necessary to change the thickness of the two materials to optimize the design, which means that in reality it is not possible to achieve exactly $R = 0$ but a very low value [11] (P.106).

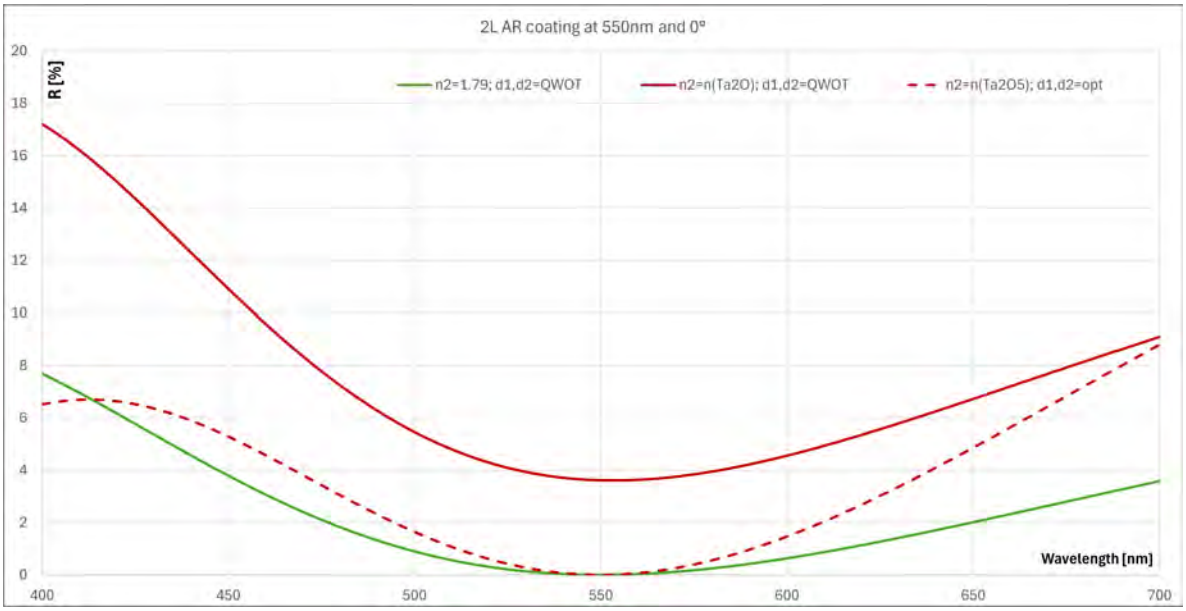


Figure 13: Three different designs are displayed. The green line shows a V coating which meets the condition 106 using $n_{SiO_2}$ at $550\,nm$ while $n_H \equiv 1.79$. The red solid line shows the same design but with $n_H = n_{Ta_2O_5}$ but both again as QWOT design. The red dashed line shows again the realistic refractive indices of $SiO_2$ and $Ta_2O_5$ but optimized in thickness with $d_L = 0.66 \cdot QWOT_L$ and $d_H = 1.67 \cdot QWOT_H$. Backside reflection is neglected in this calculation.

In figure 13 three AR coatings are presented. All are calculated on Herasil (Fused Silica) with a refractive index of $n_{Herasil} = 1.46$ at the design wavelength of $550\,nm$. With the condition from equation 106 it leaves a ratio of $\sqrt{\frac{n_{sub}}{n_0}} \approx 1.208$. For the first design, shown as the green solid line $SiO_2$ was chosen as outer low refractive index material with a refractive index of $n_{SiO_2} = 1.48$ which fixes the necessary high refractive index material at $n_H = 1.79$.
The same design but with the measured refractive index of $Ta_2O_5$ instead of the artificial $n_H$ which has a refractive index of roughly $n_{Ta_2O_5} = 2.17$ at $550\,nm$ it is evident that the design does not meet the criteria. The same pair of materials, but with optimized thicknesses of $d_L = 0.66 \cdot QWOT_L$ and $d_H = 1.67 \cdot QWOT_H$ is shown with the dashed red line.
If we need a broader AR-coating, we have to implement more layers [11] (P.117). However, this also results in the fact that it is not possible to create a realizable layer design that achieves a reflectivity value of $R = 0$ over an extended spectral range; this means not just at a single wavelength. Therefore, it is crucial to be aware of the specific requirements of the coating design. Broad anti-reflection ranges often exhibit local minima and maxima within the target spectral region. An example of a 6 layer AR coating is shown in figure 14, together with a 2, 4 and 14-layer design. The E-field together with the design structure is shown in figure 15.

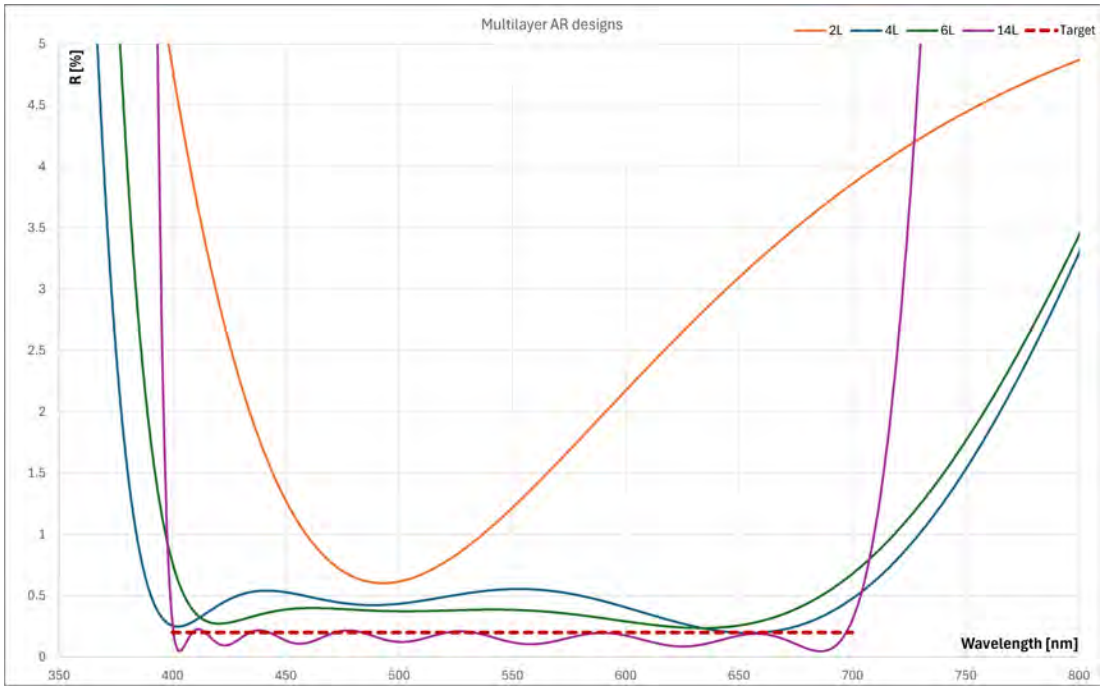


Figure 14: Four different multi layer designs for anti-reflective coatings in the visible range $400 - 700\,nm$. It is apparent, that the more layers are added to a design the higher are degrees of freedom to achieve the desired target of $R = 0\,^{+0.2}_{-0.0}$ %. Backside reflection is taken out of calculation for all designs.

The same principle applies here as in most optical coating designs: The more layers are used, the broader and more precisely defined the desired spectral regions can be, and the steeper the transitions in the design can be shaped. However, it must also be noted that this comes with certain disadvantages. A higher number of layers not only increases the production complexity as a result of increased material consumption and longer deposition times. In addition, the possibility of deviations in the process, stress, particles, and other negative impacts increases with both the number of layers and the total coating duration.

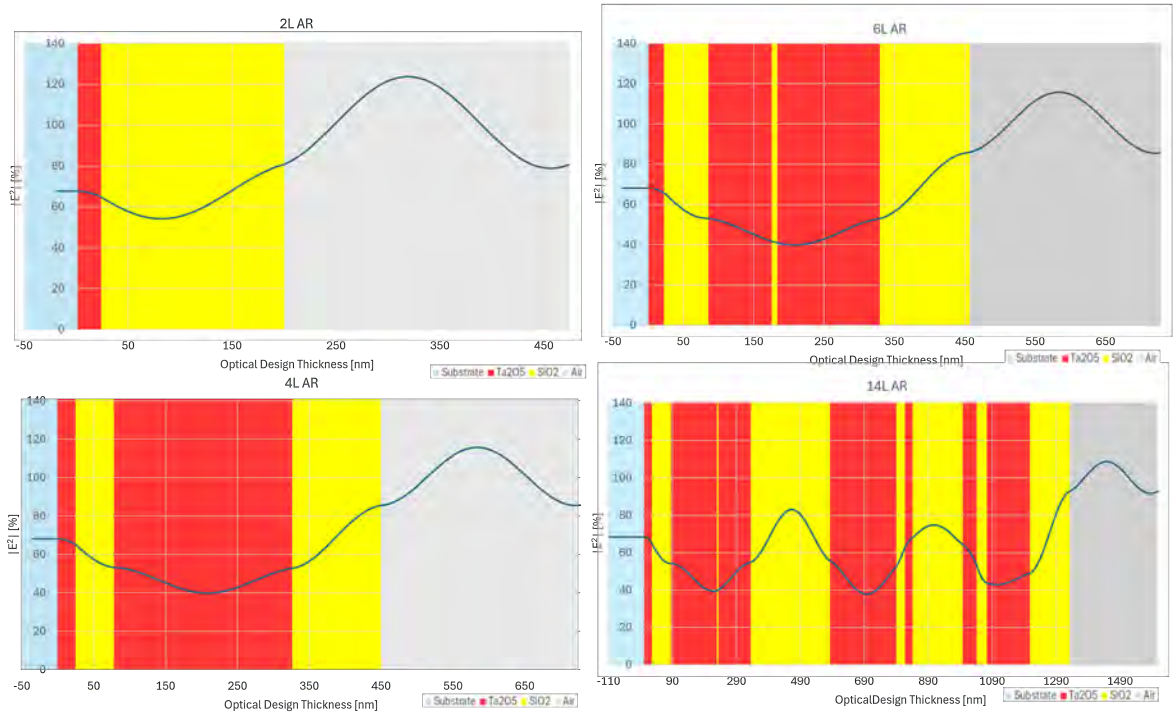


Figure 15: The figure shows the four anti reflection design where the layer structure is compared to the E-field intensity. On the left side is always the substrate, followed by red the $Ta_2O_5$, yellow the $SiO_2$ and grey the air with the incoming wave. The E-field is calculated at the design wavelength of $550\,nm$, using Optilayer.

### 3.3.2 Bragg Mirror

A Bragg- or $\frac{\lambda}{4}$- mirror is a fundamentally simple mirror design that is widely used in practice. It consists of a sequence of alternating high- and low-refractive-index layers, each with a QWOT. This configuration ensures that the reflected partial waves constructively interfere, thereby maximizing the overall reflection. Simultaneously, the transmitted wave components propagating toward the substrate experience destructive interference, resulting in the majority of the incident energy being reflected, and thus in high reflection at the design wavelength.

Rather than deriving the calculation here, it should be noted that the reflectivity can be easily estimated using the formulas provided in [11] (P.188).

$$R = \left[\frac{n_0 - n_{eff}}{n_0 + n_{eff}}\right]^2; \qquad n_{eff} = n_{Sub}\left(\frac{n_H}{n_L}\right)^N \tag{107}$$

while $N$ describes the number of layers in the system. In figure 16 four Bragg mirrors are depicted with different layer count for comparison. The higher the difference of the two used refractive indices, the wider the blocking range of the mirror. The possible range can be approximated using the formula [11] (P.193):

$$\frac{\triangle\lambda_{eff}}{\lambda_0} \approx \frac{4}{\pi} \cdot \arcsin\left(\frac{n_H - n_L}{n_H + n_L}\right) \tag{108}$$

### 3.3.3 Fabry-Pérot Interferometer

A Fabry-Pérot interferometer is an optical multilayer system based on the principle of interference. It consists of two highly reflective mirrors separated by a transparent spacer element. Although most of the incident light is reflected by the mirrors, a portion enters the cavity and undergoes multiple internal reflections between the mirrors. These repeated reflections give rise to standing waves within the cavity. At specific wavelengths where constructive interference occurs, the transmitted intensity is significantly enhanced. With each round trip, a small fraction of the light is transmitted through

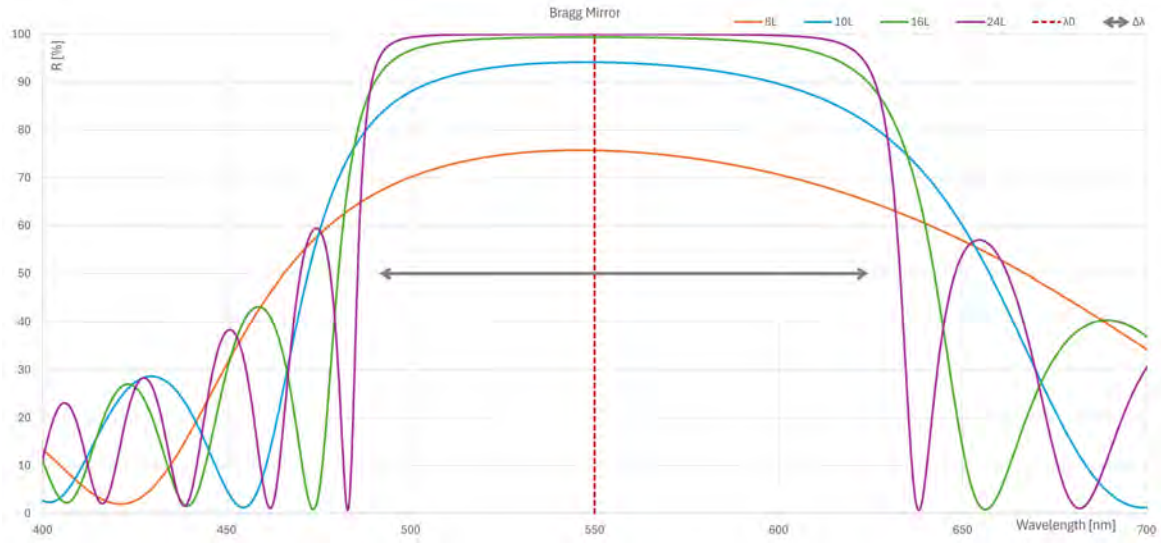


Figure 16: Bragg mirrors with a different number of layers are plotted. The maximal possible reflection at the design wavelength of $\lambda_0 = 550\,nm$ are displayed and show the increasing necessary number of layers to improve the reflectivity. Also the discussed approximation of the possible reflecting width $\triangle\lambda \approx 132.8\,nm$ is displayed. As the realistic mirror is not symmetrically around the design wavelength, the indicated range of $\triangle\lambda$ was shifted by hand by $8\,nm$.

the second mirror. This structure creates an extremely thin transmission peak, while light at other wavelengths is strongly suppressed in transmission. The position of these peaks in the spectrum depends on the optical thickness of this cavity and thus on the physical thickness and refractive index of the spacer material.
The expression for the effectively transmitted wave, which results from the superposition of multiple internally reflected waves, can be derived analogously to equation 95 using a geometric series. The resulting formula is given by [11] (P.184):

$$T_{FP}(\lambda) = \frac{(1 - R(\lambda))^2}{1 + F \sin^2 \delta(\lambda)/2} \tag{109}$$

where $\delta = \frac{4\pi nd}{\lambda}$ again describes the phase shift and $F = \frac{4R}{(1-R)^2}$ is the finesse factor of the system. So, if the resonance condition

$$\delta = 2m\pi \rightarrow \lambda = \frac{2nd}{m}; m \in \mathbb{N} \tag{110}$$

is fulfilled, the system will have a sharp transmission.
The Fabry-Pérot interferometer thus functions as a wavelength-selective filter with periodic transmission maxima. The sharpness (or finesse) $\mathcal{F}$ of these maxima is directly dependent on the reflectivity of the mirrors[8](P.686).

$$\mathcal{F} = \frac{\pi\sqrt{F}}{2} = \frac{\pi\sqrt{R}}{1 - R} \tag{111}$$

With the width of the line of [8](P.688):

$$\Delta\lambda_{FWHM} \approx \frac{\lambda_0^2}{2nd\mathcal{F}} \tag{112}$$

When $\Delta\lambda_{FWHM}$ describes the "full width at half-maximum", the width of a peak at half its height.
In figure 18 four different designs for Fabry-Pérot filters are calculated and displayed. All designs are built with two Bragg mirrors around a $2\,QWOT$ spacer layer. The designs are kept simple, but show the influence of higher reflectivity in finesse and also in bandwidth. The approximation for the bandwidth works better with higher mirror quality. As the design wavelength $\lambda_0 = 658\,nm$ was chosen,

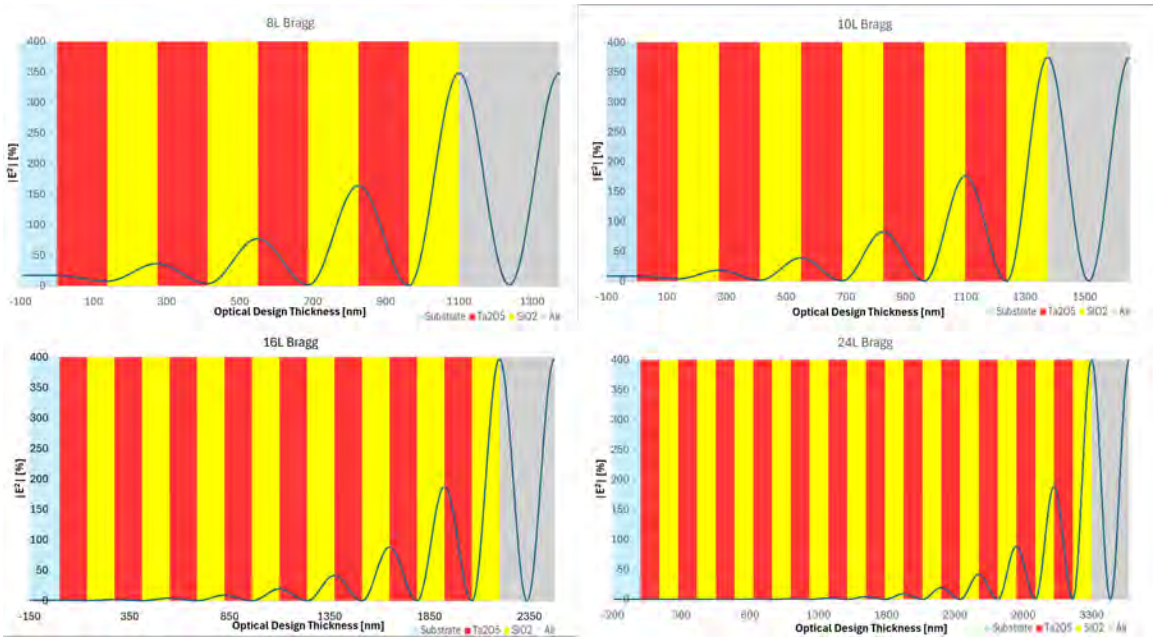


Figure 17: The figure shows the four Bragg mirror designs where the layer structure is compared to the E-field intensity. On the left side is always the substrate, followed by red the $Ta_2O_5$, yellow the $SiO_2$ and grey the air with the incoming wave. The E-field is calculated at the design wavelength of $550\,nm$, using Optilayer.

the design with $N = 9$ is planned as part of a telescopic assembly to work as a $H\alpha$-band pass. $H\alpha$ describes the first Balmer series of the hydrogen atom with a wavelength of

$$\lambda(H\alpha) = \frac{1240[eV\ nm]}{Ry^*(H)} \underbrace{\left(\frac{1}{n_1^2} - \frac{1}{n_2^2}\right)}_{=5/36 \text{ for } n_1=2;\ n_2=3} = 656.6\,nm \tag{113}$$

Where $Ry^*(H) \approx 13.6eV$ the ionization energy of the hydrogen atom and $n_1$ and $n_2$ the energy states of the electron.

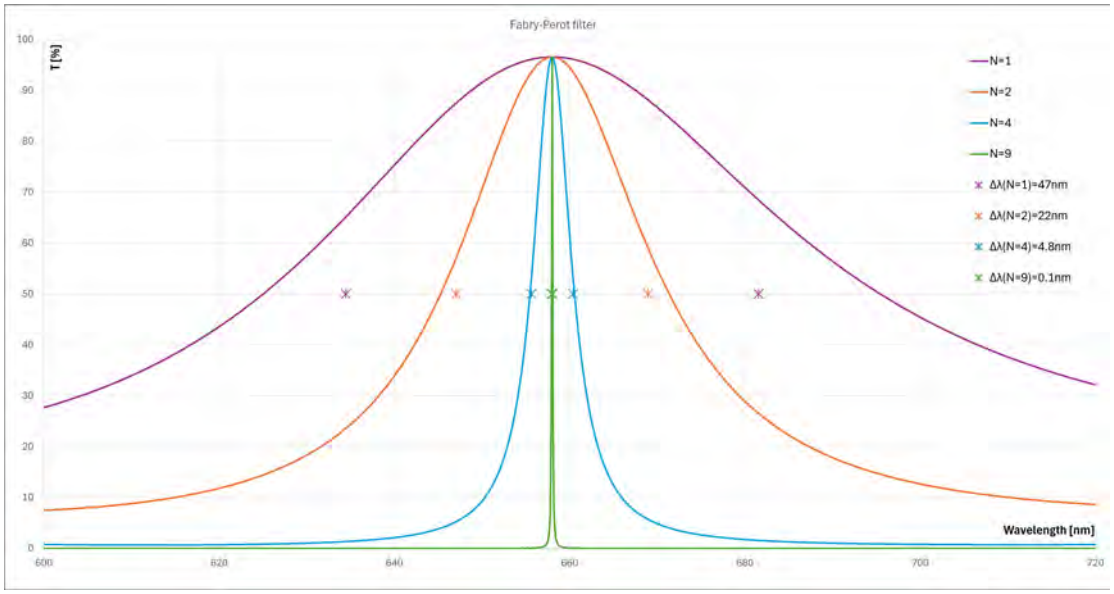


Figure 18: In the figure different Fabry-Pérot designs for a transmission line at $\lambda_0 = 658\,nm$ are presented. All of them are constructed as $(HL)^N\ H2L\ (HL)^N\ H$, while $N \in 1, 2, 4, 9$. The $2L$ layer works as spacer for the interferometer while left and right are two Bragg mirrors attached. It is visible, the higher the number of layers in the Bragg mirrors, the higher the reflectivity and the higher the finesse and the narrower the transmission line. Approximated line width is calculated and added.

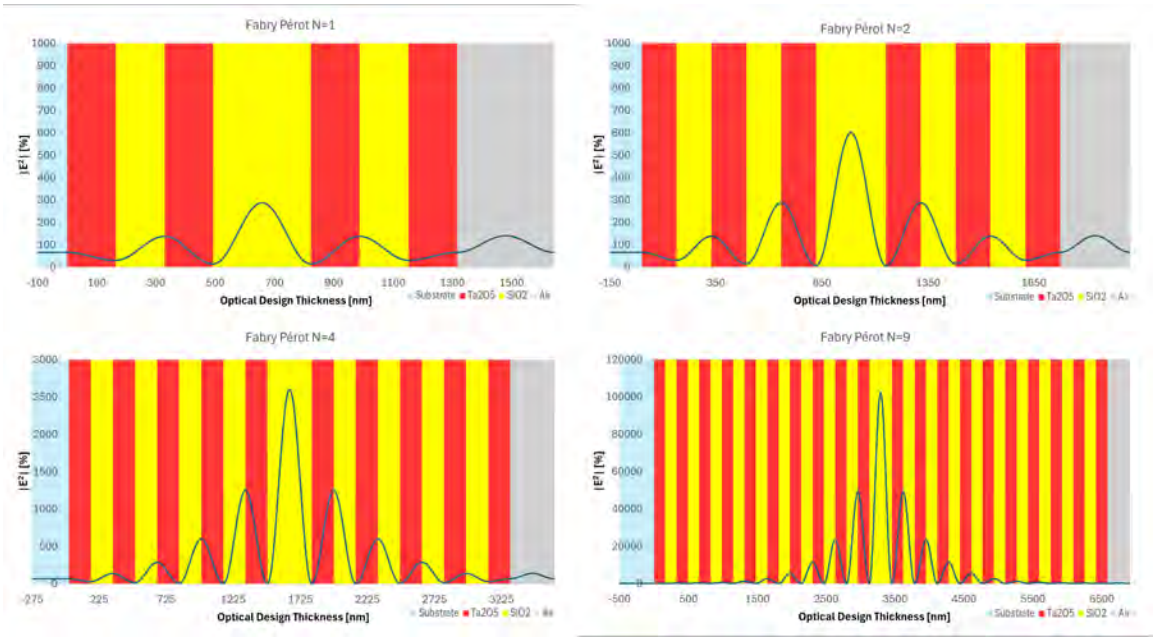


Figure 19: The different Fabry-Pérot filter designs are shown together with the E-Field. The y-axis of the different designs shows the significant differences in intensity that develop in and around the resonator layer. The E-field is calculated at the design wavelength of $550\,nm$, using Optilayer.

### 3.3.4 Further Filter Concepts

In addition to the fundamental optical coating systems discussed before, there exists a wide range of specialized filter designs aiming for specific spectral, angular, or functional requirements. These may

use additional physical principles or arise from combinations of the concepts introduced earlier.
There are, for example, other types of band pass filters which use several cavities to shape the transmitting peak [11] (P.286).
The opposite direction would be the band-stop or notch- filter [11] (P.245).
Edge filters, such as long-pass and short-pass filters, are used to block certain wavelength regions entirely while allowing a small range to pass as unhindered as possible. Their spectral sharpness of the transmission peak is largely determined by the number and design of the individual layers [11](P.251).
Beam splitters can be realized by designing structures that transmit a fixed fraction of the incoming wavefront while reflecting the rest at a specific wavelength, typically within a designated spectral range [11](P.177).
Polarization filters, such as dichroic filters or s/p selective mirrors, use the different interactions of s- and p-polarized light with thin film structures under angular incidence. These filters are particularly relevant in laser optics and for polarization separation[11](P.342).
Another important class comprises Rugate filters, in which the refractive index profile varies continuously rather than in discrete steps. This design approach allows the suppression of secondary maxima in the reflection spectrum and provides greater flexibility to meet stringent spectral specifications [11](P.403).
It is probably no surprise that I recommend the book "Thin Film Optical Filters" by Angus Macleod [11] if someone wants to learn about filter designs.

# 4 Metrology

The quality and functionality of optical coatings and complex filter systems strongly depend on the precise control of their physical properties. Characterization of coating properties begins already during process development, where attention is paid to clean and sharp absorption edges, stable yet high deposition rates, and uniform, homogeneous layer growth. To achieve this, both individual layers and complete multilayer systems are continuously characterized throughout all stages of development using a variety of measurement techniques, and processes are adjusted where necessary.
The measurement techniques used to characterize and monitor these physical properties play a central role in this development process. Not only is it important to have a broad range of measurement methods at hand, but it is also necessary to understand how these instruments operate, what is actually being measured, where the limitations of each technique lie, and how to correctly interpret the results.
This chapter presents a selection of measurement techniques, with a particular focus on those methods that are directly relevant to the experiments described in this work and to the interpretation of the results reported in the associated publications.

- This applies particularly to **Spectrophotometry**, a measurement technique that, compared to others, requires relatively little time and is easy to perform. It is excellent for process optimization, allowing for quick identification of errors in layer quality. In addition, it can be used to generate transmission and reflection spectra for individual layers, from which dispersion and absorption spectra can then be calculated.

- Furthermore, **Ellipsometry** is a highly powerful technique, although it generates in its simplest form two rather abstract measurement parameters. However, it is exceptionally suited for accurately determining the thickness and the complex refractive index components of single or multiple layers.

- **AFM**(Atomic Force Microscopy) is used for surface scanning and can provide information on surface morphology, particularly roughness.

- **XRD & XRR** (X-ray Diffraction) and (X-ray Reflectometry) are two measurement techniques often performed using the same instrument. In these methods, X-rays are directed at the sample at very shallow angles, and interference effects near the surface allow for precise conclusions about the internal structure of both single and multilayer systems.

- **LIDT** (Laser-Induced Damage Threshold) is a highly demanding measurement technique, which, in contrast to the methods mentioned above, is destructive. This process intentionally damages the sample to determine how well the coating can withstand intense laser pulses.

- **TEM** (Transmission Electron Microscopy) is also a complex measurement technique. The measurement itself is not destructive, but the sample preparation is. However, it must be said that only a very small piece of the sample is needed. By measuring the deflection of an electron beam passing through the sample, extremely high-resolution microscopy images can be created. Under ideal conditions, even individual atoms can be visualized.

## 4.1 Spectrophotometry

Spectrophotometry is a non-destructive measurement technique, meaning that the sample under investigation is not permanently altered or damaged by the measurement process in any significant way. The fundamental principle is relatively simple: a beam of light is directed through the sample, and the transmitted and reflected portions are measured. It is well understood that the optical behavior of a material specifically, the proportions of light that are transmitted and reflected depend on several factors: wavelength, angle of incidence, and polarization of the incoming light. Therefore, these parameters must be precisely controlled, adjusted, and interpreted in order to ensure high-quality, reliable measurements. The type of spectrophotometry used typically consists of the following components:

a **light source**, which must provide a high and most important stable intensity within the desired wavelength range. If the signal is too weak, the signal to noise ratio increases. If the

emitted spectrum drifts, for example due to temperature fluctuations, the measured reference differs from the actual spectrum, depending on the system configuration.

a **monochromator**, which is an optical device that transmits spectrally only a very narrow signal from a spectrum. The narrower the band, the higher the possible wavelength resolution of the measured spectrum.

a **polarization filter**, which transmits only wave components of a specific polarization. This allows the sample to be measured depending on the polarization of the measurement signal.

the **detector** measures the transmitted or reflected light from the sample. Its accuracy and sensitivity determine the quality of the measurement.

the **beam guidance and sample mounting** are important components. Firstly, it must be possible to adjust the mount precisely and reliably, and secondly, the light beam must be guided reliably through the various optical components across the entire spectrometer without suffering any unnecessary loss of intensity.

The spectrophotometry used in the projects is a Photon RT by Essent Optics [12]. Although additional spectrometers were available, this device was used almost exclusively, with only a few exceptions. Two lamps are available to provide light for the desired spectral range: a halogen lamp for the visible range extending into the near-infrared and a deuterium lamp for the UV range, enabling measurements down to $190\,nm$ wavelength.
A Czerny–Turner monochromator is used for wavelength selection.
Before a measurement is performed, a reference spectrum must be recorded. For each wavelength (with a selectable resolution down to $0.1\,nm$) and each selected polarization setting ($\phi$ can be set to parallel, perpendicular, or average), the intensity of the light is measured in the desired range and normalized using $I_{\text{Max}}(\lambda) = 100\%$. The sample is mounted in a sample holder, which can be adjusted in steps of $0.01°$ to an angle of $\alpha = 0$–$75°$. Transmission and reflection measurements are typically performed as matched pairs under identical conditions (same angle and polarization), with only the detector rotating around the sample. It must be ensured that a minimum angle of $8°$ is maintained during reflection measurements, as the detector cannot be positioned closer to the beam path. This setup has the advantage that the light always focuses on the same spot of the sample. In addition, because there is no need to change anything between the measurements manually, the measurement recipe goes very fast and without interruption.
The results are expressed as transmission and reflection values in percent relative to the reference measurement. It is important to note that the sum of the two measured values does not equal 100%, as indicated in 80, since this formula does not account for losses.

$$100\% = T(\lambda, \alpha, \phi)[\%] + R(\lambda, \alpha, \phi)[\%] + L(\lambda, \alpha, \phi)[\%] \tag{114}$$

Losses do not refer solely to absorption within the layer during a single pass of light through the material, and thus this value cannot directly be used to determine the absorption coefficient. Part of the loss results from multiple internal reflections within the structure, but light can also be scattered both at the surface of the sample and between individual layers, depending on surface roughness. In addition, the beam displacement caused by light passing through the substrate must be taken into account, especially at larger angles of incidence.
From the resulting transmission and reflection spectra, one can subsequently calculate the refractive index, extinction coefficient, and thickness of the sample layers.
Within the scope of the projects, this measurement device represented the most commonly used instrument, as it is well-suited for a variety of applications:

Due to its high measurement speed without the need for manual adjustments, it is ideal for quick measurements between coating runs to optimize process parameters. For example, it can be used to rapidly detect absorption in layers, which is particularly useful for experienced coating operators. It is also well suited for verifying refractive indices and deposition rates before initiating sensitive optical designs.

Since only the detector moves during operation, the light beam stays in the exact same spot on the sample during both transmission and reflection measurements. This minimizes the influence of local variations, such as differences in layer thickness, defects, or inhomogeneities.

Due to its simple operation and the ability to define detailed measurement recipes, samples can be handed off to other users without introducing significant variations due to inconsistent measurement procedures.

And of course, to measure, compare, and control the coated multilayer systems with the calculated designs.

However, it should be noted that since the reference signal is recorded at the beginning of the measurement sequence, potential signal drift, e.g., due to lamp temperature fluctuations, can introduce inaccuracies and increase measurement uncertainty.

## 4.2 Ellipsometry

Ellipsometry is likewise a non-destructive measurement technique. Similarly to spectrophotometry, it analyzes the interaction of light incident on a sample at a defined angle. However, unlike photo spectrometry, which compares the maximum intensity of incident light with its reflection or transmission, ellipsometry irradiates the sample with linearly polarized light at an angle near the Brewster angle and analyzes the resulting change in the polarization state of the reflected light. When polarized light strikes the sample, both the amplitude and phase of the reflected light change according to [13]:

$$\frac{r_{\parallel}}{r_{\perp}} = \tan\Psi \mathbf{e}^{i\Delta} \tag{115}$$

Here, $\Psi$ describes the amplitude ratio of $\rho_{\parallel}$ and $\rho_{\perp}$, while $\Delta$ represents the phase difference between the two polarization components. This measurement is performed over a range of wavelengths and at different angles of incidence. To evaluate the resulting spectra, a model of the layer system is constructed, characterized by the thicknesses $d$, refractive indices $n$, and extinction coefficients $\kappa$ of the layers. The theoretical values for $\Psi$ and $\Delta$ are then calculated from the model and compared to the experimental data.
The most common models are as follows:
**Lorentz model** The Lorentz model is a term that is often used as a standalone or in combinations with other names. In general, the Lorentz-oscillator is identical to the term described in equation 57. It often is also used as a multi oscillator model in which several oscillators are added as in 2.2.4. It is Kramers-Kronig consistent, which means we can calculate the refractive index as well as the extinction coefficient. However, it takes absorption only into account over the damping part of the oscillation, which makes it difficult to use in the absorption range. In addition, it tends to over-parameterize if not used correctly [13].
The **Cauchy model** is an empirical approximation, easy to use and simple but also not Kramers-Kronig consistent.

$$n_{Cauchy}(\lambda) \approx A + \frac{B}{\lambda^2} + \frac{C}{\lambda^4} + ... \tag{116}$$

Although $A, B, C...$ are the fitting coefficients and $\lambda$ the wavelength. Often only the first two coefficient terms are used. The model is not able to calculate the extinction coefficient and, therefore, is only usable in regions without absorption. [5](P.34).
**Sellmeier model** is a loss free approach of the Lorentz model:

$$n^2_{Sellmeier}(\lambda) \approx 1 + \sum_j \frac{A_j \lambda^2}{\lambda^2 - B_j} \tag{117}$$

While $A_j, B_j$ are fitting coefficients and with the $B_j$ we can now, compared to the Cauchy-model, also take the resonance frequency into account. The model is consistent with Kramers-Kronig [14] and delivers an extinction coefficient but does not mean that it is physically correct as the model is supposed to be in the loss free range $\kappa = 0$ [15] (P34).
The **Tauc-Lorentz model** uses the same basic concept as the Lorentz model with the oscillator, but it separates the extinction coefficient into two ranges [5] (P.42),[16]:

$$\begin{aligned} \epsilon_2(E) &= 0 && : E < E_{gap} \\ \epsilon_2(E) &\propto \frac{1}{E} \frac{AE_0C(E - E_{gap})^2}{(E^2 - E_0^2)^2 + C^2E^2} && : E \geq E_{gap} \end{aligned} \tag{118}$$

While:

$\epsilon_2$ which is the imaginary part of the dielectric constant $\tilde{\epsilon} = \epsilon_1 + i\epsilon_2$

**A** is a scaling factor

$\mathbf{E}_0$ is the resonance energy

**C** is the oscillator with

$\mathbf{E}_{gap}$ is the optical band gap energy

Together with the Kramers-Kronig correlation [3] (P.61):

$$\begin{aligned} \Im(\tilde{\epsilon}(\omega)) = \epsilon_2(\omega) &= -\frac{2\omega}{\pi}\mathcal{P}\int_0^\infty \frac{\Re(\tilde{\epsilon}(\omega)) - 1}{\omega'^2 - \omega^2} d\omega' \\ \Re(\tilde{\epsilon}(\omega)) = \epsilon_1(\omega) &= 1 + \frac{2}{\pi}\mathcal{P}\int_0^\infty \frac{\omega' \cdot \Im(\tilde{\epsilon}(\omega))}{\omega'^2 - \omega^2} d\omega' \end{aligned} \tag{119}$$

We get the refractive index and extinction coefficient as [17]:

$$\begin{aligned} \tilde{\epsilon} &= \epsilon_1 + i\epsilon_2 \\ \epsilon_1 = n^2 - \kappa^2; \quad \epsilon_2 &= 2n\kappa \end{aligned} \tag{120}$$

and

$$\begin{aligned} n &= \sqrt{\frac{1}{2}(\sqrt{\epsilon_1^2 + \epsilon_2^2} + \epsilon_1)} \\ \kappa &= \sqrt{\frac{1}{2}(\sqrt{\epsilon_1^2 + \epsilon_2^2} - \epsilon_1)} \end{aligned} \tag{121}$$

This model uses an approximation in the range of the optical bandgap with the exponent of $(E - E_{gap})^2$ in the denominator, which helps fitting the model to the absorption range but needs to be taken carefully as it is physically not the same optical band gap as discussed in 6.3 as it does not take into account weak absorption- (WAT) or Urbach-Tail. The tail regions are discussed and shown in 38.
Due to the phase- and amplitude-sensitive nature of the measurement, ellipsometry is a highly powerful technique with several advantages over other methods:

The measured spectra allow for the extraction of $n$, $\kappa$ and $d$ not only for a single layer but also for multiple layers, making ellipsometry valuable for the analysis of multilayer systems.

The method is highly sensitive to very thin layers, enabling the characterization of nanometer-scale coatings.

Because both polarization components are analyzed, no normalization to the overall intensity is required, rendering the results robust against fluctuations in light intensity.

The technique is sensitive to surface roughness, inhomogeneities, and anisotropy, making it a useful tool for control and verification measurements.

However, ellipsometry also has its limitations. The operation of the instrument, the selection of appropriate models, and the interpretation of the measurement results are significantly less intuitive than in spectrophotometry, thus requiring greater prior knowledge. Moreover, while the sensitivity to surface roughness, inhomogeneities, and anisotropy can be beneficial, it also complicates the analysis in many cases.
During the projects a Sentech SenResearch 4.0 was used and even if the ellipsometry is a very powerful measurement device I have to admit that I have not used it that often as it deserves it. As it has a automatic sample stage, I used it mostly to map the thickness of the coated film at several points on an 8-inch wafer to calculate the uniformity.

## 4.3 Atomic Force Microscopy

Atomic Force Microscopy (AFM) is a high-resolution imaging technique that is used to visualize the surface structure of a sample. In this context, AFM is also considered a non-destructive measurement method. The basic principle of AFM relies on a very fine tip that is scanned across the surface of the sample. The tip is mounted on a cantilever and is brought extremely close to the sample surface, maintaining a minimal distance. Due to microscopic atomic forces, such as van der Waals interactions, the tip experiences repulsion from the atoms in the sample, resulting in a slight deflection [2] (P.26). This deflection causes the cantilever to bend. A laser beam is directed at the back of the cantilever, and the resulting change in the reflection angle of the laser is detected. This change can then be used to reconstruct the vertical displacement of the tip. The sample is scanned line-by-line, and a two dimensional image can be constructed from the collected data. In this image, the height variations are represented as individual pixels, yielding a topographical map over the entire scanned area.
In the produced optical coatings, surface roughness is often very low, but this method enables visualization even at nanometer scales. However, it is important to note that the resulting measurements are not always universally transferable. When the roughness is in the nanometer or sub-nanometer range, influences such as localized electrostatic charging of the sample, tip wear, or even the scanning direction (forward vs. backward) can significantly affect the results. Additionally, the scan area is typically limited to just a few micrometers, and care must be taken to avoid excessive scanning speeds especially across step changes since this may induce vibrations.
In the context of the projects, a Park NX20[1] and a Nanosurf[2] AFM were used, primarily to assess surface roughness when investigating potential sources of elevated optical losses.

## 4.4 XRD

The measurement methods of X-ray diffraction (XRD) and X-ray reflectometry (XRR) are performed using the same instrument and both measure the reflection of X-rays, though they are based on different physical phenomena. XRD describes the diffraction of X-rays by ordered structures within the sample. During the measurement, both the X-ray source and the detector are moved synchronously over varying angles across the sample. If the used X-rays have a wavelength in the order of the lattice spacing of the material, interference effects occur, analogously to 3.1.2. When the Bragg condition is satisfied [2] (P.14):

$$m\lambda = 2d\sin\alpha; \qquad m \in \mathbf{N} \tag{122}$$

Where $\lambda$ is the wavelength used, $\alpha$ is the angle of the beam within the material, and $d$ represents the lattice plane. Interference occurs between the diffracted beams, and the detector can measure the resulting increased intensity. From the resulting peaks, the lattice constants of a crystal can be calculated on the basis of their positions, allowing for identification of the crystalline structure. The width of the peaks provides information about possible grain sizes in polycrystalline layers, as well as the presence of defects. The intensity of the peaks can provide insight into the degree of crystallization and the preferred orientation of the crystals. XRD measurements are thus well-suited for non-destructive and rapid analysis of deposited layers for crystalline characteristics. The XRD as well as the XRR measurements are carried out with the same device, the D8 Discover from Bruker[3].

## 4.5 XRR

In an XRR (X-ray reflectometry) measurement, by contrast, the X-ray beam is reflected at very shallow angles from the outermost layers of the material, providing a wealth of structural information. However, the interpretation and analysis of such measurements is non-trivial, and the underlying measurement principle is among the more complex techniques. A particularly useful reference for understanding this method is Elements of Modern X-ray Physics [18], upon which most of the theoretical derivations are based, it has also to be mentioned that inspirations on how to build up the chapter come from the manual of a lab course from the University of Siegen [19].

[1] https://www.parksystems.com/en/products/research-afm/large-sample-afm/nx20 access on 12.10.2025
[2] https://www.nanosurf.com/en/products/coreafm access on 12.10.2025
[3] https://www.bruker.com/en/products-and-solutions/diffractometers-and-x-ray-microscopes/x-ray-diffractometers/d8-discover-family/d8-discover.html access on 24.10.2025

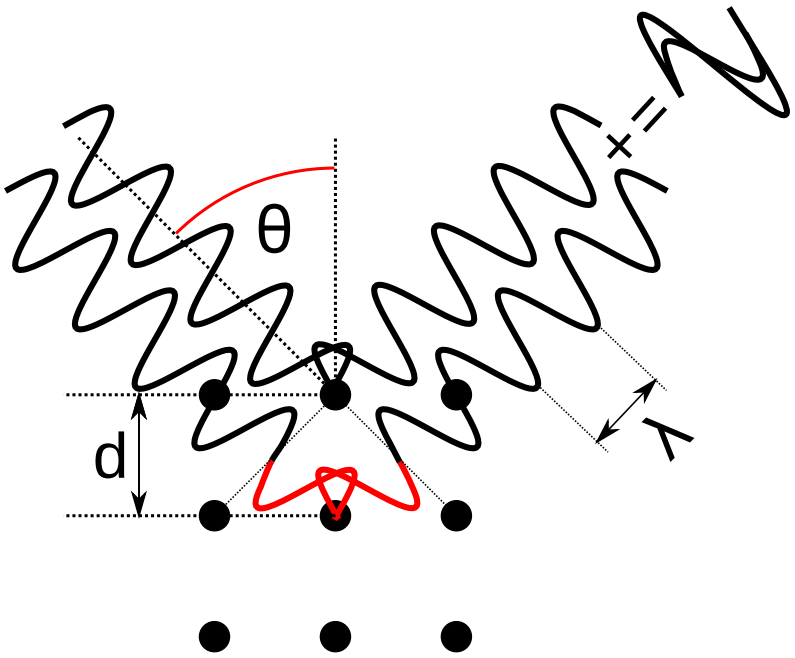


Figure 20: The figure shows the Bragg reflection at a crystal. If the wavelength or a multiple meets the condition, positive interference occurs which leads to a intensity peak in reflected intensity.

### 4.5.1 Refractive Index and Absorption

As should already be clear, the refractive index of a material depends on the wavelength. As the wavelength decreases, the refractive index increases significantly when approaching the resonance frequency. This corresponds to the regime where the photon energy is sufficient to excite the electrons in the atom, allowing absorption of the radiation. After this resonance frequency is exceeded, the refractive index decreases rapidly. For X-ray wavelengths, it becomes less than 1. Then it can be expressed as [18] (P.75):

$$n = 1 - \delta + i\zeta \tag{123}$$

Here, $\delta$ denotes the dispersive component and $\zeta$ the absorptive component of the complex refractive index, where:

$$\delta = \frac{2\pi}{k^2}\rho_e r_0 = \frac{\lambda^2}{2\pi}\rho_e r_0 \qquad and \qquad \zeta = \frac{\tilde{\alpha}}{k} = \frac{\tilde{\alpha}\lambda}{2\pi} \tag{124}$$

where $\rho_e$ is the electron density, $r_0$ the scattering amplitude per electron, and $\tilde{\alpha}$ represents the absorption coefficient.

### 4.5.2 Fresnel Reflectivity and Penetration Depth on a Smooth Surface

To maintain consistency with the literature where the incident angle is typically measured with respect to the surface rather than the surface normal, the angles here are expressed accordingly. That is, $\hat{\alpha} = 90° - \alpha$ describes the angle of incidence in the air relative to the surface, and $\hat{\beta} = 90° - \beta$ is the angle of the transmitted component within the material.
Since Snell's law 70 also applies in this context, one can define a condition for total external reflection when the transmitted angle $\hat{\beta} = 0°$:

$$n_1 \sin\alpha = n_2 \sin\beta \rightarrow n_1 \cos\hat{\alpha} = n_2 \cos\hat{\beta} \tag{125}$$

Setting $\hat{\beta} = 0°$ and $n_2 = 1-\delta$, the critical angle is derived from the equation above as $\hat{\alpha}_C = \arccos\frac{n_2}{n_1} \simeq \sqrt{2\delta}$. This approximation is derived from a Taylor expansion as described in [18](P.77).

Because the angle of incidence is very shallow with respect to the surface of the layer, the Fresnel coefficients 79 can be approximated as:

$$\rho \simeq \frac{\hat{\alpha} - \hat{\beta}}{\hat{\alpha} + \hat{\beta}} \, \tau \simeq \frac{2\hat{\alpha}}{\hat{\alpha} + \hat{\beta}} \tag{126}$$

In conjunction with the Fresnel law $n_1 \cos\hat{\alpha} = n_2 \cos\hat{\beta}$ valid at small angles and with air as incident medium, we set $\hat{\alpha} = 1 - \delta - i\zeta$ and obtain, via another approximation:

$$\hat{\alpha}^2 = \hat{\beta}^2 + \underbrace{2\delta}_{=\hat{\alpha}_c^2} - 2i\zeta \rightarrow \hat{\beta} = \sqrt{\hat{\alpha}^2 - \hat{\alpha}_c^2 + 2i\zeta} \tag{127}$$

From 79, the reflectivity is then given by $R = |\rho X R R|^2$:

$$R_F = \left| \frac{\hat{\alpha} - \sqrt{\hat{\alpha}^2 - \hat{\alpha}_c^2 + 2i\zeta}}{\hat{\alpha} + \sqrt{\hat{\alpha}^2 - \hat{\alpha}_c^2 + 2i\zeta}} \right|^2 \tag{128}$$

We can also see that the angle $\hat{\beta}$ has a real and imaginary part which inserted into a wavefunction creates damping term

$$A_t \mathbf{e}^{-ik\hat{\beta}z} = A_t \mathbf{e}^{-ik\mathbf{Re}(\hat{\beta})z} A_t \mathbf{e}^{k\mathbf{Im}(\hat{\beta})z} \tag{129}$$

This leads to the penetration depth $\Lambda$ where the intensity $I_t \propto A_t^2$ drops to 1/e of the value:

$$\Lambda = \frac{1}{2k \cdot \mathbf{Im}(\hat{\beta})} \tag{130}$$

### 4.5.3 Wave Vector Notation

In the context of scattering particularly in XRR measurements it is often useful to employ a representation based on wave vectors, as this can simplify the interpretation, which we see later in the explanation. When a wave reflects or scatters from a surface, the incident and reflected wave vectors, $\vec{k}_i$ and $\vec{k}_r$, span a plane. The component perpendicular to the film surface can then be expressed as the sum of both:

$$Q = |\vec{k}_i - \vec{k}_r| = \frac{4\pi}{\lambda} \sin\alpha \tag{131}$$

analogous $Q_c = \frac{4\pi}{\lambda} \sin\hat{\alpha}_c$ and also $Q' = \frac{4\pi}{\lambda} \sin\beta$. This allows us to express the Fresnel reflectivity as:

$$R_F(Q) = \left| \frac{Q - \sqrt{Q^2 - Q_c^2 + 2i(2k)^2\zeta}}{Q + \sqrt{Q^2 - Q_c^2 + 2i(2k)^2\zeta}} \right|^2 \tag{132}$$

As we know $Q_c = \frac{4\pi}{\lambda} \sin\hat{\alpha}_c \simeq \frac{4\pi}{\lambda}\hat{\alpha}_c \simeq \frac{2\pi}{\lambda}\sqrt{2\delta}$ and also $\delta = \frac{\lambda^2}{2\pi}\rho_e r_0$, we can calculate the electron density directly from $Q_c$. We then need some material specific quantities such as $Z_{eff}$, the effective number of electrons per atom, $M$ the molar mass, and also $N_A$ the Avogadro constant to calculate the density of the film at the surface region $\rho_m$

$$\rho_m = \frac{Z_{eff}}{M} N_A \rho_e \tag{133}$$

### 4.5.4 Surface Roughness

The previous parts are restricted on a flat surface. However, in reality, all surfaces have roughness at least in the *nm* range. This roughness has an influence on the XRR measurement as we cannot assume that the change in electron density is not abrupt. So we assume that the distribution is normally distributed [18] (P.89).

$$\frac{\partial f}{\partial z} = \frac{1}{\sqrt{2\pi\sigma^2}} \mathbf{e}^{\frac{-1}{2}(\frac{z}{\sigma})^2} \tag{134}$$

While:

$\sigma$ $[nm]$ ... is called the root mean square roughness also named $Rq$

This allows us to describe the total roughness $R(Q)$ in proportion to the Fresnel roughness as:

$$\frac{R(Q)}{R_F(Q)} = \left| \int_{-\infty}^{\infty} \frac{\partial f}{\partial z} \mathbf{e}^{iQz} dz \right|^2 \tag{135}$$

This leads to the expression:

$$R(Q) = R_F(Q)\mathbf{e}^{-Q^2\sigma^2} \tag{136}$$

This is not totally correct according to the source and $Q^2$ should be replaced by $QQ'$ but should barely make a difference.

### 4.5.5 Thin Film Thickness

To calculate the thickness of a layer, first all the partial beams from the reflection need to be summed up, similar to the backside reflection shown in figure 11. Thereby back reflected beams are phase shifted by the factor of $p^2 = \mathbf{e}^{-iQd}$. It is the same as in chapter 3.1.2 but with the adapted notation from [18] (P.81). By building the geometric series, we can show: $\rho_{Layer} = \frac{\rho_{0,1}+\rho_{1,2}p^2}{1+\rho_{0,1}\rho_{1,2}p^2}$ which leads to the expression for the reflection $R_{KF}$ on the basis of the phase shifted interference, which are known as Kiessig-fringes for a single layer [18] (P.87):

$$R_{KF} = |\rho_{Layer}|^2 = \left| \frac{\rho_{0,1} + \rho_{1,2}p^2}{1 + \rho_{0,1}\rho_{1,2}p^2} \right|^2 \tag{137}$$

Now it is not obvious at first glance, but from this description of the Kiessig fringes we can take the approximation for the thickness of the layer from the XRR measurement. As we know, the factor $p^2$ is periodic if the condition $Qd = 2\pi m$ with $m \in \mathbb{N}$ is true, so we can write the thickness of the layer depending on the distance of the fringes with:

$$d_{layer} = \frac{2\pi}{\Delta Q_{KF}} \tag{138}$$

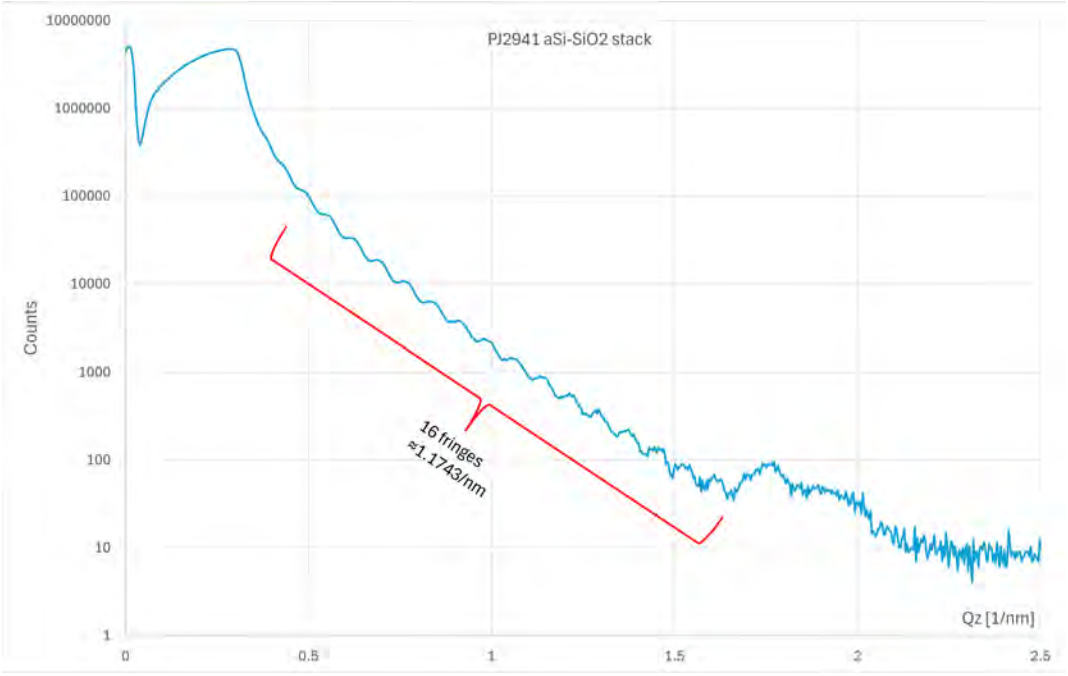


Figure 21: A measurement of a $PJ2941$, a $\alpha Si/SiO_2$-QNL stack shows Kiessig fringes. From the distance $\Delta Q$ it is possible to calculate the total thickness of the coated stack, which delivers $d_{XRR} = 85.6\,nm$ and matches very well with the photo spectroscopic calculation of $d_{pho} = 85.0\,nm$.

## 4.6 Stress Measurement

The measurement of film stress is a simple and non-destructive technique; however, it requires a preparation step that ideally should be performed prior to the coating process.
The basis for film stress measurement is the Stoney equation [20]:

$$\sigma = \frac{E_s d_s^2}{6(1-\nu_s)d_f}\left(\frac{1}{R_0} - \frac{1}{R}\right) \tag{139}$$

with:

$E_s$ $[\frac{N}{m^2}]$ ... Young's modulus of the substrate

$d_s$ $[m]$ ... the thickness of the substrate

$d_f$ $[m]$ ... the thickness of the film

$\nu_s$ ... Poisson's ratio of the substrate

$R_0$ $[m]$ ... radius of curvature of the substrate before coating

$R$ $[m]$ ... radius of curvature of the substrate after coating

The preparation mentioned above consists of measuring the curvature radius of the substrate before coating, which is then compared to the measurement taken after the film has been deposited. For this purpose, the measurement device directs a laser or a white light source across the surface of the substrate and records the reflection angle at each point along a line. Since the angle of incidence must equal the angle of reflection, this allows determination of the local surface slope at each point, from which the overall curvature radius of the substrate can be calculated. By substituting the measured values into the Stoney equation, and with knowledge of the other material-specific parameters, the resulting film stress can be calculated. Stress measurements were carried out using an FSM 128L[4]

## 4.7 Laser-Induced Deflection

In summary, Laser-Induced Deflection is a measurement method in which a pump laser is directed through a sample. Depending on the absorption effects, the sample heats up, which changes the refractive index of the sample locally. Two test beams are sent through the sample close to the pump laser, and the deflection caused by the change in refractive index can be measured.

[4]https://metrosemi.com/fsm-128l/ access on 24.10.2025

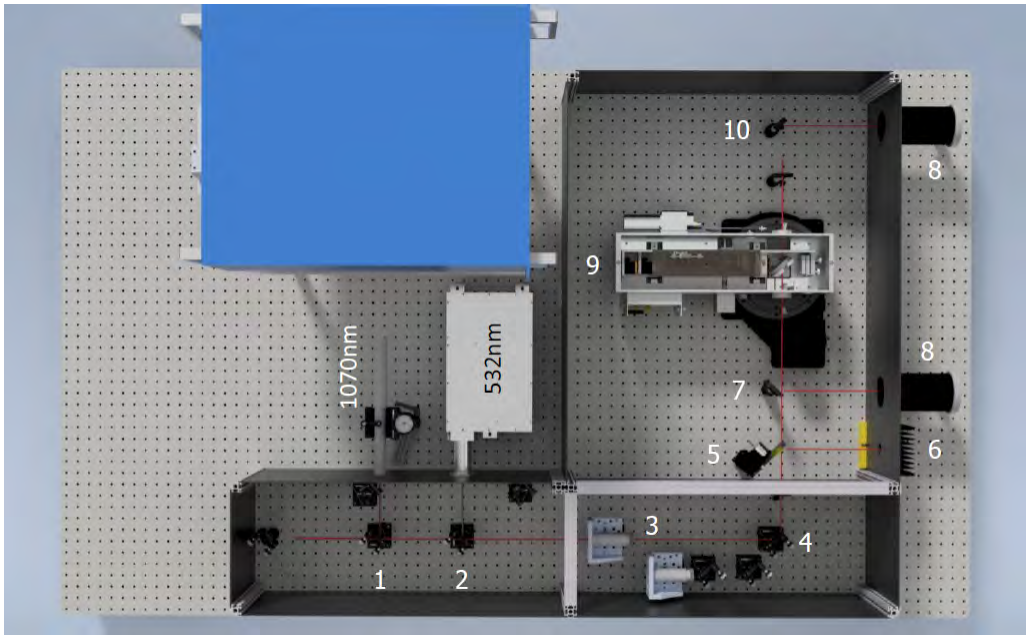


Figure 22: Schematically drawing of the LID setup used at RhySearch. Drawing adapted from the manual [21]

We use at RhySearch a setup from the Leibniz-Institut für Photonische Technologien. It is schematically drawn in figure 22. We can choose between a 532 $nm$ and a 1064 $nm$ pump laser source which is guided by mirrors (1, 2& 4) into the measurement part (9). On its way the beam gets widened up (3) and before and after the deflection measurement the intensity is measured (5, 6). The back reflected light from the sample is absorbed in a water cooled absorber (7, 8), as is the transmitted light (10, 8). The core of the setup is shown in figure 23. If the samples absorb the pump laser beam, the test beams are bent which can be measured by the sensors.


Figure 23: The figure shows on the left side the setup of beam path through the sample. On the right side the red arrows point on the sensors which measure the offset of the beam paths. The red circle shows where to calibrate the distance of the laser beams to the pump beam. The sample holder in the middle is removed. Figure adapted from the tools manual [21]

## 4.8 Total Integrated Scattering

Total Integrated Scattering (TIS) is a measurement technique in which the stray light of a sample is measured. A light source is focused on a point in the sample and the emitted stray light is collected by

an integrating sphere (Ulbricht sphere). A photo multiplier tube (PMT) on the sphere measures the light intensity, which means it cannot measure the angular dependency of stray light, but it measures the whole light reflected in all directions. In this way, the scattered light of a sample can be detected point by point over the whole surface. The source mentions a different integrating sphere, but the principle is the same as in our setup [22].

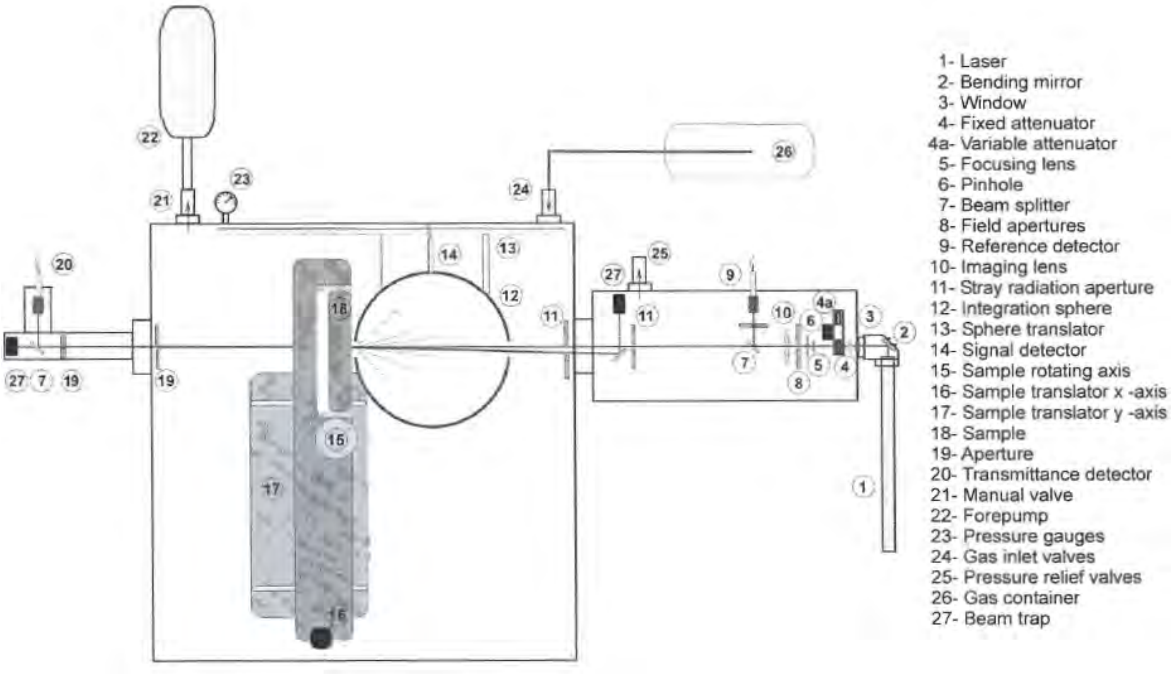


Figure 24: The figure shows the setup used to measure TIS at RhySearch. Picture adapted from the delivery contract with Laser Zentrum Hannover [23].

The setup we use at RhySearch is shown in figure 24 except for the vacuum and gas part as we use it in a closed flow box, but it is planned to operate also under vacuum or protective gas atmosphere, the figure is from the construction contract between Laser Zentrum Hannover and RhySearch. In our setup the light source is a $633\,nm$ continuous-wave laser and we can measure substrates up to a diameter of $10\,cm$. We usually placed the sample behind the Ulbricht sphere to measure only the reflected stray light, but it would be possible to measure the transmitting stray light as well.
Before measurement, the intensity is calibrated with a defined calibration sample and then the laser spot scans in a defined pattern, a spiral beginning in the center over the whole substrate in steps of usually $70\,\mu m$. The size of the spot is according to ISO 13696, a minimum of $400\,\mu m$ and the measurement speed can be up to 1500 points per second [22], [23], [24].
The setup does not differentiate which influence causes the stray light, therefore, it must be taken into consideration that there are several possible sources. Surface and transition zone roughness can cause scattering of light which emits in all angles, physical and optical density inhomogeneity can also cause deflection of light. One problem can be the use of substrates that are high quality polished on the front side, as the back side also scatters back, which can also ruin the measurement of the best possible front side coating. However, one of the main reasons that we have to deal with is mostly stray light due to particles or impurities.

## 4.9 Laser Induced-Damage Threshold

Laser-Induced Damage Threshold (LIDT) testing is a complex measurement method in which a sample is tested to determine the energy density of laser pulses for which it can withstand a without physical damage.
Generally, a lot of the information in this section is explained and defined in ISO 21254 [25] and is recommended to read if you are interested in the subject. In my experience, it can be challenging to

deal with measurement results, as they are often difficult to compare and their handling can lead to misinterpretations and false simplifications.

There are several different possible LIDT measurement methods that can be carried out, so it is important to differentiate between them and to know what influence they have. Starting with the laser, one of each lasers specific properties is its wavelength.

### 4.9.1 Wavelength

Because LIDT tests are normally performed because someone is interested in the life time or durability of a material, coating, or substrate for a specific purpose, the wavelength in the test setup is already given. It is important to mention that the LIDT value measured with two different wavelengths is not directly comparable since the photon energy determines how many photons are needed to overcome the band gap energy of the tested material [26] or which region in the absorption spectrum can be excited. More about the band gap is explained in chapter 6.3.1 and about the absorption curve in 6.3.

### 4.9.2 Pulse Duration

Another important property is the duration of the pulse. Typically used are continuous wave (cw), nanosecond (ns), picosecond (ps) or femtosecond (fs) pulse durations. The duration of the laser pulse has also a huge influence on the behavior as it determines the dominant absorption type.

- If a sample is tested for laser resistivity using a continuous Laser (**cw-LIDT**), the most dominant processes for damage on the sample will be linked to thermal absorption in or on top of the material. [27] (P.9).
- In the nanosecond regime (**ns-LIDT**), the main type of damage is also dominated by thermal effects, but also by dielectric breakdown [28]. The testing is very sensitive to particles and inhomogeneities or other defects in or on the sample.
- Pulses in the femtosecond regime (**fs-LIDT**) are much shorter. This leads to different types of damage occurring, compared to the other pulse lengths. As thermal processes are too slow the most dominant damage source is single- or multi photon absorption linked directly to the band gap of the material, while particles or surface defects are not that dominant anymore [27] (P.128).

### 4.9.3 Measurement Method

There are several different types for carrying out LIDT tests. The most common are "1-on-1", "S-on-1" or "ramp" tests.

- The mode **1-on-1** describes a test in which every measurement point is tested only once. After every laser pulse of defined radiation fluence, the testing spot is changed. Every spot gets characterized, either as "damaged" or "not damaged" and then over the spectrum of fluence the damage probability is plotted [27] (P.165).
- The mode **S-on-1** is similar to "1-on-1", but instead a defined number of pulses is shot at every spot. If carried out with several numbers of pulses it is possible to plot a time dependent laser resistance for the measured sample and differentiate how long lasting a probe is or how it degrades [27] (P.167)
- The ramp test or **R-on-1** ramps the fluence with every pulse higher at each spot until damage occurs. However, it must be noted that this can lead to self annealing effects.

Normally, a distinction is made between destruction and non-destruction in the event of damage. However, in some cases, a further condition is also distinguished in which a change in the layer can be detected, but no destruction has yet occurred. This is called **Color-mode** instead of **Catastrophic-mode** [29] and is also measured and discussed in the section about Laser Damage Competition 8.4.

### 4.9.4 Calculation

To calculate the threshold, the damage events are counted for every fluence tested. The spectrum is divided into sectors, and for every sector the ratio of damage/no-damage event is calculated, and from there a threshold is determined. It is important to understand that the value obtained does not guarantee that the sample has remained undamaged up to this amount. Figure 25 shows the measurement points from the design "$D14$" which is discussed in section 9.2.

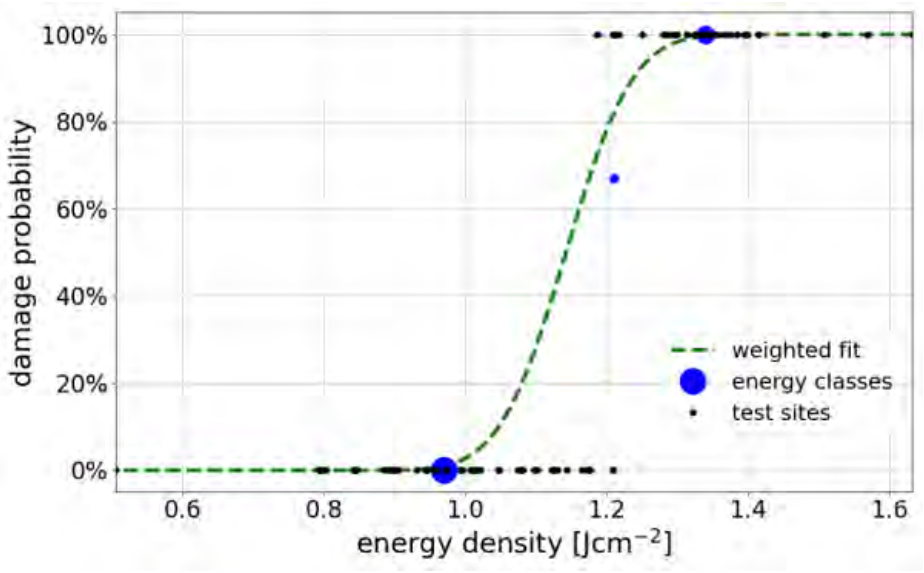


Figure 25: The figure shows the damage probability measured at RhySearch of the tested design "$D14$". It is clearly visible that the calculated threshold of $1.02\,J/cm^2$ does not specify a value that clearly indicates when the sample gets damaged.

### 4.9.5 Setup

The setup may differ at different institutes, but the one used at RhySearch is shown in figure 26.

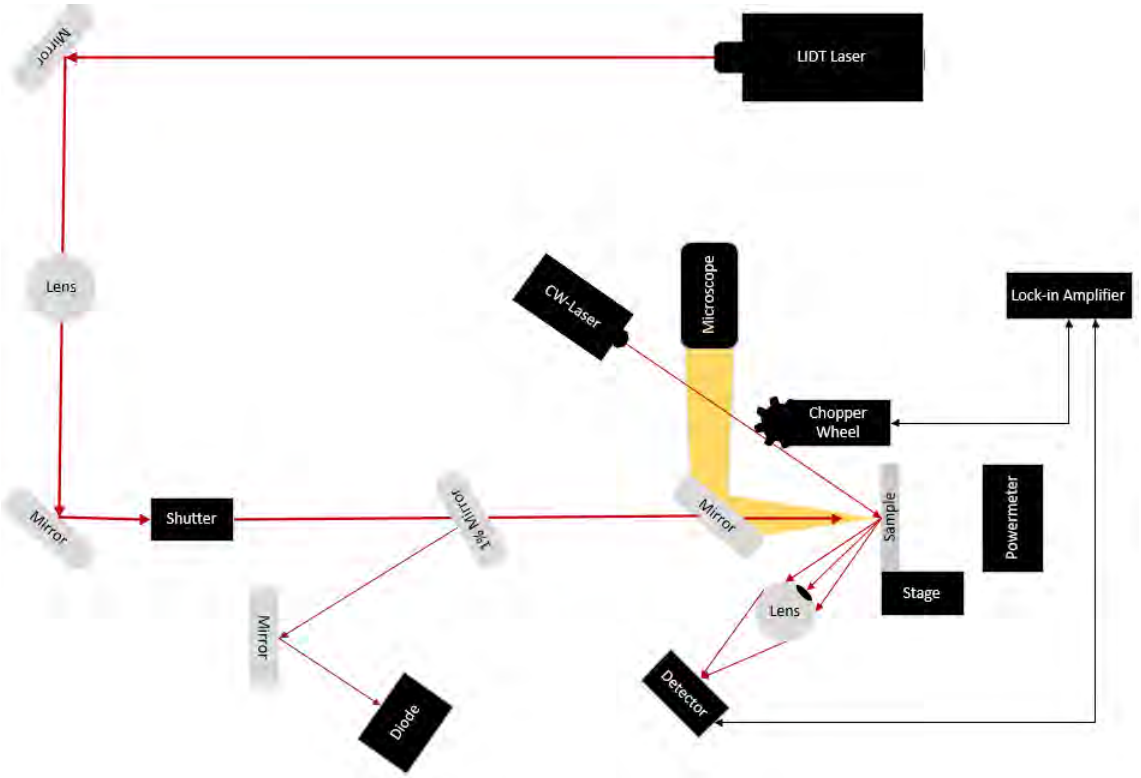


Figure 26: The figure shows a schematically drawing of the LIDT-setup at RhySearch.

Before a measurement, the laser beam is measured using the **power meter** and the **1%-mirror** on the **diode** to determine how much power reaches the diode. This value is later used to calculate the power of the pulse used in the actual measurement.
The **stage** moves the **sample** to automatically follow a configurable measurement pattern on the probe.
The **CW-Laser** is aimed at the same point as the **LIDT-Laser** and reflected on the **lens** , which has a blocker in the middle. This blocker prevents directly reflected light from hitting the **detector** behind it. Only when there is damage, light is scattered so that it also hits the lens outside the blocked area and is focused on the detector.
The **microscope** , which is equipped with a fast camera, is also aimed at the same spot to detect changes in the tested sample before the damage is fully developed.

## 4.10 Transmission Electron Microscopy

Transmission Electron Microscopy (TEM) is an analytical technique in which electrons are transmitted through an ultra-thin material sample. As electrons pass through the sample, they are scattered at various angles or lose energy because of interactions with the material, providing a wealth of structural and compositional information. The resulting image can achieve atomic resolution, although this is strongly dependent on the atomic arrangement as well as the thickness of the prepared lamella.
Since the lamella must first be extracted from the original sample, TEM is not a non-destructive measurement technique. However, it should be noted that measurements can often be performed in very small regions or at the edge of a substrate, which minimizes the large-scale impact on the sample.

### 4.10.1 Sample Preparation

Sample preparation is typically performed using a Focused Ion Beam (FIB) [30]. In this process, an ion beam is used to cut a very thin lamella from the sample. The lamella is then further thinned and polished. Care must be taken to avoid structural damage or modification of the sample during this step. The thinner the lamella can be polished without inducing damage or loss of information,

the more transparent it becomes to the electron beam and consequently the higher the achievable resolution in the subsequent measurement.

### 4.10.2 Measurement

During the measurement, a high-energy electron beam is directed at the sample. Electrons are absorbed, scattered, or transmitted depending on the influences such as the density, thickness, or internal structure of the material. The detected signal can then be analyzed to determine detailed information about the sample.
Elastic scattering processes can occur, where electrons are deflected without energy loss. This includes diffraction at atomic nuclei or crystalline lattice planes, potentially resulting in diffraction patterns. In contrast, inelastic scattering involves energy transfer from the electrons to the atoms, typically through excitation or ionization processes [31] (P.17).
Multiple measurement modes exist, each providing different types of information:

- **Bright Field (BF)** , in which only directly transmitted electrons are detected, which can show structure contrasts, defects, and grain sizes [32] (P.262).
- **Dark Field (DF)** similar but this time directly transmitted electrons are blocked and only deflected get detected. In this measurement, only areas that scatter electrons are considered and therefore increase the sensitivity to crystalline effects [32] (P.263).
- **Selected Area Diffraction (SAED)** measures the diffraction of electrons in certain areas, also to measure crystallinity [33] (12.2.1 P.1143)
- **Energy Dispersive X-ray Spectroscopy (EDX)** measures the X-rays of inelastic interactions and gives information about elemental analysis [34]

**STEM** stands for the mode where the beam scans the sample in a pattern and creates a map of the measured information.
**HAADF** stands for High-Angle Annular Dark-Field [35] (P.179), which describes a dark field measurement method with a high angle in which the intensity of the scattered electrons is highly sensitive to the atomic number of the measured medium. So it is really suited to measure the elemental distribution of the sample in high resolution.
A HAADF-STEM tool, the Titan Themis 200 G3 from EMPA was mostly used in this project and also for the TEM images shown in this work.

## 4.11 Measured Thin Film Characteristics

Thin films are characterized not only by their intrinsic optical properties, such as refractive index and absorption coefficient, but also by a range of structural characteristics that significantly influence their performance and application. These structural factors include, for example, internal stress, which can lead to film deformation or even substrate fracture; surface roughness, which may cause scattering losses at interfaces; and adhesion quality, either to the substrate or between successive layers, which affects mechanical stability and durability. Furthermore, thin films may exhibit inhomogeneities, unsaturated chemical bonds, variations in crystallinity (including mixed amorphous and crystalline phases), and contamination. Such imperfections can result in shifted absorption features and unpredictable optical behavior, thereby limiting the film's functional reliability in high-precision optical systems.
Therefore, it is important to deal with the content about real effects that can happen to the material and thin films and to gain knowledge about what to look out for, which influence can have an impact on the results, and where the realistic limits are. So, the most common which occurred during the two projects are explained.

### 4.11.1 Thickness

The thickness of the layer has been mentioned several times already and is relatively self explanatory. However, it is important to distinguish which type of thickness is referred to. There is the **physical thickness**, which denotes the actual geometric thickness, as well as the **optical thickness** [5] (P.83). The optical thickness is defined as a combination of the refractive index and the

physical thickness, given by $d_{opt} = d_{phy}n(\lambda)$. It must be noted that the refractive index is wavelength-dependent, which means that the optical thickness depends on the target wavelength and is therefore only meaningful when this additional information is provided. Optical thickness is often used to simplify design representations; for example, in a Bragg mirror, all layers typically have the same optical thickness. As an example, a mirror designed for $1000\,nm$ using materials $n_{SiO_2}(@1000\,nm) = 1.47$ and $n_{Ta_2O_5}(@1000\,nm) = 2.1$ consists of alternating layers of $SiO_2$ and $Ta_2O_5$, each with an optical thickness of $\frac{\lambda}{4}$, i.e., $d_{opt} = 250\,nm$. However, the physical thicknesses of the two materials differ: $d_{phy}(SiO_2) = \frac{\lambda}{4 \cdot n_{SiO_2}} = 170\,nm$ and $d_{phy}(Ta_2O_5) = \frac{\lambda}{4n_{Ta_2O_5}} = 119\,nm$. Since in the nanometer range it is not feasible to simply measure thicknesses with a ruler, they must be determined indirectly via other measurement techniques. This is commonly achieved through spectroscopy (see Section 4.1), ellipsometry (see Section 4.2) or transmission electron microscopy (see Section 4.10).

### 4.11.2 Density

The density of a layer is a measure of the packing fraction of the material and can vary significantly. This is not immediately apparent, but it can have a considerable impact on the refractive index and optical thickness, thereby influencing the overall layer design [5] (P.29). Density fluctuations are difficult to measure directly as the film cannot simply be weighed. However, they can be partially inferred from the calculated refractive indices. For more reliable conclusions, XRR measurements are required (see Section 4.5). Too low or too high ion energies during deposition can lead to an increased porosity, within which water molecules may become embedded. This, in turn, affects the refractive index and can negatively impact the performance of the optical system because the amount of absorbed water can vary depending on ambient temperature and humidity. Consequently, the optical properties may change under varying environmental conditions. However, this effect also provides a relatively straightforward means of detecting such porosity using appropriate measurement techniques. spectrophotometry with heated sample holders can be employed. If the sample is heated high enough, the embedded water evaporates, causing a measurable shift in the transmission spectrum as a function of the substrate temperature.

### 4.11.3 Roughness

The roughness of the layer surface has a significant influence on the scattering of light at the interface. Roughness is critical not only at the outermost surface but also at intermediate interfaces within multilayer structures. Excessive roughness leads to a loss of intensity because of increased scattering and stray light. Even when individual layers exhibit otherwise high quality, surface roughness can impose a strict limitation on the achievable performance of the resulting optical filter [5] (P.63) Roughness on the surface of a film, design or substrate can be measured with AFM, see section 4.3. A measurement method which is sensitive to stray light but which does not necessarily refer to surface roughness, however, is TIS, see section 4.8.

### 4.11.4 Crystallinity and Amorphous Structure

Molecules and atoms can arrange themselves in different ways depending on the material and the conditions under which they form. Generally, we distinguish three types of structural orders [2] (P.403): Cristalline, polycrystalline, and amorphous.
Some other books also mention other types like quasi crystalline, but for our understanding the general three are enough[36].
When atoms are arranged in regular, repeating lattice structures over extended regions, the material is said to have a crystalline structure. Such materials often exhibit anisotropic properties. Materials composed of multiple small crystal domains, referred to as polycrystalline, consist of "islands" of individual crystallites. These crystallites are typically randomly oriented and not aligned within a larger, ordered context. The size of these domains can vary and is characteristic of the specific material and growth conditions. The third structural type is the amorphous material. In amorphous structures, atoms are disordered over large volumes and lack any periodic arrangement. However, this does not imply a completely random configuration. Amorphous materials can still contain atomic chains with preferred bond angles, lengths, and local orientations. As mentioned above, the refractive index is closely related to the density of the material [5] (P30). Since crystalline materials typically exhibit

a higher packing density than their amorphous counterparts [37], they also tend to possess a higher refractive index when comparing the same chemical compositions. Whether a material grows in a crystalline or amorphous phase depends on various factors, including temperature, ion energy, deposition method, material type and substrate [38]. The structural nature of the material can be reliably determined using X-ray diffraction (XRD), see 4.4 or transmission electron microscopy (TEM), see4.10.

### 4.11.5 Stress

Due to growth mechanisms, temperature-dependent differences in thermal expansion coefficients, or inhomogeneities within the material, stress can develop both within the deposited layers and at the interface with the substrate or other layers. These types of stress are typically classified as compressive or tensile and can exert significant mechanical force [39]. The magnitude and nature of this stress depend heavily on the coating material, the deposition technique, and the thickness of the deposited layers. In many optical coating systems, the stress generated during deposition represents a critical limiting factor in the design architecture and is therefore considered a key parameter to monitor and control. Within the scope of the present projects, particularly when working with the two materials $SiO_2$ and $Ta_2O_5$, the average stress levels observed were relatively low, so stress control played only a minor role in the overall process.

# 5 Experimental Setup

The core component of both projects is the "BPM 200 Clusterline" magnetron sputter tool from Evatec. For this reason and as it was used for all the shown coated layers and designs, this chapter explains the setup of the system and its most important components.

## 5.1 Magnetron Sputtering

Magnetron sputtering is a type of a "physical vapor deposition" (PVD) method and represents one of the most commonly used sputtering systems in industry. Shortly summarized, it uses a magnetic field to stabilize a plasma that sputters a target material via ion bombardment. These ions then form a thin layer on a substrate.
In magnetron sputtering, the target material and the substrate are aligned in parallel. A gas, typically argon, is used in front of the target material. By applying a voltage between the substrate (acting as the anode) and the target (serving as the cathode), free electrons are accelerated from the target toward the gas. Either DC, pulsed DC, or RF (or a combination of them) excitation is used, depending on the target material. These electrons can collide with the gas and ionize the atoms or molecules. The ionized gas particles are then accelerated toward the target by the applied field. These ions then hit the target with high kinetic energy as a result of the acceleration voltage, knocking out neutral atoms or molecules from the target material. This describes the actual sputtering process, as these particles are ejected toward the substrate. A key feature of magnetron sputtering is the additional magnetic field generated behind the target, which extends into the space in front of it. This magnetic field is designed so that the free electrons, which are accelerated into the gas by the electric field, also spiral around the magnetic field lines. As a result, they travel a significantly longer path in the area in front of the target. This greatly increases the probability of collisions between electrons and gas atoms, which increases the ion yield of the gas, and also increases the sputter rate. Magnetron sputtering offers the advantage that the process gas can include an oxygen component, allowing the sputtered material to be directly oxidized during the coating process. This enables the use of fully metallic targets to achieve a desired oxidation state without the need for an additional assist source. The same principle can also be applied, using nitrogen to form nitrides. However, a potential issue arises when part of the target is oxidized, which reduces its electrical conductivity and can negatively impact the process. For this reason, magnetron sputtering is often used in combination with an assist source. This allows the oxidation step via the use of oxygen in the assist source to be integrated into the deposition process without excessive interaction of oxygen with the target. The assist source can also be used to implement an additional amount of energy into the coating to increase the density or to etch the material. Another method of preventing the oxidation of the target is the variant mostly used in our coating tool, which employs a plasma emission monitoring (PEM) that precisely regulates the exact amount of oxygen and therefore prevents an excess of oxygen and target poisoning.
Magnetron sputtering offers the advantage that very high sputter rates can be achieved, particularly when using metallic targets. The use of RF sources also enables the sputtering of insulating target materials. By introducing reactive gasses into the process gas, the deposited material can be oxidized or nitrated in situ. The energy of the sputtered particles is typically very high, which allows for the formation of dense films, although usually not quite as dense as those produced by an Ion Beam Sputtering (IBS) system.

## 5.2 Clusterline 200 BPM

The system used in the projects is a magnetron sputtering system of the type "BPM 200 Clusterline" from Evatec, which was made available for the duration of the projects. This coating system belongs to the latest generation of equipment and offers versatile applications with a modular design that allows flexible upgrades. A schematic representation is shown in Figure 28, illustrating the three main sections of the system: The clean room partition with the control console and loading unit on the left side of the image, the central transfer module and the coating chamber located on the right side. Each of these components will be described in more detail in the following sections.

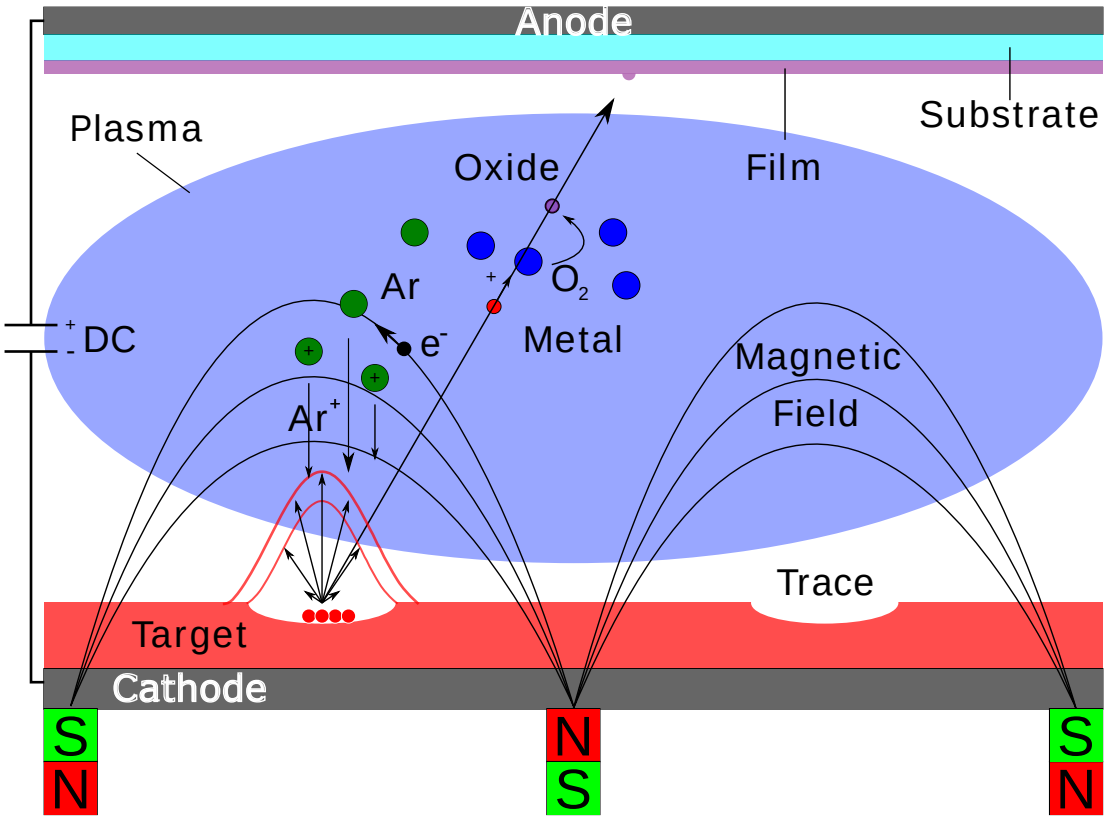


Figure 27: This Image shows the principle of a magnetron sputter source. Between the substrate (Anode) and the target (cathode) is the process gas. Behind the target, magnetic fields are generated to increase the path of the electrons to ionize the gas atoms. Those are breaking out the neutral molecules of the target material which are sputtered through the process gas towards the substrate.

### 5.2.1 Front

The front section of the system consists of a partition wall that separates the clean-room from the grey-room. By isolating the main body of the system, except for the loading area and control console from the clean-room, it is possible to reduce the environmental requirements and thereby minimize associated operational costs. In this project, however, the entire system is located within the clean-room, which is significantly more expensive but offers the advantage of improved accessibility and easier maintenance in a R&D project. A drawback, in addition to higher costs, is that the fore-line pumps cannot be positioned directly under or beside the system. This increases dead volume and results in longer pump-down times.

Located in the clean-room area is the control console and the two load-locks. The console features two integrated touchscreen panels for system operation and control of connected devices, along with a built-in keyboard and mouse.

The two load-locks are individual vacuum chambers, each equipped with its own connection to the roughing vacuum line and two turbo-molecular pumps capable of reaching base pressures in the range of $10^{-7}\,mbar$. Inside each chamber is a platform with a cassette holder designed to accommodate up to 16 eight-inch substrates or wafers.

During a loading cycle, the platforms along with the cassettes move vertically within the chamber through a lift mechanism. The movement is monitored by an array of light barriers, which serve as sensors to detect the presence and position of the substrates. This allows the system to map and register the substrates accurately.

The substrates are then transferred by the handler, through vacuum interlocks, to the central processing chamber.

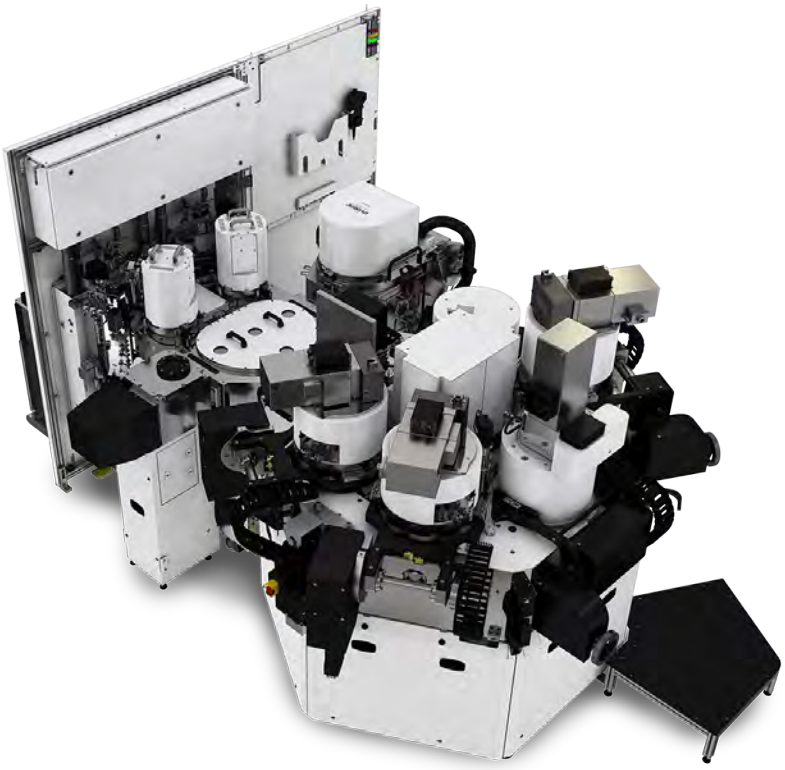

Figure 28: This Figure shows a 3D-CAD of a BPM 200 Clusterline from Evatec, the in the projects used coating device. The image shows additional equipment which was not used in the project. On The left side is the wall which separates the gray-room from the clean-room, with the two load locks. Behind in the middle is the VTM section, where a handler moves and aligns the substrates. On the right side is the coating chamber with the sources sitting on top facing downwards. © Evatec

### 5.2.2 Vacuum Transfer Module

The Vacuum Transfer Module (VTM) is located between the load-locks and the process chamber and connects them via the central handler. The VTM has its own roughing pump line shared with the load-locks and an independent turbo-molecular pump, which maintains vacuum levels in the low $10^{-7}\,mbar$ range.
The chamber features several flanges that allow for optional equipment integration. In the configuration used for this project, a flipper was installed. This component allows substrates or substrate holders to be rotated, enabling backside coating without breaking the vacuum.
The handler is a centrally located robot equipped with two independently movable arms. Each arm has a ceramic fork specifically designed for wafer transfer; see figure 30. When substrates are transferred from the load-locks to the VTM, they are first placed on the aligner to accurately determine their position. This step ensures precise positioning in the process chamber.

- **Aligner** The aligner is located within the VTM, between the interlocks of the two load-locks. It consists of a rotating stage that holds the substrate. A diode array measures the blocked light at the edge of the rotating substrate, allowing the system to determine the angular position of the wafer relative to the handler with an accuracy of approximately $\pm 10\,\mu m$.

### 5.2.3 Coating Chamber

The Batch Process Module (BPM) is the coating chamber. It is equipped with its own roughing pump, turbo-molecular pump, and a cryo pump, and achieves a pressure range in the low to mid $10^{-7}$ mbar regime. The core of the chamber is the rotating substrate table with 15 chucks arranged in a circular configuration. All chucks, with the exception of one, namely the monitor chuck, are motorized and


Figure 29: The front side of the used BPM Clusterline 200 is shown. On the left side is the control panel with the two screens and on the right side the two load locks. On the left behind the front, the rack with its service control panel can be seen behind the pillar.

rotate during the coating process. The monitor chuck is attached to the table and has a 3 $cm$ diameter hole in its center that extends throughout the table.

- The **substrate table** rotates during the coating process at adjustable speeds and can be operated at different heights depending on the specific process. When substrates are loaded or unloaded by the handler, the table moves the relevant chuck into position directly in front of the transfer lock and aligns it so that a pin lift can raise the substrate through the table and through holes in the chuck at three contact points. This allows the handler to place or retrieve the substrate. The substrates are loaded with the side to be coated facing upward. Magnets embedded in the chucks enable the use of magnetizable substrate holders to ensure better stability at high rotational speeds.

The process chamber is hexagonal shaped, providing six positions for sputter or etching sources. The front side, designated as station 1, is the interface with the vacuum lock used to load and unload the substrates. Due to spatial constraints, no source is installed at this position under the standard configuration. Instead, a heater is installed in the center, surrounded by additional assemblies that are discussed in the following.

- The **heater** is a heating coil embedded in the lower section of the chamber ceiling and directed downward. It can operate at up to 3 $kW$ and emits a substantial amount of thermal energy directly onto the substrates. In addition to serving during process, it is also highly effective for chamber bake-out to remove residual water via evaporation.

Sputter sources are installed at stations 2 and 6. Station 2 houses the source with a silicon target, while station 6 is equipped with a tantalum target.

- The **sputter sources** are magnetron sputtering sources, their operating principle is described in 5.1. The targets are oriented downward, facing the substrates, and rotated during the deposition process. This results in a rotation-symmetric "race track" distribution on the target. Behind the target, a material-dependent configuration of neodymium magnets is mounted to shape the magnetic field in a way that locally adjusts the sputtering performance, thereby optimizing the material distribution on the substrate. Depending on the target material, the sources can be operated with either DC or RF pulses. However, only pulsed-DC was used in this project.

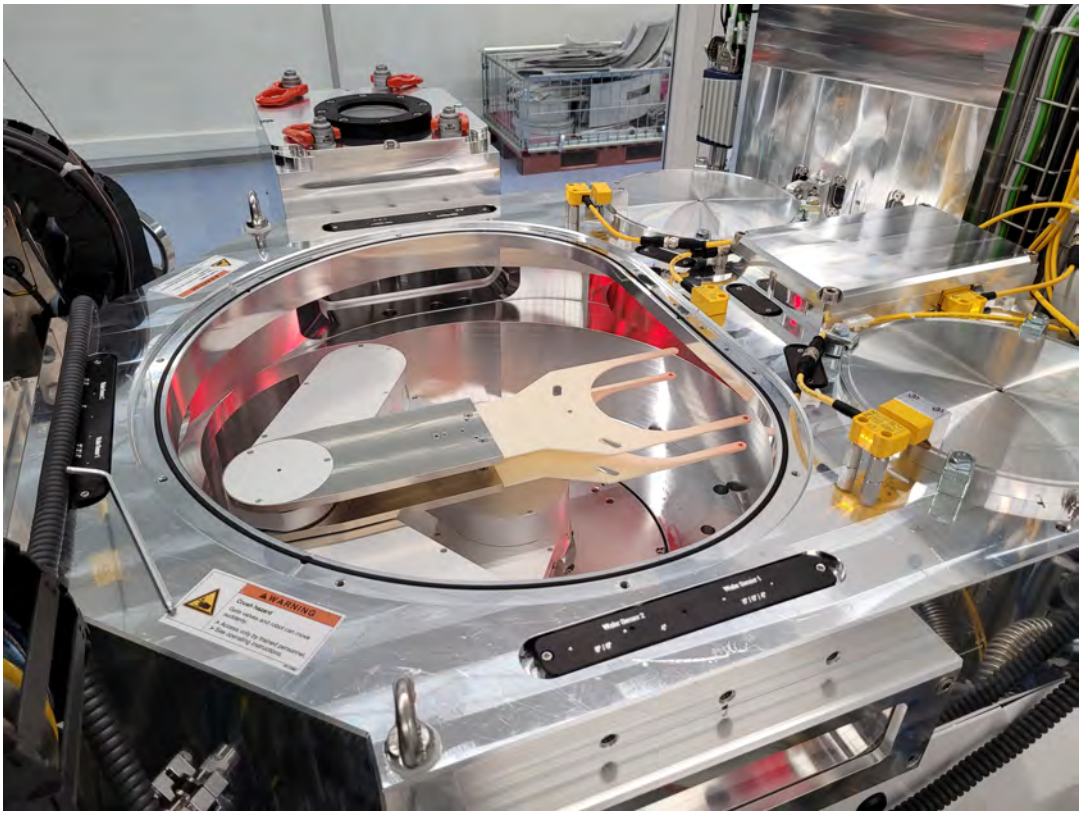


Figure 30: This figure shows the Vacuum Transfer Module with detached lid so the handler with the two arms can be seen. On the right side are the load-locks and the aligner and on the left side is the coating chamber. In the back the substrate flipper is attached.

Although stations 3 and 5 are not equipped and are covered with blank flanges, a plasma etching source is installed at station 4.

- The **plasma etching source (PSC)** is a capacitive coupled plasma source that generates a 13.6 $MHz$ RF-signal between the internal cup and the tungsten mesh placed in front of it. Various gasses can be introduced into the source; typically, oxygen with an argon admixture is used. A generated voltage accelerates the ions through the mesh so that they strike the passing substrates below. These ions can be used for post-oxidation of previously deposited layers or for surface etching.

Attached to the bottom of the system is, among other components, a residual gas analysis device, which is suitable for analyzing the background gas in the chamber and serves as a useful auxiliary instrument for leak identification.

- **Residual Gas Analysis (RGA)** is a measurement device designed for vacuum environments in which molecules passing a filament are ionized by an electron beam. These ions are then analyzed using a quadrupole mass spectrometer, providing information about the composition of the background gas present in the chamber. During processing, it is generally not used, as the higher pressure in this phase leads to rapid filament degradation.

In addition, the system is equipped with a pyrometer for measuring the substrate temperature. This device is also installed below the substrates. Through the hole in the table at the position of the monitoring chuck, the backside of the substrate located on the chuck is measured during each rotation of the table passing over the pyrometer. The advantage of the backside configuration is that it enables the production of interference filters in the infrared range without influencing the pyrometer measurements, which would occur if the measurements were measured from the front side of the

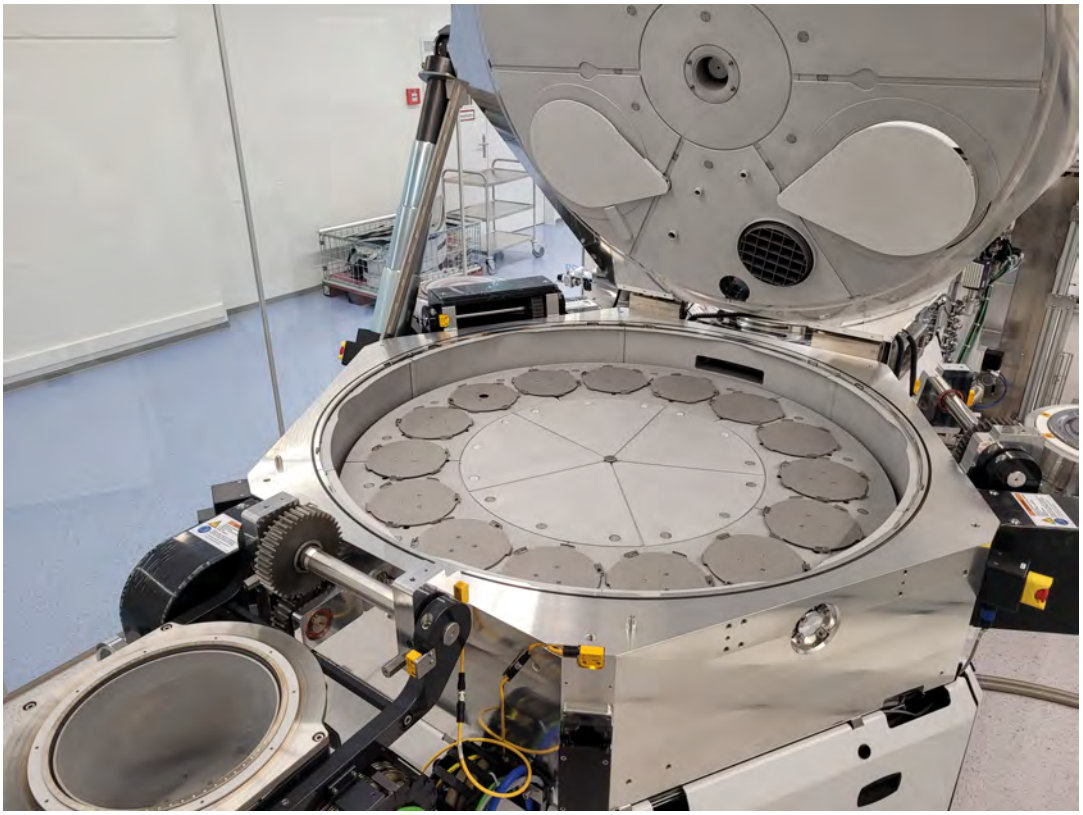

Figure 31: This figure shows the opened tool with the chucks on top of the table. On the left side is the PSC with its grid visible. In the right back is the silicon source and in the background the tantalum source recognizable.

substrates. However, this configuration limits measurements to a single chuck and can be affected by very thick substrates or holders.

- **Pyrometer** The pyrometer measures infrared radiation focused on the backside of the substrate in a short, triggered interval as the table passes over the pyrometer. The measurement signal outputs a voltage value that can be calibrated to a temperature range depending on the emissivity of the measured material.

Mounted on the ceiling of the chamber, in the center between the sources, is the defined anode.

- The **defined anode** serves as an additional element for process stability. As described in the chapter on magnetron sputtering 5.1, in a sputtering setup, the target is connected as the cathode and the substrate as the anode. In this system, the default mode uses the entire chamber, including the substrate table with its chucks connected, as the anode. However, the substrates themselves are electrically isolated from the table, and thus float. Because both conductive and insulating materials are deposited onto the table and substrates, the effective counter electrode of the cathode can shift within the chamber, potentially leading to process drift. To prevent this, the defined anode was introduced as an optional feature in the processes. In this configuration, a gas supply located at the center of the chamber ceiling, isolated from the rest of the chamber, serves as the anode, while the potential of the entire remaining chamber is allowed to float. Because the anode is always at a defined position, drift effects can be minimized.

Also on top of the coating chamber is the plasma emission monitoring (PEM) mount.

- **Plasma Emission Monitoring (PEM)** is a spectrometer with fast signal processing that regulates the reactive gas, which helps to control and optimize the reactive sputter process. Because every atom has its characteristic emission line if it is excited, the intensity ratio of the

lines can be used to control the mixing ratio of the gas types in real time. Depending on the process, other control variables such as the bias voltage can also be used. PEM enables reactive sputtering stabilized at a defined stoichiometry and at a high deposition rate.

close to the PEM housing is the optic head of the optical monitoring system (GSM)

- **the optical monitoring system (GSM)** was developed by Evatec [40][41]. GSM is a shortcut for a german designation (Genaues Schichtdicken Messgerät) which is not used anymore. It is a fast spectrometer that measures the reflectance of the coating within milliseconds at every pass of the rotating table. It can be used in broadband and also monochromatic mode and helps to determine the termination time for each layer in a coating process as accurately as possible. With each rotation, the monitoring system calculates the deviation of the measured spectrum from the target spectrum, and when the difference is as low as possible, sends the shutdown command for the process to the tool. It enables the coating of highly complex designs and is also able to compensate for drifts in the process to a certain degree.

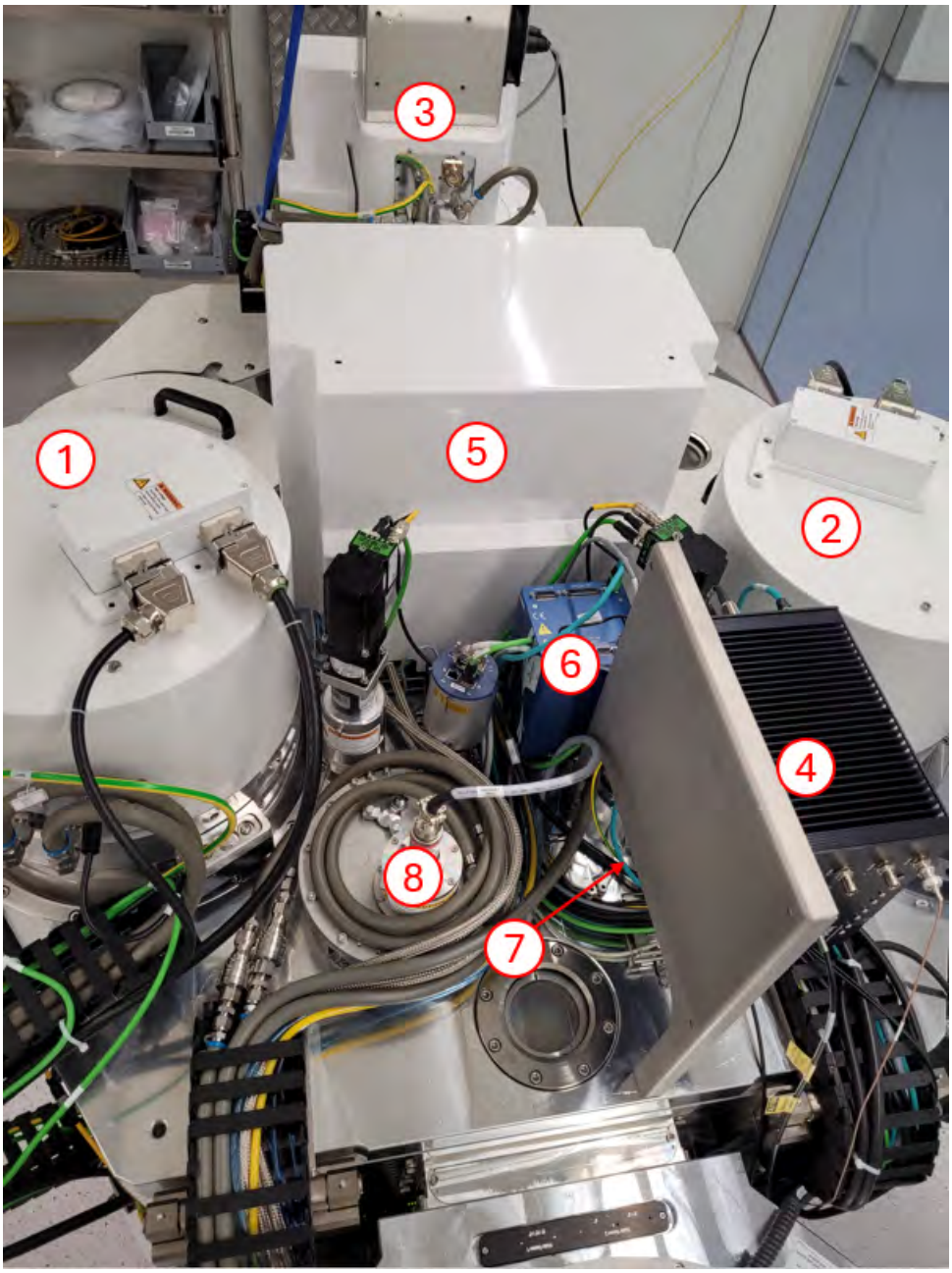


Figure 32: The figure shows the top of the coating chamber with several devices. (1) and (2) are the Si- respective Ta- sources. (3) is the additional plasma etching source (PSC). (4) is the housing of the plasma emission monitoring (PEM) and (5) for the additional defined anode. (6) is the RGA and (7) indicates the GSM optic head below the PEM housing. (8) is the front side heater.

# 6 Theoretical Description of Quantized Nanolaminates

The main focus of this work lies in the investigation of quantized nanolaminates (QNL). This includes a theoretical background to gain an understanding of the function and the principle behind, the process of coating them, and also methods, how to measure and characterize the physical properties.
The term was first used in 2016 [42], it must be said, however, that the idea has been floating around under other names before, making it difficult to trace its origins [15]. The principle of structured materials with differing band structures has existed for a longer time in semiconductor physics and even led to a Nobel Prize in 2000 for the development of hetero-structured semiconductor materials [43].
QNL represents a quantized meta material as they consist of a sequence of various optical materials which are structured periodically. The two materials build periodic ultra thin films with different band gaps. Due to the periodic layout, each of the high refraction layers with the lower band gap not only has the same thickness but also lays between two low refraction layers with the same higher band gap and also the same thickness. Through this spatial limitation, the movement of valence electrons is restricted, which leads to an increase in energy for the optical band gap [44]. As a result, the absorption edge of the whole system shifts to shorter wavelengths.
Because the effective refractive index of the system is built by the volume ratio of the two materials and their individual refractive indices, this leads to a method where it is possible to have the same refractive index as a homogeneous mixture but with different absorption edge [44], [45], [46],[47].

## 6.1 Refractive Index

If we mix two different optical materials, the resulting refractive index also changes. Calculating the effective refractive index ($n_{eff}$) depends on the properties of the material and also on the structure how it is mixed and also how light interacts with the medium [48]. In the literature dealing with QNL, often the Drude-model is referred to [44],[49],[46]:

$$n_{mix}^2 = \sum_i f_i n_i^2 \quad \text{with:} \quad f_i \in [0,1]; \sum_i f_i = 1 \tag{140}$$

Describing the effective refractive index of a mixture with the number of $i$ materials, each with an individual refractive index $n_i$ and the volume ratio factor $f_i$. With two materials as for the quantized nanolaminates, this leads to the expression of:

$$n_{eff}^2 = f n_{Low}^2 + (1-f) n_{High}^2 \quad ; \quad f \in [0,1] \tag{141}$$

This model assumes that the polarizations of the atoms in the material are only influenced by the external electromagnetic field and are completely shielded by the surrounding atoms [48].

## 6.2 Quantization Effect

As mentioned above, QNL are composed of two different optical materials arranged alternately in ultrathin layers. Taking into account that light travels along the optical axis through a stack of QNL on a substrate, it experiences a periodic series of different band gaps, shown in Figure 33. The lower energy levels indicate the potential energy of the electrons in the valence band and the higher potential energy indicates the level of energy that the electron needs to overcome to recombine with the hole in the conduction band [50] (P.5). The distance between the two bands is called the band gap and a material specific value. To explain it roughly, the wider the gap, the higher needs to be the energy of, for example, a photon to get absorbed and excite the electron in the valence band. If the photon energy is lower than that gap, it cannot be absorbed as the area between the states represents the "forbidden" zone and therefore the material is transparent for this photon with its energy specific wavelength [2] (P.489).
However, this represents only a simplified version, as the spatial limitation of the energy potential leads to the discretizations of the energy states that the electrons and also the holes can occupy.
This effect is the key to the principle of QNL and to be able to understand what happens we have to look at a finite potential well as it is shown in figure 34. In this well, electrons or holes can be described by wave functions $\Psi(x,t)$, while those wave functions describe the probability of their localization with

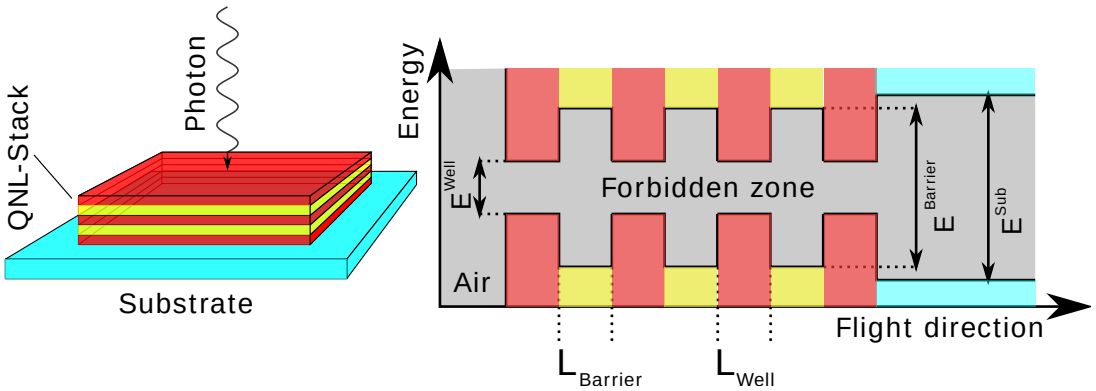


Figure 33: This figure shows the bandgap a photon experiences by transmitting a QNL system on its optical axis. On the left side, a stack of two different materials coated on a substrate and the indicated path of a photon and on the right side, the bandgap of the two materials with the lower laying valence band and the upper conduction band. The material with lower refractive index has a wider bandgap and works as a barrier. The other is the well material.

$P(\Psi(x,t)) = |\Psi(x,t)|^2$ [2] (P.123). To describe how the wave functions behave, we have to solve a simple Schrödinger equation:

$$i\hbar\frac{\partial}{\partial t}\Psi(x,t) = -\frac{\hbar^2}{2m}\frac{\partial^2}{\partial x^2}\Psi(x,t) + V(x)\Psi(x,t) \tag{142}$$

With:

$h \simeq 6.626... \cdot 10^{-34}$ $[J \cdot s]$ ... the Planck constant

$V(x)$ $[J]$ .. The potential of the described system

As it is a time invariant situation the term $\Psi(x,t) = \psi(x) \cdot \phi(t)$ can be separated which leads to the time invariant Schrödinger [51]:

$$E_n\psi_n(x) = -\frac{\hbar^2}{2m^*_{e,h}}\frac{\partial^2}{\partial x^2}\psi_n(x) + V(x)\psi_n(x) \tag{143}$$

$\hbar = \frac{h}{2\pi} \simeq 1.055... \cdot 10^{-34}$ $[J \cdot s]$ ... the reduced Planck constant

$E_n$ $[J]$ ... the energy eigenvalue

$m^*_{e,h}$ $[kg]$ ... the effective mass of the particle, in this case an electron or hole;

In this equation, the effective masses of the electron or hole are already inserted. It should be considered that the mass of an electron (and also hole) is different if it moves through material and is bound compared to its mass in free space [52] (P.163).
The eigenenergy values $E_n$ are solutions that are valid to meet the right side of the equation. The number of solutions and corresponding wave functions is indicated with the letter "$n$".
It is recognizable in figure 34 that the potential of the well material ($Ta_2O_5$) between the barrier material ($SiO_2$) consists of three different parts. The area before $-\frac{L_{well}}{2}$, indicated with the corresponding wave function $\psi_{I,n}(x)$, the area in the potential well between $-\frac{L_{well}}{2}$ and $\frac{L_{well}}{2}$, indicated with the corresponding wave function $\psi_{II,n}(x)$, and the third part after the potential at $\frac{L_{well}}{2}$ with its wave function $\psi_{III,n}(x)$. Leading to the expression of the potential [50] (P.38):

$$V(x) = \begin{cases} V_0 & for \quad x \leq -\frac{L_{well}}{2} \\ 0 & for \quad -\frac{L_{well}}{2} \leq x \leq \frac{L_{well}}{2} \\ V_0 & for \quad \frac{L_{well}}{2} \leq x \end{cases} \tag{144}$$

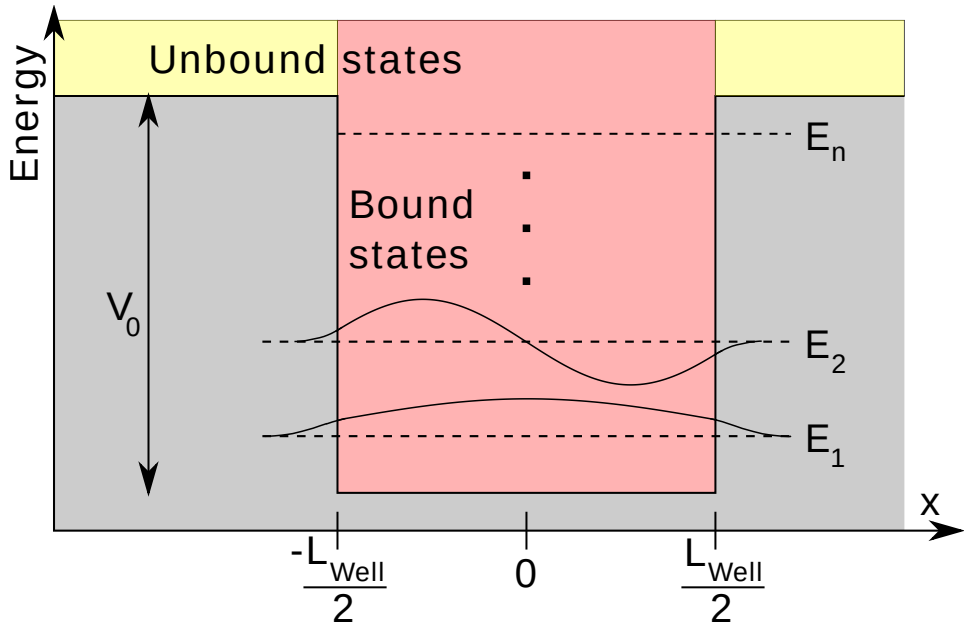


Figure 34: This figure shows a finite potential well with the length $L_{well}$ and the height $V_0$. Due to its spatial limitation, the first energetic state lays above the ground of the well.

As we defined our potential for the situation, we can choose some general wave functions which meet the requirements.

$$\begin{aligned} \psi_{I,n}(x) &= A \cdot e^{\alpha_n x} + B \cdot e^{-\alpha_n x} \\ \psi_{II,n}(x) &= C \sin k_n x + D \cos k_n x \\ \psi_{III,n}(x) &= E \cdot e^{\alpha_n x} + F \cdot e^{-\alpha_n x} \end{aligned} \tag{145}$$

With:

$\alpha_n$ $[\frac{1}{m}]$ ... describing the damping of the wave function in the barrier medium

$k_n$ $[\frac{1}{m}]$ ... normalizes the wave function in the well to its length

Those are typical forms of wavefunctions used in this situation [50] (P.39), [2] (p.457). With the condition of having a continuous function also at the transition for the meeting wave functions and also their derivations, we can determine the variables [50]:

$$\begin{aligned} \psi_{I,n}(\frac{L_{well}}{2}) &= \psi_{II,n}(\frac{L_{well}}{2}) \\ \frac{\partial}{\partial x}\psi_{I,n}(-\frac{L_{well}}{2}) &= \psi_{II,n}(-\frac{L_{well}}{2}) \\ \psi_{II,n}(\frac{L_{well}}{2}) &= \psi_{III,n}(\frac{L_{well}}{2}) \\ \frac{\partial}{\partial x}\psi_{II,n}(\frac{L_{well}}{2}) &= \frac{\partial}{\partial x}\psi_{III,n}(\frac{L_{well}}{2}) \end{aligned} \tag{146}$$

With the assumption that the wave function of the particle in the well only flows out and there is no incoming component (Furthermore, this is also necessary to ensure normalizability), we can delete $B = 0$ and $E = 0$. And remove either the odd or even term of the function $\psi_{II,n}$ with $C = 0$ or $D = 0$. Set back in the Schrödinger equation leads to the two equations:

$$\begin{aligned} \alpha_n &= \sqrt{\frac{2m^*_{e,h}(V_0 - E_n)}{\hbar^2}} \\ k_n &= \sqrt{\frac{2m^*_{e,h}E_n}{\hbar^2}} \end{aligned} \tag{147}$$

This means that we get physical expressions for both function arguments.
If we use the boundary condition and divide the equations of the wavefunctions and its derivations, we get two equations

$$\begin{aligned} k_n \tan(\frac{k_n L_{well}}{2}) - \alpha_n = 0 \\ k_n \cot(\frac{k_n L_{well}}{2}) + \alpha_n = 0 \end{aligned} \tag{148}$$

With substitution of $z = \frac{k_n L_{well}}{2}$ and $\sigma = \frac{L_{well}}{2}\sqrt{k_n^2 + \alpha_n^2}$ we get the two equations for odd and even functions of:

$$\underbrace{\frac{\sqrt{\sigma^2 - z^2}}{z}}_{f_1(z)} = \underbrace{\begin{cases} \tan z & \text{(even)} \\ -\cot z & \text{(odd)} \end{cases}}_{f_2^{e/o}(z)} \tag{149}$$

While:

$$\begin{aligned} z &= \frac{L_{well}}{2\hbar}\sqrt{2m^*_{e/h} E_n} \\ \sigma &= \frac{L_{well}}{2\hbar}\sqrt{2m^*_{e,h} V_0} \end{aligned} \tag{150}$$

To explain this situation, the points where the functions $f_1(z) = f_2(z)$ are the points where the energy eigenvalues $E_n(z_n)$ meet the criteria of the Schrödinger equation 143 for the given particle in the given potential 144. To obtain the solutions, a numerical approach is used, shown in figure 35. This also corresponds to the description for quantized nanolaminates in [44].

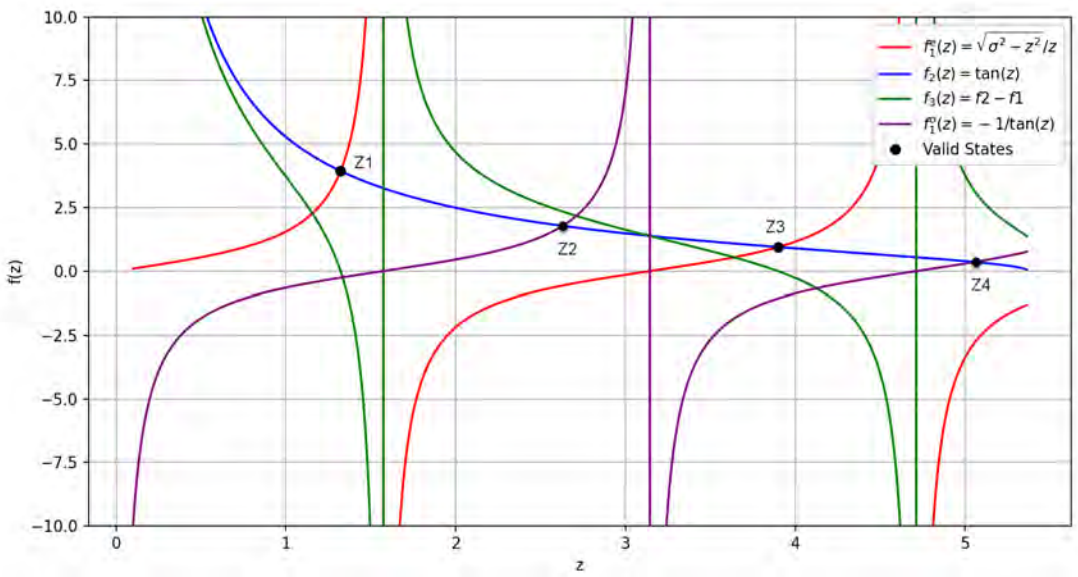


Figure 35: This figure shows the calculation of the energy eigenvalues for a $Ta_2O_5$ well with a length of $L_{well} = 2\,nm$ between $SiO_2$ as the barrier material. The red line indicates the even functions $f_1^e$ from the equation 149. The blue line indicates the function $f_1$. The green line shows the difference of the two functions $f_1$ and $f_2$, indicating the intersections of them and therefore the even energy eigenvalues $E_1, E_3, ....$ The purple line shows the solutions for the odd wave functions, its intersections with $f_2$ would indicate the odd functions $E_2, E_4, ....$

While we let $z$ run over a range, we see for both functions $f_1(z)$ and $f_2^{e,o}(z)$ how they would behave and we can also see where they meet $(z_n)$. As we are interested in the lowest possible energy eigenvalue, which is always an even wave function in a symmetric potential [50] (P.40), we need to look only at the intersections of the even function $f_1(z) = f_2^e(z)$. We can set the first intersection $z_1$ in the equation

150 to get $E_1$.
As you can see, the odd and even functions alternate with each other until there is no possible solution with the given criteria being $\sqrt{\frac{\sigma^2 - z^2}{z^2}} \to 0$.
In the calculation shown in figure 35 a $Ta_2O_5$ layer is calculated with a thickness of $L_{well} = 2\,nm$ within $SiO_2$, showing the possible four energy eigenvalues with $z_1 = 1.33$ leading to an increase of $\triangle E = V_0 - E_1 = 0.13\,eV$.
Now it needs to be said that in this simulation only the difference for the electron is calculated as the mass of the hole is larger by about a factor of 10, leading to a negligible influence [51], . The effective electron mass for this calculation is set as $m_e^* = 0.8 \cdot m_e$, as the factor tends to be between $0.5 - 1$ and $Ta_2O_5$ in this setup [51], [45]. Since this is only a simulation to aid in understanding, this assumption is sufficient. In reality, this mass would have to be calculated precisely, as it can change depending on the surrounding structure [50] (P.5,46).
To visualize this effect, two potential wells with different thicknesses are drawn in figure 36.

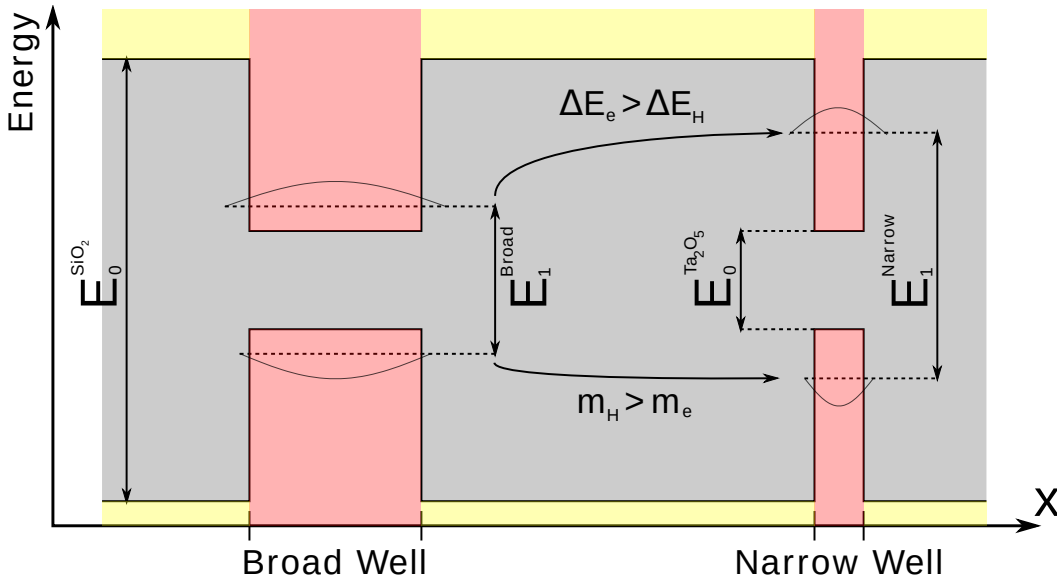


Figure 36: This figure visualizes the difference between two $Ta_2O_5$ layers with different thickness in $SiO_2$. The influence of the thickness of the well is recognizable. The thinner it gets, the higher the first state is shifted and the less states fit in the potential. Also the minor shift for the much heavier hole is indicated.

As we can see, it is possible to make a first approximation of how much the band gap of a single nanolaminate changes with the thickness of it in a block of another medium with a higher band gap.

### 6.2.1 Penetration Depth and Tunneling Effect

In quantum physics, unlike classical physics, the wave used to describe the localization of particles can penetrate a barrier and travel even through it, reaching another well [50] (P.64).
If we again look at the wavefunction $\psi_{III}(x)$ from equation 145 and figure 34 we can see that it consists of two parts. One which describes a wave which comes from the right side towards the wall and grows the further away we get from the transition zone. This one we neglect here with $E = 0\,eV$ as we have only one wave function in the middle of the well, flowing "away" from there. Then we also have the second part, which describes the decreasing wave the deeper it gets into the barrier layer.
Using the equation for the damping factor 147, we can calculate how far the wave reaches into the barrier until it falls below a certain fraction of the original amplitude $\psi(d)$ with:

$$\psi(d_{Tunnel}) = \mathrm{e}^{-\alpha d_{Tunnel}} \Rightarrow d_{Tunnel} = \frac{-\ln \psi(d_{Tunnel})}{\alpha} \tag{151}$$

With:

$\psi(d_{Tunnel})$ ... the fraction intensity left while $\psi \in ]0, 1]$

$d_{Tunnel}$ $[m]$ .. The distance the wave penetrates the depth

We can see that the tunnel distance depends not only on the mass, but also on the difference in the barrier height and the energy state $\alpha_n \propto \sqrt{V_0 - E_1}$.
This means, combined with the insight from the previous subsection, that the thinner the laminate gets, the higher the first state, and the further the wave function reaches the barrier material.

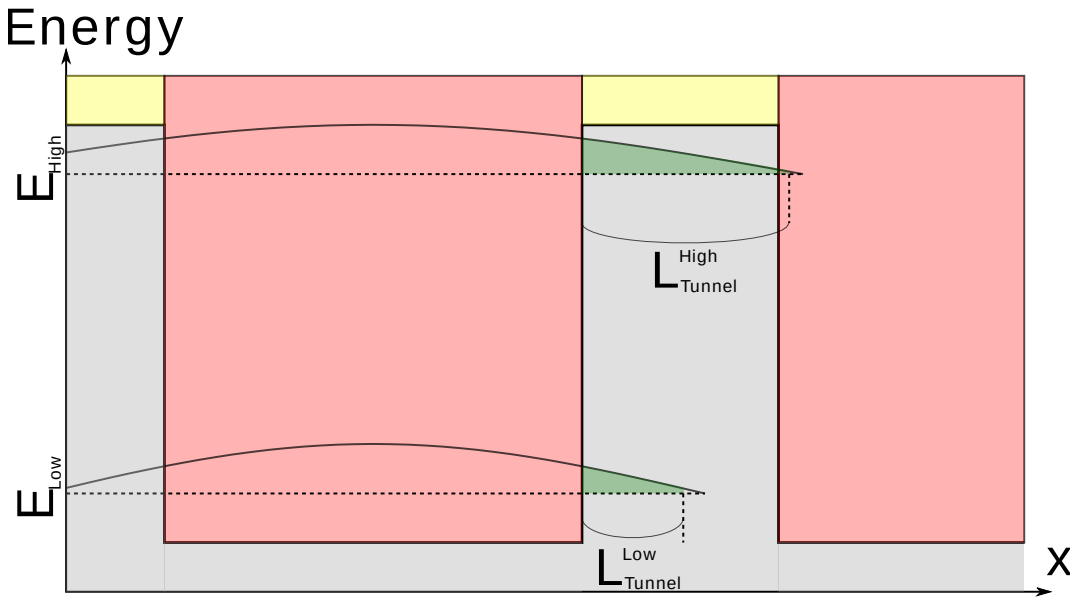


Figure 37: As evident from equation 147 the damping term and therefore the penetration depth depends on the height of the state relative to the height of the barrier. The thinner the barrier layer is, the easier it gets for the electron to tunnel through.

The fact that two neighboring potentials can influence each other must serve as a reminder at this point that we know that we cannot make the barriers arbitrarily thin. To calculate the correct effect, we would have to use a multi-potential model [50] (P.51, 108). This is briefly mentioned in the discussion section, but since I lack the expertise to verify this, I am refraining from doing so here. However, according to the literature, care should be taken to ensure that the barrier depth is at least high enough so that the intensity of the wave drops to less than $1/e^2$ [51].

## 6.3 Absorption Edge

Now the widening of the band gap explains the shift of the fundamental absorption edge in the spectrum, but it is important to understand that the whole absorption spectrum consists of different regions each depending on specific mechanisms [5] (P.36). The calculated absorption coefficient from the transmission and reflection measurement of a coated nanolaminate stack is shown in figure 38. Expressing the coefficient in a logarithmic scale shows the different regions.

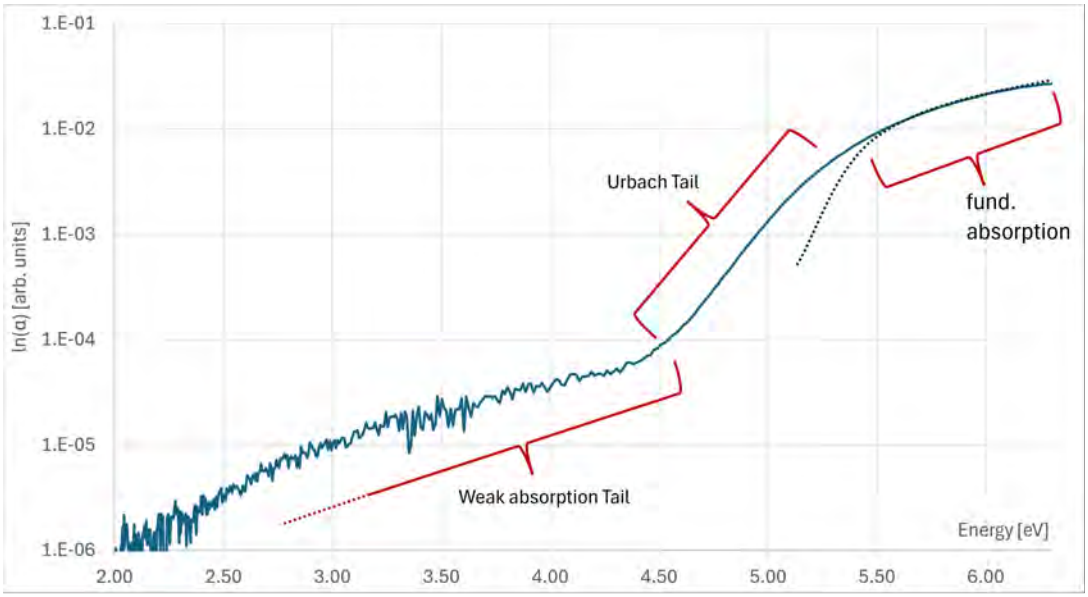


Figure 38: The real absorption of a measured $QNL - PJ3035$ coating is shown. Starting with the weak absorption tail, followed by the Urbach-absorption and in the end the absorption given by the actual band gap. Inspired by [53] (P.19).

On the right side, the "*fundamental absorption*" is the range described by the multi oscillator model; the loss of energy due to several oscillators, excitation of valence electrons and influenced by the band gap shift described in the previous section.
The Urbach-tail describes the region close to the band gap energy and is a cumulative effect of impurities, disorders, and electron-phonon interactions and is strongly temperature dependent [54]. The Urbach-tail region and its absorption coefficient $\alpha_U$ can be described as [54],[55]:

$$\alpha_U(E,T) \propto \mathbf{e}^{\frac{E-E_0}{E_U(T)}} \tag{152}$$

While $E_0$ describes the Urbach-Edge, the energy where the Urbach-Tail starts and $E_U(T)$ the temperature-dependent Urbach-Energy measure how steep the exponential absorption tail gets.
The Weak absorption Tail (WAT) differs a little bit in description and range depending on the literature, but it is also an exponentially decaying tail below the energy of the Urbach-region. It describes mainly defects with localized states but low state densities [56]. The figure 39 is adapted from J. Tauc [57], it shows not only the optical band gap but also the tail region with its lower state density.

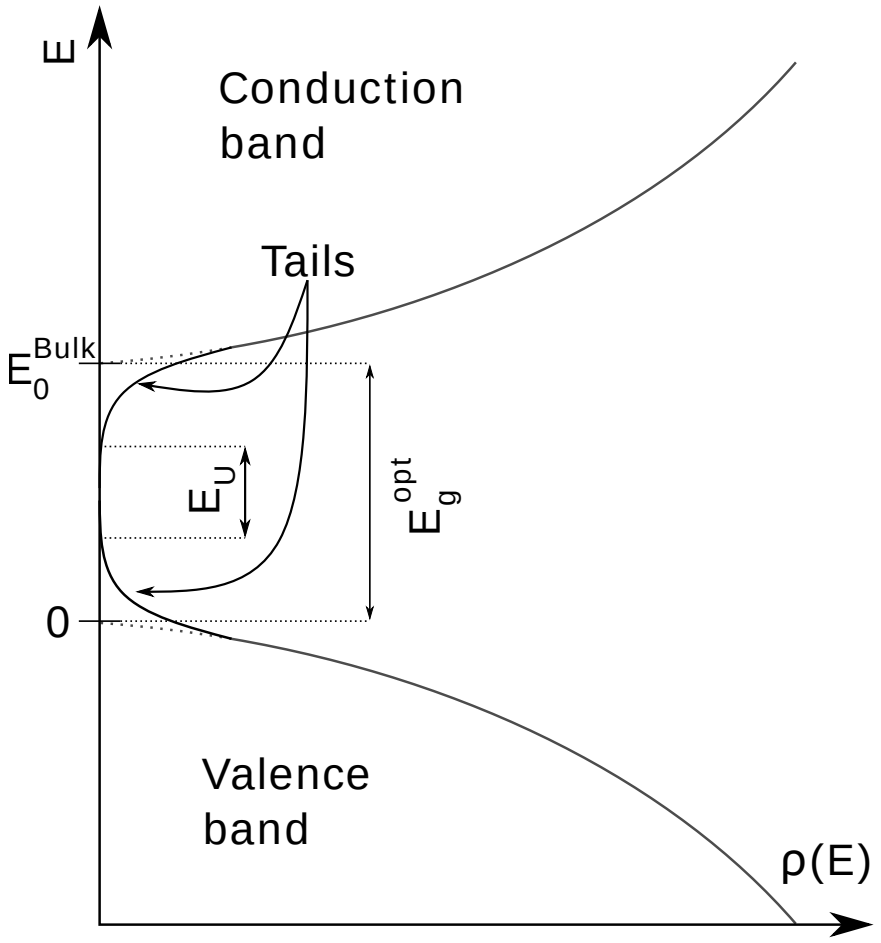


Figure 39: Displayed are the density of states $\rho(E)$ of an amorphous insulator for the valence and conduction bands with the (Urbach) absorption tails.

It is important to note that the diagram in the original source shows a semiconductor and not an insulator, which would be the case for us. This means that the two bands and also the tails should be separated so that they do not overlap, as in [58]. However, in imperfect insulators, there are individual states caused by defects with very low densities that can be very far away from the actual band and may even show overlaps with individual bands on the other side. I have not found any source that would describe it, but as a defect of $SiO_2$ could be a $\alpha Si$ compound which is a semiconductor with a band gap of $E_{gap}^{\alpha Si} \approx 1.7\,eV$ [59] for me it would be a good explanation for the very low- lying and very weak absorption plateaus that we have already seen in measurements.

### 6.3.1 Tauc-Plot

Because the band gap determines the fundamental absorption region of the absorption coefficient, it is possible to calculate the band gap from the measured spectra.
J. Tauc developed the Tauc-Plot [57]. The equation is based on the Tauc equation:

$$(\alpha E)^n = A(E - E_g) \tag{153}$$

$\alpha$ as the absorption coefficient, $E$ describes the photon energy, $A$ is a proportion factor which falls out for the band gap calculation as we are looking for the zero point and $E_g$ the energy gap. The exponent $n$ depends on the type of transition with

$n = 2$ for direct allowed,

$n = \frac{1}{2}$ for indirect allowed,

$n = \frac{2}{3}$ for direct forbidden and

$n = \frac{1}{3}$ for indirect forbidden transitions.

The different types of transition are shown in figure 40.

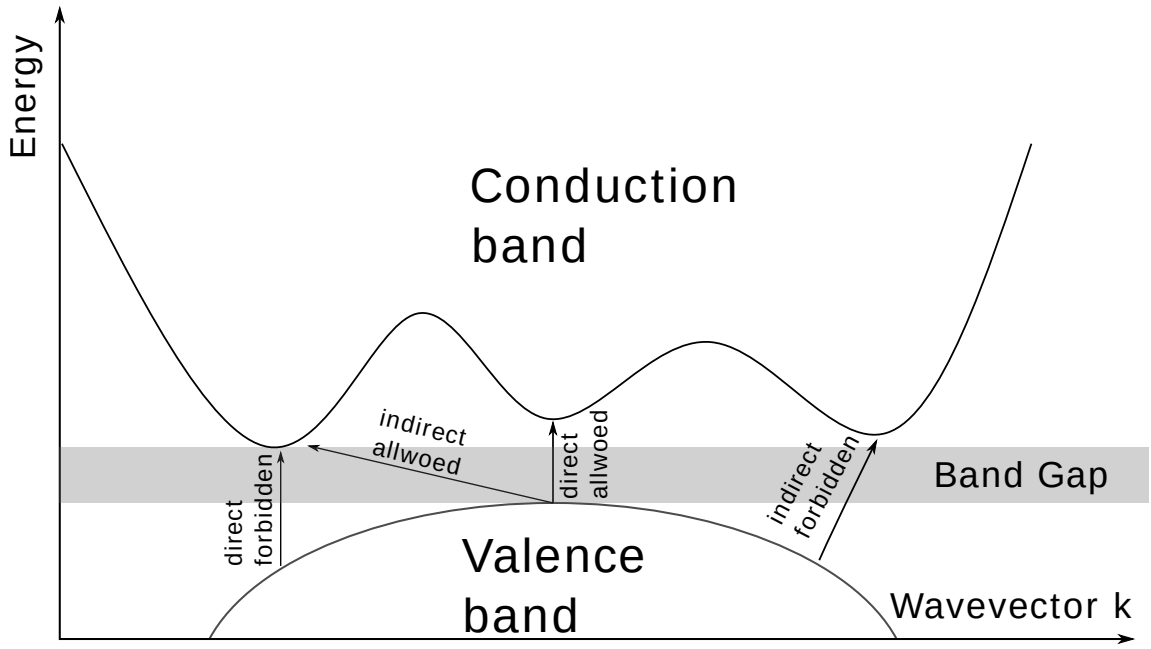


Figure 40: The figure shows the different types of transition. The direct transitions are just vertical jumps of an electron from the valence to the conduction band while the impulse $k$ stays constant. They need only an energetic excitation from a photon with the missing energy. The indirect transitions have a change in $k$ and need an additional pulse to occur. As a photon has mostly low momentum it is mostly a phonon which "helps". The allowed transitions start from the highest possible valence band state and the forbidden from a lower level.

To calculate the optical gap from this formula, the term with the absorption coefficient is plotted against the photon energy, so $(\alpha h\nu)^n$ vs $(h\nu)$. The fundamental absorption is dominated by one of the described transitions, and the energetic region of this transition is straightened under the correct exponent $n$. This straight region is linearly extended until it crosses the x-axis where it defines the optical energy gap, see fig 44. The usual method to estimate the correct transition is to plot all possible exponents and see where the largest linear portion occurs [60].

# 7 Evaluation in Practice

This chapter first explains how the previously described QNLs can be produced specifically and efficiently with our system. Subsequently, a series of QNL stacks is used to explain how we evaluate them and what needs to be considered, as a basis for the following chapters, where further layer properties are discussed.

## 7.1 Setup Advantages

A significant number of studies in the field of QNL had been published using IBS and ALD coating systems at the time we began our own investigations [51], [44], [42]. These coating technologies offer very high precision in layer growth, making them particularly well suited for fabricating layers with extremely accurate thicknesses. However, when using IBS-produced layers, there is the drawback that a new process must be initiated after each layer to deposit the next material. Consequently, when a nanolaminate stack is to be fabricated as part of a multilayer system, this can become extremely time consuming and significantly reduces the economic efficiency of the resulting coating. Furthermore, it can be challenging to maintain all the process parameters—such as rate, density, and others over such long deposition times without experiencing drifts, which would compromise the uniformity of the nanolaminate structure.
In ALD systems, the problem typical of all ALD processes is their slow deposition rate, which also negatively impacts their economic feasibility. However, the changeover between individual layer materials is less problematic, since every atomic layer is inherently deposited in a separate cycle [61]. Even so, long process durations may still result in drifts, and due to the extremely small thicknesses of the layers, such drifts are difficult to detect.
Due to the specific configuration of the coating tool used in this project, it was possible to eliminate or at least reduce many of the issues encountered with other coating systems. At that time, the system was equipped with a single DC generator and a main switch unit (MSU) to direct the generator's signal to the specific sputter source. We implemented a system upgrade by adding a second generator and replacing the MSU configuration by directly connecting each source to its own generator. The generators were then synchronized using a trigger signal, ensuring simultaneous signal initiation during concurrent operation. This modification enabled both sputter sources to be operated simultaneously.

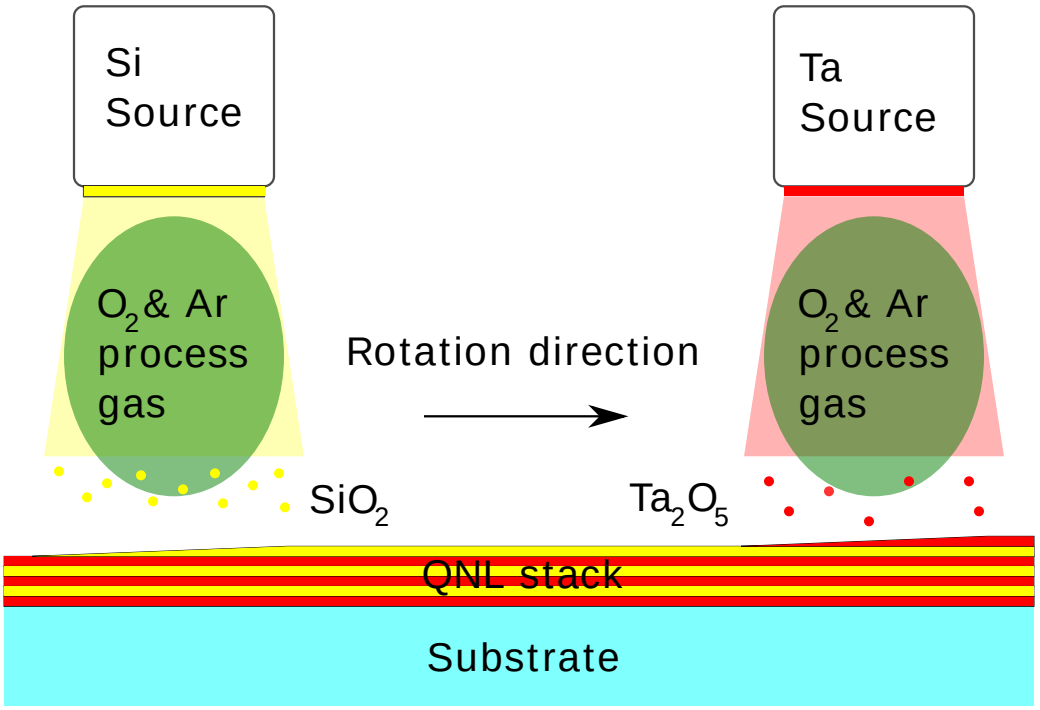


Figure 41: As the table rotates below the sources, those run continuously coating one NL pair at each rotation without interruption, leading to a high deposition rate.

The benefit of this upgrade for fabricating QNL layers becomes evident when compared to the previous setup.
In a standard coating process, a specific material is deposited with a defined thickness. To do this, the substrate is loaded into the chamber, and the table begins to rotate. This rotation is maintained throughout the entire coating process. Next, gas is introduced, and the plasma is ignited at one of the sources behind a shutter. Once ignition is successful, the shutter opens, the source power is increased, and a stable sputtering process is established. To enhance the sputter rate, the oxygen flow is reduced and typically regulated to a defined value monitored by the plasma emission monitor (PEM). With each rotation of the table, the substrate passes the source and is coated with a thin layer of the target material. The thickness of each layer is determined after each rotation by rate calculation or optical monitoring. Once the desired thickness is achieved, the deposition process is terminated by reducing the source power, closing the shutter, and increasing the gas flow to further reduce the deposition rate. At this point, the first layer has been deposited, and the second layer follows. To accomplish this, the MSU switches the generator output to the second source, which contains a different material, and this process starts again just for the second material. It must be noted that parameters such as gas flow, PEM intensity, table distance, voltage, and others can differ significantly between materials. By repeating this process, layer by layer, a multilayer system is gradually constructed.
To coat a stack of QNL, the process is similar, but with a crucial difference. With the two synchronized generators, it is possible to run both sputter sources at the same time. While the substrate table rotates, both sources are ignited. Shortly after the two plasmas stabilize, the shutters open simultaneously and the power rises to its process value, while the two gas flow controllers aim for the different setpoints. This step can be challenging to adjust to precise accuracy, as both controllers have the oxygen flow as their manipulated variable. While the process for $SiO_2$ sputtering uses the bias voltage as control , the $Ta_2O_5$ process uses the amplitude of the oxygen plasma emission line divided by the amplitude of the argon line. Both values are provided by the PEM, described in 5.2.3.
As both plasmas burn close to each other in the same chamber, both processes can be quite unstable and start to oscillate, or one controller closes the oxygen line completely while the other does the whole work. Even though this step of setting up the process cleanly can be a bit tricky, in my experience, once the process is stable, it remains stable. Once you have the process, you can also increase and decrease the power of the respective source within a limited range. The sputter power is approximately proportional to the sputter rate.
While the sources are running, the table rotates continuously at a constant speed, so the substrates on the table pass the first source and get a thin layer (about $0.1 - 1\,nm$) of the first material deposited on them. After they passed the first source they reach the second and also get a thin layer of the second material. This process continues as long as desired to coat a stack of quantized nanolaminates. As the process once started does not need to change anything like gas flow, power, or other process relevant parameters, the process and, therefore, the composition of the laminates remain the same for the duration of the whole stack. As in every other tool or process, of course, drifts can occur but with the high deposition rate these can be neglected.

## 7.2 Results

In order to be able to produce QNL in a controllable and targeted manner, the mixing ratio of the two materials is necessary first to control the refractive index as described in the chapter 6.1. As already mentioned, there is no generally applicable procedure for this step. I proceeded by selecting settings for both materials in a parallel process that were close to the values used for the individual materials. In doing so, I made sure that $Ta_2O_5$ was given a relatively higher control value than $SiO_2$, as it seems that $SiO_2$ binds oxygen much faster. From this point on, the process can be optimized to reach the desired mixing ratio, which requires some practice.
With the mixing ratio, the refractive index of the QNL is given, which defines the thickness of the individual layers in each pair.
Measurement of the thickness of a coated stack and knowing the number of turns the rotating table made, the thickness of each layer pair is easily calculable. With the ratio factor $f$ from 6.1 the thickness of the individual layer pairs is calculable.
In order to demonstrate the effect described in chapter 6.2, which depends mainly on the thickness of the barrier material, all that needs to be done is to change the rotation of the table. The faster the table rotates, the thinner the layer pairs get, while keeping the same ratio.

## 7.3 Process Series

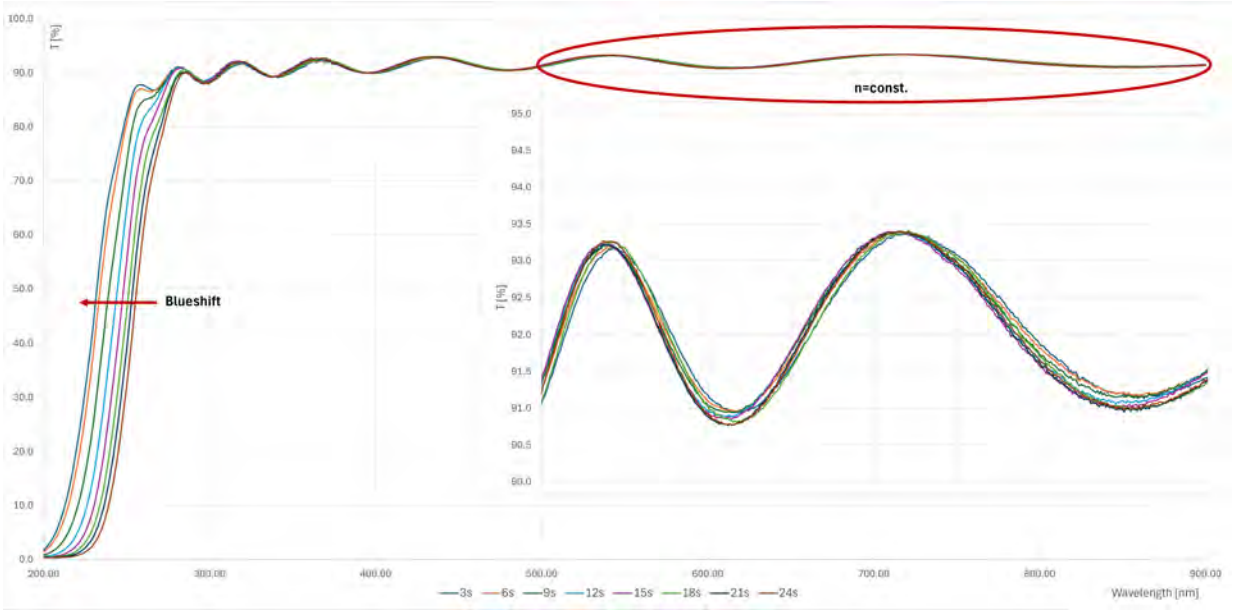


Figure 42: This figure shows the shift of the absorption edge of a QNL stack in dependence of the table rotation time. In the region of higher wavelength the refractive index stays constant which indicates a constant refractive index. The figure uses the data from [62]

The first proof of this effect we could demonstrate is shown in figure 42.
I am using a similar illustration as in the paper [46] because I think it presents several important points about QNL very clearly and elegantly.
A stable process was selected, and then a stack of QNL was coated onto a separate substrate for each of the different table rotation speeds. The coatings were measured with the spectrophotometer described in 4.1. On the right side of the spectra between 500 $nm$ and 900 $nm$ two main points can be seen. First, the refractive index is about the same for all the samples in the specific region, which can be seen as the height difference between the peaks and valleys being the same. The second point is the thickness of the samples. Each stack was coated for the same time and therefore the total thickness of each stack is the same. This can be seen by the overlapping of the peaks in the x-direction. On the left side, on the other hand we see that the transmission line shifts towards the short wavelength for the samples with the higher rotation speed. As mentioned, a higher rotation speed means a thinner well layer and therefore a larger band gap, at least in a restricted range.
In summary, this first impression of the QNL effect coated on our tool shows not just the shift in the band gap through the shifted transmission spectrum but also a perfect match in refractive index and rate stability for the several coatings on the longer wavelength side.
Later, EMPA performed a TEM analysis of a coated QNL stack where we could see for the first time that it has high uniformity over a longer coating process 43. The chosen process took 30 $min$ to deposit and coated 536 $nm$ of $Ta_2O_5/SiO_2$-QNL.

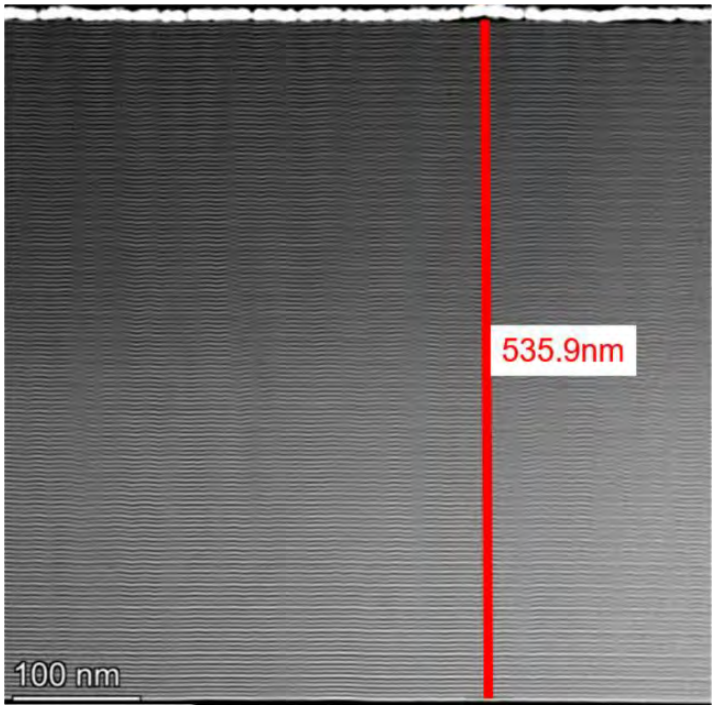


Figure 43: High angle annular dark-field scanning electron microscopy (HAADF-TEM) picture done by EMPA using a Titan Themis 200G. The whole stack has a thickness of roughly 536 $nm$ and took 30 $min$ to coat while the table rotation speed was 6 $s/pass$.

### 7.3.1 Band Gap Calculation

To express this shift in numbers, the Tauc-plot method 6.3.1 was used. The first step is to obtain the absorption coefficient. One method is to calculate it from the extinction coefficient with $\alpha = \frac{4\pi\kappa}{\lambda}$. The other method is to calculate it directly from the transmission and reflection spectra of $T_{tot}$ and $R_{tot}$ using $A = \mathbf{e}^{-\alpha d}$ 3.1.2. We decided to use the second approach but had a problem using the formula for the total reflection or transmission, since these terms cannot be easily resolved simply to alpha. We took only the first transmission term, a simplification that ignores all the following terms 95.

$$\begin{aligned} T_{tot} \approx T_1 = (1-R)\cdot \mathbf{e}^{-\alpha d} \\ R_{tot} \approx R_1 = R \end{aligned} \tag{154}$$

which means:

$$\alpha = \frac{-1}{d}\ln(\frac{T}{1-R}) \tag{155}$$

This equation is used often in the literature, but one has to be careful as it ignores backside reflection as well as all further internal reflection and absorption effects. This came out as a problem, and will be discussed later in the section 10.1.

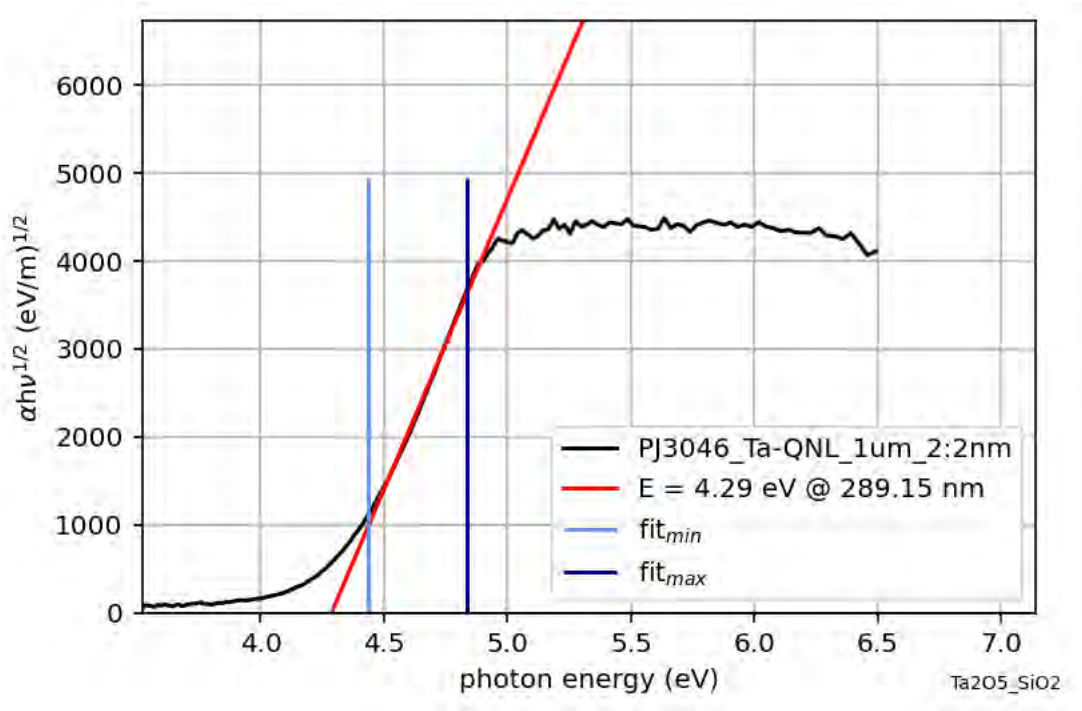


Figure 44: The figure shows a tauc plot for the QNL-stack $PJ3036$ with the fit for a straight line. the calculated optical gap is calculated as $E_{opt} = 4.29\,eV$.

### 7.3.2 Process Variety

Several processes with different mixing ratios and therefore different refractive indices were developed. The QNL stacks were then coated with the same thickness and the band gaps determined.
From the calculation of the mixing ratio, the thickness of the well layer ($Ta_2O_5$) follows directly. This can be seen in figure 45. The refractive index is plotted against the thickness of the $Ta_2O_5$-layers in figure 46. it can be seen that it is stable over the different values with a slight tendency towards higher values at higher thickness.

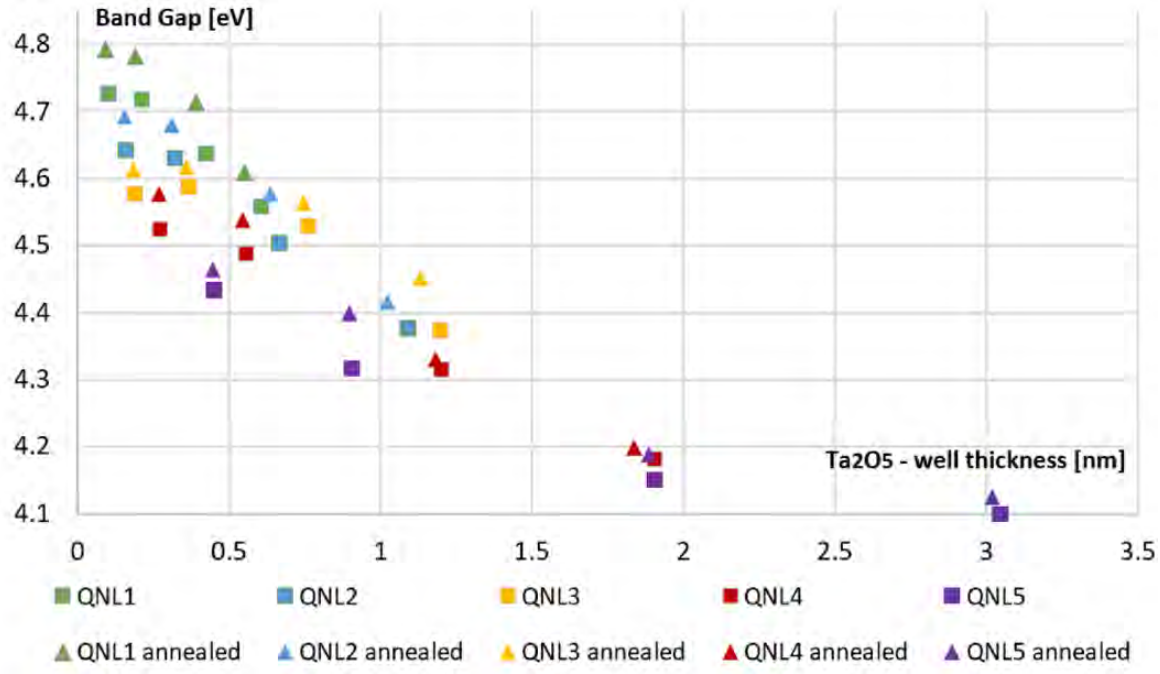


Figure 45: Several QNL combinations were sputtered and the table rotation varied for each setting. The rise in Bandgap shows the influence of the $Ta_2O_5$ layer thickness on the band gap. The figure is from [62].

With this we were able to show not only that we have an effect of rising band gap with a thinner barrier layer but also that we can coat any refractive index between $SiO_2$ and $Ta_2O_5$ with the right process setting which is a great opportunity using the QNL process as tunable mixed material. This fits the observation of Willemsen et al. [63].

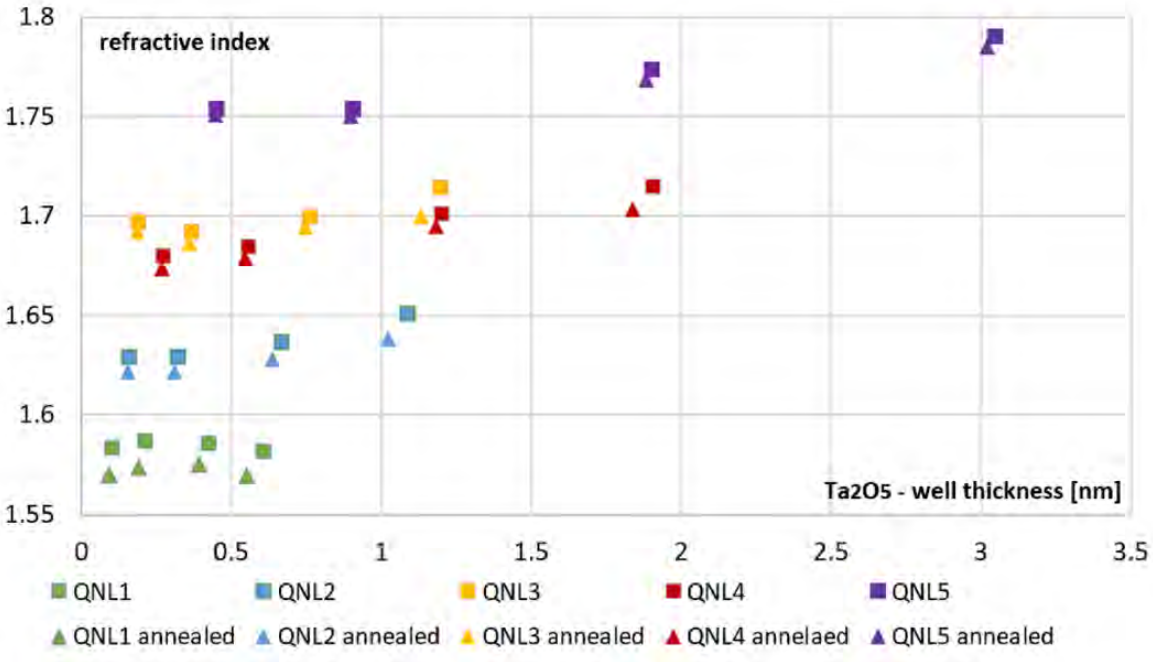


Figure 46: This figure completes figure 45 and shows that the refractive index for the series stays constant over different $Ta_2O_5$ layer thickness. The figure is from [62].

# 8 Laser Damage Competition

Building on the previous chapter, this section shows how we successfully used QNLs to coat complex multilayer systems.
As I built up this chapter a little story like, I have to admit that I sometimes changed chronological orders a little bit for dramaturgy reasons. But as it has no influence on the scientific part and the conclusions, I assume that is fine.
At the laser damage conference of SPIE[5] which takes place in the United States, they organize a competition every year with always changing requirements (as far as I know).
The organizers issue different specifications each year that the coatings must meet. These specifications pose a challenge for coating manufacturers, tool manufacturers, and research laboratories, who create an optimized design and coat it. The samples are then sent to the organizers who test them for characteristics and compliance with the specifications in a blind study and publish the results anonymized at the corresponding conference.
For the competition in the year 2024, the requirements for the design was a fs-LIDT measurement carried out by Lidaris [6]. The competition in 2024 was about fs-LIDT with a wavelength of 1030 $nm$. The conditions were that the coating needs to be a high reflecting mirror with more than 99.5 % reflectivity at the design wavelength. Each contestant was allowed to send two samples to SPIE which were then anonymously sent to Lidaris, which carried out the measurements.
As described in chapter 4.9 fs-LIDT is primarily about measuring the band gap of the tested material, which gave us the idea that we could have an advantage as we can increase the band gap with the QNL which Willemsen et al. showed could work [64].
This chapter begins by explaining the planned strategy for participating in the laser damage competition.
This is followed by a characterization of the individual layers. We did this to gain an understanding of how the materials behave and to be able to rule out any unforeseen properties from the outset and use individual values to optimize the designs. This is followed by a subchapter explaining the designs we created and how we optimized them. It explains the various approaches and also shows the results of the LIDT tests at RhySearch.
This is followed by participation in the laser damage competition and the classification of the results achieved.
As we expected that we could further optimize the results achieved, we carried out a second series of coatings after the competition to find out where there was still potential for improvement. How we proceeded and what results we achieved is described afterwards, followed by a final conclusion of the potential of QNL designs in laser resistance designs.

## 8.1 Strategy

The fs-LIDT value a design can achieve depends not only on the materials used but also on the electric field in the specific materials [26].

$$LIDT_{Design} = \min\left[LIDT_{intrinsic} \cdot \frac{|E_{inc}|^2}{|E_{max}|^2}\right] \tag{156}$$

The formula states that the LIDT value of a design can be estimated by knowing the intrinsic LIDT value of the materials used and the highest electric field intensity in the specific material layers ($E_{max}$) in proportion to the incident electric field intensity ($E_{inc}$). It has to be mentioned that this formula assumes that the behavior of the material is the same in a design as in a single layer QNL stack and that there are no other influences, which is a rough approximation.
With this in mind and the possibility of manipulating refractive index and band gap of QNL we came up with a strategy to participate in the competition. Our plan was as follows.

- Deposit different QNL single layer stacks, measure them with photo spectrometry and compile an overview of band gap and refractive index for a bundle of different processes.

[5] https://spie.org/conferences-and-exhibitions/laser-damage access on 24.10.2025
[6] https://lidaris.com/ access on 24.10.2025

- Select three promising QNL settings and together with $Ta_2O_5$ and $SiO_2$ single layer coatings perform measurements on different devices like LID, TIS and AFM to check for unexpected influences.
- We further measure the samples on our own LIDT measurement set up at RhySearch to get the intrinsic LIDT values.
- Use Optilayer as design software to simulate the electric field intensity and optimize the design with the presented formula.
- Measure the LIDT value as well for the whole mirror design at RhySearch to make sure that the calculation is correct.
- Send the best possible samples to SPIE and participate in the contest.

As good this plan sounded, unfortunately it obviously did not work that way. Nevertheless, I consider the participation and the final results as a success and will explain what happened and how I interpret it.

## 8.2 Single Layer Characterization

Putting the samples together was pretty straightforward. As showed in 46 we already had a good assortment of different stable settings and I thought choosing some with a high difference in refractive index would be helpful. So we took three different settings shown in table 1. Each of those settings was

| Sample | Power Si [kW] | Power Ta [kW] | Rate [nm/s] | refractive index @ 550nm |
|---|---|---|---|---|
| $SiO_2$ | 6 | - | 0.44 | 1.47 |
| $Ta_2O_5$ | - | 5 | 0.3 | 2.1 |
| $QNL_1$ | 6 | 4 | 0.42 | 1.6 |
| $QNL_2$ | 4 | 5 | 0.4 | 1.7 |
| $QNL_3$ | 6 | 7 | 0.38 | 1.8 |

Table 1: The different base settings used in the preliminary tests.

coated with 4 different table rotation speed and thicknesses to see dependencies during the different characterization measurements. In the end, we coated 28 different single layers with different combinations of properties, shown in table 2. The base recipes for $Ta_2O_5$ and $SiO_2$, as well as all different QNL settings, were coated with two different optical thicknesses, once with $1030\,nm$ and once with $515\,nm$ $\frac{3}{4}$-optical thickness. This was to identify thickness dependent influences and to see whether the processes behave in a time stable manner. Also, for LIDT we have the measuring wavelength at $1064\,nm$ and $532\,nm$, which gives a good opportunity to compare the coatings and measurements.

| PJ-Nr. | Description | Material | optical thickness $[\ \frac{3}{4n(\lambda)} \cdot nm\ ]$ | Table rotation [s] |
|---|---|---|---|---|
| PJ2740 | SL Ta2O5 1030 | $Ta_2O_5$ | 1030 | 3 |
| PJ2741 | SL Ta2O5 515 | $Ta_2O_5$ | 515 | 3 |
| PJ2743 | SL SiO2 515 | $SiO_2$ | 515 | 3 |
| PJ2744 | SL SiO2 1030 | $SiO_2$ | 1030 | 3 |
| PJ2749 | SL QNL1.4 1030 | $QNL_1$ | 1030 | 1.5 |
| PJ2750 | SL QNL1.4 515 | $QNL_1$ | 515 | 1.5 |
| PJ2751 | SL QNL1.3 1030 | $QNL_1$ | 1030 | 3 |
| PJ2752 | SL QNL1.3 515 | $QNL_1$ | 515 | 3 |
| PJ2753 | SL QNL1.2 1030 | $QNL_1$ | 1030 | 6 |
| PJ2754 | SL QNL1.2 515 | $QNL_1$ | 515 | 6 |
| PJ2755 | SL QNL1.1 1030 | $QNL_1$ | 1030 | 9 |
| PJ2756 | SL QNL1.1 515 | $QNL_1$ | 515 | 9 |
| PJ2757 | SL QNL2.4 1030 | $QNL_2$ | 1030 | 1.5 |
| PJ2758 | SL QNL2.4 515 | $QNL_2$ | 515 | 1.5 |
| PJ2759 | SL QNL2.3 1030 | $QNL_2$ | 1030 | 3 |
| PJ2760 | SL QNL2.3 515 | $QNL_2$ | 515 | 3 |
| PJ2761 | SL QNL2.2 1030 | $QNL_2$ | 1030 | 6 |
| PJ2762 | SL QNL2.2 515 | $QNL_2$ | 515 | 6 |
| PJ2763 | SL QNL2.1 1030 | $QNL_2$ | 1030 | 9 |
| PJ2764 | SL QNL2.1 515 | $QNL_2$ | 515 | 9 |
| PJ2781 | SL QNL3.4 1030 | $QNL_3$ | 1030 | 1.5 |
| PJ2782 | SL QNL3.4 515 | $QNL_3$ | 515 | 1.5 |
| PJ2783 | SL QNL3.3 1030 | $QNL_3$ | 1030 | 3 |
| PJ2784 | SL QNL3.3 515 | $QNL_3$ | 515 | 3 |
| PJ2785 | SL QNL3.2 1030 | $QNL_3$ | 1030 | 6 |
| PJ2786 | SL QNL3.2 515 | $QNL_3$ | 515 | 6 |
| PJ2787 | SL QNL3.1 1030 | $QNL_3$ | 1030 | 9 |
| PJ2789 | SL QNL3.1 515 | $QNL_3$ | 515 | 9 |

Table 2: The list gives an overview over the single layer coatings we did for the preliminary tests to characterize the different material combinations. The PJ number gives a clearly identifiable number for the respective coating process. The description is used in later depictions so the name is also identifiable but also meaningful in differences of sample settings, the optical thickness is for every combination in a version of 515 $nm$ and 1030 $nm$ regarding its own optical thickness and the table rotation time gives a proportional value to the pair thickness of the coated QNL layers.

To explain the table, each coating process carried out at the sputtering tool gets a unique PJ-number, which is mentioned in the table. "PJ" means *Process Job* and is a unique number assigned to a coating process on the used tool. The description is a short overview of the process or coating settings and is often used to replace the PJ-number in a set to compare differences in graphs. Explanations for "what stands for what" can differ, but in this case the first part, "$SL$" stands for single layer. Later also "$ML$" appears and describes multilayer. The second part with the material description is partially obvious. For $QNLx.y$ the first number stands for the settings also used in table 1 and separates the samples in the process differences. The second number is used to show the table rotation time as it is proportional to the pair thickness of the nanolaminates. So, QNLx.1 stands for processes with a table rotation time of 9 $s$, QNLx.2 $\rightarrow$ 6 $s$, QNLx.3 $\rightarrow$ 3 $s$, and QNLx.4 $\rightarrow$ 1.5 $s$. The single layers $Ta_2O_5$ and $SiO_2$ are always coated with 3 $s$ table rotation time.

### 8.2.1 AFM Roughness

An important characteristic that is easy and fast to measure is roughness 4.5.4 with the atomic force microscope 4.3. It can give a good idea how suitable the surface of a coated film is. If the roughness is too high, stray light effects can occur and reduce the quality of the coating. Further, it is important to have low values at single layer coatings as in my experience roughness gets only higher the thicker

a design gets and does not level out as it could be expected.
Measured was a square of $2.5 \times 2.5 \mu m$ and the $S_a$ and the calculated $S_q$ value. The $S_a$ describes the arithmetic average of the area and is a common measure. Compared to $S_q$ the "quadratic-mean", $S_a$ weights outliers less and was expected to better fit the general expression to describe the material itself instead of probable particles on the surface. Choosing which one to use is often a matter of preference and does not really make a difference in this case.

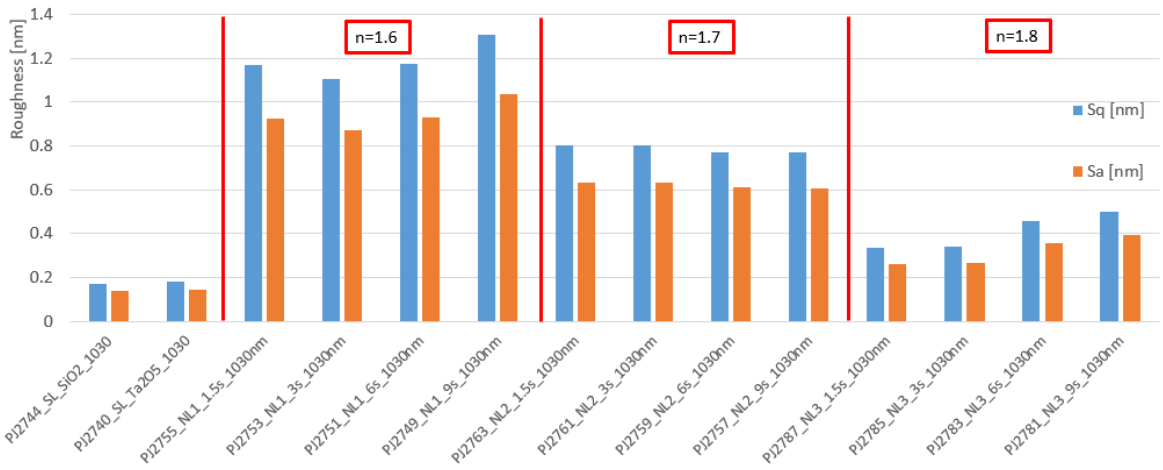


Figure 47: The roughness measurement with the AFM of the QNL $1030\,nm$ single layer samples. The measurements show that the single materials $Ta_2O_5$ and $SiO_2$ have much lower roughness than the QNL. The rotation speed of the table doesn't seem to have an influence. The QNL seem to have higher roughness the higher the $SiO_2$ content.

The roughness of the single materials $Ta_2O_5$ and $SiO_2$ is much lower compared to all variations of the QNL coatings. This result is not surprising, as $Ta_2O_5$ has in my experience always a really low roughness while $SiO_2$ has a high roughness when it is coated using only the sputter source. In our coatings, all standalone $SiO_2$ coatings and such in designs were made using the additional PSC-source to insert additional energy through the ion bombardment which smoothens the surface. However, during the QNL process the PSC was not used for process stability reasons, which means the roughness of the QNL would increase with the higher $SiO_2$ part, which is what we see. However, the roughness is not too high compared to the actual thickness of the coatings.
Also, the measurements do not show obvious dependence of the roughness compared to the table rotation time, which I would consider positive because it shows a certain consistency.

### 8.2.2 Laser Induced Deflection

We did two series of laser induced deflection measurements (LID). The $515\,nm$ samples with the $532\,nm$ setup and the $1030\,nm$ samples with the $1064\,nm$ setup. We chose to carry out experiments with both wavelengths to see how the absorption behavior in different wavelength regions acts. For the low wavelength of $532\,nm$ the measured absorption is shown in figure 48.

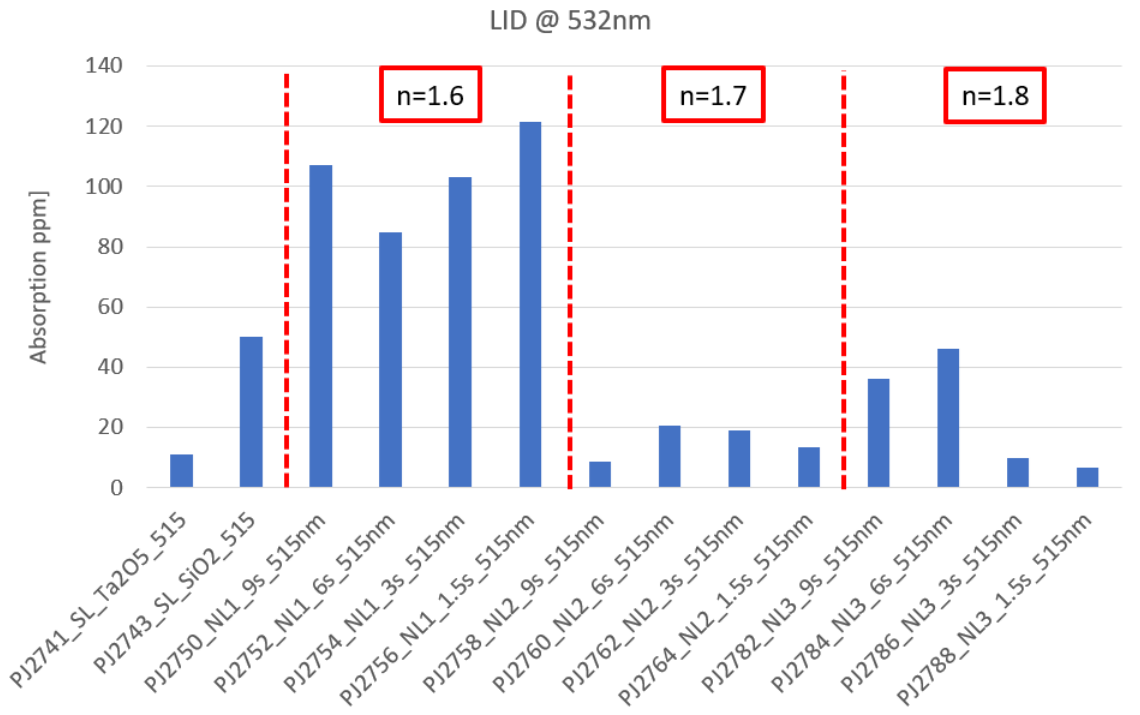


Figure 48: $SiO_2$ has by the higher absorption in the 532 $nm$ LID measurement than $Ta_2O_5$. The QNL vary but show a small correlation to the $SiO_2$ content.

As we can see, $SiO_2$ has a higher value than $Ta_2O_5$ which is surprising to me, since its absorption edge is below that of $Ta_2O_5$. Although the mixed layers $QNL_2$ and $QNL_3$ lay somewhere between the two bare materials, which was expected, $QNL_1$ has much higher absorption for all table rotation speeds. This is hard to explain, as the spectra of the layers do not give a hint. There seems to be no influence of the table rotation speed.

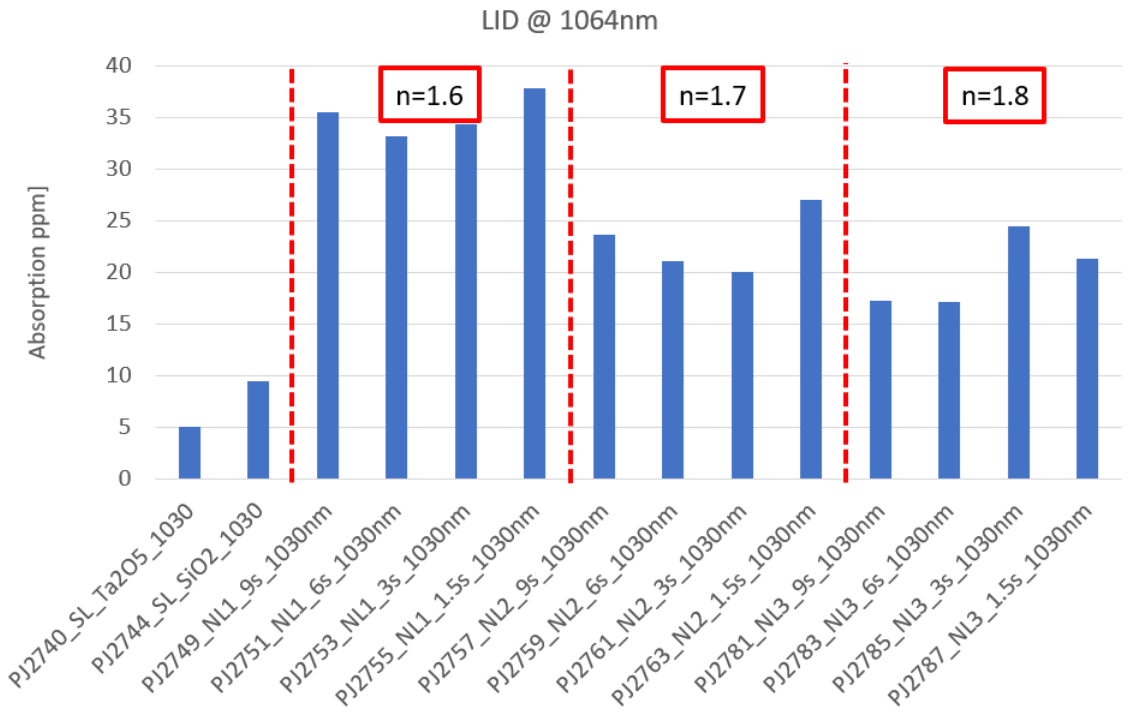


Figure 49: This figure shows the measurement of the 1030 $nm$ QWOT-stack samples measured for LID at 1064 $nm$.

With 1064 $nm$ pump beam, again $Ta_2O_5$ has a lower absorption than $SiO_2$ and here we can see that the higher the percentage of $SiO_2$, the higher the absorption for all QNL. Again, it is higher than the two bare materials, which was surprising. Again, there is no noticeable influence of the table rotation. Even if the values of the QNL samples are higher than the values of the bare materials, the absorption of all of them is in an acceptable range.

### 8.2.3 Total Integrated Scattering

We measured all single layer samples with the Total Integrated Scattering (TIS) setup at RhySearch, the measurement data is shown in figure 50.
We decided to use a $minimal - TIS$ mode to calculate the resulting value, where the quality of the background of the layer is considered mainly. The diameter of 4 $mm$ with the lowest possible average is displayed. There are different possible calculation methods, like average over the whole sample or median over all points, etc. However, with this method, we focus on the quality of the coating itself, so the influence of dirt and particles gets reduced. In this way, we can see what is theoretically possible with the process without wrong handling, particles creating random events or outliers.
We can see that the quality of the coating itself is pretty high in all of the samples, as they are close to the value of a bare substrate. $Ta_2O_5$ has a slightly higher value than $SiO_2$, and the QNL seems to correlate with the ratio $Ta_2O_5/SiO_2$. There is no obvious correlation between TIS and table rotation speed, and the thicker versions of the same settings seem to have slightly higher values.
Therefore, there is no surprising effect, which is a good sign to use the process settings in further coatings.

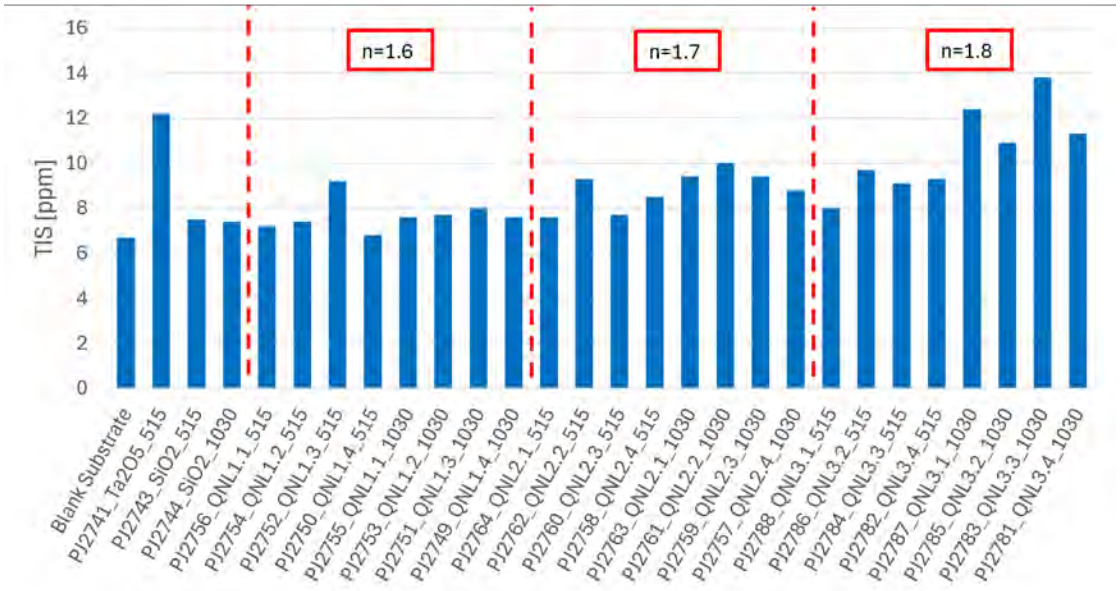


Figure 50: The figure shows the TIS measurements of the single layers. $Ta_2O_5$ has a slightly higher scattering behavior than $SiO_2$ and the higher the $Ta_2O_5$ content in the mixed QNL, the higher the TIS-value.

In figure 51 the measurement result of the sample $PJ\,2744$ $SiO_2$ is shown, it is selected because it shows several different effects and also the chosen calculation method. On the left side, the map with various different sources of scattering is shown. It should be mentioned that the defects and particles are in reality not that huge. Through the fact that the laser beam diameter is much bigger than the step size, every event is detected over several measuring sites, making it easier to detect problems but also makes the samples appear worse than they are. One advantage of the used method is that it excludes the big event, which is probably a particle in the lower half, as it would dominate the whole sample. The red arrow in the map shows an event which looks like a curved pixel error. That's a dust particle which flies through the laser beam and because the beam moves pretty fast over the sample in a spiral pattern, they have a typical appearance. On the right side, the distribution of the measured scattered light intensity shows that the peak and also medium value do not have to correlate with the chosen calculation method which would lie at $7.5\,ppm$.

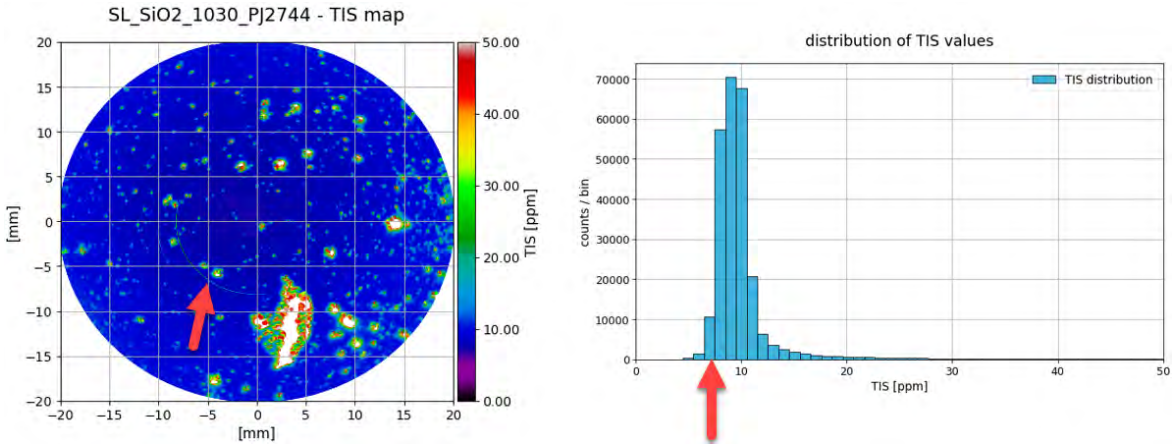


Figure 51: On the left side the measured sample with the density of straying defects is shown. The left red arrow points at a defect triggered by a dust particle falling through the laser beam. On the right side the distribution of the measured points. The right red arrow shows where the minimal-TIS value of $7.5\,ppm$ would lay.

### 8.2.4 Annealing

From experience we know that annealing coatings can shift the absorption edge and therefore the band gap but also reduces absorption from defects and can help oxidize some stoichiometric molecules in the layer [65] (p.621), [66]. To see if we can use this effect, we conducted an annealing test series with two different QNL settings to see how they behave. First, a lot of substrates are coated with processes $A$ or processes $B$ which were coated and measured at intervals of several months. Both are different QNL processes. Each one was measured individually with the photo spectrometer and then each one was annealed with a different temperature and was taken out of the oven at a specific time. In the end, every one was measured again, and the band gap calculated using the Tauc plot was compared before and after annealing. As QNL $A$ shifted much further than QNL $B$, the band gap shift was normalized to the largest shift of each series and plotted in figure 52. Because the annealing tests were originally conducted in a different context, the processes involved are slightly different from those used for the other QNL stacks. For this reason, they are labeled here as processes "A" and "B" so that they are not confused with each others.

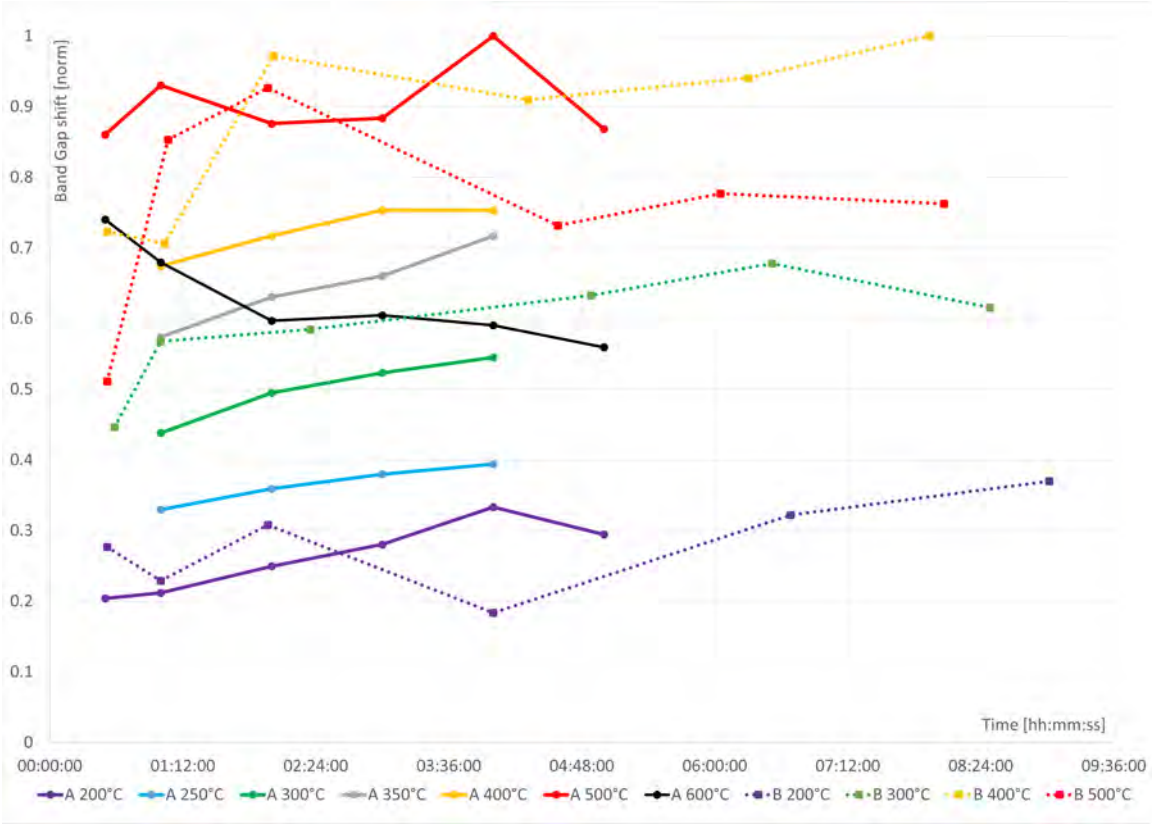


Figure 52: Two annealing test series were done with two different QNL settings. As the shift in band gap differed greatly between the two series, both were normalized to the highest value. The highest shift in series $A$ got the sample at $500\,°C$after 4 hours with $E^{\Delta}_{gap}(500°, 4h) = 0.077\,eV$ while the sample has a band gap of $E_{gap} = 4.77eV$. The highest shift in series $B$ got the sample at $400\,°C$after 8 hours with $E^{\Delta}_{gap}(400°, 8h) = 0.035\,eV$ while the sample has a band gap of $E_{gap} = 4.47eV$.

The first thing that stands out is that it seems that the highest influence on the band gap happens in the first minutes. Afterwards, the change is much less. However, since opening the oven, placing the substrates, and also cooling them takes time and increases the uncertainty, I decided not to try measuring lower annealing times.
It is also important to mention here that the shift in the band gap is very small $0.0065 - 0.078\,eV$ compared to the original band gap$E_{gap}(A) = 4.77\,eV$ and $E_{gap}(B) = 4.47\,eV$. The absolute values are shown in figure 53

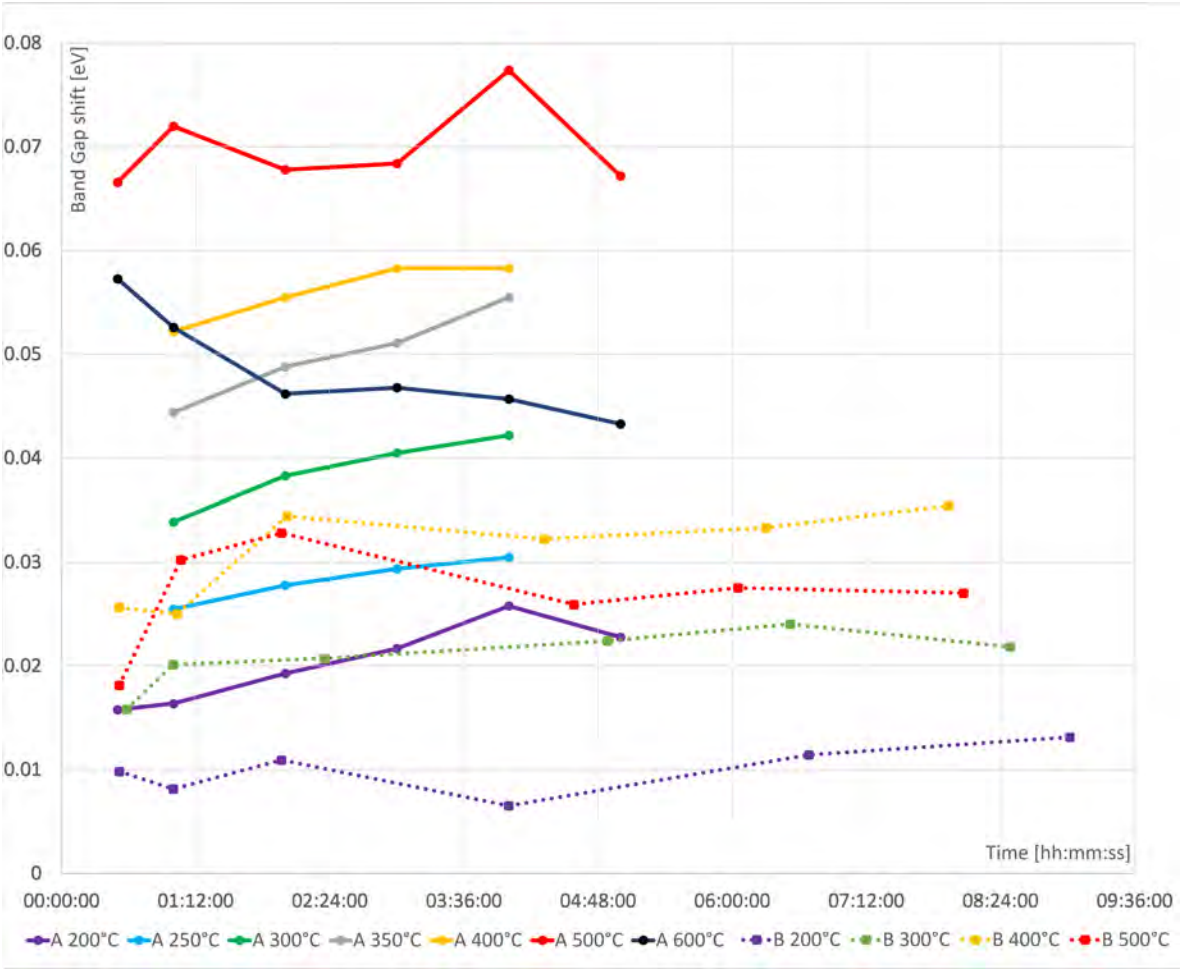


Figure 53: The absolute calculated values for both series are shown. Series "A" showed a much higher shift than "B". Both show the highest values around $400 - 500°C$. For series "A" one can see that the value decreases again at $600°C$.

This can become problematic, as I decided not to implement error bars. This is because if the absolute error of the photo spectrometer is implemented in the calculation, the total error exceeds the band gap shift $Error_{total} > 0.1\,eV$. Since the data are consistent, the relative error must be significantly smaller and in the end more relevant if it is about choosing the right temperature and time to anneal the mirror designs. I calculated an error that comes only from the fit uncertainties of $Error_{fit} \approx 0.002\,eV$, but as depicted in the graph this would suggest a wrong accuracy; I left the graph without any error bars.
For the lower temperatures it seems like putting them in the oven, letting them jump up, an afterward progress is slowly but continuously. The interesting part I aimed for seems to happen in series $B$ at $500\,°C$. After an increase in the band gap, it reached a peak at $1.5h$ and seems to decline afterward. This could of course also be a coincidence within the mentioned high uncertainty, but the $600\,°C$ line from series $A$ which is lower than the $500\,°C$-series and continuously declining indicates also that after a threshold value the band gap starts to decrease again. I am not sure why this happens, but I could imagine that the amorphous materials start to crystallize or that stress between the materials could cause cracks and damages in the coatings.
It seems like between $400\,°C$ and $500\,°C$ with a shorter annealing time is a maximum, while at $500\,°C$ the shift in band gap starts to decline after some time again. In previous tests, this effect is even stronger at $600\,°C$ which fits this experiment. We chose to anneal from every process a sample at $450\,°C$ for $1.5\,h$.

### 8.2.5 Kerr-Effect

To be able to calculate the optimal design using formula 156, with the material used, the LIDT value of the single layer materials is necessary. Unfortunately, there happened to be a problem. As we had to focus the laser on $SiO_2$ to damage the layer, damage to the substrate occurred. The explanation is that through the focus the field intensity gets to high, which leads to a self focusing Kerr-effect. This effect causes the material to increase the refractive index through the high field, which leads to a focus of the beam which increases the field even further. Under the high energy density, the material will become a plasma, which drastically lowers the refractive index, which widens the beam again. The widened beam with the now lower field is not strong enough anymore to ionize the material, which increases the refractive index again and the whole process starts again. This if it is set right, the beam can repeatedly self focus itself over a huge distance leading to a filament of damage in the material. This effect is used in cutting wine glasses at Zwiesel [67] and also in manipulating lightnings [68]. As interesting this effect is, it is a problem to calculate our LIDT value. We took 180 images with the microscope in different depths of the substrate and overlaid them to show the filament in 54 on the left side. On the right side of the image the photo shows plasma lightning just as it happens in the substrate.

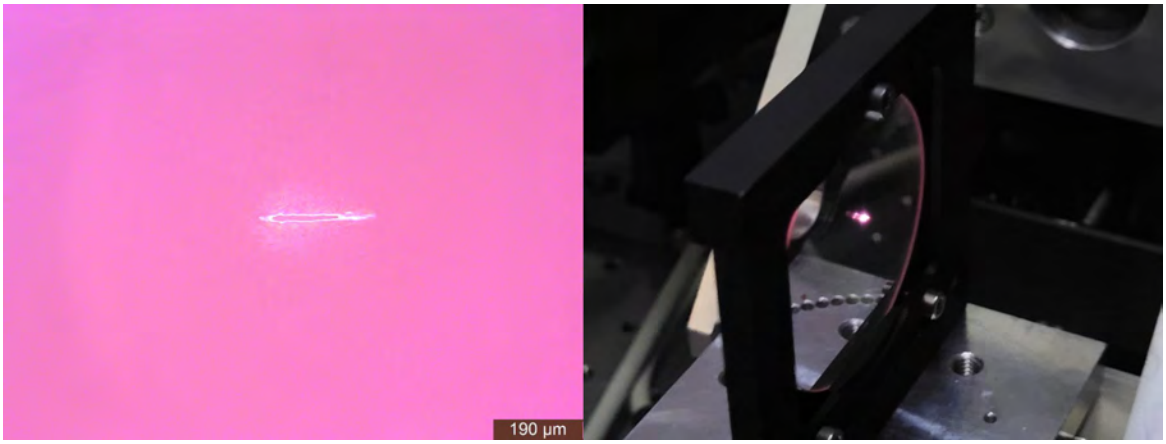


Figure 54: On the right side, you can see the damage induced in the substrate by the Kerr effect caused by the laser pulse from the LIDT measurement. On the left side, an overlay of 180 photos taken through the microscope with different depth focus points, which together show the filament induced by the Kerr-effect in the 2 $mm$ thick substrate.

### 8.2.6 LIDT Single Layer

The LIDT measurements for 1030$nm$ single layers that are used in the designs in the following chapters are shown in the diagram 55. We tried to estimate the value for $SiO_2$ as well by excluding the obvious measurement points that showed the filament effect mentioned, but as it influences the statistical value, we did not trust it enough to continue the calculation with it. However, the QNL samples have shown that they have a higher value the higher the ratio of $SiO_2$ and, accordingly, the lower the refractive index. QNL1 (n=1.6) even shows a very high LIDT value, coming close to the uncoated substrate, and $SiO_2$ will probably only represent a lower estimation, as the value will presumably lie between QNL1 and the bare substrate.

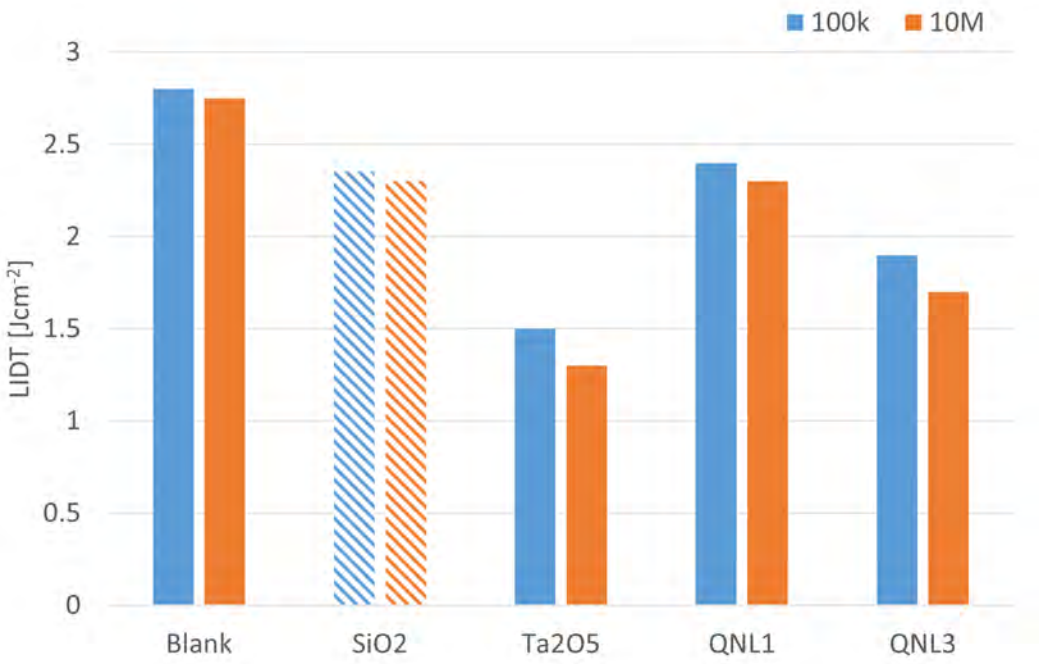


Figure 55: The diagram shows the measured LIDT values for the blank substrate as well as the single layer coatings for $10^5$ and $10^7$ pulses. As the value for $SiO_2$ is an estimation the result is hatched.

## 8.3 Design

The occurrence of the Kerr effect in $SiO_2$ poses a severe problem as it makes it impossible to determine the LIDT value of $SiO_2$. This in turn makes it impossible makes it impossible to calculate the LIDT value of a interference stack was $SiO_2$ is used in all our designs as low index material. This means that the optimizing part needs to be done by "educated guessing" and experience.
The new approach was to build a base stack of a Bragg-mirror and add a cap layer to reach a reflectivity at $1030\,nm$ greater than 99 % and add a stack of different QNL between the cap layer and the rest of the mirror to reach up to 99.9 % reflectivity. Afterwards, optimize the design in terms of E-field intensity, especially in high refractive index materials, but keep an eye on keeping at least 99.5 % reflection to fulfill the criteria for the competition.
The steps and designs are explained in figures 56, 57

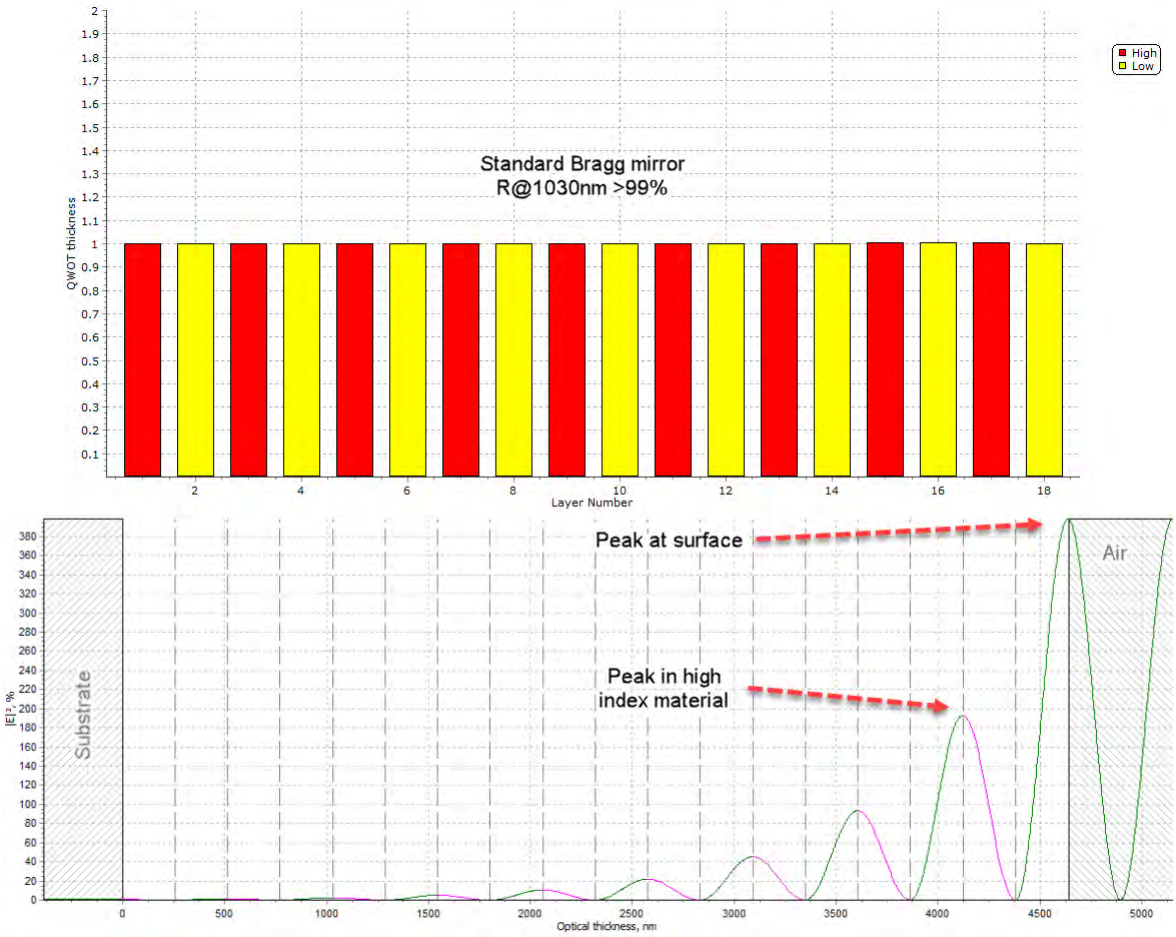


Figure 56: This shows the standard base design used for all optimized designs. A simple Bragg mirror with 18 Layers, each one quarter wave thickness at 1030 $nm$ design wavelength. The upper figure shows the thickness of each layer in optical quarters of the design wavelength, the lower figure shows the E-field intensity in each layer. The E-field is at a maximum at the surface which makes the design sensible for defects at the surface. Further the electric field grows to a peak in the high index material, makes it likely to damage the coating at the shown interface. Depicted with Optilayer.

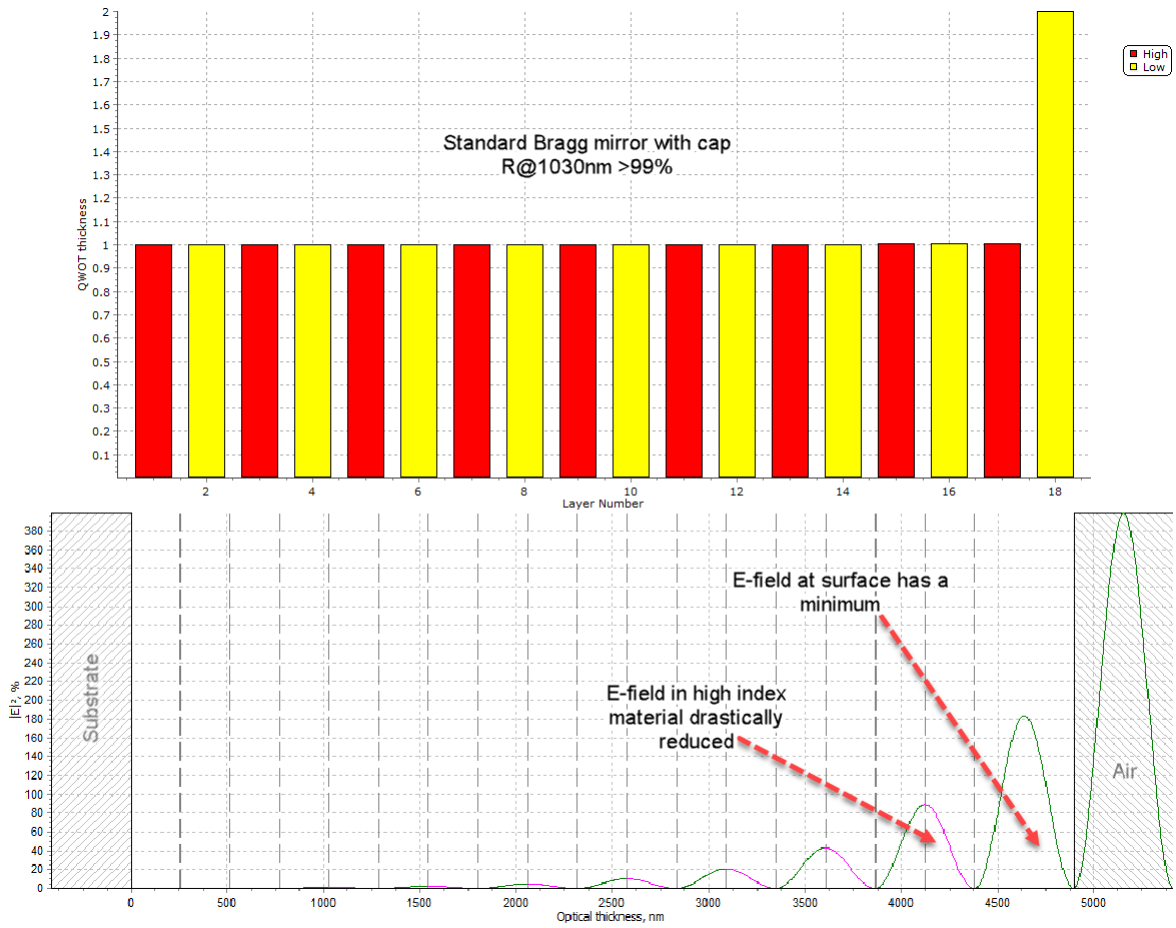


Figure 57: Changing the thickness of the last layer of a Bragg mirror drastically changes the behavior of the E-field intensity. At the surface of the coating, the field intensity develops a minimum which decreases the risk of laser damage induced by surface defects. At the same time the maximum intensity in the low and especially in the high index material is reduced drastically. The cap layer has no significant effect on the reflectivity of the mirror at the design wavelength compared to the same mirror completely without the final low refractive index layer. Depicted with Optilayer.

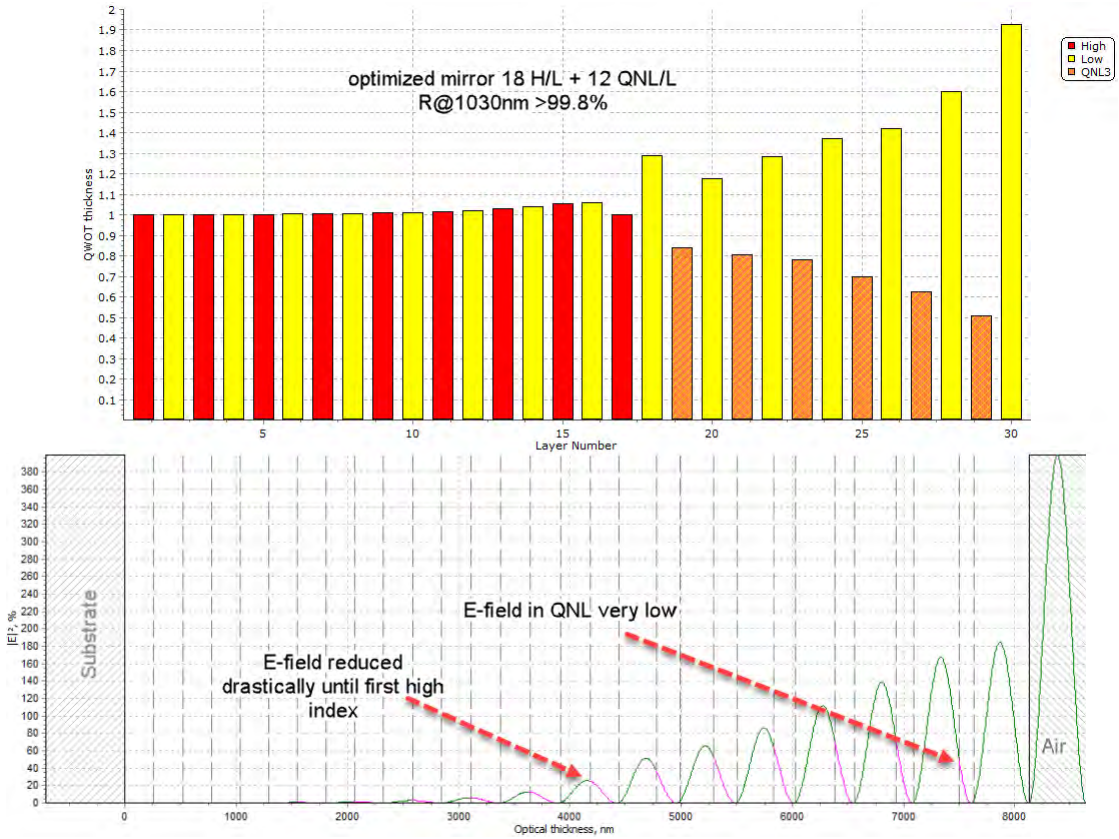


Figure 58: After the cap layer a stack of $QNL_{1/3}$ and $SiO_2$ were inserted so the reflectivity increases to $> 99.9\,\%$. Afterwards the design gets optimized in terms of E field intensity while the focus lies primarily on the $QNL_{1/3}$ and $Ta_2O_5$ layers to reduce the probability of laser induced damage. This process reduces the reflectivity again but was kept at a minimum of $\geq 99.6\,\%$. Here the design for $PJ2799$ is shown, a design which was sent to the Laser Damage competition. Depicted with Optilayer.

Based on the fundamental principle explained above, we came up with 9 different designs to test in our own setup and see which one has the highest LIDT. The designs are described in table 3. The designs are a combination of classical and also optimized designs using $Ta_2O_5/SiO_2$ and $QNL_{1/3}$ components. The $QNL_2$ processes were excluded from all subsequent experiments as the middle refractive index showed no specific advantage compared to the other QNL processes.

| Run Nr. | Ref. | Composition | Description |
|---|---|---|---|
| PJ2793 | $Ta_2O_5$ $V1$ | $(H:L)^{11}/22$ | QWOT with Cap, $Ta_2O_5/SiO_2$ |
| PJ2794 | $Ta_2O_5$ $V2$ | $(H:L)^{11}/22$ | optimized, $Ta_2O_5/SiO_2$ |
| PJ2798 | $QNL_3$ $V1$ | $(H:L)^9(QNL_3:L)^6/30$ | QWOT with Cap, base $Ta_2O_5/SiO_2$ 6 endpairs $QNL_3/SiO_2$ |
| PJ2799 | $QNL_3$ $V2$ | $(H:L)^9(QNL_3:L)^6/30$ | optimized, base $Ta_2O_5/SiO_2$ 6 endpairs $QNL_3/SiO_2$ |
| PJ2804 | $QNL_3$ $V3$ | $(H:L)^9(QNL_3:L)^6/30$ | optimized, base $Ta_2O_5/SiO_2$ 6 endpairs $QNL_3/SiO_2$ |
| PJ2806 | $QNL_1$ $V1$ | $(H:L)^9(QNL_1:L)^6/30$ | QWOT with cap, base $Ta_2O_5/SiO_2$ 6 endpairs $QNL_1/SiO_2$ |
| PJ2807 | $QNL_1$ $V2$ | $(H:L)^9(QNL_1:L)^6/30$ | optimized, base $Ta_2O_5/SiO_2$, 6 endpairs $QNL_1/SiO_2$ |
| PJ2818 | $QNL_{3+1}$ $V1$ | $(H:L)^9(QNL_3:L)^2(QNL_1:L)^5/30$ | QWOT with cap, base $Ta_2O_5/SiO_2$ two pairs $QNL_3/SiO_2$, 5endpairs QNL1/SiO2 |
| PJ2819 | $QNL_{3+1}$ $V2$ | $(H:L)^9(QNL_3:L)^2(QNL_1:L)^5/30$ | optimized, base $Ta_2O_5/SiO_2$, two pairs $QNL_3/SiO_2$, 5 endpairs QNL1/SiO2 |

Table 3: 9 designs were chosen to get coated. The first two are classic $Ta_2O_5/SiO_2$ mirrors, one as a Bragg with cap layer and one optimized. This pair is mostly for comparison with the QNL. Than we chose to coat with $QNL_1$ and $QNL_3$ each a pair as again normal Bragg mirror with cap and one optimized. The last pair is a combination of descending refractive index where both QNL process are used.

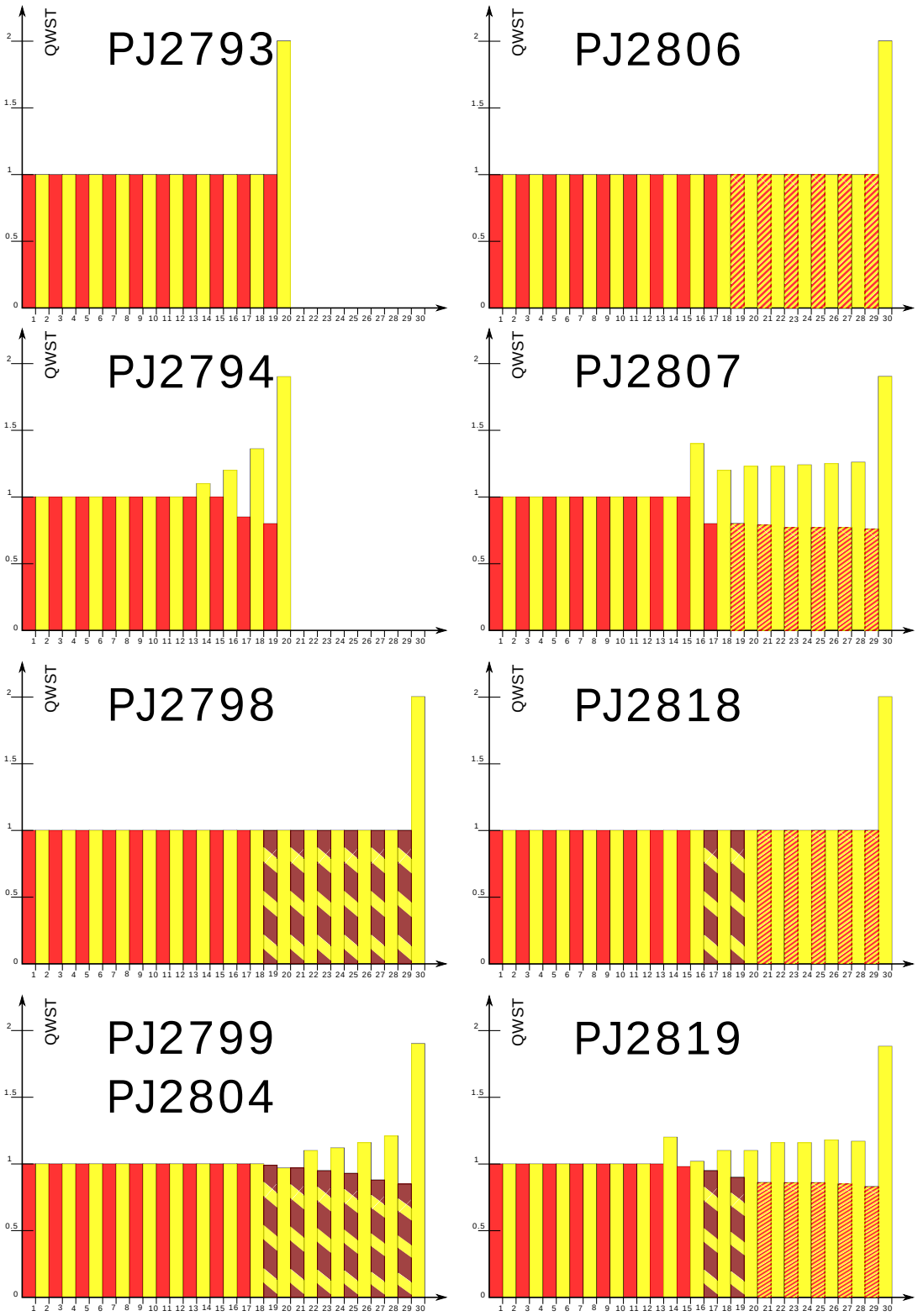


Figure 59: The different designs are displayed. $PJ2799$ and $PJ2804$ are not displayed separately as the are both the same type with slightly changes in the optimization and look pretty much the same. Further so it fits on one page nicely. $PJ2793$ and $PJ2794$ are both pure $Ta_2O_5/SiO_2$ designs with each 22 layers. $PJ2806$ and $PJ2807$ use both QNL type 1. $PJ2798$, $PJ2799$ and $PJ2804$ use all three QNL type 3 and $PJ2818$ and $PJ2819$ use a combination of all three high refractive index materials.

### 8.3.1 LIDT-Multilayer Measurement at RhySearch

We measured all the 9 mirror designs first without annealing at RhySearch for various numbers of pulses to see the time dependent behavior. The coatings were done on 2-inch substrates and the substrate was divided into 90 test points. 6 S-on-one series were divided and tested on each substrate. The test pulse numbers are $P = 10^4, 10^5, 10^6, 5 \cdot 10^6, 10^7, 2 \cdot 10^7$. With the wide range of pulse numbers, a time dependent behavior can also be tested. The diameter of the beam was $\varnothing = 30\,\mu m$, the duration of the pulse $t_p = 300\,fs$ and the repetition rate $200\,kHz$. With the repetition rate of the number of pulses tested in this setup, an irradiation time of $t_{irradiation} = 0.5 - 100\,s$ was reached. The measured values are presented in figure 60.

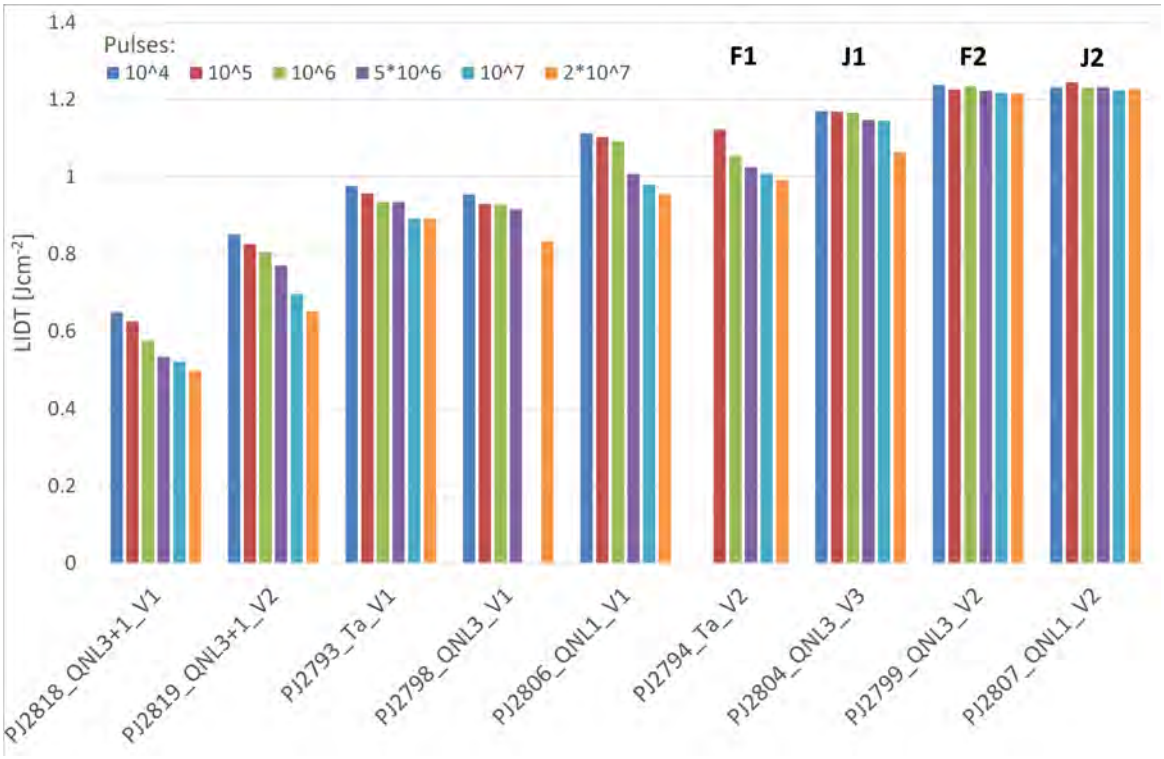


Figure 60: The fs-LIDT values of the test series are shown in the figure. The number of pulses varied for every sample between $P = 10^4 - 2 \cdot 10^7$ which means the irradiation time is between $t_{irradiation} = 0.5 - 100\,s$. The diagram is sorted by the reached LIDT value.

The first part which is nice to see is the fact that in every case the optimized version has a better performance than the non optimized version. Which means even if its not the best possible design, we did not make it worse.
The most surprising thing is that the designs with two different QNL settings are worse than all other designs. I would have expected that those behave much better. The optimized mirror which uses only $Ta_2O_5/SiO_2$ ($PJ2794$) has a very good performance and shows that the use of QNL is not without competition. However, the two highest QNL designs show a significantly higher LIDT, especially after a high pulse count. At $10^5$ pulses, the difference between $PJ2794$ and $PJ2799$ respectively $PJ2807$ is approximately 10%, while at $10^7$ pulses it is already around 20% higher. But in the end, the best two are two optimized designs with the use of QNL ($PJ2799$ and $PJ2807$).
What is also remarkable is the fatigue-ratio of the last two designs. That describes the ratio how fast the laser resistance falls with increasing laser pulse number and as the most designs show a steep decrease, the last to remain really high, which indicates a good long time performance.
We used a new sample from every design, annealed it with the mentioned 450° for $1.5h$ and measured all the samples again to see how much annealing increases the performance.
We were very surprised to see that the annealed mirrors get mainly worse after annealing 61.

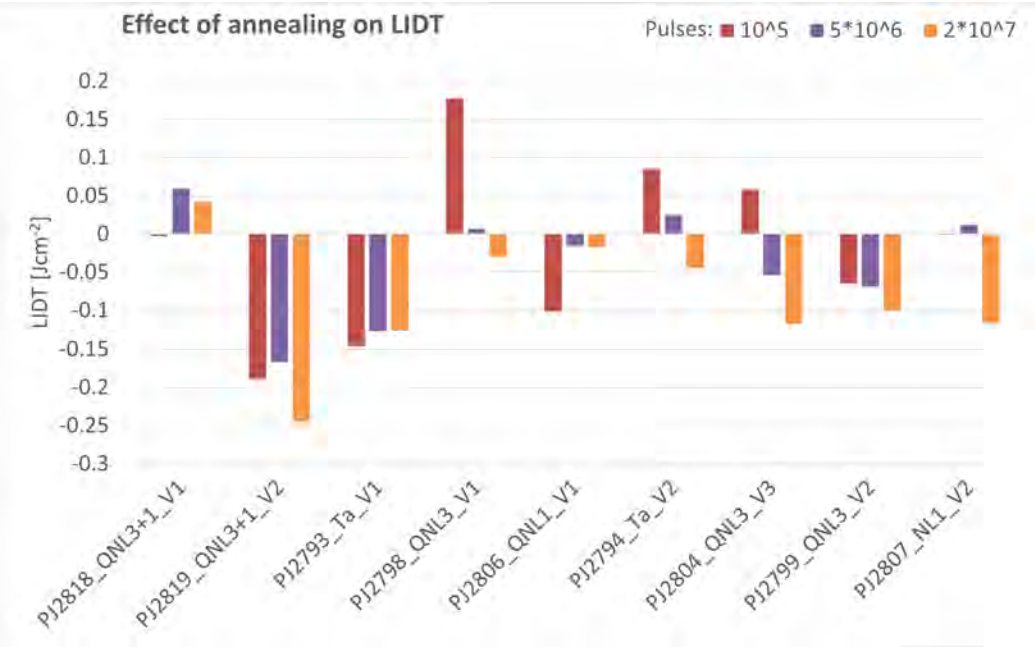


Figure 61: The annealing tests showed that the used annealing method has mostly a negative effect on the tested laser resistance which was surprising.

This was a drawback as I expected the values to clearly increase or at least stay the same. As we ran out of time, we were unable to repeat the tests with a different and more gentle annealing. We thought that maybe the annealing process was carried out too harsh as we put the coatings in the already heated oven instead of heating them slowly up with the oven, and also took them out after the oven finished instead of letting the oven ramp down gently.
We decided to send in 4 different samples, two from Evatec and two from RhySearch. $PJ2799$ and $PJ2794$ were sent from Evatec and $PJ2804$ and $PJ2807$ from RhySearch. So we would have the 4 best samples, but also the $Ta_2O_5/SiO_2$ to compare.
As we did not know what went wrong with the annealing, we decided to anneal only two of the samples with a changed annealing procedure. $PJ2804$ and $PJ2807$ were gradually ramped up in 2 hours to $350\,°C$ and kept there for one hour. After the program was finished, the oven turned off and we let it cool down slowly over night before we took the samples.

## 8.4 Participating at the Laser Damage Competition

At the Laser Damage Competition, 29 participants submitted 57 samples which all were measured in a double blind test by Lidaris in the same setup. 33 samples were coated using an IBS technique, 12 magnetron sputtering, and 9 E-Beam.
While the vast majority of 37 used $HfO_2$ as a high refractive index material, 15 used $Ta_2O_5$ and the rest something else.
Lidaris used a 200-fs pulse with a diameter of $60\,\mu m$ at a repetition rate of $500\,kHz$ [29].
The samples $PJ2804/PJ2807$ from RhySearch got the code $J1/J2$ and the samples $PJ2794/PJ2799$ submitted by Evatec got the code $F1/F2$. The reached fs-LIDT values by all participants is displayed for the catastrophic mode in 62, for the color mode in 63 and for the fatigue ratio in 64. The raw data from the anonymized participants was kindly provided by Colin Harthcock from Lawrence Livermore National Laboratory.

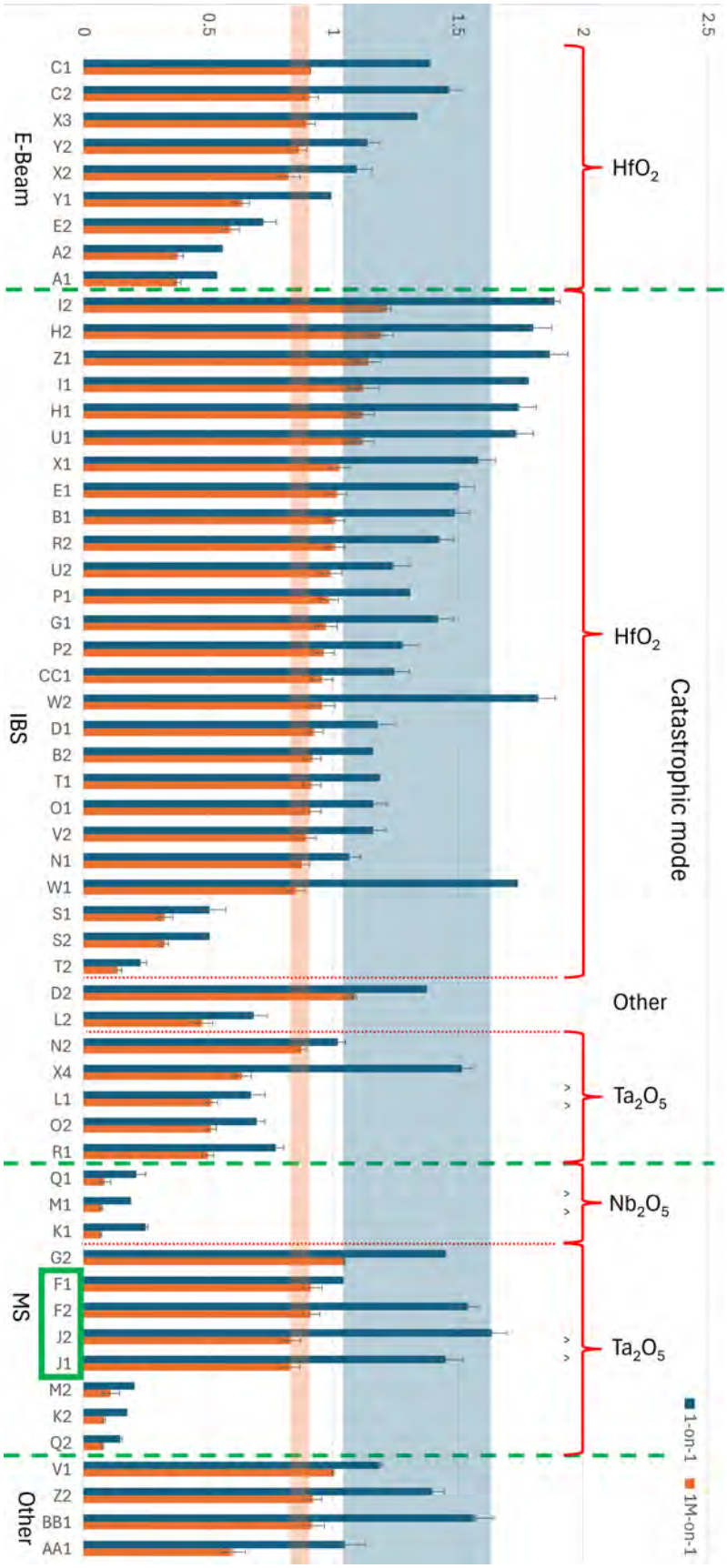


Figure 62: The measured fs-LIDT in catastrophic mode is displayed for all participants. The results are separated in $1-on-1$ (blue) and $10^6-on-1$ (orange) results. The results are separated in coating type and high refractive index materials. Our coated mirrors are marked with a green rectangle. Our highest and lowest value of both modes are displayed with two transparent bands for better comparison with other participants.

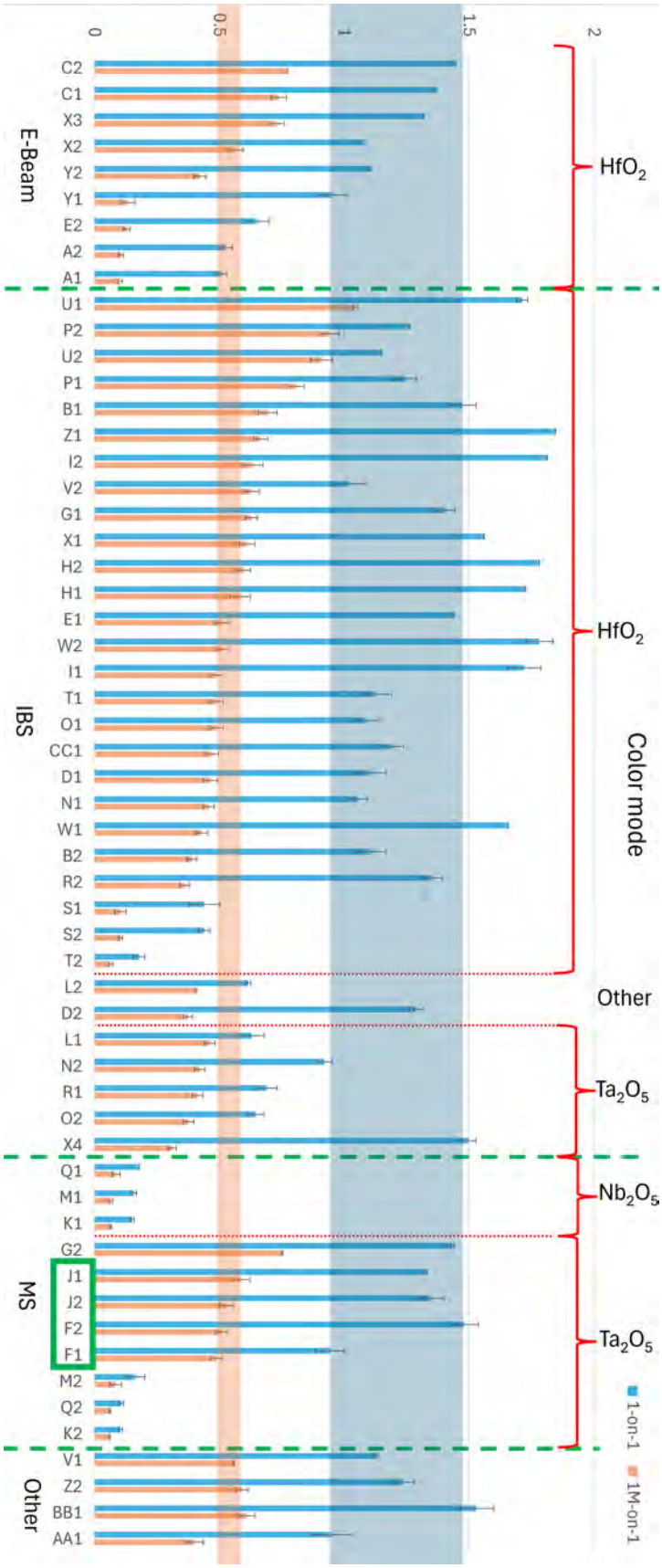


Figure 63: The measured fs-LIDT in color mode is displayed for all participants. The results are separated in $1-on-1$ (light blue) and $10^6-on-1$ (light orange) results. The results are ordered in coating type and high refractive index materials. Our coated mirrors are marked with a green rectangle. Our highest and lowest value of both modes are displayed with two transparent bands for better comparison with other participants.

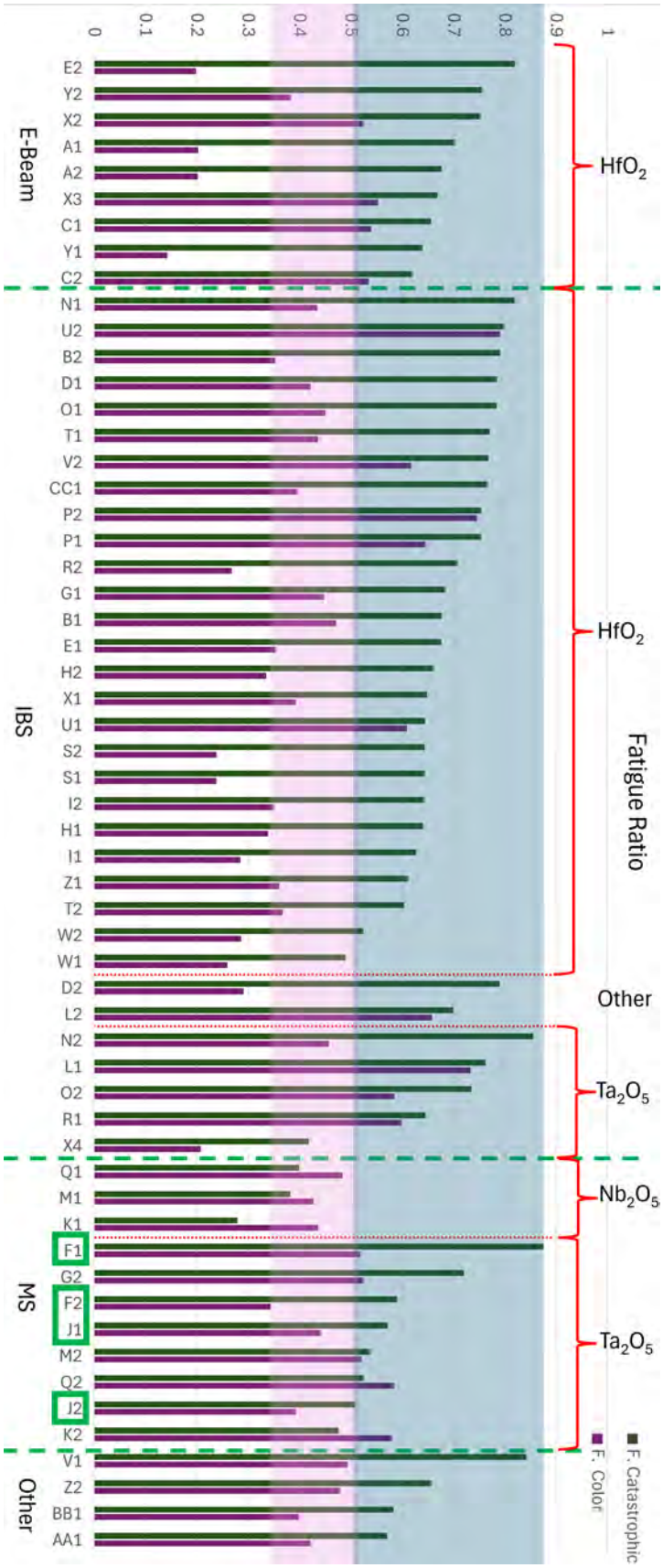


Figure 64: The measured fatigue $f = \frac{LIDT(1-on-1)}{LIDT(10^6-on-1)}$ is displayed for all participants. The results are separated in catastrophic (dark green) and color mode (dark purple). The results are separated in coating type and high refractive index materials. Our coated mirrors are marked with green rectangles. Our highest and lowest value of both modes are displayed with two transparent bands for better comparison with other participants.

As the graphs provide a lot of data, it is necessary to explain and put them into perspective.
The first 62 shows the catastrophic measurements for the measurement methods $1-on-1$ and $10^6-on-1$. Measurements of $10^{0,1,2,3,4,5\&6}-on-1$ were also made by Lidaris, but to improve readability only the lowest and highest results are shown. Similarly to the proceedings [29] I sorted the data by the coating device used, the high refractive index material was used as the base material, and the result was reached $10^6-on-1$.
At first glance our results lay somewhere in the middle and so are not spectacular in any direction. Most of the participants used $HfO_2$ which is no surprise, as it has a great advantage with a band gap somewhere between $E_{gap}^{HfO_2} \approx 5.5-5.9\,eV$ [69] which is definitely above our QNLs 45. Especially if we compare the higher band gap with the also higher refractive index of $n^{HfO_2}@550\,nm \approx 1.9$ [70]. But for us it is more interesting if the results are compared within the other $Ta_2O_5$ based coatings. If we do that, unfortunately there will not be enough data left to proper statistic but it shows that we do not need to hide. Within all magnetron sputtered samples and also all $Ta_2O_5$ based samples we have the highest $1-on-1$ fs-LIDT values with $J2$. More important, I would say, is the $10^6$ value where we have a serious competitor, $G2$ which is also coated by magnetron sputtered $Ta_2O_5$. What is also noticeable is that $F1$ which is the pure $Ta_2O_5$ design without QNL layers performs in the same range as our designs with QNL which means clearly that it is not possible to derive an advantage from QNL from those measurements.
Also, it seems that even the soft annealing method used for $J1$ and $J2$ did not help to increase the laser resistance, at least in catastrophic mode.

For the graph with the color mode 63 it is a little bit harder to make clear statements. The $10^6-on-1$ results look better since we are even in the middle of the IBS coated $HfO_2$ which I consider a great compliment to the processes and designs. But also with the $1-on-1$ results we are in a pretty good sector.
In color mode it looks like the annealed samples are slightly better than the not annealed samples. But also here in Color mode I have to admit that $G2$ has outdone us.

If we take a look at the fatigue ranking, there is a reason to cheer, but it is necessary to put in perspective. Fatigue is the ratio between the single shot and the one million shots to see how the coating degrades over time $f = \frac{LIDT(1-on-1)}{LIDT(10^6-on-1)}$. For catastrophic fatigue, we have the highest value with $F1$ on all samples, which is a great surprise.
The big "but" on this good news is that fatigue does not say that much in my opinion. First, there are samples with worse fatigue but still higher LIDT result than $F1$ as they just started higher while $F1$ stayed at the same value. I would state that fatigue would make more sense if the radiation time was higher than the 2 seconds the $10^6$ pulses in this test provide. It is completely understandable that Lidaris restricted the experiments to a short time, as they provided the huge amount of measurements for free. But for me this puts the achieved first rank in perspective as I am not sure if this is not just a nice coincidence and with the next higher $S-on-1$ a slightly different result would appear.
What is also worth to mention is that $F1$ again is our only pure $Ta_2O_5$ design, which means also that here there is no superior behavior from QNL compared to classical material noticeable.
All in all I am happy with the attempt even if we could not prove any beneficial behavior of the QNL, but in the end it showed that we can totally keep up with other international coating experts. Especially if we keep in mind that the tool used is developed for a high yield and throughput.
Also, that the soft annealing method did not improve the resistance was surprising, as I totally expected it. But to be honest, its also not clearly worse, it seems that its somewhere around the uncertainty.
In summary we can say, that at RhySearch the three optimized QNL designs $PJ2807\,(J2)$, $PJ2799\,(F2)$ & $PJ2804\,(J1)$ performed the best followed by the optimized $Ta_2O_5$ design $PJ2794\,(F1)$. At Lidaris the optimized $Ta_2O_5$ $PJ2794$ $(F1)$ and the optimized QNL design $PJ2804$ $(J1)$ performed the best, depending on catastrophic or color mode.

# 9 Design Optimization

As it was still open to verify whether the QNL provides any benefits in terms of fs-LIDT, we decided to repeat the whole competition for ourselves.
We planned to send the single layers to Lidaris so that they could measure them with the exact same settings they used at the competition, from there we should be able to optimize the designs, using the mentioned formula 156 and see if the QNL proves an advantage compared to classical materials. In addition, we can measure again with our own setup to compare.

## 9.1 LIDT Single layer

As we changed targets and shielding of the tool, new settings for gas flow, power, and PEM setpoint were necessary, which means that we did not have the same QNL composition as in the first attempt at the competition. We found new promising coating settings shown in figure 65

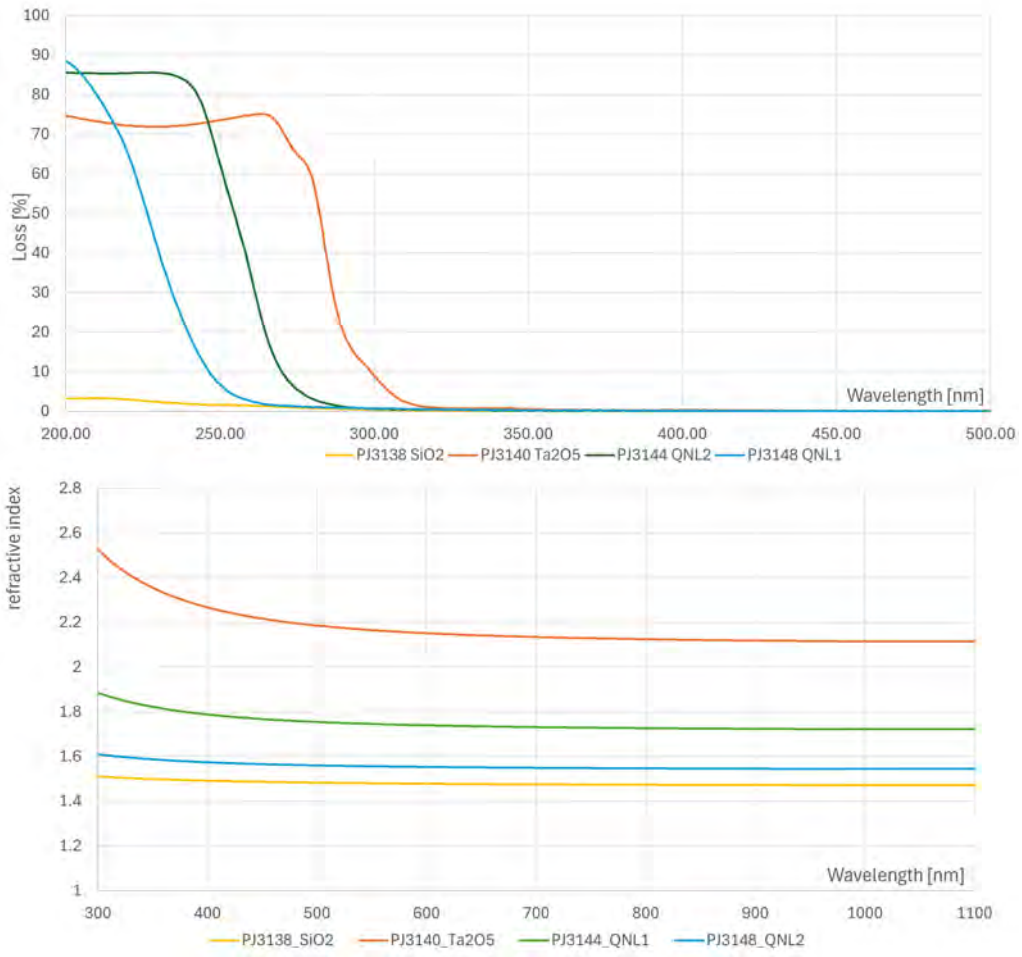


Figure 65: Standard $SiO_2$ and $Ta_2O_5$ processes and also two different QNL were chosen for the new attempt.

We decided not to do all the preliminary tests again as in the previous attempt as the process settings were close to the old and I did not expect new insights.
Lidaris tested the samples for catastrophic 66 and color mode 67 with $10^{0,1,2,3,4,5,6} - on - 1$ pulses as before in the laser damage competition, again with a beam diameter of $60\,\mu m$, a repetition rate of $500\,kHz$ and $200\,fs$ pulses.
Unfortunately, they were also unable to measure the $SiO_2$ samples in catastrophic mode. The report does not say it clearly, but I guess they had the same problem as we did. Lidaris warned us that

this could happen, but attempts to suppress the effect would have influenced the comparability of the results. So we decided to take the risk.

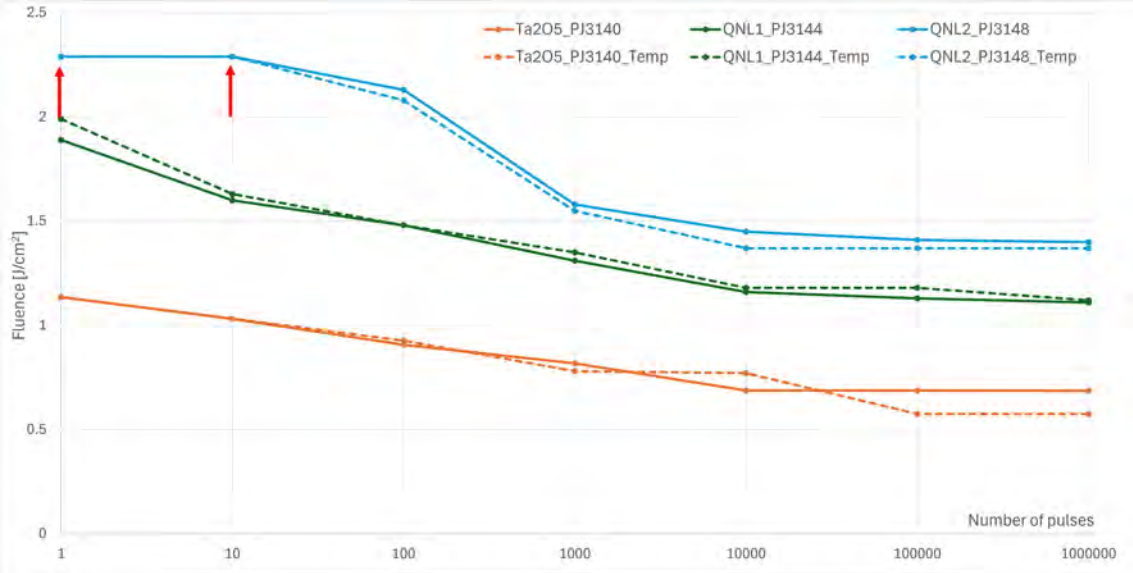


Figure 66: Shows the fs-LIDT results for the single layer in catastrophic mode. The solid lines are the untreated and the dashed the annealed samples. The red arrows on the left side indicate that those measurement points show a minimal estimation as they reached the maximum fluence and no final value could be determined. Unfortunately the $SiO_2$ measurement did not work. Error bars are not shown as it would be to crowded but for $10^6 - on - 1$ they are shown in figure 68.

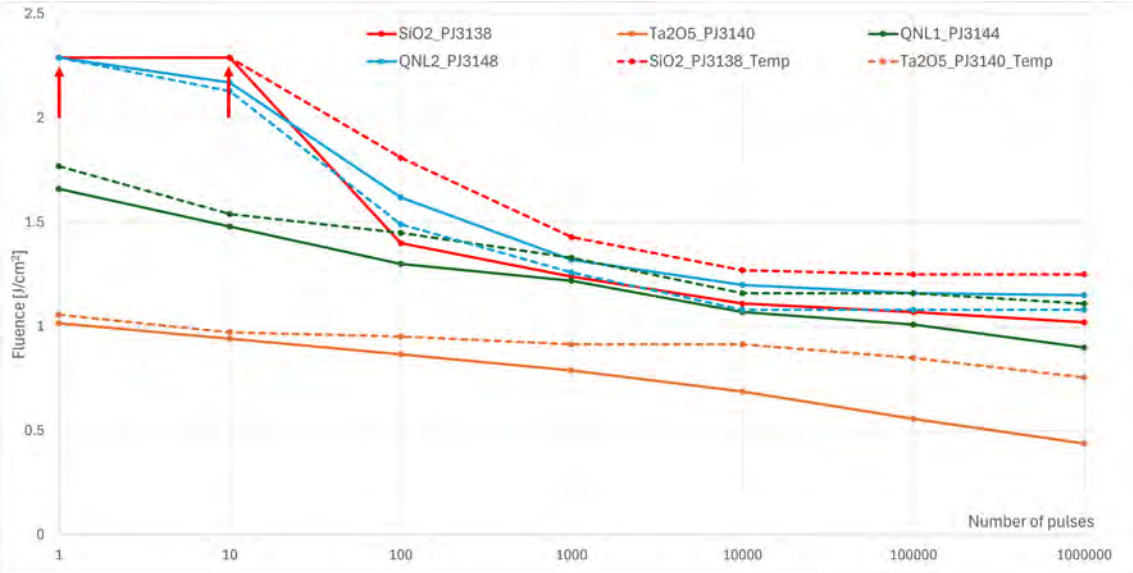


Figure 67: Shows the fs-LIDT results for the single layer in color mode. The solid lines are the untreated and the dashed the annealed samples. The red arrows on the left side indicate that those measurement points show a minimal estimation as they reached the maximum fluence. Error bars are not shown as it would be to crowded but for $10^6 - on - 1$ they are shown in figure 68.

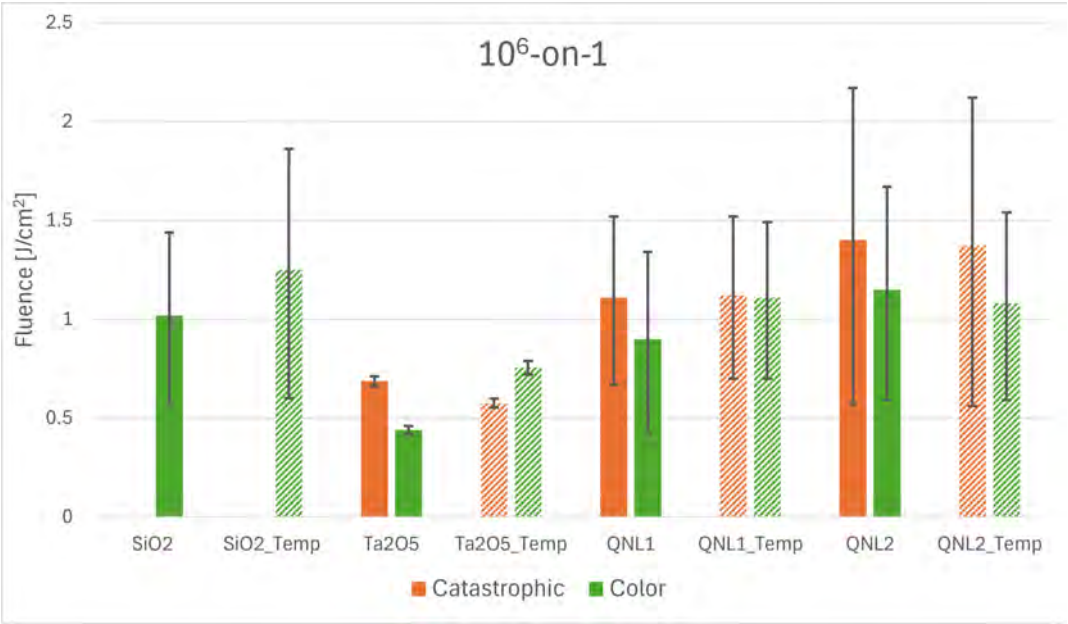


Figure 68: This comparison shows the $10^6 - on - 1$ results, separated in catastrophic/color mode (orange/green) and pre-/ post annealed (filled/hatched).

For the catastrophic mode, we can see that the influence of annealing is limited. For the QNL it does not make a difference and for $Ta_2O_5$ it seems slightly worse but is also within error bars. For color mode it seems like there is a tendency that annealing improves the stability, but here it is also within error bars. All in all, it seems that even for single layer coatings, annealing does not help in terms of fs-LIDT tests.

## 9.2 Design Calculation

As we did not get results for the $SiO_2$ single layer in catastrophic mode, this was a setback, but I tried this time to see if it would be possible to approximate it so we could still optimize the designs. All the sample results were treated like a design consisting of a single layer and set into equation 156 to calculate the intrinsic LIDT value for the specific material.

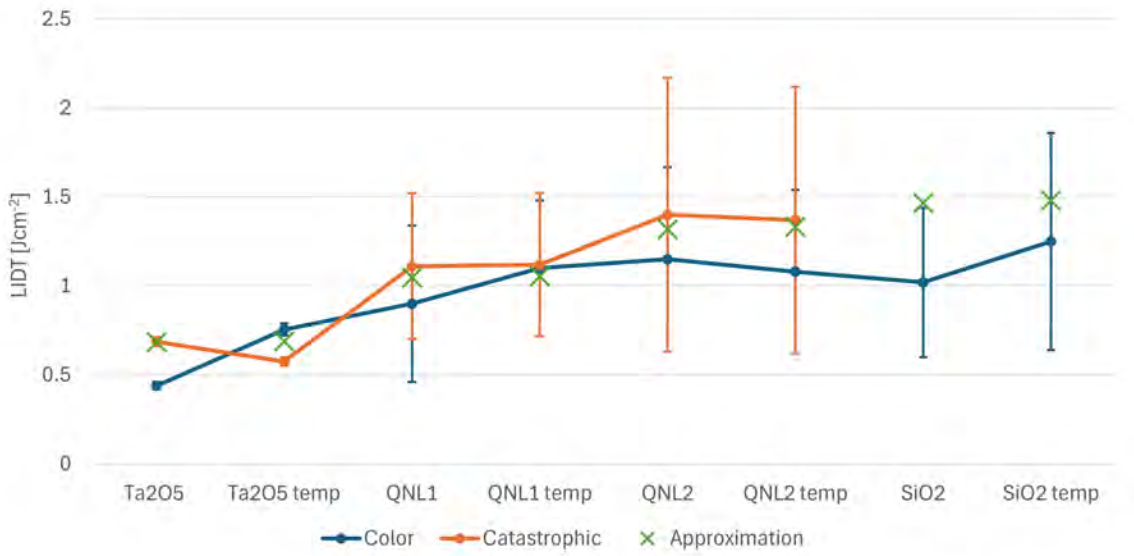


Figure 69: The fs-LIDT for the single layer samples for catastrophic and color mode is shown, together with a try to estimate the value for $SiO_2$. For the further calculation I assumed $SiO_2 = 1.46 \pm 0.6\, J/cm^2$ and $SiO_2^{temp} = 1.48 \pm 0.6\, J/cm^2$.

My attempt was to use the refractive index of the samples as $LIDT_{sample} \propto n_{Sample}^{-2}$ which worked pretty well. To be honest, with the huge error bars that is most probably just a coincidence as I have no deeper explanation. But leaving this insight in my scientific tinkering away would feel like lying. With the intrinsic LIDT values of the single layer samples, we were able to use the mentioned formula 156

$$LIDT_{Design} = \min\left[LIDT_{intrinsic} \cdot \frac{|E_{inc}|^2}{|E_{max}|^2}\right] \tag{157}$$

The idea was to create different designs with different properties in order to see several dependencies and check how the measured and calculated values differ.

| Run Nr. | Ref. | Composition/ No. of Layers | Description |
|---|---|---|---|
| PJ3332 | $D2$ | $(H:L)^{15}/30$ | $Ta_2O_5/SiO_2$-QWOT with $SiO_2$-cap |
| PJ3331 | $D4$ | $(H:L)^9(Q_1:L)^6/30$ | $Ta_2O_5/SiO_2$- and $QNL_1/SiO_2$-QWOT with $SiO_2$-cap |
| PJ3330 | $D10$ | $(H:L)^{14}H/29$ | optimized with $Ta_2O_5$ as last layer |
| PJ3333 | $D11$ | $(H:L)^9(QNL_1:L)^6/30$ | optimized $Ta_2O_5/SiO_2$ and $QNL_1/SiO_2$, last layer 2 QWOT $SiO_2$ |
| PJ3335 | $D13$ | $(H:L)^9(QNL_2:L)^6/30$ | QWOT $Ta_2O_5/SiO_2$, optimized $QNL_2/SiO_2$, last layer 2 QWOT $SiO_2$ |
| PJ3336 | $D14$ | $(H:L)^8(QNL_2:L)^6QNL_2/29$ | QWOT $Ta_2O_5/SiO_2$, optimized $QNL_2/SiO_2$, last layer $QNL_2$ |
| PJ3326 | $D15$ | $(H:L)^8(Q_1:L)^6Q_1/29$ | optimized with $QNL_1$ as last layer |

The design $D2$ was planned as a simple quarter wave stack with a cap layer of $SiO_2$ at the end, a classical design. The cap layer has in a simple Bragg mirror the function to reduce the E-field intensity at the surface to a minimum to reduce the damage probability due to surface defects and damage and

particles. Further, it reduces the E-field intensity in the first two layers drastically compared to simple quarter wave stack.
By calculation, the weak points of the two materials used in the specific design should be at $0.68\,J/cm^2$ in the last layer $Ta_2O_5$ and $1.47\,J/cm^2$ in the cap layer $SiO_2$.
The design $D4$ was chosen because it is also a simple quarter wave stack, but this has the last 6 layer pairs with $QNL_1$ instead of $Ta_2O_5$ as a high refractive index material. This way the damage probability should be decreased in the high refractive index materials. For $SiO_2$ it should make no difference.
The design $D10$ has a layer less than $D2$ but still consists only of $Ta_2O_5/SiO_2$ but has high refractive index material as end and an optimized design to lower the field intensity in the outer layer.
The design $D11$ is the optimized version of the design $D4$. The further out the high refractive layers are located, the thinner they become, while the low refractive layers become thicker. The last is a two quarter wave thick $SiO_2$ layer.

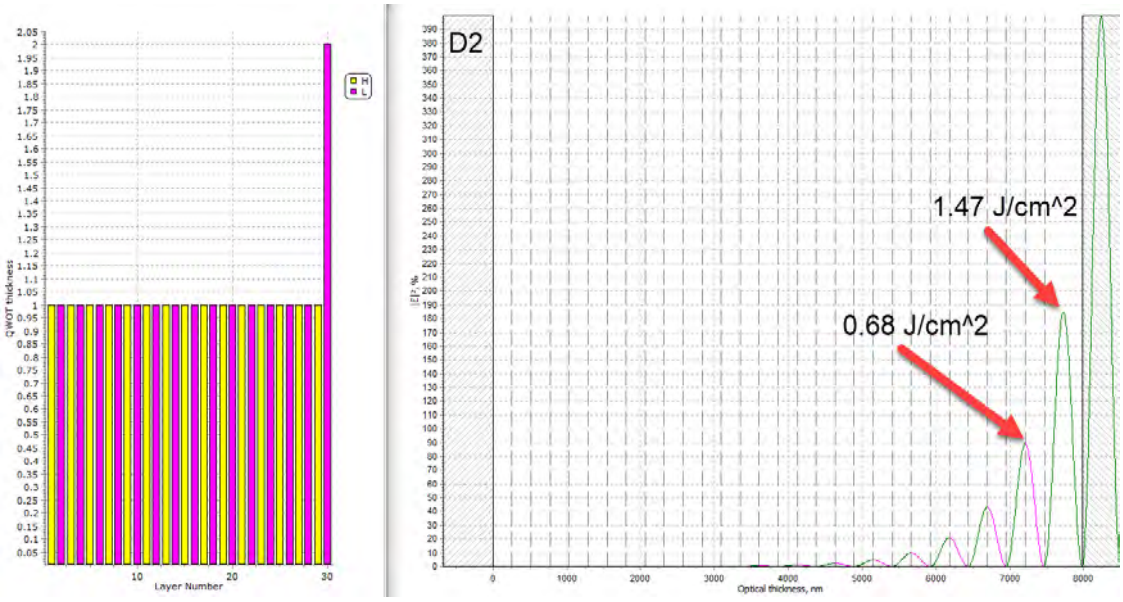


Figure 70: The design $D2$ is a simple Bragg mirror with a $SiO_2$-cap layer. The cap layer reduces the E-field intensity in the first $SiO_2$ and also $Ta_2O_5$ layer compared to a standard structure. It also reduces the surface intensity. The calculated weakest point of the two used materials in the design are pointed out with $1.47 \pm 0.6\,J/cm^2$ in the outer $SiO_2$ layer and $0.68 \pm 0.02\,J/cm^2$ in the last $Ta_2O_5$ layer.

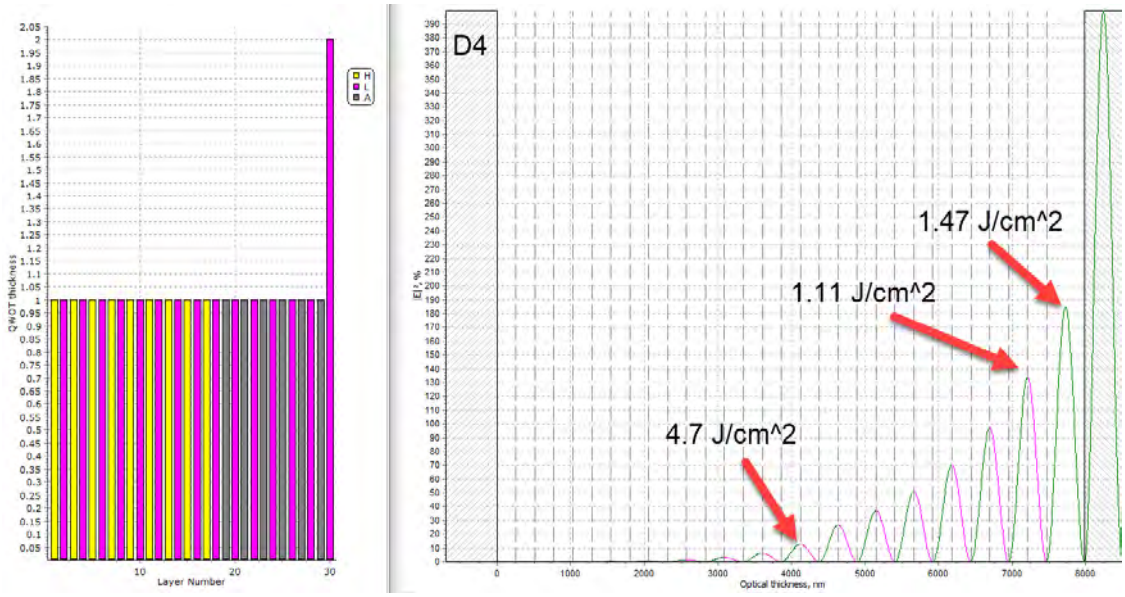


Figure 71: The design $D4$ is also a Bragg mirror with a $SiO_2$-cap layer but in this design the last 6 layers of high refractive index are replaced with $QNL_1$ stacks. The outer $QNL_1$ layers should have higher laser damage resistance and reduce the E-field before it reaches the first $Ta_2O_5$ layers. The calculated weakest point of the three used materials in the design are pointed out with $1.47 \pm 0.6\, J/cm^2$ in the outer $SiO_2$ layer, $1.11 \pm 0.17\, J/cm^2$ in the outer $QNL_1$ layer and $4.7 \pm 0.41\ J/cm^2$ in the last $Ta_2O_5$ layer.

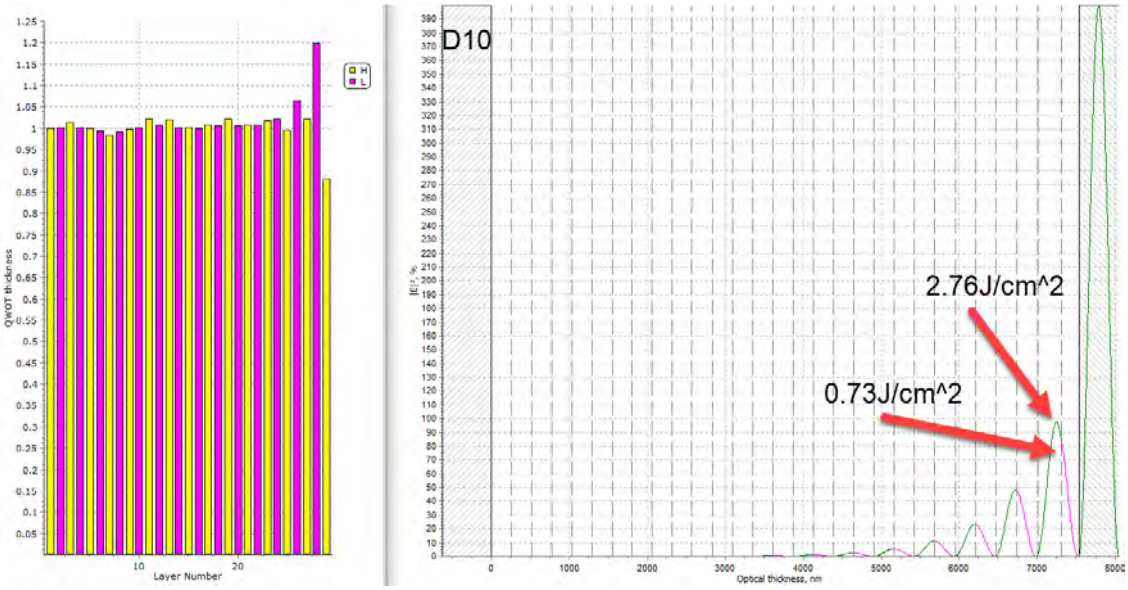


Figure 72: The design $D10$ consists like $D2$ only of $Ta_2O_5/SiO_2$ but doesn't end with a cap layer but with $Ta_2O_5$ and is optimized in the E-field intensity. $Ta_2O_5$ increased its resistance slightly to $0.73 \pm 0.03\, J/cm^2$ and the second layer, $SiO_2$ has $2.76 \pm 1.13\, J/cm^2$.

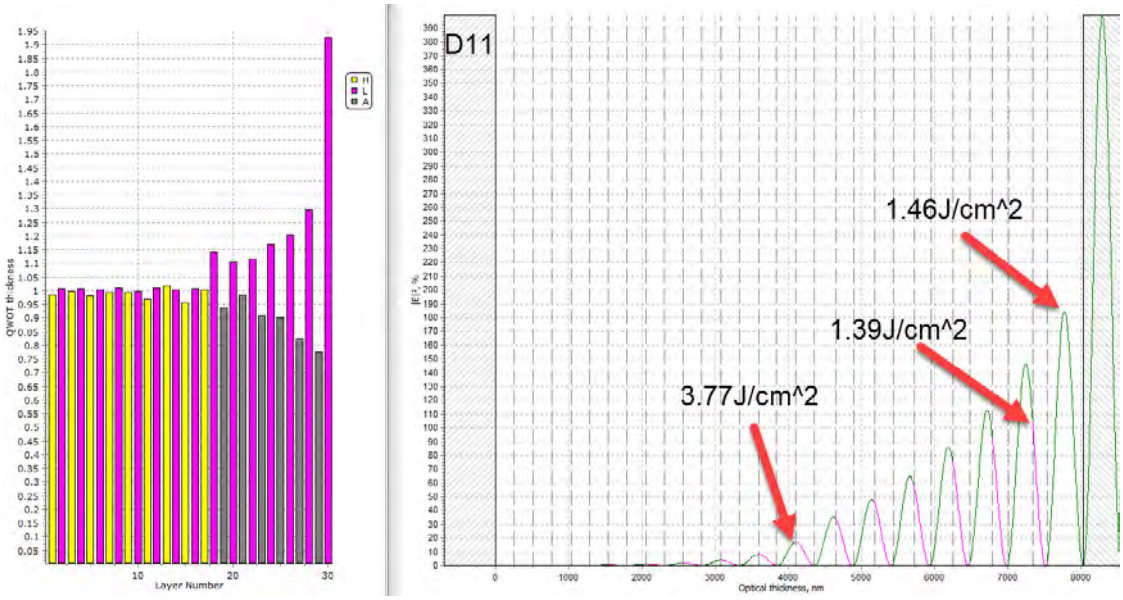


Figure 73: The designs $D11$ is an optimized version of $D4$. It has a two quarter wave thick $SiO_2$ layer at the end and the calculated weakest points are $1.46 \pm 0.6\, J/cm^2$ in the last $SiO_2$ layer, $1.39 \pm 0.14\, J/cm^2$ in the outer $QNL_1$ and $3.77 \pm 0.52\, J/cm^2$ in the last $Ta_2O_5$ layer.

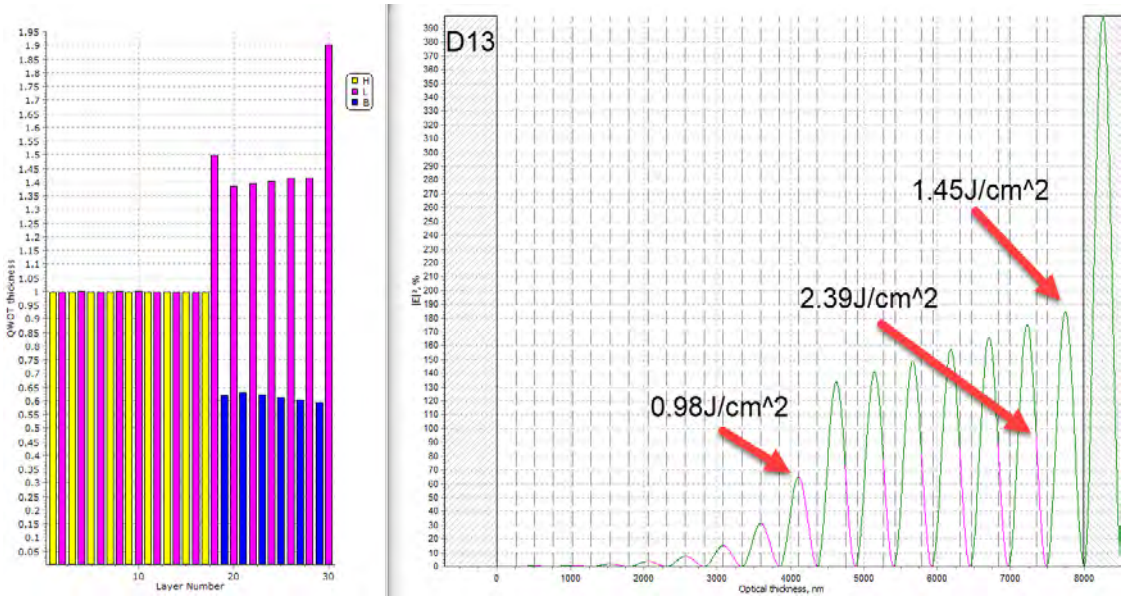


Figure 74: $D13$ is a design similar to $D11$ where the $QNL$ layers are replaced with the settings with lower refractive index. The decline of outer $QNL$ layers is not that steady and more abrupt from the last $Ta_2O_5$ layers. The last two quarter thick $SiO_2$ layer has a calculated laser resistance of $1.45 \pm 0.59\, J/cm^2$. The first $QNL_2$ layer from the outside has $2.39 \pm 1.31\, J/cm^2$ and $Ta_2O_5$ is still at $0.98 \pm 0.04\, J/cm^2$.

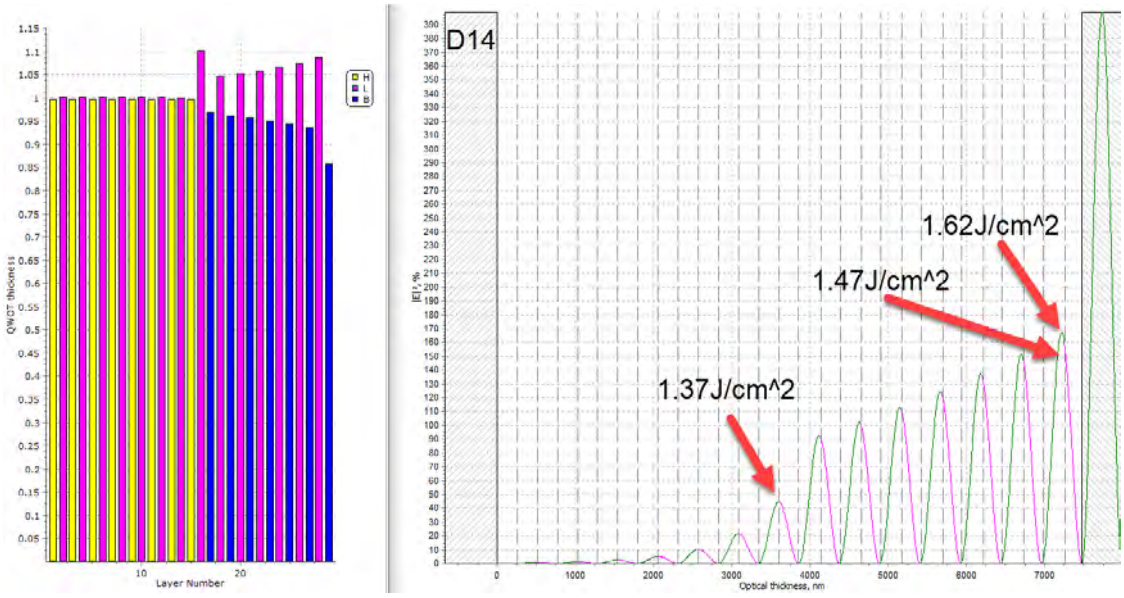


Figure 75: The design $D14$ uses similar to $D13$ the second $QNL_2$ process but closes the design with the high refractive index material. It is also optimized. The laser resistance is better distributed over the different materials with $1.47 \pm 0.81\, J/cm^2$ for the last layer of $QNL_2$, $1.62 \pm 0.66\, J/cm^2$ for the $SiO_2$ and $1.37 \pm 0.05\, J/cm^2$ for the $Ta_2O_5$ layer. Together with $D15$ and $D11$ it is the most promising design.

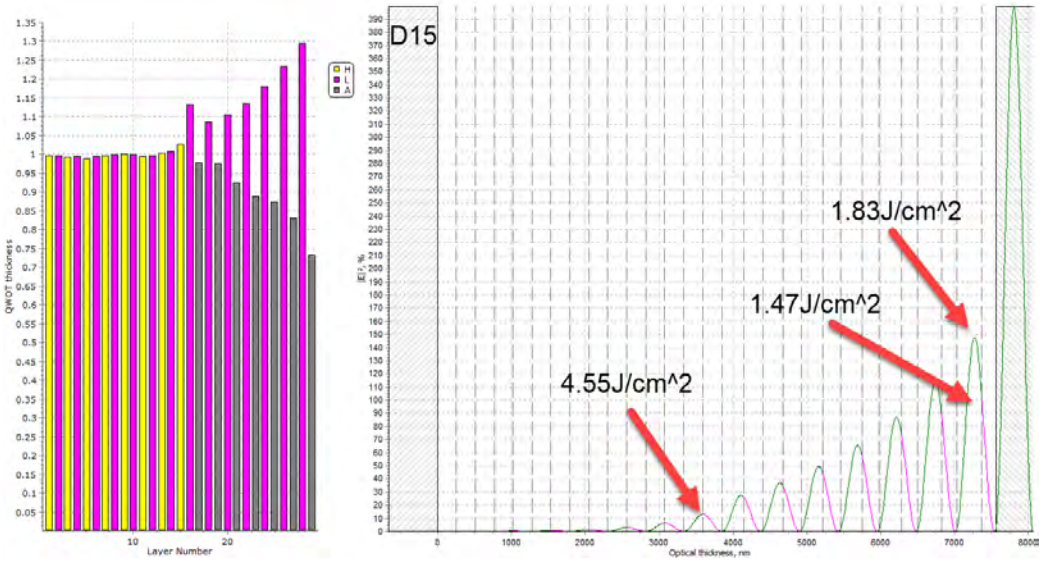


Figure 76: $D15$ is again a mirror using $QNL_1$. It is optimized and similar to $D11$ but ends with the high refractive index material, like $D14$. But compared to $D14$ it uses the second QNL settings. With a minimal laser resistance of $4.55 \pm 0.17\, J/cm^2$ in the last $Ta_2O_5$ layer, $1.83 \pm 0.75\, J/cm^2$ in the last $SiO_2$ layer and $1.47 \pm 0.54\, J/cm^2$ in the interface $QNL_1$ layer it has one of the highest calculated LIDT values.

The designs $D13$ and $D14$ have a different process of $QNL$ with a lower refractive index. Although $D13$ is a similar setup as $D11$ with a two quarter thick $SiO_2$ layer as the ending, the thickness variation is different. The probability of damage is transferred more towards the $Ta_2O_5$ layers.
As described $D14$ uses also the second $QNL2$ as an outer high refractive index material, but instead to $D13$ it ends with it as a high index material instead of the $SiO_2$ layer. It also has a smoother thickness distribution that transfers the probability of damage from $Ta_2O_5$ towards the $QNL_2$ layers.

$D15$ has similarities with $D14$ and $D10$ as it uses high refractive index material as the last layer but instead of the other two it uses $QNL1$ as the outer stack to protect the $Ta_2O_5$ layers below. Together with $D14$ and $D11$ it is the most promising design.
The lowest value of the design defines the expected value that the design can achieve and, therefore, gives the $LIDT_{Design}$. We used the same formula also for the color mode to compare both calculated with both measured modes which can be seen in figure 77. The hatched bars are the calculated values, while the full bars are the measurements.

## 9.3 Results

Lidaris measured the coated designs with the same setup as before with the single layers and also as at the laser damage competition. The data is presented together with the two calculated values in figure 77. The catastrophic mode is colored orange, and the color mode is colored green. The calculated value is hatched, and the measured is filled. It is clearly visible that the calculated and measured values rarely overlap. $D2$ and $D10$ seem to fit and also color mode of $D14$ but the others differ partially a lot and it is not clear if the fittings are not just coincidence. From experience, LIDT has a high uncertainty, especially in the absolute error but is more accurate relative in the same measurement series. The results and also calculations from different measurement setups are not comparable, which can be seen with the measured values from RhySearch for the same samples. The main differences in the setup are listed in table 4. That is why I normalized every series to one in figure 78. The error bars from the RhySearch measurements are not added as I expect the error calculation from Lidaris is strongly underestimated and also not calculated the same as at RhySearch which would suggest a false comparison. Further, at RhySearch we count every visible change as "event" and don't distinguish between color and catastrophic mode which means it is a combination of both.

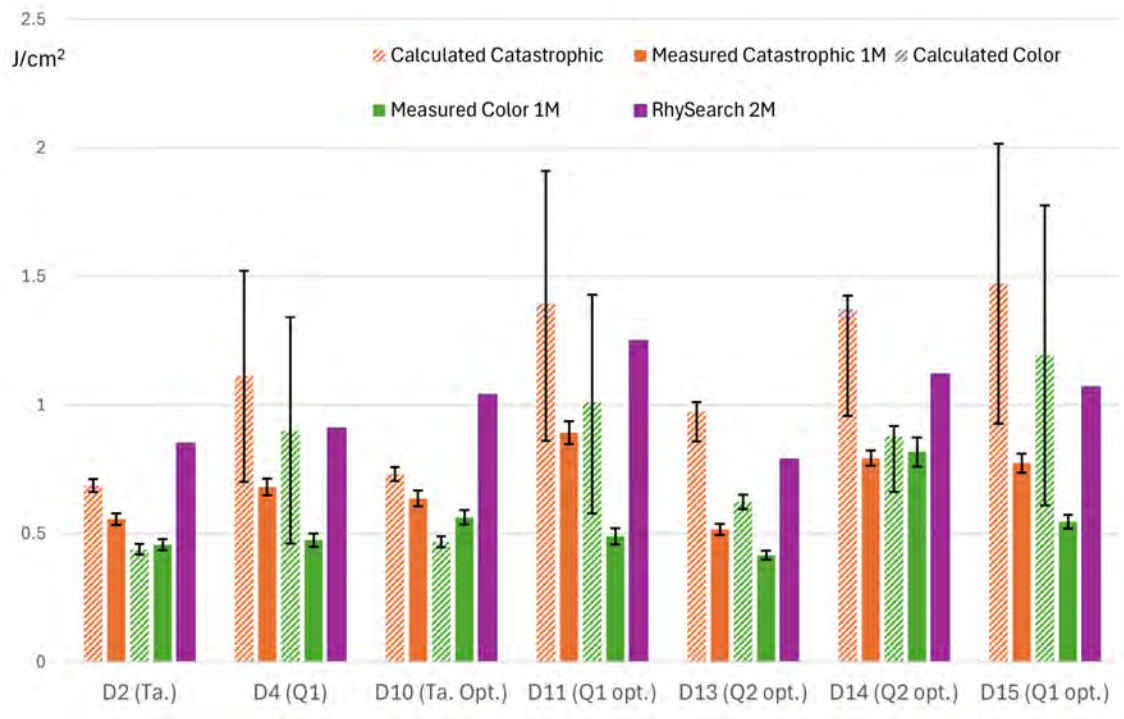


Figure 77: The figure shows for the catastrophic and also the color mode the difference between the calculated and measured fs-LIDT values.The catastrophic LIDT is orange while the color mode is green. Calculated is each hatched while measured is kept full. The comparison shows mostly that the calculated and measured values diverge.

Normalizing to the maximum value of each series is clearly not the key for a correct interpretation, but it shows for me the more important parts of the comparison. Normalized the previously well matching calculated and measured values of $D2$ and $D10$ do not fit anymore. But at this point I guess

| Characteristics | Lidaris | RhySearch |
|---|---|---|
| Wavelength $[nm]$ | 1030 | 1030 |
| Repetition rate $[kHz]$ | 500 | 200 |
| Pulse duration $[fs]$ | 200 | 300 |
| Beam diameter $[\mu m]$ | 60 | 35 |
| Number of Pulses | $10^{0,1,2,3,4,5,\mathbf{6}}$ | $10^{4,5,7}$, $2 \cdot 10^{\mathbf{6},7}$and $5 \cdot 10^6$ |
| max. Exposure time [s] | 2 | 100 |

Table 4: This table shows the different settings used at Lidaris and RhySearch. In the following diagrams the measurement from Lidaris with $10^6$ pulses is shown, while the values for the $2 \cdot 10^6$ measurement from RhySearch is added.

it is clear that the formula used is more to get an estimated value than a precise calculation, especially for the high uncertainty of LIDT measurements.
More interesting for me is to compare the properties of the different designs with each other. However, it must also be said that there are very few samples here, making it practically impossible to perform statistical analysis. Nevertheless, some trends can be identified.

- **Classical design vs optimization:** While $D2$ is the classical design with a quarter wave stack and a cap layer, $D10$ has no cap layer and is slightly optimized and ends even with high refractive index material. $D10$ has the highest value for all calculated and measured modes.
  The same is true for $D4$ and its optimized versions $D11$ and $D15$. While $D11$ also ends with a two quarter wave thick low refractive layer and $D15$ like $D10$ ends with a high refractive index material. This leaves the conclusion that optimizing increases the laser resistance in both variations while the cap layer is not necessary.

- **Classical material vs. QNL:** To compare the classical material $Ta_2O_5 - SiO_2$ with $QNL$, we can compare $D2$ with $D4$ both are the same quarter wave stack with cap layer, but $D4$ has 6 pairs of $QNL_1$ in the end. QNL also reaches in all all calculated and measured categories with a higher value than the classic material combination. The same is true for $D10$ compared with $D14$ and $D15$. All three are optimized and end with high refractive material in the end. As the optimization is slightly different on each design its not that easy to compare directly, but also here all the calculated and measured modes are better using some $QNL$ layer instead only $Ta_2O_5$.

- **Calculation vs. measurement:** It is clearly visible that the calculation does not really work as a good approximation. For the absolute value, it seems that the classical materials with the designs $D2$ and $D4$ work the best, but I would assume it is by coincidence, as there is no explanation why this would be. For the rest, we can see tendencies as the expected designs $D11$, $D14$ and $D15$ are calculated and also measured the best values.

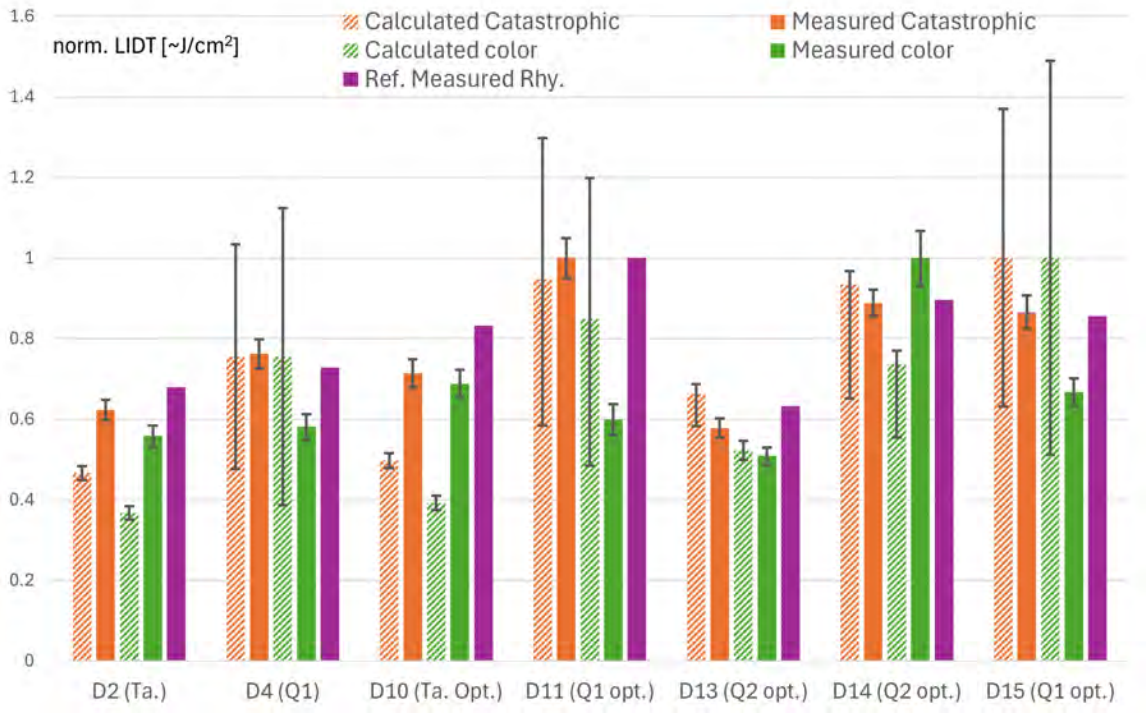


Figure 78: The calculated and measured results are normalized and also a reference measurement from RhySearch with a $300\,fs - LIDT$ measurement but with slightly different setup is added.

In the end, the conclusion for me is that the calculation does not work as I hoped or expected. We can assume some tendencies such that using $QNL$ in the last layer pairs as a high refractive index material can increase the LIDT value of the design compared to the expected exclusive use of the classical material.
Further optimizing the design in terms of E-field also increases the LIDT value compared to the classical quarter wave stack with cap layer, further even the cap layer does not seem to be necessary to reach a high laser resistance but the proper placement of E-field intensities in the design.
As expected also measurements of different LIDT setups are not comparable, which can be seen with the values we measured at RhySearch.
The measured values from Lidaris are added to the table of competitors from the Laser Damage Competition to see where we would stand. But it has to be said clearly that this has to be treated with a lot of care, as it is not clear if the reached value would have been the same at the competition. The new designs are added on the left side of each diagram. The transparent bars are kept the same as before to see the difference.
For the catastrophic mode, it can be seen that we lay below the value of best sample we had at the actual competition. This shows me two things, first that my educated guessing I used in the beginning for the designs isn't that bad and second that the absolute error bars as said are probably bigger than displayed.
For the color mode, we got a much higher result compared to the previous designs and we see that we would be somewhere in the higher IBS coated designs $HfO_2$ especially with $D14$. As good as this looks, I would be careful using the absolute value of this result, but it is still a great success to see that we can get in the same range of LIDT values with our high yield magnetron sputtering tool and $Ta_2O_5 - SiO_2$ as base materials.
For the fatigue mode, it is suspicious that we reach through all new designs such high values and especially with $D15$ nearly no degradation for color and also catastrophic mode. But I also need to say that the fatigue results should be the least affected by an absolute error, which means they should be the most realistic. Even after taking the results again with care, I guess we can take the credit of reaching high fatigue with our materials as it fits our experience.

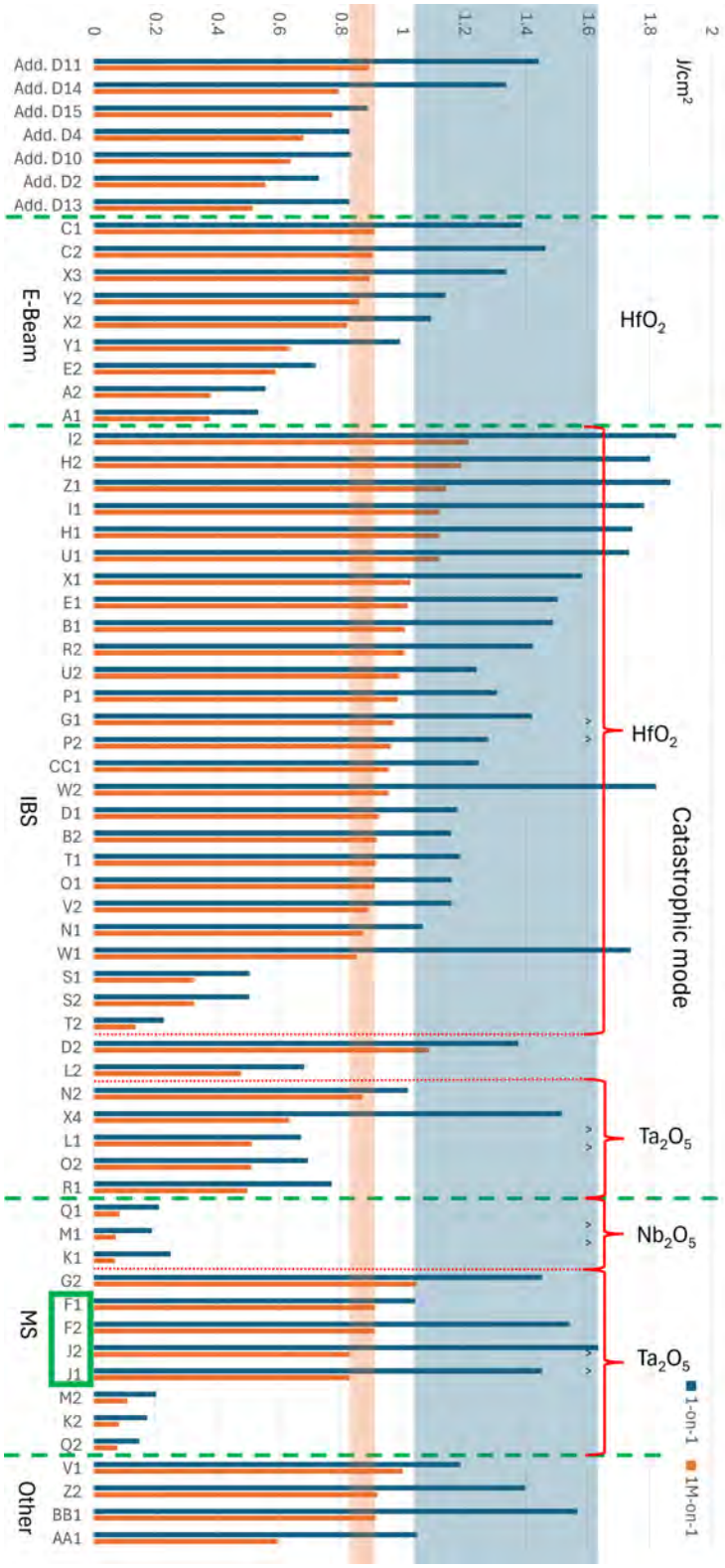


Figure 79: The measurements done at Lidaris from the new designs are added on the left side of the Laser damage Competition evaluation. It shows lower maximum results as before at our participation. The results need to be taken with care as i expect the absolute error to be higher than depicted even if it is the same setup in both series. Shown are the $1 - on - 1$ and $10^6 - on - 1$ results in catastrophic mode.

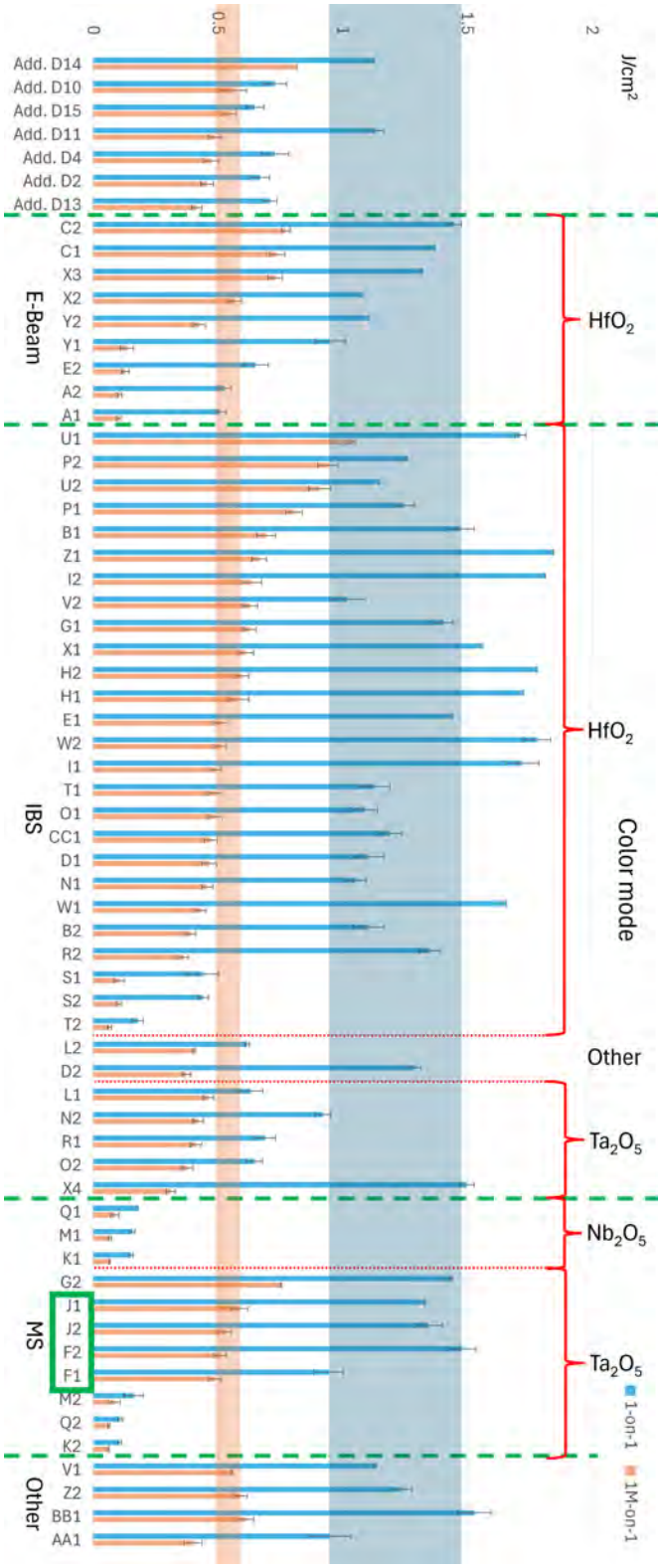


Figure 80: The measurements for color mode are again added on the left side of the Laser damage Competition evaluation. It shows a much higher reached value especially for $D14$. It needs to be said again, that the results need to be taken with care. Shown are the $1 - on - 1$ and $10^6 - on - 1$ results in color mode.

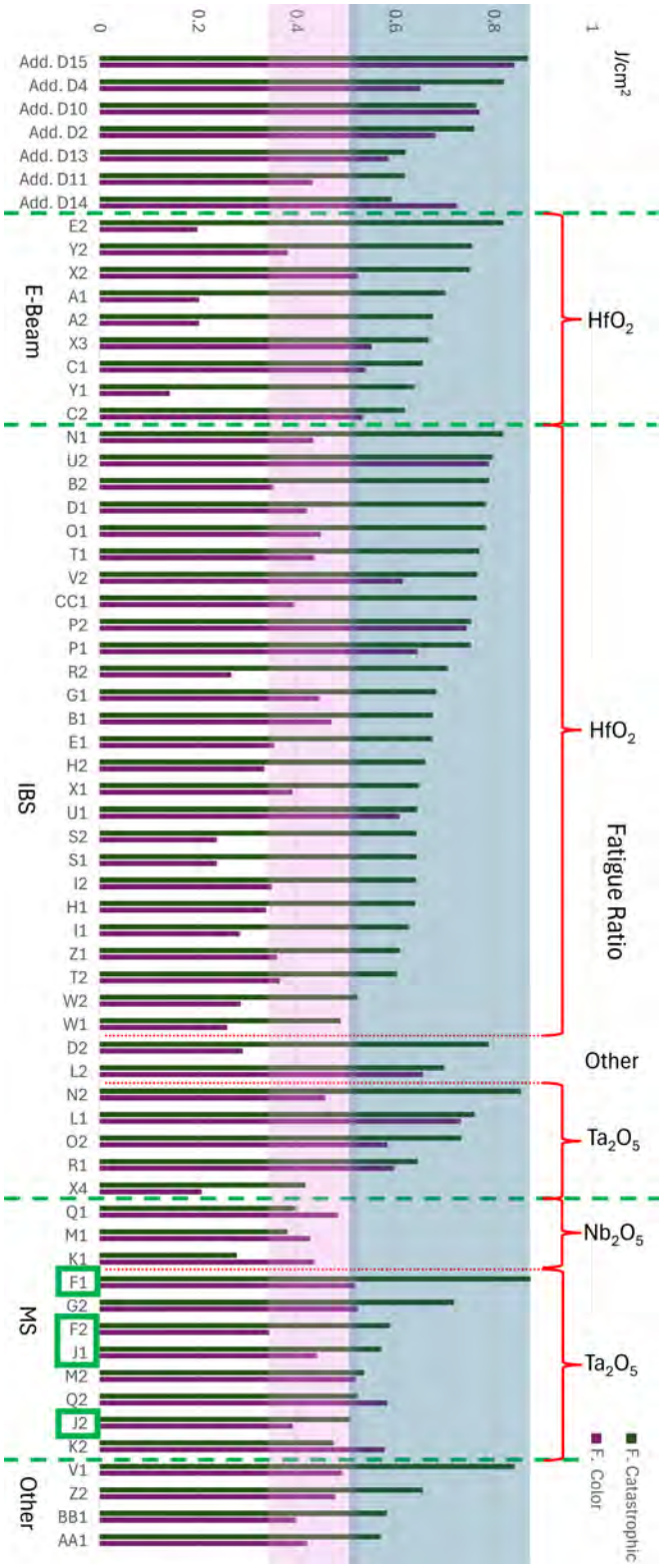


Figure 81: The reached fatigue $f = \frac{LIDT(1-on-1)}{LIDT(10^6-on-1)}$ is displayed for all participants, separated in color and catastrophic mode. Even if I expected from experience that we reach high values it is suspicious that the results are that high. I expect the fatigue results to be less influenced by the absolute error.

# 10 Open Topics

Since this work was written in the middle of a project, there are naturally a number of problems on which we are working, challenges that we face, and plans for how to deal with them in the future. So, here is a brief discussion of where we currently stand in terms of understanding and what we still have planned.

## 10.1 Band-Gap Calculation

I already explained where the Tauc plot comes from, but have not talked about the problems which can occur.
There are two major issues we have to address; the first is about the exponent used in the plot.

### 10.1.1 Choose the right Transition Type

We know that the exponent refers to the type of transition. The problem is that this theory refers to a crystalline semiconductor but the materials we use are primarily amorphous, which means that we do not have a periodicity and therefore not a clear dominant transition. This leaves the Tauc plot with some superimpositions of many different transitions [53].
This effect is depicted in figure 82. Both diagrams show the absorption for the same sample, but the left assumes a direct transition while the right diagram assumes an indirect transition. With the difference in the exponent, other areas of the same absorption coefficient are straightened.
This does not mean we can not use the Tauc plot to describe the band-gap, we just need to be aware that the calculation is a generalization in which the absolute value is likely to be incorrect. However, within a series of similar systems that are all evaluated in the same way, the relative values can be compared and make physical sense.
As already explained, the literature recommends trying the different exponents and selecting the best linear fit[60] (P.5). So, you would try out which transition is dominant and use that one. Some literature even uses some values in between for amorphous material [53] (P.6).

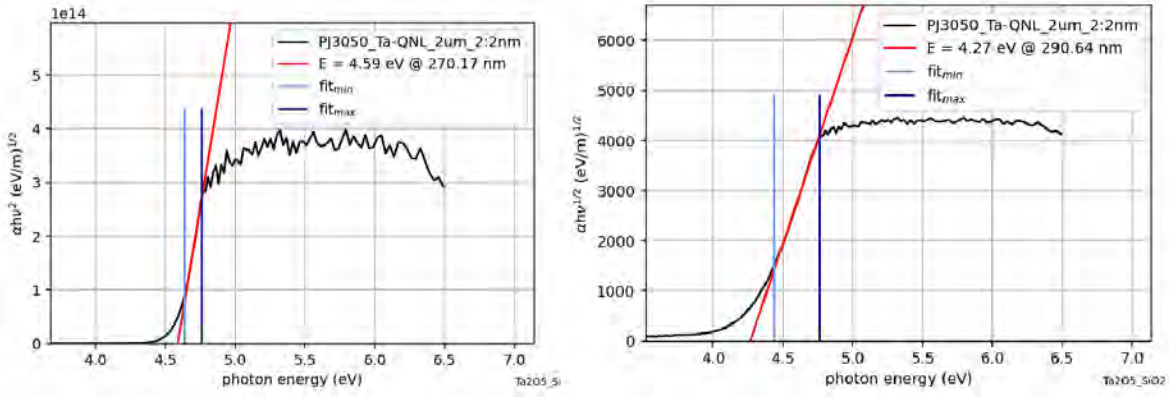


Figure 82: The diagram shows two different plots, the left side shows the Tauc plot assuming a direct transition and on the right side an indirect. Both use for the same absorption coefficient showing a significantly different outcome in band-gap calculation.

### 10.1.2 Calculation of the Absorption Coefficient

The second issue about the Tauc-plot is about where the absorption coefficient comes from. The script we used in the beginning used a formula that is an approximation of the assumption:

$$(T+R) \approx \mathbf{e}^{-\alpha d_{film}} \rightarrow \alpha \approx \frac{1}{d_{film}} \cdot ln\left[\frac{1}{T+R}\right] \tag{158}$$

This formula works as a rough approximation and if R is small.
We changed the formula slightly and used the first approximation of the transmission of the internal

multi reflection 3.1.2 with:

$$T \approx (1-R) \cdot \mathbf{e}^{-\alpha d_{film}} \rightarrow \alpha \approx \frac{-1}{d_{film}} \ln\left[\frac{T}{1-R}\right] \tag{159}$$

The resulting Tauc-plot is not that sensitive to backside reflection anymore. However, to avoid complications with materials with higher reflectivity such as $\alpha Si$ or $\alpha Si/SiO_2$-QNL, we have taken care to coat only such thin layers during determination coatings that interference effects do not yet occur at this point. This approach worked reasonably well, but it would be better to use a generally applicable method.
To calculate the absorption coefficient with more accuracy, we could use either a more complex formula based on geometric series, or we could use the Beer-Lamberts law of 2.2.5 which uses directly the extinction coefficient.

$$\alpha = \frac{4\pi\kappa}{\lambda} \tag{160}$$

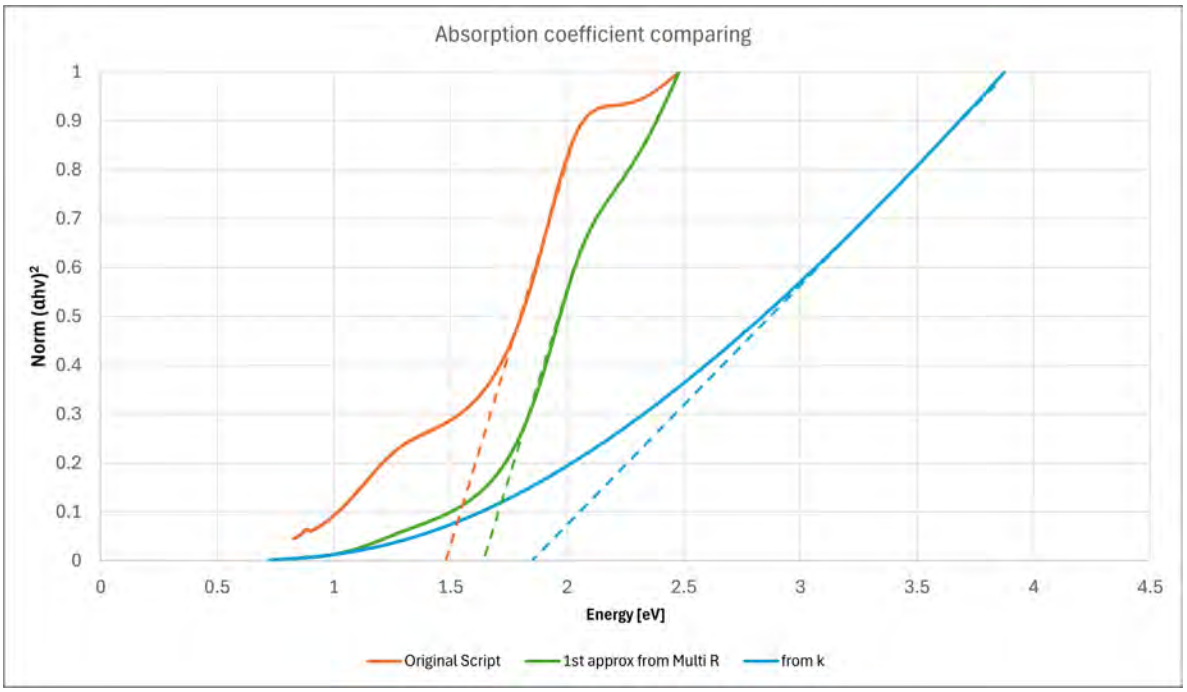


Figure 83: The diagram shows the problem in calculating the band-gap using the transmission and reflection spectra compared using the extinction coefficient, calculated using Optichar.

Both ways have some advantages and could cause problems.
The attempt with the geometric series includes also Urbach and Weak absorption. As we are interested in the fundamental optical absorption, these regions can affect the fitting range and therefore greater care must be taken when selecting the fit range, so that the fundamental absorption curve is not influenced by the underlying absorption areas.
If the extinction coefficient is used to calculate the absorption coefficient, a cleaner curve is generated, and the calculation is easier to automate and evaluate. However, the calculation of the extinction coefficient is very sensitive in the absorption edge region and can be distorted by lower lying absorptions like before the Urbach- and weak absorption regions that are not described by the oscillator model.
Both models are planned to be tested to see if one of them is more accurate or reliable.

## 10.2 Refractive Index of Mixed Materials

The description of the calculation of the mixing ratio uses the formula of the Drude model[48]. We tested it and it came out pretty accurate. But we compared to the model in the beginning only once (PJ1983).

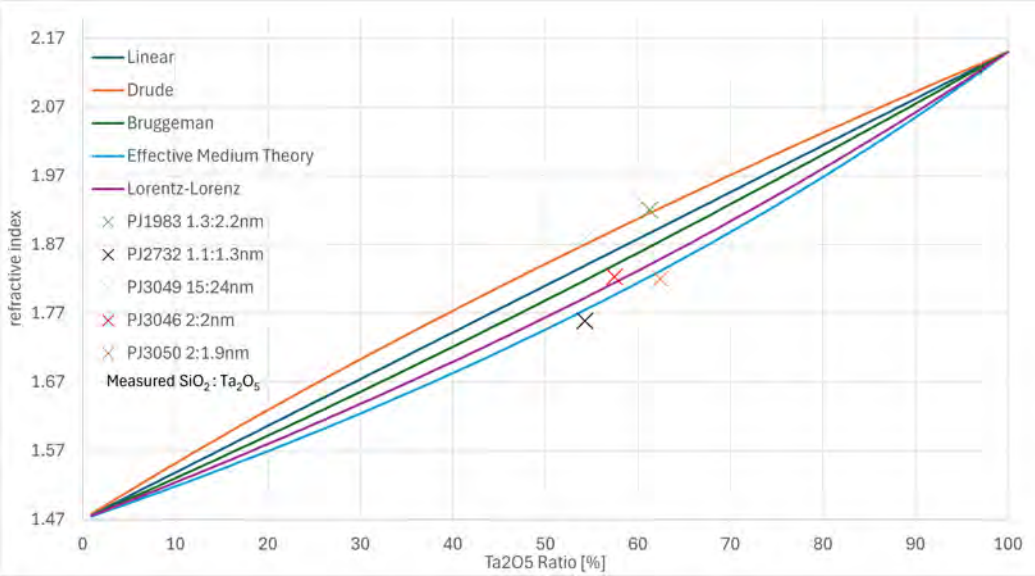


Figure 84: We checked in the beginning of the project the used "Drude" model with the TEM measurement and it worked pretty well (PJ1983). Later TEM-measurement points showed a higher deviation to the used model.

The used Drude-model describes a simple approximation for a mixture where the molecules or atoms are polarized only by the external field and the internal field interaction is completely shielded [48]. Since the assumptions of the model were difficult for us to explain, we carried out further TEM measurements and saw much more variation, which indicates that it might be helpful to conduct further tests, as there are likely to be other dependencies that influence which model is more suitable in which situation. In figure 84 the calculated ratios from TEM measurements are shown together with other models discussed in the literature [48]. Another important point could be the measurement uncertainty. Although TEM is an excellent and accurate measurement method for measuring layers at high resolution, determining where a boundary layer is located is still a matter of interpretation, as even this method does not always provide completely clear results. An example that clearly illustrates the problem is the zoom-in from a TEM measurement of the $\alpha Si/SiO_2$-QNL $PJ3012$, as shown in figure 85.

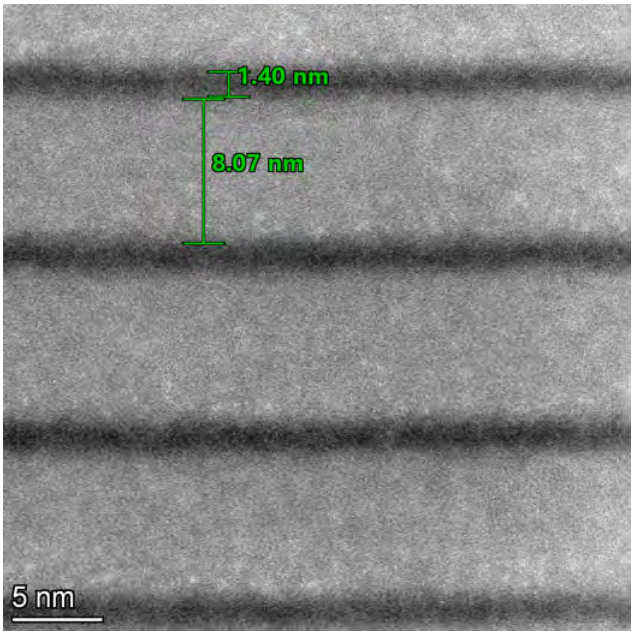


Figure 85: The figure shows the problem in determining the thickness of the different materials as the border can be unclear. Measurement done by EMPA.

## 10.3 Multi Potential Well

For a simple finite well, it is easy to set up the equations and solve them, as discussed in chapter 6.2. If there are several potentials it is not just a number more of the same equations as the wave functions start to influence each other, which increases the effort drastically. A research group at Laserzentrum Hannover around Paschel et al. described how they calculate the optical band-gap of QNL [71]. Unfortunately, their work was published after I had already tried to solve the same problem with a Transfer Matrix Method (TMM)3.2. Since I am not sure whether my approach works and I currently lack both the expertise and the time to test it, I have decided to include this approach here in the appendix, as I plan to continue working on it later.
The whole approach is based on the same method as in 6.2 but uses, as said, a transfer matrix method like in [50] (P.51). So even though I am not yet sure whether this approach should work, I haven't found any reason why it should not. However, this is a topic that I still need to look into together with someone who has greater expertise in this topic (or any expertise at all). So, there is no claim to correctness or completeness, but I would like to share these thoughts here.

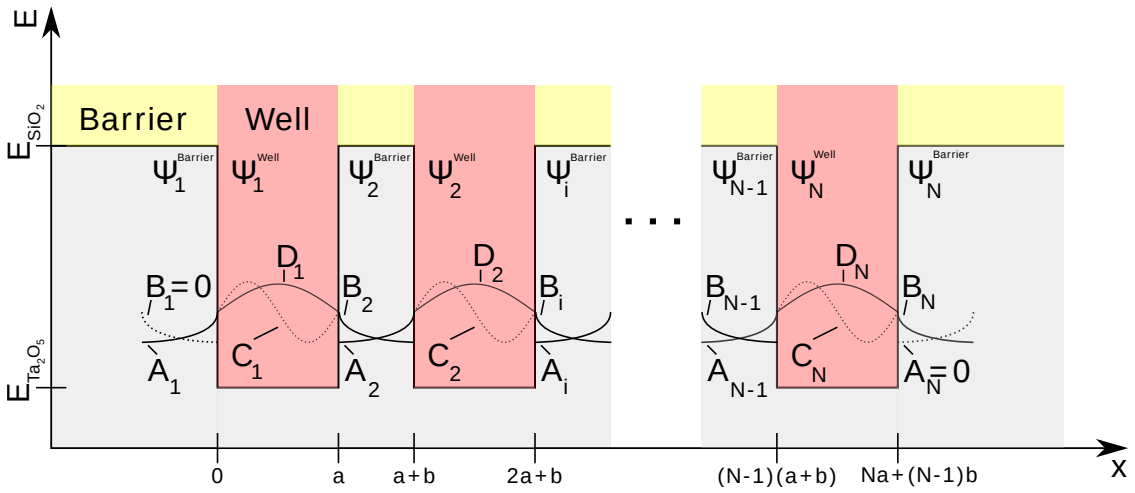


Figure 86: In a periodic potential with all the same depth and length, the wave functions of the wells start to interfere with each other.

So we examine a series of the identical wells in bulk barrier material. This means we assume that in both directions of the well laminates is an infinite thick barrier material. The barriers and also the wells are numbered and as shown in figure 86 we start from left with the bulk barrier material, followed by the first well as $i = 1$, the last well is well number $i = N$ followed by the ending bulk material as $i = N + 1$. We can describe the wavefunctions generally again as:

$$\psi_i^{barrier}(x) = A_i \mathbf{e}^{\alpha_i x} + B_i \mathbf{e}^{-\alpha_i x} \tag{161}$$

$$\psi_i^{well}(x) = C_i sin\kappa_i x + D_i \cos\kappa_i x \tag{162}$$

As we always have the same two materials and we plan to keep all the layers with the same materials the same thickness, we can simplify some parts of the equations. $\alpha = \alpha_i$ & $\kappa = \kappa_i$ : $\forall i$.
Further, again, the functions and also their derivations need to be continuous. So for the first transition zone $x = 0$ applies:

$$\begin{aligned} \psi_1^{barrier}(x=0) = \psi_1^{well}(x=0) &\Rightarrow A_1 + B_1 = D_1 \\ \frac{\partial}{\partial x}\psi_1^{barrier}(x=0) = \frac{\partial}{\partial x}\psi_1^{well}(x=0) &\Rightarrow \alpha A_1 - \alpha B_1 = \kappa C_1 \end{aligned} \tag{163}$$

To describe the first transition zone from the well to the barrier, we can write as:

$$\begin{aligned} \psi_1^{well}(x=a) = \psi_2^{barrier}(x=a) &\Rightarrow C_1 sin\kappa a + D_1 \cos\kappa a = A_2 \mathbf{e}^{\alpha a} + B_2 \mathbf{e}^{-\alpha a} \\ \frac{\partial}{\partial x}\psi_1^{well}(x=a) = \frac{\partial}{\partial x}\psi_2^{barrier}(x=a) &\Rightarrow \kappa[C_1 cos\kappa a - D_1 \sin\kappa a] = \alpha[A_2 \mathbf{e}^{\alpha a} - B_2 \mathbf{e}^{-\alpha a}] \end{aligned} \tag{164}$$

We can write this down for more transition zones and realize that we always get the same expression for the two pairs of equations at the well number $i \in 1, ..., N$ for
**barrier**$_i \rightarrow$ **well**$_i$:

$$\begin{aligned} \psi_i^{barrier}(x=(i-1)(a+b)) = \psi_i^{well}(x=(i-1)(a+b)) \\ \Rightarrow A_i \mathbf{e}^{\alpha(i-1)(a+b)} + B_i \mathbf{e}^{-\alpha(i-1)(a+b)} = C_i sin[\kappa(i-1)(a+b)] + D_i \cos[\kappa(i-1)(a+b)] \\ \& \\ \frac{\partial}{\partial x}\psi_i^{barrier}(x=i(a+b)) = \frac{\partial}{\partial x}\psi_i^{well}(x=i(a+b)) \\ \Rightarrow \alpha[A_i \mathbf{e}^{\alpha(i-1)(a+b)} - B_i \mathbf{e}^{-\alpha(i-1)(a+b)}] = \kappa[C_i cos\kappa(i-1)(a+b) - D_i \sin\kappa(i-1)(a+b)] \end{aligned} \tag{165}$$

and

**well**$_i \rightarrow$ **barrier**$_{i+1}$:

$$\begin{aligned}
\psi_i^{well}(x = ia + [i-1]b) &= \psi_{i+1}^{barrier}(x = ia + [i-1]b) \\
\Rightarrow C_i sin[\kappa(ia + [i-1]b)] + D_i \cos[\kappa(ia + [i-1]b]) &= A_{i+1}\mathbf{e}^{\alpha(ia+[i-1]b)} + B_{i+1}\mathbf{e}^{-\alpha(ia+[i-1]b)} \\
&\& \\
\frac{\partial}{\partial x}\psi_i^{well}(x = ia + [i-1]b) &= \frac{\partial}{\partial x}\psi_{i+1}^{barrier}(x = ia + [i-1]b) \\
\Rightarrow \kappa[C_i cos[\kappa(ia + [i-1]b)] - D_i \sin[\kappa(ia + [i-1]b)]] &= \alpha[A_{i+1}\mathbf{e}^{\alpha(ia+[i-1]b)} - B_{i+1}\mathbf{e}^{-\alpha(ia+[i-1]b)}]
\end{aligned} \tag{166}$$

As we have now a general expression for the transition zones, we can write it in matrix form. We use the same principle of the transfer matrix method as in calculating optical layer design, but here for particle wave behavior. We can write the first two equations:

$$\begin{pmatrix} 1 & 1 \\ \alpha & -\alpha \end{pmatrix} \begin{pmatrix} A_i \\ B_i \end{pmatrix} = \begin{pmatrix} 0 & 1 \\ \kappa & 0 \end{pmatrix} \begin{pmatrix} C_i \\ D_i \end{pmatrix} \tag{167}$$

We can write all the possible transition equations for $N$ wells.
**barrier**$_i \rightarrow$ **well**$_i$:

$$\begin{aligned}
&\underbrace{\begin{pmatrix} \mathbf{e}^{\alpha(i-1)(a+b)} & \mathbf{e}^{-\alpha(i-1)(a+b)} \\ \alpha\mathbf{e}^{\alpha(i-1)(a+b)} & -\alpha\mathbf{e}^{-\alpha(i-1)(a+b)} \end{pmatrix}}_{\hat{L}_{I,i}} \begin{pmatrix} A_i \\ B_i \end{pmatrix} \\
&= \underbrace{\begin{pmatrix} sin[\kappa(i-1)(a+b)] & \cos[\kappa(i-1)(a+b)] \\ \kappa\cos[\kappa(i-1)(a+b)] & -\kappa sin[\kappa(i-1)(a+b)] \end{pmatrix}}_{\hat{L}_{II,i}} \begin{pmatrix} C_i \\ D_i \end{pmatrix}
\end{aligned} \tag{168}$$

and for
**well**$_i \rightarrow$ **barrier**$_{i+1}$:

$$\begin{aligned}
&\underbrace{\begin{pmatrix} sin[\kappa(ia + [i-1]b)] & \cos[\kappa(ia + [i-1]b)] \\ \kappa\cos[\kappa(ia + [i-1]b)] & -\kappa sin[\kappa(ia + [i-1]b)] \end{pmatrix}}_{\hat{R}_{I,i}} \begin{pmatrix} C_i \\ D_i \end{pmatrix} \\
&= \underbrace{\begin{pmatrix} \mathbf{e}^{\alpha(ia+[i-1]b)} & \mathbf{e}^{-\alpha(ia+[i-1]b)} \\ \alpha\mathbf{e}^{\alpha(ia+[i-1]b)} & -\alpha\mathbf{e}^{-\alpha(ia+[i-1]b)} \end{pmatrix}}_{\hat{R}_{II,i}} \begin{pmatrix} A_{i+1} \\ B_{i+1} \end{pmatrix}
\end{aligned} \tag{169}$$

For unoriginal reasons I gave the two pairs of matrices the names $\hat{L}_{I,i}, \hat{L}_{II,i}, \hat{R}_{I,i}\&\hat{R}_{II,i}$ for $L$ left and $R$ for right regarding the side of the barrier$_i$ and the subscripted $I/II$ for the wave term on the left or right side of the referred transition.
We can now rearrange the equations using the inverse matrices as follows:

$$\begin{aligned}
\hat{L}_{I,i} \begin{pmatrix} A_i \\ B_i \end{pmatrix} &= \hat{L}_{II,i} \begin{pmatrix} C_i \\ D_i \end{pmatrix} \\
\Rightarrow \begin{pmatrix} A_i \\ B_i \end{pmatrix} &= \hat{L}_{I,i}^{-1}\hat{L}_{II,i} \begin{pmatrix} C_i \\ D_i \end{pmatrix}
\end{aligned} \tag{170}$$

And:

$$\begin{aligned}
\hat{R}_{I,i} \begin{pmatrix} C_i \\ D_i \end{pmatrix} &= \hat{R}_{II,i} \begin{pmatrix} A_{i+1} \\ B_{i+1} \end{pmatrix} \\
\Rightarrow \begin{pmatrix} C_i \\ D_i \end{pmatrix} &= \hat{R}_{I,i}^{-1}\hat{R}_{II,i} \begin{pmatrix} A_{i+1} \\ B_{i+1} \end{pmatrix}
\end{aligned} \tag{171}$$

from this follows the combination of all matrices of the entire stack of layers as:

$$\begin{pmatrix} A_1 \\ B_1 \end{pmatrix} = \underbrace{\hat{L}_{I,1}^{-1} \cdot \hat{L}_{II,1} \cdot \hat{R}_{I,1}^{-1} \cdot \hat{R}_{II,1} \cdot ... \hat{L}_{I,N}^{-1} \cdot \hat{L}_{II,N} \cdot \hat{R}_{I,N}^{-1} \cdot \hat{R}_{II,N}}_{\hat{\mathbf{M}}} \begin{pmatrix} A_{N+1} \\ B_{N+1} \end{pmatrix} = \hat{\mathbf{M}} \begin{pmatrix} A_{N+1} \\ B_{N+1} \end{pmatrix} \quad (172)$$

With:

$$\hat{\mathbf{M}} = \prod_{i=1}^{N} \hat{L}_{I,i}^{-1} \cdot \hat{L}_{II,i} \cdot \hat{R}_{I,i}^{-1} \cdot \hat{R}_{II,i} \quad (173)$$

With this last equation, we get again a $(2 \times 2)$-matrix and therefore two equations we can express as:

$$\begin{aligned} A_1 &= M_{11} A_{N+1} + M_{12} B_{N+1} \\ B_1 &= M_{21} A_{N+1} + M_{22} B_{N+1} \end{aligned} \quad (174)$$

As we know, we do not have an incoming wave in the barrier material from both sides, so we can delete the two amplitude coefficients $B_1 = A_{N+1} = 0$. If we express the coefficients $\alpha$ and $\kappa$ as a function of the energy states as in 147 for the single potential well, we can solve the equation:

$$M_{22}(E_n) = 0 \quad (175)$$

and get the energy states, which fits the description in [72] (P.53) for a double quantum well.
If we can describe the behavior of a whole series of potentials we should be able to calculate the shift in band-gap with much higher accuracy than with the single potential well since we take into account the influences of neighboring potentials.
We started building a program that should be able to fit the possible band-gap shift depending on the materials used 87 with the measurements data.

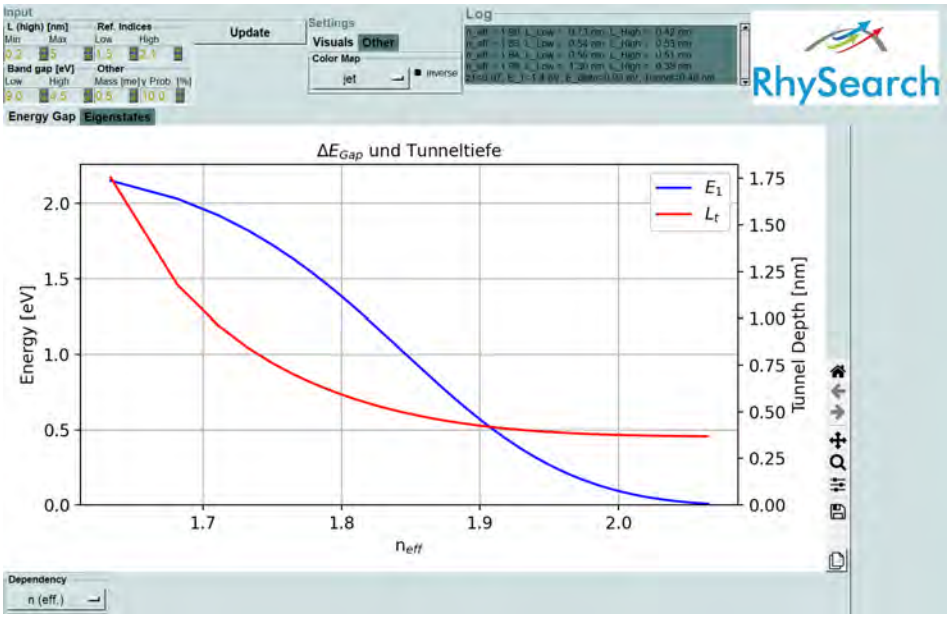


Figure 87: One can see with the blue line the shift in band-gap energy compared to the thickness of the well material. Calculated is $Ta_2O_5$ as well material in $SiO_2$ as barrier material. In red the tunnel depth is displayed it is explained further in subsection 6.2.1. The needed values like band gap of the two materials, thickness range and the factor for the effective electron mass of both materials are adjustable. The programming work was carried out by Daniel Schachtler.

The screenshot of the program shows the maximum achievable shift in the band gap for a given refractive index (blue) together with the expected tunnel depth (red).

### 10.3.1 Outlook

As good as that sounds, there are some problems that we did not consider at the beginning. The system becomes extremely unstable due to the multiplication of various exponential terms 88.

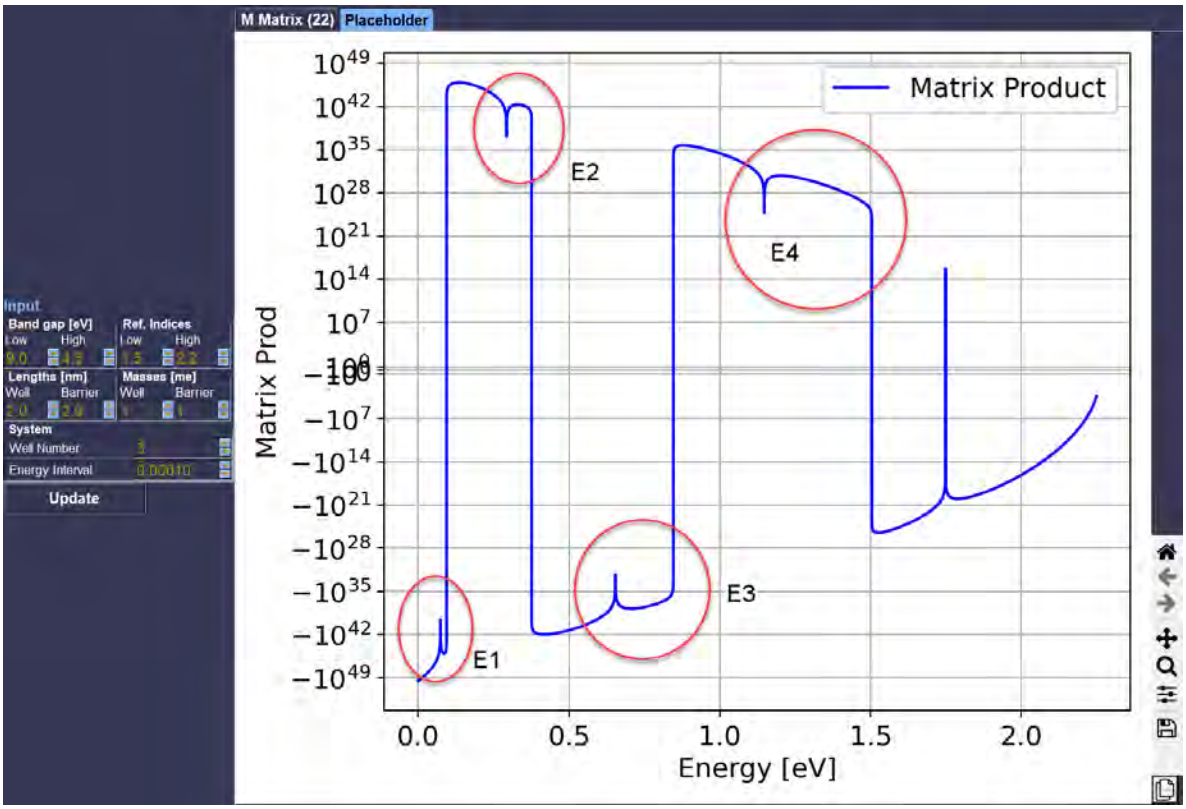


Figure 88: At every point the equation gets = 0 should be an energy state. Due to the interference of neighboring potentials, the individual states should form bands, which are only indicated with the red circles due to the lack of step size.

Due to the enormous amplitude of the calculations, it is hardly possible to perform the calculation with such a small increment that no states are forgotten with certainty. Furthermore, it is difficult to find errors in the program or approach, as each calculation takes a very long time. However, there are certainly mathematical tricks that can prevent this behavior. Since neither of us is familiar with numerical simulations, we will probably have to find an expert to help us find a better approach.
In general, it is very important to me to have a method that allows us to calculate the effect as accurately as possible from a physical point of view. Not only for practical reasons, but also because it is personally important to me to understand the physics behind the whole topic, and if you are able to calculate an effect reasonably accurate, you can at least assume that you are not completely wrong. The figure shows where the bands should be located. Due to the lack of resolution, the width is only indicated. With a smaller step size and significantly longer computing time, this distribution of states could be calculated. The problem that still needs to be solved is clearly visible here.

## 10.4 Ellipsometry

As mentioned, ellipsometry is a mighty measurement device but I rarely used it in the past and I took most of the needed characteristics of the coated materials from the photo spectrometer. However, I expect that ellipsometry offers a significant advantage, particularly when determining refractive indices and extinction coefficients, but also when it comes to birefringence.

### 10.4.1 Refractive Index and Extinction Coefficient

In the first publications [46] we can see that the refractive index is not really constant with the same mixture but with different thicknesses of QNL-pairs. This effect could be due to the model used in Optichar for the QNL.

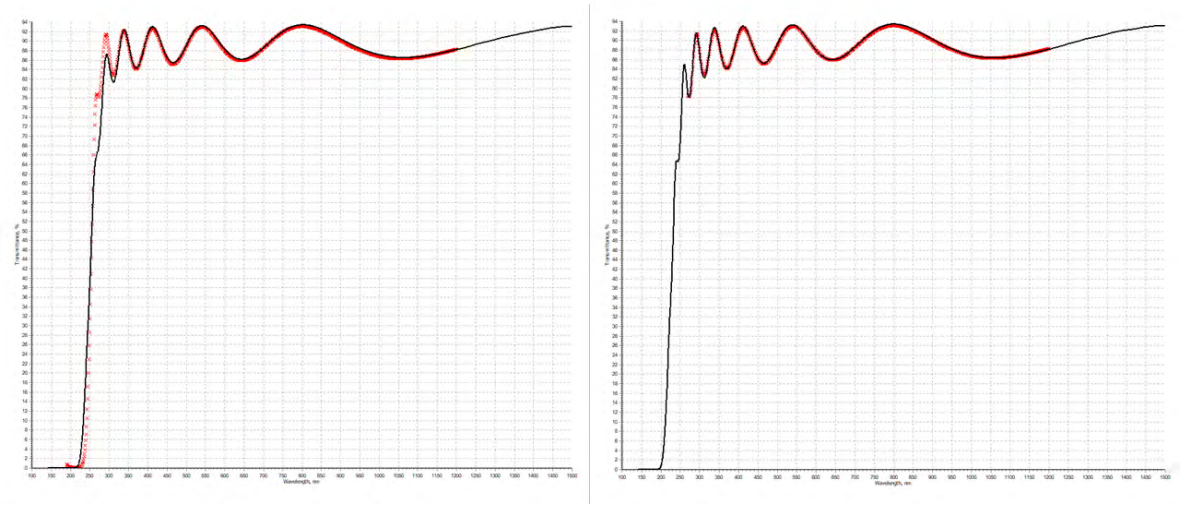

Figure 89: The figure shows the fitting of the refractive index close to the absorption edge using $Standard - UV - Vis$ model in Optichar. On the left side the model shows problems when the range down to 200 $nm$ is used. On the right side the absorption area is excluded and the refractive index seems to fit.

Fitting the refractive index with the used model over the absorption edge shows a high deviation in the specific range. excluding the said range shows a better fit but now leads to a high uncertainty for the extinction coefficient.
In Optilayer more complex models, such as Tauc-Lorentz are not available, thus it is not possible to fit the absorption region sufficient for refractive index and extinction coefficient. In the transparency region with low absorption, however, the refractive index and absorption coefficient can be determined reliably and are listed typically at a wavelength of 550nm The ellipsometry with a model suited for the close absorption range like Tauc-Lorentz will probably better fit the situation.
So we could use ellipsometry not just for a better refractive index calculation but also to accurately determine the extinction coefficient to be able to use it to calculate the absorption coefficient from it for the band-gap calculation mentioned in section 10.1.
For these reasons, we have firmly planned to carry out more measurements and experiments on the ellipsometer in the near future.

### 10.4.2 Birefringence

O. Stenzel et al. depicted why QNL should have birefringent behavior [73]. To prove the birefringent behavior and also its dependencies on different thickness combinations, ellipsometry would fit really well. We have already done measurements and have seen strong indications of birefringent behavior, but further measurements are needed to describe the effect correctly.

## 10.5 XRR

Because TEM measurements are really time consuming to perform, we are looking at how we can get different information from other sources without losing accuracy. A good opportunity would be XRR-measurements. As described in section 4.5, from the measurements many details can be extracted. We have already seen that we can use XRR-measurement as a quick measurement method to distinguish if we have a structure or just a homogeneous mixture. A problem that is more dominant with $aSi/SiO_2$ QNL than with $Ta_2O_5/SiO_2$.

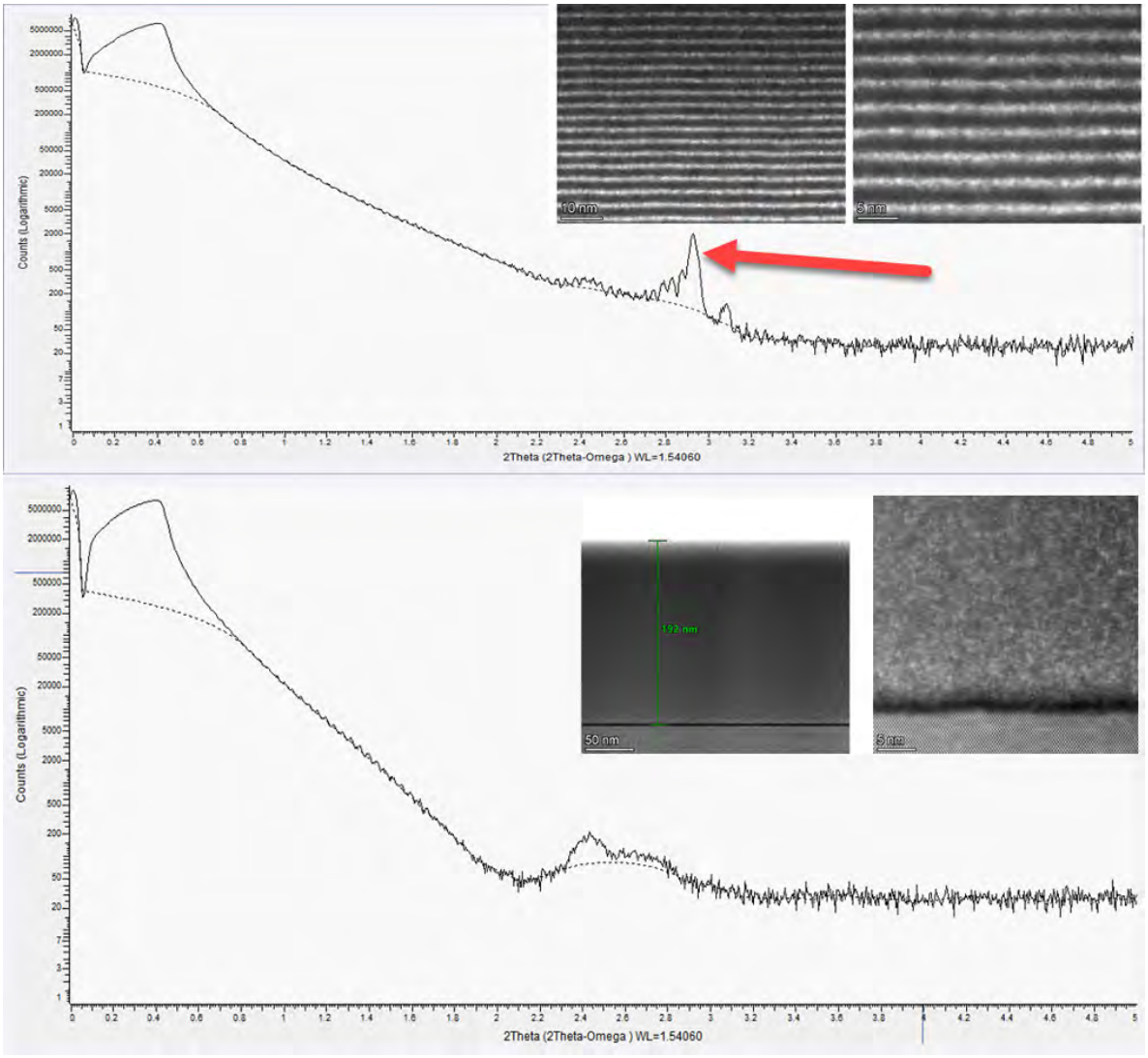


Figure 90: In the upper picture a $aSi/SiO_2$ QNL structure is shown compared with its XRR measurement. The peak indicates that it has a structure and is not just a homogeneous mixture like in the lower picture. In the TEM-measurement with the close picture the single Si-atoms from the wafer can be seen, indicating that the resolution is high enough to make sure it is not just because of the resolution

But, as explained in the section, the XRR measurements would hold much more information.For this reason, we plan to focus more on the use of the XRR measurement device and the interpretation of the measurement results in the near future.

## 10.6 Mechanical Properties

We coated a series of QNL where every sample had a thickness of $d_{tot} = 1\,\mu m$ while the thickness of the two materials was the same. So, the mixing ratio was $50:50$. The samples were coated with layer thicknesses of $d_{Ta_2O_5} = d_{SiO_2} = 0.5/1/2/5/10/20/100/167\,nm$.
Vivek Devulapalli and Xavier Maeder from EMPA carried out a series of nano indentation measurements on those samples to see if the hardness changes with thickness [74]. As we saw, the hardness did not increase with thinner lamination but decreased. Even if the experiment did not come out as expected, we expect from the results that the lamination increases the ductility.
Higher ductility could be interesting for higher abrasion resistance, and therefore we plan experiments on the nano scratch test device at RhySearch, indentation tests at EMPA, and simultaneously carry out abrasion tests at Evatec.

We coated a series of $Ta_2O_5/SiO_2$-QNL stacks, while each stack has the same total thickness of $d_{tot} = 1\,\mu m$ and all laminates have the same thickness ratio of $x : x$ while $x = 1, 2, 5, 20, 100\,nm$. In this way, all three partners can perform different mechanical tests on identical samples, enabling us to achieve the highest possible comparability.

## 10.7 Demonstrator

At RhySearch, we are looking for demonstrators who can explain the field of optical coatings to non-experts. Together with Christoph Sturzenegger, we came up with a plan in which we coat several substrates to have a set of hands-on demonstrators. It consists of two series of substrates, one series with anti reflective coatings and one without, to illustrate how a series of lenses in a camera would lower the quality if they would not be coated. The anti reflection coating is the one shown in figure 14.
In addition a beam splitter shows the separation of a blue and red mixed light source in a transmitting blue and reflecting red part.
We are still experimenting with possible coatings to show how optical coating works understandable but at the moment we are working on a $H\alpha$-filter. A Fabry-Perot interferometer with a wavelength at $656.3\,nm$. $H\alpha$ describes the first line of the Balmer series of hydrogen and the filter should allow, if pointed at the sun, to see only the light emitted by the $n_3 \rightarrow n_2$ transition of the hydrogen atom in the chromosphere of the sun [2] (P.107) also nice explanation on the website of a VDS- Fachgruppe Sonne in Berlin[7].
In the beginning, this seemed easy, but seems to be more complicated than expected.
First, if we point a telescope with a diameter of $20\,cm$ directly at the sun we get something around $40\,W$ into the aperture, which could damage the interior. This means that we designed a chirped mirror for the whole range from $300 - 1000\,nm$, which should roughly reflect $90\,\%$ of the power to reduce the risk of damaging the device. This filter is coated on a substrate $8"$ and placed in front of the telescope. Coating on such a high diameter always leads to problems with the uniformity of the coatings. After some tests the uniformity on $8"$ with $5\,mm$ edge exclusion was around $0.5\,\%$ and also for a chirped mirror the uniformity should not cause any major problems if its not too much off, for design reasons.

[7] https://www.vds-sonne.de/de/AG-H-alpha.php access on 24.10.2025

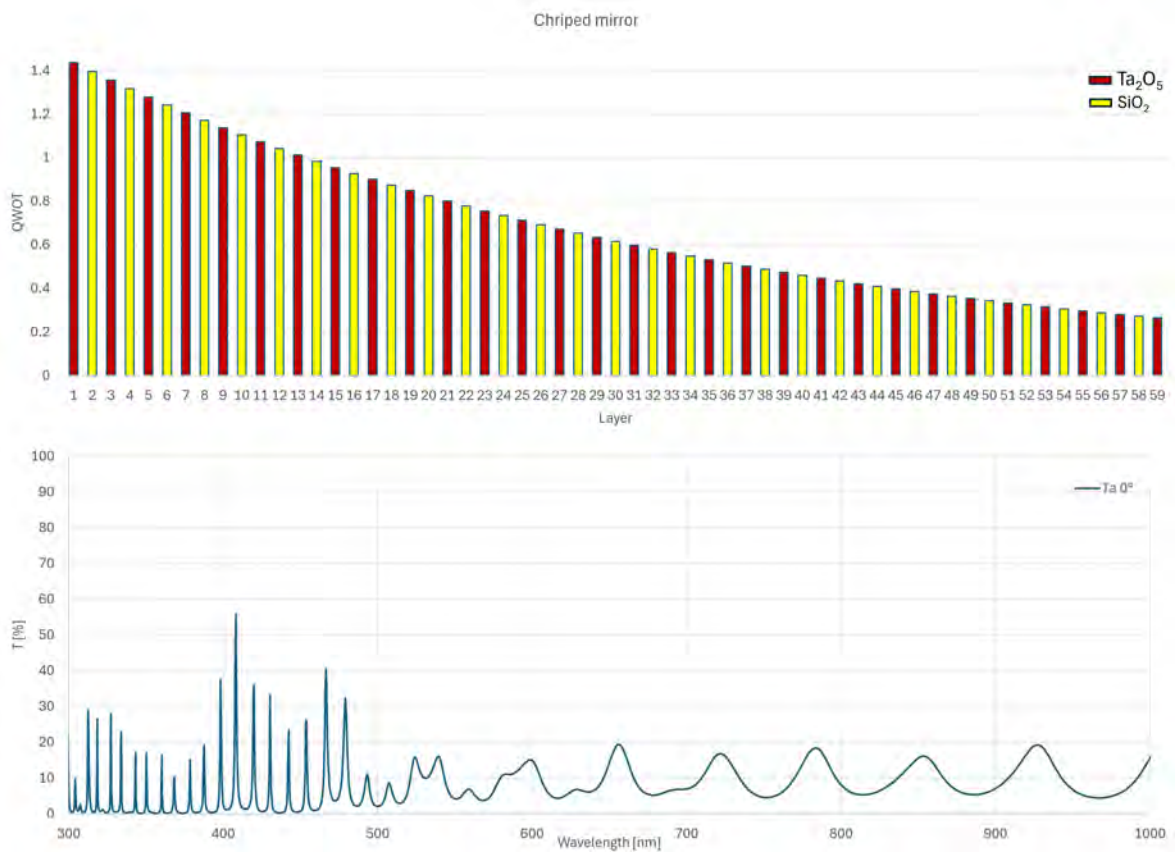


Figure 91: The picture shows the design and the transmission spectrum of the chirped mirror to reflect an average of 90 % of the sun intensity over the range from UV to NIR

In order not to roast our retinas with $UV$-radiations if we look at a $VIS$-dark spectrum, we need to make sure that the further design blocks not just the visible, but also the $UV$ range completely. So we decided to create a design with $aSi/SiO_2$ nanolaminates that shifts the absorption edge just below $600\,nm$. Together with $SiO_2$ a design similar to a mirror below the design wavelength reflects a part of the visible range where the Fabry-Pérot filter is too small to bypass until the absorption of the $\alpha Si/SiO_2$-QNL takes care of the rest.

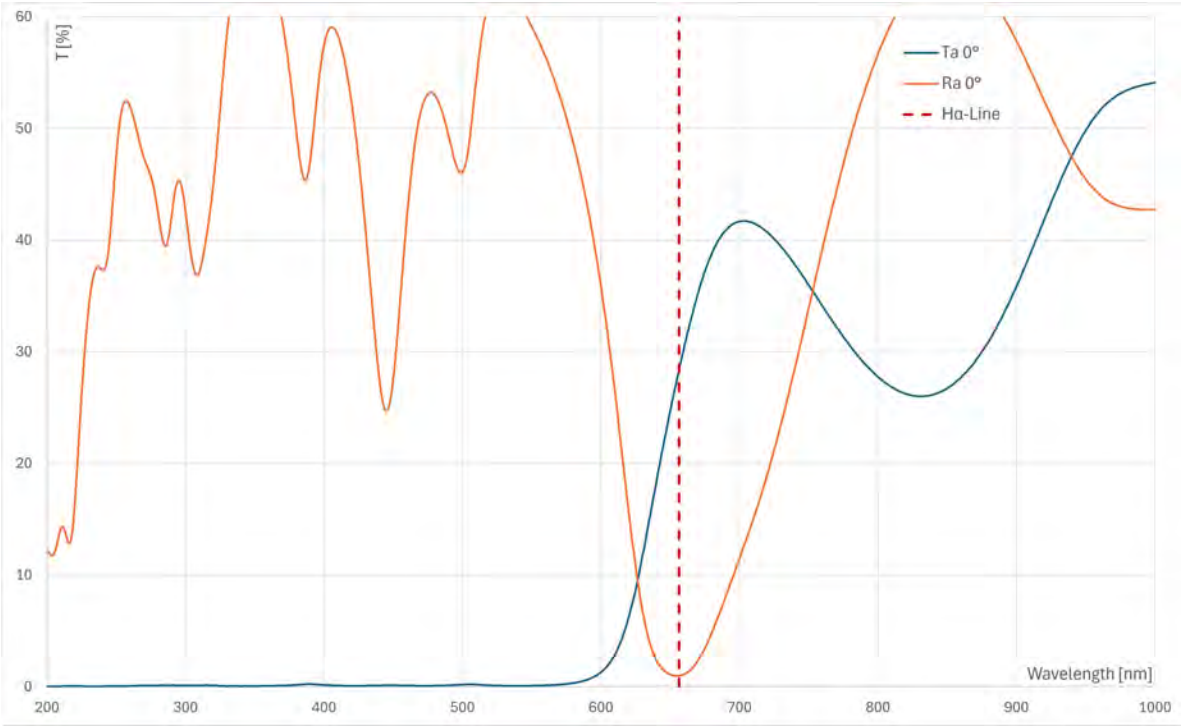


Figure 92: The figure shows the spectrum of the planned $UV - Vis$ blocker. The design consists of 18 layers of $\alpha Si/SiO_2$-QNL stacks and $SiO_2$ which shifts the absorption edge right below $600\,nm$. At the target wavelength of $656.28\,nm$ the reflection reaches a minimum. The designed reflection supplements the increasing absorption so that no light passes through below $\approx 600\,nm$.

In this way, we do not need to create a design that reflects all the incoming $UV$ light but only absorbs it. With the chirped mirror in front, this should not cause too many heating issues. Coated on both sides of the substrate 8" and placed in front of the telescope, it should be safe even if there are scratches or errors in the coating due to uniformity issues.
This now leaves the core part of the $H\alpha$-filter, the Fabry-Perot interferometer. It is not completely clear, but after some internet research, the band pass needs to have an FWHM of $0.1\,nm$, which is pretty challenging. We decided to design the filter some $nm$ above the design wavelength to be able to lower it by tilting the substrate. This way we don't have to hit it directly. The coated design should have an FWHM thickness of $x\,nm$, but I am not sure if a single cavity has a high enough resolution. With several cavities it would be possible to straighten the peak and make it more a rectangle peak, but then it would be much more difficult to position the cavities with the spacer with sufficient accuracy.

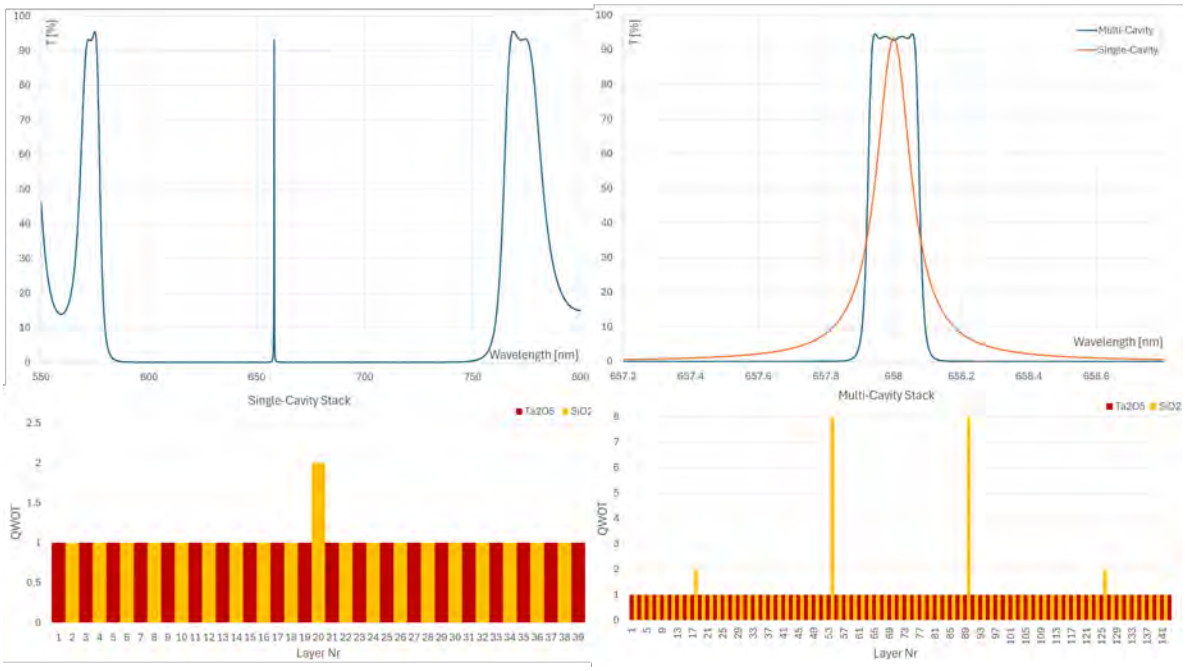


Figure 93: The interferometer design on the left side is simple and already coated. On the right side the designs consists of more cavities and is able to change the shape of the filter.

The simple one-cavity filter is already coated, but because of the extremely thin filter, it is not possible to measure if it worked or not, but it needs to be tested with the rest of the setup.
As this is a project we are working on on the side, it takes some time to finish.

# 11 Conclusion

At the beginning of this thesis, the general foundations of optics were reviewed. Starting from Maxwell's equations, the most important optical quantities were introduced and explained, providing the basis for understanding all subsequent chapters. This was followed by a discussion of the most commonly used characterization methods, including their underlying models and the limitations associated with each approach.

In the next step, the principle of magnetron sputtering was explained, and the specific sputtering system used in this work, the Clusterline 200 BPM was described in detail together with additional subsystems as optical monitoring (GSM) or plasma emission monitoring (PEM).

However, the main focus of the thesis lies on quantized nanolaminates (QNL). For this topic, an additional theory chapter was included, in which it is explained in detail how QNL can be understood and where the underlying effects come from. Furthermore, it is shown why the chosen coating system is particularly well suited for the fabrication of such QNL structures.

The experimental part begins with a series of QNL coatings with different individual bi-layer thicknesses in order to demonstrate their effect on the absorption edge. This is followed by an extended set of different QNL stacks, showing that the refractive index of the effective mixed material can be tuned continuously between the values of the two used materials, while at the same time the band gap can be shifted towards shorter wavelengths.

The main part of the experimental chapter is devoted to the participation in the Laser Damage Competition 2024 in San Ramon (CA). For this purpose, various QNL stacks were fabricated and characterized using a wide range of measurement techniques. The resulting insights were then used to design optimized Bragg mirrors with an increased laser damage threshold. Subsequently, these designs were coated and the corresponding samples were again measured and analyzed. In the end, four coatings were selected for participation in the competition, and the results obtained there were evaluated and put into context.

Building on this, the lessons learned from the competition were used to refine the designs once more and to produce and characterize a new set of coatings, demonstrating that the resistance to damage can be further improved. A second set of results was also presented and the corresponding measurements were discussed and compared with the previous findings.

In order to relate the work back to the actual project, a number of open, pending, and particularly interesting points were carried out and commented on, including topics that are currently under investigation or are expected to be addressed in the future. Finally, my scientific contributions are summarized. The peer reviewed papers to which I contributed were listed and briefly described, as well as the contributions made to each publication.

Together, this thesis shows that quantized nanolaminates can be reliably fabricated by the used magnetron sputtering system and that their optical properties can be specifically tuned. The demonstrated adjustability of refractive index and band gap, together with improved laser damage resistance in optimized mirror designs, underlines the potential of QNL-based coatings for demanding optical applications. At the same time, the identified open questions and future directions provide a solid basis for further advancing both the fundamental understanding and the practical implementation of QNL structures in high performance optical designs.

# 12 Scientific contribution

During the two projects, four peer reviewed papers have been written in which I have contributed a part. The peer reviewed papers are listed below, each with a short explanation. Afterwards, the patent and the conference contributions are listed, each with a short explanation.
The peer reviewed papers mentioned are attached, each with a previous summary and an explanation about my contribution.

# Peer Review Paper

[Peer1] S. Schwyn Thöny, **M. Bärtschi**, M. Batzer, M. Baselgia, S. Waldner, M. Steinecke, H. Badorreck, A. Wienke, and M. Jupé. Magnetron sputter deposition of ta2o5-sio2 quantized nanolaminates. *Opt. Express*, 31(10):15825–15835, May 2023.
→ *The paper was the first peer reviewed paper we published about the production of QNL. It describes the experimental setup and the production to coat QNL based on* $Ta_2O_5/SiO_2$*. Further it explains the theoretical background and shows the first proof of the effect we could measure with coated QNL stacks. It also shows in the end AR as well as HR coatings using QNL and compares them with classical* $Ta_2O_5 - SiO_2$ *designs.*

[Peer2] **Bärtschi, Manuel**, Stephan Waldner, Silvia Schwyn Thöny, Xavier Maeder, Fabian Steger, Thomas Frei, and Vivek Devulapalli. Uv coatings using ta2o5-sio2 quantized nanolaminates. *Journal of the European Optical Society-Rapid Publications*, 21(1):24, 2025.
→ *This paper is a continuation of the previous one on* $Ta_2O_5/SiO_2$*-QNL. It explains the production of QNLs and describes them in general terms. It then presents the first TEM measurements carried out at EMPA and shows that the laminates are of very high quality in terms of their uniformity. It also shows that the calculations for determining thickness are highly accurate. Finally, it shows two designs, again an anti reflective design at* $266nm$*, clearly demonstrating that this is no longer possible with a classic design using* $Ta_2O_5$*. Finally, a short-pass filter with an edge in the range of* $330nm$ *is shown, which has a larger transparent range in the UV range than its counterpart made of* $Ta_2O_5$ *instead of QNL.*

[Peer3] Silvia Schwyn Thöny, **Bärtschi, Manuel**, Marietta Batzer, Manuel Baselgia, Raphael Gmünder, Amit Sharma, Tijmen Vermeij, Xavier Maeder, and Stephan Waldner. Magnetron sputter deposition of amorphous silicon–sio2 quantized nanolaminates. *Advanced Photonics Research*, 5(12):2400057, 2024.
→ *The paper shows the first* $\alpha Si/SiO_2$*-QNL stacks coated with the tool setup where we use the etching source instead of a second sputter source to coat the second barrier materials. TEM images clearly show that it is possible to produce both aSi and SiO2 as separate layers in the same chamber. It was also demonstrated that the refractive index can be varied, thereby shifting the absorption edge with the QNL into the VIS range. The loss of refractive indices and further calculations and evaluations are presented and at the end, a practical example with a mirror is used to compare this with* $TiO_2$*, which has a significantly narrower blocking range.*

[Peer4] Vivek Devulapalli, Fedor F. Klimashin, **Manuel Bärtschi**, Stephan Waldner, Silvia Schwyn Thöny, Johann Michler, and Xavier Maeder. Interface mediated softening and deformation mechanics in amorphous/amorphous nanolaminates. *Not Published yet - Arxiv*, 2025-2026.
→ *EMPA did a series of nano indentation tests in several different* $Ta_2O_5/SiO_2$*-QNL with all the same ratio of materials but different pair thicknesses.Contrary to expectations, the thinner QNLs did not prove to be harder, but rather softer. However, it was also found that ductility had increased, indicating higher deformation resistance and abrasion resistance. The paper has not yet been published, but is currently in progress. .*

# Patents

[Pat1] Silvia Schwyn Thöny, **Manuel Ilias Bärtschi**, Manuel Baselgia, and Marietta Christina Batzer. Process to deposit quantized nano layers by magnetron sputtering - wo2024056313a1.
→ *The patent covers the production of QNL using a magnetron sputtering system and rotating substrate table, both in the cosputtering process and with a single source, followed by post-oxidation with an ion etching source.*

# Conference Contributions

[Conf1] **Bärtschi, Manuel**, Schachtler, Daniel, Schwyn Thöny, Silvia, Südmeyer, Thomas, and Botha, Roelene. Investigation of the influence of plasma source power on the properties of magnetron sputtered ta2o5 thin films. *EPJ Web Conf.*, 255:03005, 2021.
→ ***Abstract and Presentation of a Poster*** *at EOSAM 2021 in Rome. The Topic was about the shift of refractive index in Ta2O5 coated layers due to the ion energy of an additional Argon plasma source which effects density changes in the material (my first participation and contribution at a scientific conference).*

[Conf2] Silvia Schwyn Thoeny, Daniel Schachtler, Stephan Waldner, Thomas Frei, and **Manuel Baertschi**. Pre-production simulation of optical monitoring combining monochromatic and broadband monitoring strategies. In Michel Lequime and Detlev Ristau, editors, *Advances in Optical Thin Films VII*, volume 11872, page 118720O. International Society for Optics and Photonics, SPIE, 28.09.2021.
→ ***Presentation and Proceedings*** *by Silvia Schwyn Thöny about Magnissimo, a Software to simulate errors, noise, shifts and other influences in the optical monitoring system.*

[Conf3] S. Schwyn Thöny, **M. Bärtschi**, St. Waldner, and Th. Frei. Improving particle performance in plasma enhanced magnetron sputtering. In *Optical Interference Coatings Conference (OIC) 2022*, page WC.4. Optica Publishing Group, 2022.
→ ***Abstract, Presentation and Poster*** *by Silvia Schwyn Thöny about reducing particle formation in our magnetron sputter device.*

[Conf4] Silvia Schwyn Thoeny, **Manuel Bärtschi**, Marietta Batzer, Manuel Baselgia, Raphael Gmünder, and Stephan Waldner. Quantized nanolaminates of Ta2O5-SiO2 and amorphous silicon-SiO2 manufactured by magnetron sputter deposition. In Christopher Wren Carr, Detlev Ristau, Carmen S. Menoni, and Michael D. Thomas, editors, *Laser-Induced Damage in Optical Materials 2023*, volume PC12726, page PC127260N. International Society for Optics and Photonics, SPIE, 24.11.2023.
→ ***Presentation*** *by Silvia Schwyn Thöny about manufacturing of QNL.*

[Conf5] **Manuel Bärtschi** and Silvia Schwyn Thöny. Magnetron sputtering of Quantized Nanolaminates, Optical Coatings for Laser Applications OCLA 29.03.2023.
→ ***Presentation*** *about the newest results of QNL manufacturing and analysis.*

[Conf6] **Bärtschi, Manuel**, Waldner, Stephan, Thöny, Silvia Schwyn, Maeder, Xavier, Steger, Fabian, Frei, Thomas, and Devulapalli, Vivek. Uv coatings using ta2o5-sio2 quantized nanolaminates. *J. Eur. Opt. Society-Rapid Publ.*, 21(1):24, 2025.
→ ***Abstract and Presentation*** *about Coatings using $Ta_2O_5/SiO_2$-QNL in the UV range. .*

[Conf7] **Manuel Baertschi**, Stephan Waldner, Fabian Steger, Thomas Frei, Silvia Schwyn Thoeny, Xavier Maeder, Daniel Schachtler, and Christoph Sturzenegger. Process development of Ta2O5-SiO2 quantized nanolaminates for the use of complex optical filter systems. In Christopher Wren Carr, Detlev Ristau, Carmen S. Menoni, and Michael D. Thomas, editors, *Laser-Induced Damage in Optical Materials 2024*, volume 13190, page 1319006. International Society for Optics and Photonics, SPIE, 2024.
→ ***Abstract, Presentation and Proceedings*** *about process optimization to coat Mirrors to participate at the Laser Damage competition.*

[Conf8] Stephan Waldner, **Manuel Baertschi**, Silvia Schwyn Thoeny, Fabian Steger, Daniel Schachtler, Christoph Sturzenegger, and Xavier Maeder. Design, manufacturing, and characterization of multilayer mirrors based on magnetron sputtered quantized nanolaminates. In Christopher Wren Carr, Detlev Ristau, Carmen S. Menoni, and Michael D. Thomas, editors, *Laser-Induced Damage in Optical Materials 2024*, volume 13190, page 131900O. International Society for Optics and Photonics, SPIE, 2024.
→ ***Abstract, Poster and Proceedings*** *by Stephan Waldner about design optimization to coat mirrors to participate at the Laser Damage competition.*

[Conf9] Stephan Waldner, **Manuel Bärtschi**, Silvia Schwyn Thoeny, Fabian Steger, Daniel Schachtler, Christoph Sturzenegger, Thomas Frei, and Xavier Maeder. Efficient manufacturing of quantized nanolaminate multilayer coatings. In *Optica OIC — Optical Interference Coatings Conference 2025*, page WE.3. Optica Publishing Group, 2025.
→ ***Abstract, Presentation and Poster*** *by Stephan Waldner about the manufacturing of QNL designs for fs-LIDT optimization.*

[Conf10] Silvia Schwyn Thoeny, Stephan Waldner, **Manuel Bärtschi**, and Thomas Frei. Antireflection coatings using nanolaminate layers with intermediate refractive index. In *Optica OIC — Optical Interference Coatings Conference 2025*, page WE.7. Optica Publishing Group, 2025.
→ ***Abstract, Presentation and Poster*** *by Silvia Schwyn Thöny about the use of QNL to make designs less sensitive by inserting layers with intermediate refractive indices into anti refelctive coatings.*

## 12.1 Magnetron Sputter deposition of Ta2O5-SiO2 quantized Nanolaminates

The paper "Magnetron sputter deposition of $Ta_2O_5 - SiO_2$ quantized nanolaminates" [46] was the first peer reviewed paper we wrote on the topic of nanolaminates. Before that, several experiments by other research groups have proven the concept of quantized nanolaminates but mostly with IBS or ALD [75][45], [44].
With our setup of the rotating substrate table combined with the co-sputtering technique, we were able to coat the structured laminates for the first time with such a high rate that it became economically viable.
Although the theory behind has already been discussed and explained by other research groups, we revisited the issue. We explain first how to calculate the effective refractive index of a laminate stack [48] from photospectrometric measurements, followed by the theoretical background on how the quantization effect can be explained[42], [50].
Afterwards, it is explained how the specific design of the tool can be used to coat the layered system without interruption of the process, leading to a high deposition rate, while the process can be monitored in situ with broad band optical monitoring [40],[41].
We coated a series of QNL with the same material ratio but different laminate thicknesses and were able to show a shift in the absorption edge while the refractive index at $550\,nm$ remained constant. This proved for us the first time that we are capable with our magnetron sputter setup of producing the quantization effects described theoretically [76],[77].
We varied the process settings and coated for different refractive indices from $n \approx 1.55 - 1.9$ series of QNL stacks which showed, depending on the well thickness, a shift in the optical band gap while the refractive index determined the possible achievable maximum.
One of the settings with a high band gap shift was later used to coat a 2 layer anti reflection design on a fused silica substrate. The design wavelength was $280\,nm$ so below the absorption edge of $Ta_2O_5$.
Afterwards a 30 layer mirror was designed and coated. The mirror showed a much smaller reflecting range than the classic comparing mirror made from $Ta_2O_5$ and $SiO_2$ which is not surprising, but the transmission part of the coating indicated a much wider usable range in UV.

### Contribution

My contribution was to develop stable processes to coat the variety of QNL stacks and series, as well as optimization of the standard materials and writing recipes for the multilayer coatings. Furthermore, I carried out a majority of the photo spectrometry measurement. I also participated in the evaluations, interpretations and discussions.

Research Article Vol. 31, No. 10 / 8 May 2023 / Optics Express 15825
Optics EXPRESS

# Magnetron sputter deposition of $Ta_2O_5$-$SiO_2$ quantized nanolaminates

S. Schwyn Thöny,[1,*] M. Bärtschi,[2] M. Batzer,[1] M. Baselgia,[1] S. Waldner,[1] M. Steinecke,[3] H. Badorreck,[3,4] A. Wienke,[3,4] and M. Jupé[3,4]

[1]Evatec AG, Hauptstrasse 1a, 9477 Trübbach, Switzerland
[2]RhySearch, Werdenbergstrasse 4, 9471 Buchs, Switzerland
[3]Laser Zentrum Hannover e.V., Optical Components Department, Holleritallee 8, 30419 Hannover, Germany
[4]Cluster of Excellence PhoenixD (Photonics, Optics, and Engineering innovation across Disciplines), Leibniz University Hannover, Welfengarten 1A, 30167 Hannover, Germany
*silvia.schwyn-thoeny@evatecnet.com

**Abstract:** Quantized nanolaminates are a type of optical metamaterials, which were discovered only recently. Their feasibility was demonstrated by atomic layer deposition and ion beam sputtering so far. In this paper, we will report on the successful magnetron sputter deposition of quantized nanolaminates based on $Ta_2O_5$-$SiO_2$. We will describe the deposition process, show results and material characterization of films deposited in a very wide parameter range. Furthermore, we will show how quantized nanolaminates deposited by magnetron sputtering were used in optical interference coatings such as antireflection and mirror coatings.



## 1. Introduction

Optical coatings are a basic requirement for the efficient function of optical components. Almost all optical components derive a large part of their spectral properties from the quality of the interference filters applied to the optics. Even though the manufacturing concepts and the complexity of the designs have increased in recent years, most coatings are still based on established oxide materials, which are combined in a layer system to form an interference filter. As the demands on the filters continue to increase, there is also a growing need for alternative materials with better performance. Metamaterials are increasingly being considered, in which the functionality is not based exclusively on the material properties themselves, but new physical properties are achieved through the artificially engineered structural modification of the materials.

Quantized nanolaminates (QNL), which were first proposed in 2017 [1,2] belong to this new class of engineered materials. In QNLs, sub-nanometer thin dielectric layers of high and low refractive index materials are stacked. The limited structure size leads to quantization effects, which enable to shift not only the material's refractive index but also the band gap of the material independent of each other. This is in contrast to classical dielectric materials, in which the refractive index and the energy of the absorption edge are fundamentally linked [3].

Previous work aiming at decoupling refractive index and band gap focused on self-organizing structures, which acquire their functionality through localized or unlocalized porous structures and reduce the refractive index [4]. One approach for their preparation is glancing angle deposition [5–9], in which a columnar film structure is formed, which reduces the effective refractive index. Interference effects will occur between bulk-like layers and layers with columnar structure of one and the same material. Another approach uses self-organizing structures achieved by ion etching [10–13], which also reduces the effective refractive index. The reduction of the index is especially beneficial in the case of $SiO_2$, since lower indices can be achieved than available by standard materials opening up a wide field of applications.

#487892 https://doi.org/10.1364/OE.487892
Journal © 2023 Received 16 Feb 2023; revised 3 Apr 2023; accepted 4 Apr 2023; published 26 Apr 2023

Optics EXPRESS

In the above approaches, only the optical property of refractive index is manipulated, whereas the energy gap defined by electronic properties remains unchanged. In this paper, however, structures will be shown, which selectively couple back to the electronic properties of the material. Similar approaches are currently only available in multi quantum well (MQW) structures in optoelectronics where the optical emission wavelength and power is adjusted by the state densities of the electrons via confinement. Even though the MQW concept is based on crystalline structures, Willemsen et al. [2,14] have shown that the crystalline structure is by no means the precondition for the occurrence of quantum effects and that they can also be observed in amorphous dielectric materials.

In the practical application the shift of the energy gap in QNL can be adjusted by the physical thickness of the high index material, whereas the thickness ratio of the high and low index materials determines the effective refractive index of the QNL. Thus, a two-dimensional parameter field is obtained in which the energy gap and the refractive index can be adjusted separately from each other in a defined range.

The objective for the application of such quantizing metamaterials is to extend the useful range of specific materials below the band gap of the high index material of the QNL. As an example, in the UV range the band gap of $Ta_2O_5$ can be pushed towards shorter wavelengths and so provide an alternative to the use of $HfO_2$. This is desirable since hafnium targets are expensive and because $HfO_2$ tends to form polycrystalline grain boundaries while growing, which can cause losses by scattering of light.

The QNL effect has been demonstrated experimentally for atomic layer deposition (ALD) and ion beam sputtering (IBS) [15] coatings, but not until now for magnetron sputtering. Although both of former methods lead to good results, they do have drawbacks with regards to volume production. ALD has low growth rates since only one atomic layer is deposited per coating cycle, whereas, in IBS a zone target needs to be mechanically translated from one material of the nanolaminate to the other also limiting the deposition rate.

In contrast, the turntable configuration of the Evatec Clusterline 200BPM magnetron sputter system is ideally suited to the deposition of QNL, since both materials can be deposited in one table rotation. We will show in this paper how the process is implemented for the material combination $Ta_2O_5$ and $SiO_2$ in this magnetron sputter deposition system and we will demonstrate that the quantizing effect is observed as predicted. Furthermore, we will take this result and show that an antireflection coating at 280 nm and a mirror at 355 nm can be manufactured consisting of the $Ta_2O_5$-$SiO_2$ QNL and $SiO_2$.

## 2. Theory

To understand why QNL should be used, one can consider the general classical mode of action for interference filters. Optical interference coatings such as anti-reflection, mirror or filter coatings are based on stacks of materials with at least two different refractive indices, $n$ in alternating layers. The resulting effect of the interference is correlated with the difference in refractive index between the materials. As a consequence, layer stacks with high refractive index difference require a smaller number of individual layers in the optical design and thus less overall thickness than stacks with a low difference in index. In addition to the refractive index the materials have to fulfill another requirement, namely a high transparency with negligible losses in the wavelength range of interest. The absorption of an optical material is mainly determined by its band gap energy, which determines the upper limit for the energy of transmitted photons.

However, in dielectric materials the refractive index and the energy of the absorption gap are fundamentally linked [3]. Materials with high refractive index have their absorption gap at a low photon energy while low refractive index materials have the absorption edge at high photon energies.

Optics EXPRESS

Figure 1 shows a schematic diagram of the periodic structure of a quantized nanolaminate. The theory of the quantized nanolaminates is based on the combination of the quantum mechanical and the classical approach. A canonic solution is described in [16,17]. The optical properties of the QNL can be calculated by the effective medium theory. Actually, the QNL are defined by the upper Wiener limit [18,19]. The effective refractive index of the resulting meta-material $n_{eff}$ is defined by the ratio of high and low refracting materials and can be calculated by applying the effective medium theory. $f$ denotes the volume ratio between high and low refracting materials [20]:

$$n_{eff}^2(\lambda) = f n_{high}^2(\lambda) + (1-f) n_{low}^2(\lambda) \tag{1}$$

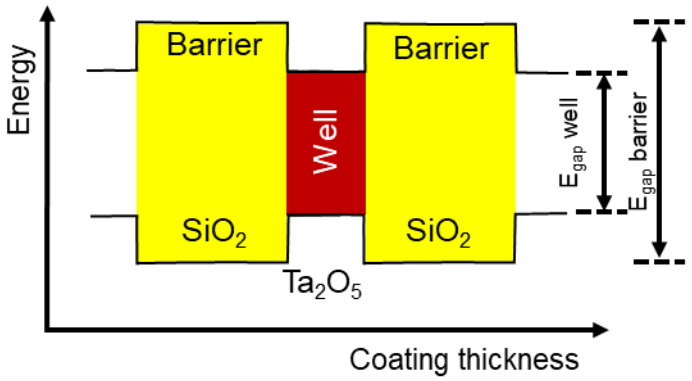


**Fig. 1.** Periodic structure of high and low band gap areas, which limit the electron mobility.

The thickness of the individual high and low refractive index layers in the QNL can be calculated by multiplying the total thickness per rotation with the volume ratio $f$ of the high index material, respectively (*1-f*) for the low index material. This simple formula shows that the refractive index of the QNL metamaterial is always between the values of the high and low refractive index materials and defines the physical refractive index limits of the metamaterial. The actual gain of the material comes from the displacement of the band gap. First of all, a brief look at the electronic material properties is necessary. As already mentioned, optical coatings mostly produce amorphous or polycrystalline materials whose band structure is not clearly defined. Thus, the band gap itself can be regarded as a depletion zone of states and the densities between bound and free states are so low that they can be neglected [21]. Thus, the potential wall, which is necessary for the quantization is clearly defined. Figure 2(a) shows the band structure of amorphous $Ta_2O_5$, according to the density functional theory (DFT) calculation using hybrid functionals by MedeA/VASP [22,23]. Obviously, the gaps are clearly defined, but there are no bands for the bound and the quasi-free states. Actually, the gap is covered by ensembles of states which are related to the random long-distance order of the atoms.

The situation is more complicated with respect to the mobility of the quasi-free electrons. In crystals the mobility is connected to the curvature of the bands. This is not applicable to amorphous solids; therefore, the effective mass of holes and electrons have to be fitted.

Independent of the band structure the mobility of the carrier can be limited by an electronic confinement. In the case of the QNLs, a periodic structure of high and low band gap materials (blue solid line) is generated in the growth direction. Figure 2(b) shows the probability of electronic states as a green solid line for an example of a QNL consisting of 10 quantum wells. The probability is concentrated towards the center of the QNL in the high index material $Ta_2O_5$. With respect to the correlation between band gap and refractive index, the low index material will act as a barrier whereas the high index material acts as the quantum well, as shown in Fig. 1. As

Optics EXPRESS

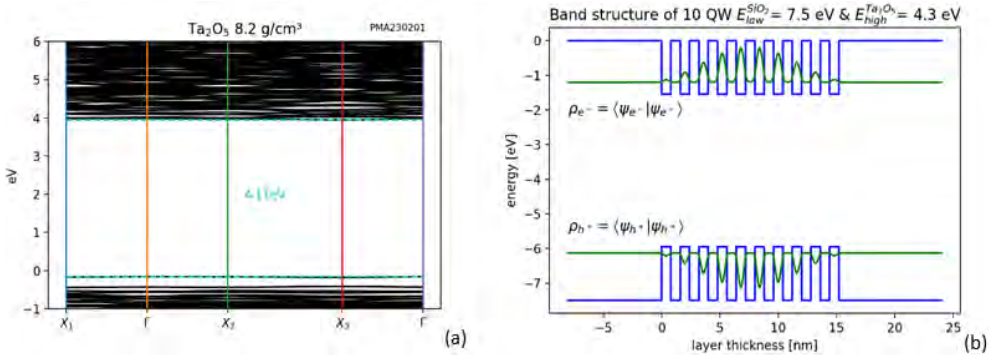


**Fig. 2.** Electronic structure of amorphous $Ta_2O_5$ with a gap of $E_{Gap}^{Ta_2O_5} = 4.11\ eV$ (a) and band structure of QNL with 10 quantum wells of $SiO_2$ and $Ta_2O_5$ (b).

already indicated, the reduction of the layer thickness leads to new states which can be calculated by solving the Schrödinger equation. A closed analytic solution can be given only for a few potentials, like the infinite quantum well or the parabolic form [16]. For this work we assumed finite quantum wells and a periodic sequence. The energy levels in the singular quantum well can be obtained numerically via the algorithms already quoted [2,15]. However, this solution neglects the interaction between the quantum wells, so for this work a matrix solution of the discretized Schrödinger equation was used, adapted to the boundary conditions. For the solution we refer here to the literature [17].

Thus, the thickness of the quantum well will determine the shift in band gap, whereas the thickness ratio of high to low band gap material will determine the refractive index. Thus, the novel concept of so-called quantizing nanolaminates (QNLs) allows for independent adjustment of the optical band gap and refractive index. To achieve the desired quantization, the thickness of each quantum well layer should be smaller than 2 nm, with barrier thickness in the same range. As an example, for a thickness of 2 nm the offset is 0.08 eV, which is very small compared to about 4.1 eV of band gap energy and represents a shift of only 5 nm. To achieve a shift, which is of practical use, the quantum well should be chosen much smaller, since the energetic offset is proportional to $d_{well}^{-2}$ in first order. Since this is a simple potential consideration, even non-closed atomic layers can lead to a suitable periodic potential. The thickness of the barrier influences the refractive index of the QNL (see Eq. (1)). On the other hand, the simulations show that a reduction of the barrier layer thickness below 0.5 nm leads to significant tunneling and thus the energy levels decrease and the blue shift is reduced. The matrix solution offers a flexible possibility to handle different potential curves and the numerical solution does not depend on a periodicity of the potential, as it is necessary for the Bloch solution. However, such potential adjustments are not part of the investigations presented here.

## 3. Experimental

The deposition system used for this development was the *Evatec Clusterline 200 BPM* magnetron sputter deposition system, which was discussed in detail in [24–26]. As shown in Fig. 3(a), the system has a turntable and uses a sputter down configuration with a maximum of four magnetron sputter sources (2). For the deposition of $Ta_2O_5$ - $SiO_2$ QNL two sputter sources equipped with a silicon and tantalum target respectively were powered simultaneously. The plasma source (3) seen in the foreground is used in standard deposition to influence layer properties such as stress or surface roughness. In the deposition of QNL the plasma source was run optionally since it

Optics EXPRESS

enabled operation of the two sources in an even wider parameter range. This tool configuration is shown schematically in Fig. 3(b).

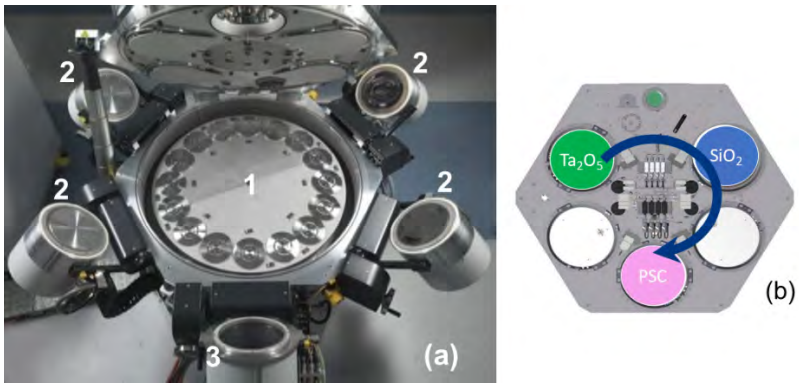


**Fig. 3.** (a): Open Evatec BPME magnetron sputter system: turn table (1), sputter sources (2), plasma source (PSC) (3) in maintenance position. (b) Schematic of sputter process for the QNL layers of $Ta_2O_5$ - $SiO_2$.

This deposition system has a capacity of 15 substrates of diameter 200 mm. Substrate loading is executed automatically through a load-lock. Oxides are deposited reactively in pulsed DC mode and use plasma emission monitoring (PEM) to exploit the hysteresis effects and assure full oxidation at a high deposition rate. It is also equipped with broad band and monochromatic optical monitoring [27].

The turntable configuration is perfectly suited for the deposition of QNL. With the continuous table rotation substrates pass repeatedly beneath the active tantalum and silicon sources, where sequentially a thin layer of $SiO_2$ and $Ta_2O_5$ is deposited with each rotation. The total thickness deposited in one turn is determined by the rotation speed of the table, a parameter which can easily be varied in a wide range. The thickness ratio of the well and barrier materials is determined by sputter power of the two sources and the related deposition rate. Further deposition parameters, which influence the deposition rate and material properties are the gas flows of argon and oxygen and the PEM set-point. Deposition rates for QNL layers tend to be higher than those for single oxides since they are deposited from two active sources.

The samples were deposited on double side polished fused silica samples. These were characterized by spectrophotometry in transmission and reflection both at an angle of 8° on the exact same spot on the sample by using a *PhotonRT* photospectrometer by *EssentOptics*.

The effective refractive index $n$ and the extinction coefficient k in the transparent range of the coating were determined using *OptiChar* by *Optilayer*. The models used were *normal dispersion* for $n$ and *UV-Vis* mode for the extinction coefficient $k$. This evaluation also allows us to determine the physical thickness $d$ of the metamaterial.

The effective refractive index $n_{eff}$ is derived from the spectral measurements in T and R as detailed above. The refractive indices of $n_{high}$ and $n_{low}$ are derived from $Ta_2O_5$ and $SiO_2$ single layers. The values used were: $Ta_2O_5$ $n_{high} = 2.168$ and $SiO_2$ $n_{low} = 1.474$, both indices relate to a wavelength of 500 nm. Formula (1) then allows us to calculate the volume ratio $f$ of the two materials.

The thickness per table pass can be calculated by dividing the physical thickness d of the metamaterial by the number of table passes in the deposition run. The optical band gap was determined using the Tauc-plot method [28].

Optics EXPRESS

## 4. Results

### 4.1. Quantum nanolaminate layers of $Ta_2O_5$-$SiO_2$

In a first experiment, the Si and Ta sources were run at 6 and 5 kW respectively, however with a PEM setting for $Ta_2O_5$ which resulted in a relatively low deposition rate. The table speed was varied from 3 to 15 seconds per pass, which means that the thickness ratio of high to low layers stayed constant, but the individual layer thickness increased with the slower table speed. The well thickness, i.e. thickness of $Ta_2O_5$ was determined to be in the range of 0.2-1 nm. According to the theory discussed in section 2, it was expected that the absorption edge would shift towards shorter wavelengths the thinner the individual well layers became, whereas the effective refractive index would remain constant for all five samples. As shown in Fig. 4(a), this behavior was observed in the transmission measurements. The absorption edge of the 3s/pass sample lies at the shortest wavelength, whereas the 15s/pass results in the longest wavelength edge with a difference of 18 nm between the samples. For reference the absorption edge of a $Ta_2O_5$ layer is indicated by a dotted line. In the longer wavelength range above 280 nm, all curves overlay since they all have the same effective refractive index and optical thickness. Furthermore, they touch the solid line for λ/2 optical thickness indicating very low absorption of the QNLs in the longer wavelength range. From these measurements, we can conclude that the magnetron sputtered nanolaminates do show the quantization effect as predicted in [4,5].

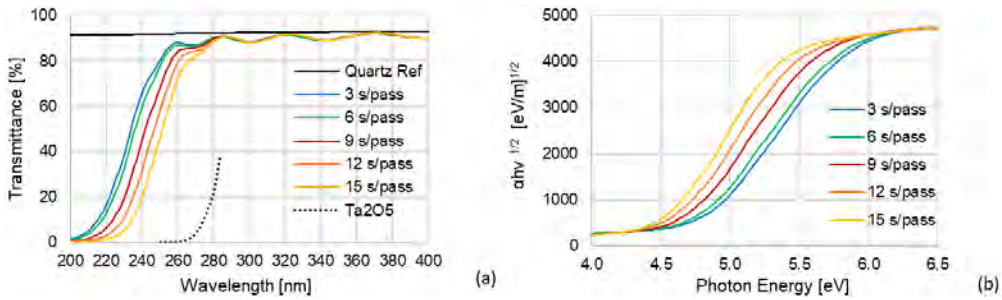


**Fig. 4.** Transmittance (a) and Tauc-plot (b) of QNL layers with the same power ratio of $Ta_2O_5$ to $SiO_2$, but with table speeds (3/6/9/12/15 s/pass).

For this set of samples, the effective refractive index was determined as described in the experimental section. The band gap energy was determined from the Tauc-plot as shown in Fig. 4(b) [29]. The total physical thickness of the QNL layers is in the range of 700 nm, which translates to 600 pairs of nanolaminate layers at a table speed of 3 s/pass.

Figure 5 shows that the gap energy increases with the decrease of well thickness. However, the refractive index remains nearly constant at a value of around 1.56, which corresponds to a thickness ratio of 5.3 of $SiO_2$ to $Ta_2O_5$. Both findings are in perfect agreement with the conclusions, which were already drawn from the observation of the transmission measurements. The shift in absorption edge proves that this stack consists of nanolaminates and is not simply a mixture of both materials. The calculation procedure as mentioned in Section 2 [16] was applied to simulate the gap shift of the deposited QNL coatings, and good agreement between measured energy shifts and the calculation results was found as shown in Fig. 5.

A series of experiments were performed subsequently varying the ratio of the thicknesses of $Ta_2O_5$ to $SiO_2$. The power on each source was varied as a main parameter. Since both sputter processes are PEM-controlled, the PEM settings also had to be adjusted to the values appropriate to the sputter power. With these optimized settings the deposition rates of the nanolaminate layers were higher than for the corresponding single material layers, since nanolaminates are sputtered from two sources.

Optics EXPRESS

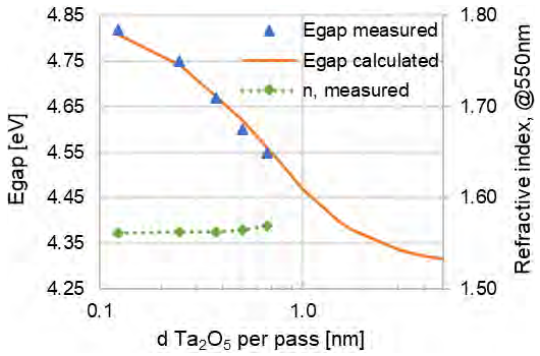


**Fig. 5.** Representation of gap energy and refractive index as a function of the well thickness showing good agreement of the calculated $E_{gap}$ compared to the experimental data.

For each H:L ratio a set of deposition runs with different table speeds was completed in order to vary the thickness of the individual nanolaminate layers. Typically, table speeds of 1.5/3/4.5/6/9/12/15 s/pass were chosen. Figure 6(a) shows that the energy of the gap increases as the well thickness gets thinner as also predicted by the theory. For $Ta_2O_5$ with quantum-well thickness exceeding 2–3 nm however, the gap energy becomes constant because thicker layers do not show quantization effects.

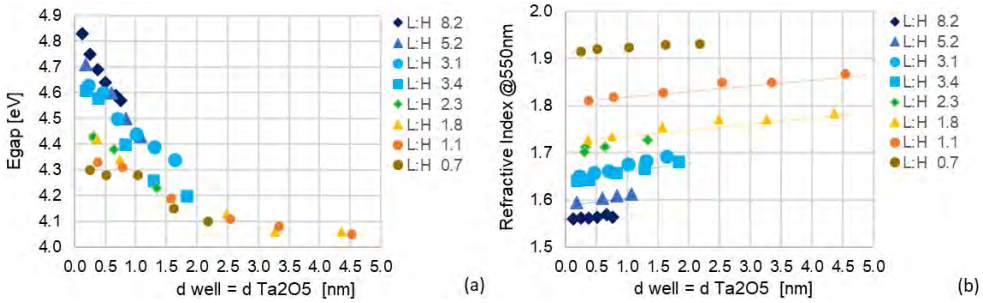


**Fig. 6.** Gap energy and refractive index for a wide range of power ratios. (a) and (b) with relation to the well thickness

On the other hand, the refractive index shows only a slight, but steady increase, with increasing well thickness, the effect being more pronounced the higher the refractive index. As can be seen from Fig. 6(b) the refractive index can be tuned in a very wide range and can basically span a large range between the indices of $SiO_2$ to $Ta_2O_5$.

Figure 7 shows the dependence of band gap energy with refractive index. This representation nicely shows that the band gap energy can indeed be varied for a given refractive index thus decoupling index and gap energy.

### *4.2. Antireflection coating*

The results above demonstrated that magnetron sputter deposition is capable of manufacturing nanolaminates showing the quantum effect. In a next step, we investigated whether optical interference coatings such as antireflection coatings, mirrors or filters could be designed and manufactured by replacing the high refractive material by a QNL stack of the appropriate total thickness.

Optics EXPRESS

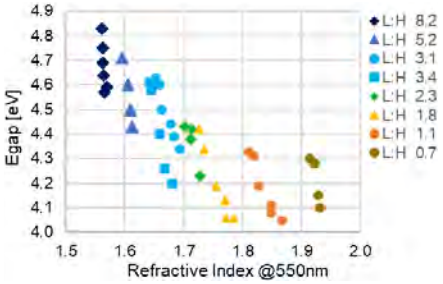


**Fig. 7.** Dependance of gap energy to refractive index.

An antireflection coating for an UV LED centered at 280 nm was chosen as an example for the viability of the QNL concept for optical interference coatings. The design consisted of 2-layers in analogy to a classical V-coating, however with the first layer being a QNL instead of $Ta_2O_5$. For the experiment, a QNL with an effective refractive index of n = 1.7 at a wavelength of 550 nm and a bandgap energy of $E_{gap} = 4.48$ eV was chosen. Such a nanolaminate stack consists of $Ta_2O_5$ and $SiO_2$ layers with a thickness of 0.31 and 0.76 nm, respectively. The design uses a thickness of 136 nm for $SiO_2$ and a thickness of 120 nm for the QNL, which equals around 120 individual nanolayers of each material. The thicknesses correspond to an optical thickness of around 3 times $\lambda/4$ at $\lambda = 280$ nm, which is more than the minimum required 1 $\lambda/4$ to enable an antireflection coating. The thicker layers allowed us to test broad band optical monitoring thickness control in the same experiment.

Figure 8 shows the transmission (a) and reflection (b) measurement curves at 8° angle of incidence of a double side coated quartz substrate. Minimum reflection and maximum transmission occur at the design wavelength of 280 nm and the curves correspond nicely with the design. The transmission of the double side coated sample reaches 98.3% as deposited and 99.2% after annealing for 1 hour at 300 °C in air. The corresponding absorption losses are 1% and 0.3%. In comparison, a 2-layer antireflection coating composed of $Ta_2O_5$ and $SiO_2$ optimized for 266 nm resulted in good reflectance at the design wavelength, but 66% and 25% absorption at 266 and 280 nm respectively. This clearly shows that bulk $Ta_2O_5$ cannot be used at these UV-wavelengths, whereas with a QNL consisting of $Ta_2O_5$-$SiO_2$ a very good performance can be obtained, enabling to overcome the bandgap limitations of the high refractive index material and opening up the field for a wide range of applications.

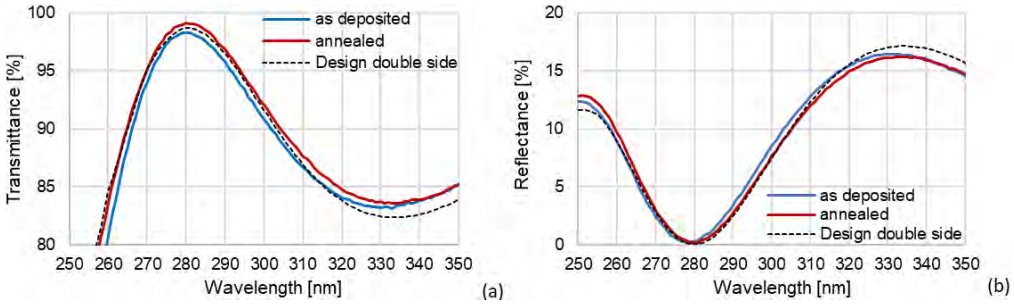


**Fig. 8.** Transmittance (a) and reflectance (b) measurement of the antireflective coating of $SiO_2$ and QNL layers showing excellent transmission at 280 nm

In-situ broadband optical monitoring in reflection in a wavelength range of 380-980 nm was used to monitor the coating thickness. Thanks to the thicker layers, the evolution of the signal

Optics EXPRESS

could be observed over longer time also through reflection maxima. It turned out, that the reflection signal of the QNL developed in a completely regular way, exactly as a layer with the corresponding effective refractive index would evolve. We can therefore conclude that optical monitoring is perfectly suited for controlling the thickness in film stacks with QNLs in turntable configuration.

### 4.3. Mirror coating

As a second example of an optical interference coating, a mirror for 355 nm was deposited consisting of 30 layers each of $SiO_2$ and QNL $Ta_2O_5$-$SiO_2$ with quarter wave optical thickness. As a comparison, the equivalent mirror with a standard design was deposited with 26 layers total of $SiO_2$ and $Ta_2O_5$ of quarter wave optical thickness.

Both designs were deposited using broadband optical monitoring. The good agreement between measurement and design indicates, that the QNL-layers could be terminated as if they were regular layers, see Fig. 9. Both mirrors are centered nicely at the design wavelength. As expected, the mirror with QNLs has a narrower reflection band due to the lower effective refractive index of the QNL. When comparing the transmission region below the wavelength of 300 nm it becomes obvious, that the standard design only shows poor transmission, whereas the QNL-mirror only has losses in the range of 2-5% above the absorption edge.

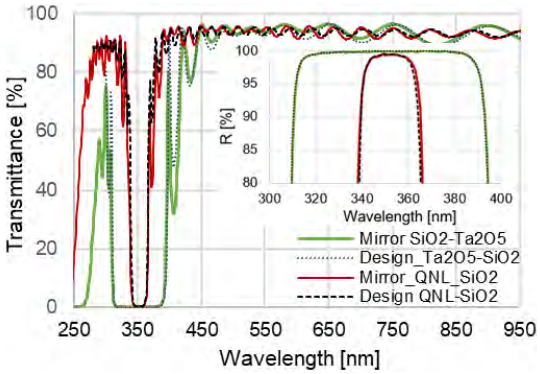


**Fig. 9.** Transmittance and reflectance (inset) measurement at 8° of the mirror for 355 nm comparing a quarter wave design of SiO2-QNL with a standard Ta2O5 - SiO2 coating.

In conclusion, QNL's can be treated in both design and optical monitoring as regular bulk layers with the corresponding effective refractive index. Since two sputter sources are running the deposition rate is also typically higher than for the corresponding single layers of $SiO_2$ or $Ta_2O_5$.

## 5. Conclusion

In our paper we show that magnetron sputtering using a deposition tool with turntable configuration is ideally suited to depositing quantum nanolaminate layers. The individual layers of the nanolaminate stack are deposited sequentially when passing under the $SiO_2$ and $Ta_2O_5$ sputter sources, a sequence which is repeated with every rotation of the turntable. The setting of the table rotation speed allows to select the total thickness of $SiO_2$ and $Ta_2O_5$ per turn, whereas the power setting of the sources allows to select the thickness ratio of $Ta_2O_5$ to $SiO_2$. We demonstrated individual layers with a few tenth of nm and a wide range of $SiO_2$ to $Ta_2O_5$ ratios of 0.7-8.

The paper also shows that the predicted shift in the absorption edge is observed. In accordance with theory, the shift becomes larger as $Ta_2O_5$ thickness is reduced. The refractive index is given by the ratio of $SiO_2$ to $Ta_2O_5$ layer thicknesses. At a given ratio, the index remains constant or

Optics EXPRESS

increases only very slightly when the total thickness of both layers is increased. This finding is also in good agreement with the prediction from theory.

Furthermore, QNL layers were used as the high index material in optical interference filters. We demonstrated that the turntable configuration of the sputter system leads to a viable manufacturing process for an antireflection coating at a wavelength of 280 nm and a mirror at 355 nm. From a technical standpoint the deposition of these filters runs like standard processes with the difference that in the QNL layer both sources are powered. Furthermore, optical monitoring can also be used without any adaption.

Both antireflection and mirror coatings were in good agreement with the respective designs, and both showed good transmission in the wavelength range below 300 nm where coatings using standard $Ta_2O_5$ already operate in their absorptive spectral region. These results confirm that the concept of QNL indeed opens up a wide field for novel applications.

**Funding.** Innosuisse - Schweizerische Agentur für Innovationsförderung (Project 39986.1 IP-ENG); Allianz Industrie Forschung (QuantUV (21364 N)); Deutsche Forschungsgemeinschaft (Cluster of Excellence PhoenixD (390833453, EXC 2122)).

**Acknowledgments.** The authors thank Innosuisse - Swiss Innovation Agency and the Deutsche Forschungsgemeinschaft (DFG, German Research Foundation) for funding under Germany's Excellence Strategy within the Cluster of Excellence PhoenixD (EXC 2122, project ID 390833453).

**Disclosures.** The authors declare no conflicts of interest.

**Data availability.** Data underlying the results presented in this paper are not publicly available at this time but may be obtained from the authors upon reasonable request

## References

1. M. Jupé, T. Willemsen, H. Liu, M. Steinecke, L. Jensen, and D. Ristau, "Manufacturing of Quantized Nanolaminates," in *Optical Interference Coatings 2019, OSA Technical Digest (online)* (Optical Society of America, 2019), paper TB4.
2. T. Willemsen, M. Jupé, L. Gallais, D. Tetzlaff, and D. Ristau, "Tunable optical properties of amorphous Tantala layers in a quantizing structure," Opt. Lett. **42**(21), 4502–4505 (2017).
3. H. Finkenrath, "The moss rule and the influence of doping on the optical dielectric constant of semiconductors-i," Infrared Phys. **28**(5), 327–332 (1988).
4. H. Badorreck, M. Steinecke, L. Jensen, D. Ristau, M. Jupé, J. Müller, R. Tonneau, P. Moskovkin, S. Lucas, A. Pflug, L. Grinevičiūtė, A. Selskis, and T. Tolenis, "Correlation of structural and optical properties using virtual materials analysis," Opt. Express **27**(16), 22209 (2019).
5. T. Tolenis, L. Grineviciute, R. Buzelis, L. Smalakys, E. Pupka, S. Melnikas, A. Selskis, R. Drazdys, and A. Melninkaitis, "Sculptured anti-reflection coatings for high power lasers," Opt. Mater. Express **7**(4), 1249–1258 (2017).
6. L. Grineviciute, M. Andrulevicus, A. Melninkaitis, R. Buzelis, A. Selskis, A. Lazauskas, and T. Tolenis, "Highly Resistant Zero-Order Waveplates Based on All-Silica Multilayer Coatings," Phys. Status Solidi A **214**(12), 1700764 (2017).
7. T. Tolenis, L. Grineviciute, L. Smalakys, M. Ščiuka, R. Drazdys, L. Mažule, R. Buzelis, and A. Melninkaitis, "Next generation highly resistant mirrors featuring all-silica layers," Sci. Rep. **7**(1), 10898 (2017).
8. R. Tonneau, P. Moskovkin, A. Pflug, and S. Lucas, "TiOx deposited by magnetron sputtering: a joint modelling and experimental study," J. Phys. D: Appl. Phys. **51**(19), 195202 (2018).
9. R. Tonneau, P. Moskovkin, J. Muller, T. Melzig, E. Haye, S. Konstantinidis, A. Pflug, and S. Lucas, "Understanding the role of energetic particles during the growth of TiO2 thin films by reactive magnetron sputtering through multi-scale Monte Carlo simulations and experimental deposition," J. Phys. D: Appl. Phys. **54**(15), 155203 (2021).
10. U. Schulz, "Review of modern techniques to generate antireflective properties on thermoplastic polymers," Appl. Opt. **45**(7), 1608–1618 (2006).
11. U. Schulz, B. Schallenberg, and N. Kaiser, "Symmetrical periods in antireflective coatings for plastic optics," Appl. Opt. **42**(7), 1346–1351 (2003).
12. U. Schulz, F. Rickelt, P. Munzert, and N. Kaiser, "A double nanostructure for wide-angle antireflection on optical polymers," Opt. Mater. Express **4**(3), 568–574 (2014).
13. J. Dervaux, P.-A. Cormier, P. Moskovkin, O. Douheret, S. Konstantinidis, R. Lazzaroni, S. Lucas, and R. Snyders, "Synthesis of nanostructured Ti thin films by combining glancing angle deposition and magnetron sputtering: A joint experimental and modeling study," Thin Solid Films **636**, 644–657 (2017).
14. T. Willemsen, M. Jupé, M. Gyamfi, S. Schlichting, and D. Ristau, "Enhancement of the damage resistance of ultra-fast optics by novel design approaches," Opt. Express **25**(25), 31948–31959 (2017).
15. M. Steinecke, H. Badorreck, M. Jupé, T. Willemsen, L. Hao, L. Jensen, and D. Ristau, "Quantizing nanolaminates as versatile materials for optical interference coatings," Appl. Opt. **59**(5), A236–A241 (2020).

Optics EXPRESS

16. T. Willemsen, P. Geerke, M. Jupe, L. Gallais, and D. Ristau, "Electronic quantization in dielectric nanolaminates," Proc. SPIE **10014**, 100140C (2016).
17. P. Harrison and A. Valavanis, "*Quantum Wells, Wires and Dots: Theoretical and Computational Physics of Semiconductor Nanostructures*", 4th Edition (Wiley, 2016).
18. C. Franke, O. Stenzel, S. Wilbrandt, J. Wolf, N. Kaiser, and A. Tünnermann, "Estimation of the composition of coelectron-beam-evaporated thin-mixture films by making use of the Wiener bounds," Appl. Opt. **54**(9), 2362–2370 (2015).
19. R. Jansson and H. Arwin, "Selection of the physically correct solution in the n-media Bruggeman effective medium approximation," Opt. Commun. **106**(4-6), 133–138 (1994).
20. A. Feldman, "Modeling refractive index in mixed component systems," in Modeling of Optical Thin Films, Vol. 0821, (1988).
21. T. Amotchkina, D. Ristau, M. Lappschies, M. Jupe, A. Tikhonravov, and M. Trubetskov, "Optical Properties of TiO2-SiO2 Mixture Thin Films Produced by Ion-Beam Sputtering," in *Optical Interference Coatings (OIC) 2007, OSA Technical Digest* (Optica Publishing Group, 2007), paper TuA.8.
22. "MedeA," https://www.materialsdesign.com/medea-software.
23. M. Turowski, T. Amotchkina, H. Ehlers, M. Jupé, and D. Ristau, "Calculation of optical and electronic properties of modeled titanium dioxide films of different densities," Appl. Opt. **53**(4), A159–A168 (2014).
24. S. Schwyn Thöny, M. Chesaux, S. Gees, and A. Frigg, "Innovative sputter system for high volume production of demanding optical interference coatings," in *Optical Interference Coatings 2016, OSA Technical Digest (online)* (Optical Society of America, 2016), paper WA.7.
25. M. Chesaux, S. Schwyn Thöny, S. Gees, and A. Frigg, "Rotating target source: novel shaperless concept for magnetron sputtering with excellent uniformity," in *Optical Interference Coatings 2016, OSA Technical Digest (online)* (Optical Society of America, 2016), paper WA.2.
26. S. Schwyn Thöny, S. Gees, and E. Schüngel, "Improving film stress and surface roughness by using a plasma source in magnetron sputtering," in *Optical Interference Coatings 2019, OSA Technical Digest (online)* (Optical Society of America, 2019), paper WC.4.
27. S. Waldner, J. Buchholz, and R. Benz, "Hybrid Mode Optical Monitoring – Monochromatic and Broadband Algorithms in the same Coating Process," in *Optical Interference Coatings Conference (OIC) 2019, OSA Technical Digest* (Optica Publishing Group, 2019), paper WA.9.
28. B. D. Viezbicke, S. Patel, B. E. Davis, and D. P. Birnie, "Evaluation of the tauc method for optical absorption edge determination: ZnO thin films as a model system," Phys. Status Solidi B **252**(8), 1700–1710 (2015).
29. O. Stenzel, "*The physics of thin film optical spectra*", Berlin/Heidelberg, Germany (Springer, 2015).

## 12.2 UV-coatings using Ta2O5-SiO2 quantized nanolaminates

The paper "UV coatings using $Ta_2O_5 - SiO_2$ quantized nanolaminates" [62] is a continuation of the first paper of QNL [46]. It describes the design and production of two multilayer coatings, an anti reflection coating with a design wavelength at $266\,nm$ and a short pass with the edge at $330\,nm$. In addition, it presents the first TEM measurement of the $536\,nm$ thick QNL stack and shows the regularity of the coated pair over the whole depth.
In the beginning, the principle of QNL is explained briefly with the calculation of the formula used for the calculation of the thickness of laminate materials [48] and the expected shift in the optical band gap due to the thickness of the well material [42].
Also, as in the previous paper the magnetron sputtering tool and the principle used to coat QNL with a high deposition rate are shown.
We again coated several series of QNLs and showed that the refractive index in each set of QNLs remains roughly constant while the band gap increases with a smaller$Ta_2O_5$ thickness. The used refractive indices are around $n \approx 1.57 - 1.8$. EMPA provided us with high resolution TEM measurements and was able to show the high value of uniformity and regularity of the coated stack of $536\,nm$ with a total of 180 laminates while the whole deposition process took $30\,min$. Also with the measurements we were able the first time to verify the used Drude-model [48] to calculate the two laminate thicknesses with high accuracy and comparable to TEM.
We chose two different process settings to design and coat two multilayer filters using the optical monitoring system [41]. One is a short pass filter where the high reflection part is centered at $366\,nm$. The blocking edge is set at around $330\,nm$ with the transmitting part below. The design and process were chosen to illustrate the difference in the absorption edge of $QNL - SiO_2$ compared to a classical $Ta_2O_5 - SiO_2$ design. As expected the reflecting range of the classical material design is much broader than the QNL because of the higher difference in refractive index of the two used materials. But apart from that the absorption of $Ta_2O_5$ starts right at the edge between $310 - 330\,nm$ leaving the UV range unusable for further applications.
The QNL based design on the other hand extends with the chosen refractive index the usable range down to $280\,nm$ leaving a much broader transparent part of the filter.
The second design uses different QNL settings, resulting in a lower refractive index and even lower absorption edge. A 6 layer anti reflective design coated on both sides of the substrate at $266\,nm$ is demonstrated well below the absorption edge of $Ta_2O_5$. With an effective refractive index of $n_{QNL1} \approx 1.57$ 6 layers were needed to bring the reflection to $R_{266\,nm} = 0.2\%$ while transmission is still above $T_{266\,nm} > 99\,\%$. The coated filter shows the opportunities given by the shift of the absorption edge of a high refractive index material, especially when combined with the high deposition rate and precision of the used coating device.

### Contribution

My contribution was to develop the process for the materials and multilayer designs used as well as the corresponding process recipes. In addition, the photo spectrometric measurements, analysis and calculation. I also participated in the discussions and interpretations of the results as well as in writing the paper and preparing the figures.

J. Eur. Opt. Society-Rapid Publ. 2025, **xx**, xx
© The Author(s), published by EDP Sciences, 2025
https://doi.org/10.1051/jeos/2025021
Available online at: https://jeos.edpsciences.org

EOSAM 2024
Guest editors: Luca De Stefano and Raffaele Velotta

**Journal of the European Optical Society-Rapid Publications**

RESEARCH ARTICLE OPEN ACCESS

# UV coatings using $Ta_2O_5$-$SiO_2$ quantized nanolaminates

Manuel Bärtschi[1,*], Stephan Waldner[2], Silvia Schwyn Thöny[2], Xavier Maeder[3], Fabian Steger[1], Thomas Frei[2], and Vivek Devulapalli[3]

[1] RhySearch, Institute for Optical Coatings and Characterization, Werdenbergstrasse 4, 9470 Buchs, Switzerland
[2] Evatec Ltd, Hauptstrasse 1a, 9477 Trübbach, Switzerland
[3] EMPA, Laboratory for Mechanics of Materials & Nanostructures, Feuerwerkerstrasse 39, 3602 Thun, Switzerland

Received 31 January 2025 / Accepted 15 April 2025

**Abstract.** The use of Quantized Nanolaminates (QNL) in optical interference coatings has gained significant attention in recent years. By using a magnetron sputtering tool from Evatec with rotating substrate table and multiple sputtering sources operating simultaneously, we are able to deposit these metamaterials consistently at exceptionally high rates, comparable to and sometimes even exceeding magnetron sputter rates for standard materials. This combination of high deposition rate and precision enables us to treat QNL as a stand-alone material, effectively replacing high-refractive index materials in complex interference filter designs. In our experiments, we used a combination of $Ta_2O_5$-$SiO_2$ QNL to produce filters like anti-reflective and shortpass coatings within the UV range of 266–350 nm, which would be not possible with $Ta_2O_5$ as bulk material in similar designs.

**Keywords:** Optical interference coatings, Quantized nanolaminates, Magnetron sputtering, $Ta_2O_5$, $SiO_2$.

## 1 Introduction

Quantized Nanolaminates (QNL) represent an innovative material system for optical coatings which was first developed by the Laser Zentrum Hannover (LZH) in 2016 [1]. This system involves the alternate deposition of two optical materials with different refractive indices as extremely thin layers, typically 0.1–2.0 nm thick. When numerous such layers are sequentially deposited on top of each other, they form a system which, as a stand-alone material has new optical properties compared to the standard bulk oxide materials. The refractive index of the resulting material is determined by the thickness ratio of the two constituent layers. However, the extreme thinness of the high index material layers in the stack, restricts the valence electron mobility, causing a shift in the absorption edge towards shorter wavelengths. This phenomenon has been demonstrated multiple times, primarily using Ion Beam Sputtering (IBS) or Atomic Layer Deposition (ALD) systems [1–3]. Unfortunately, the process of switching between the deposition of the two different coat materials, is time consuming, limiting the practical application of QNL in complex layer designs due to significant effort and costs. We have developed a magnetron sputtering process that allows the production of QNL systems from $Ta_2O_5$ and $SiO_2$ as a continuous process [4]. This process achieves sputtering rates of up to 0.8 nm/s and enables the deposition of up to 2400 laminate pairs per hour without interruption during the process. For the first time, this advancement enables the economical use of QNL as an independent high refractive index material for complex optical filter systems. In this paper we demonstrate first our approach to develop QNL single layers. Subsequently, we use two different QNL variants as high refractive index materials to create two complex multilayer systems. The first is a shortpass filter below 320 nm with a reflective region after 340 nm. We compare it with a similar shortpass made with standard $Ta_2O_5$ layers as high refractive index material. Next, we present a double-side coated anti-reflective filter on quartz glass, which shows no significant absorption at 266 nm. This highlights the great potential of $Ta_2O_5$-$SiO_2$ QNL compared to standard $Ta_2O_5$ based coatings when it comes to manufacturing filters for the UV range.

## 2 Material and methods

### 2.1 Quantized nanolaminates

At first glance the idea behind QNL appears to be a relatively simple system. They consist of the periodic and alternating stacking of materials with different band gap energies. The band gap energy describes the amount of energy that a photon must have to be absorbed by the

* Corresponding author: manuel.baertschi@rhysearch.ch

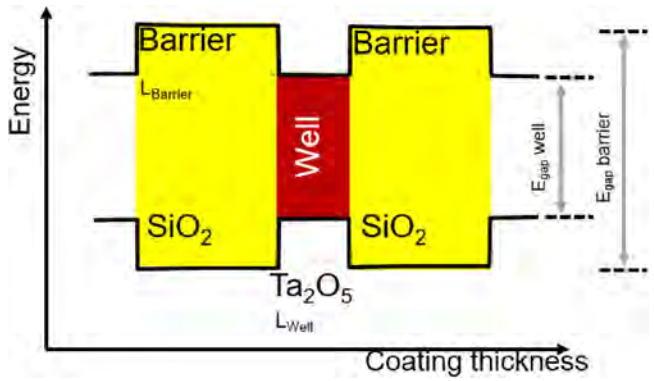


**Figure 1.** In this figure, the bandgap of the two different materials, building a QNL system are shown [5].

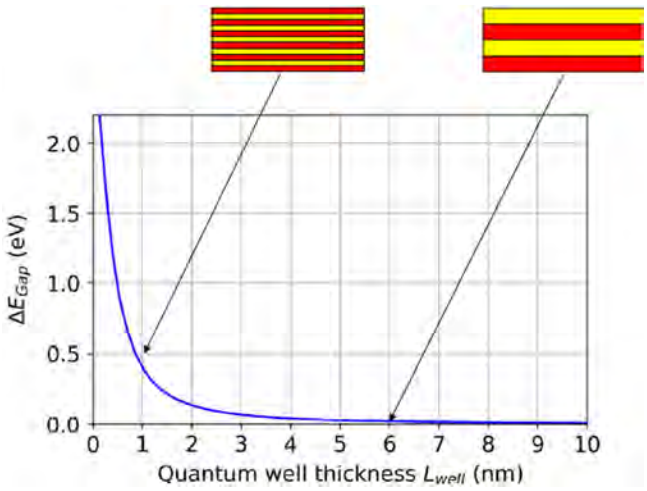


**Figure 2.** The graph shows the expected effect of QNL. Both systems shown schematically have the same mixing ratio of materials and consequently the same refractive index. However, the thinner layer structure increases the band gap of the left system. The figure has been modified from [2].

valence electrons of the respective material. When a photon passes through these QNL, it experiences a periodic sequence of different potential energies, as shown in Figure 1.

If the layer thickness of the "well" material is chosen to be sufficiently thin, an effect occurs where the bandgap of the entire system increases [1]. This can be understood as a restriction of the valence electron mobility within the material due to the thinness of the material layers, thereby making the absorption of light more difficult. The effective refractive index of the entire stack, on the other hand is only given by the volume ratio of the two materials and their own specific refractive indices [6].

$$n^2_{\mathrm{QNL}} = f \times n^2_{\mathrm{Barrier}} + (1-f) \times n^2_{\mathrm{Well}}.$$

This means, that by structuring mixed materials into ultra-thin layers instead of homogeneous mixtures, it is possible to obtain different bandgaps with the same refractive indices, since the band gap change depends only on the thickness of the well layers, but the refractive index depends on the mixing ratio, visualized in Figure 2.

## 2.1 Experimental setup

The properties of QNL have already been demonstrated several times in different experiments and working groups, using different coating technologies. As each individual layer of the two different materials is extremely thin, a large number of them are required to produce a layer with a thickness in the range required for optical thin film designs. This leads to a problem for many standard manufacturing methods when it comes to producing QNL stacks economically and efficiently. One reason for this is that different processes are required for the different materials used, which have to be carried out alternately. Each of these must be set, stabilized, carried out and ramped down again before the next one can begin, which can greatly reduce the coating rate. Furthermore, it is hardly possible to monitor individual layers, as the sensitivity of both optical monitoring and the oscillating quartz method does not allow such high resolution to reliably measure layers below one nanometer. Due to possible drifts in processes, there is always a high risk that the thickness of the material layers cannot be kept constant in a stack of hundreds of them, which severely limits reproducibility. We benefit from a structural advantage provided by the Clusterline 200 BPM from Evatec, a magnetron sputtering system equipped with a rotating substrate table. To understand the benefits of this coating tool, it is necessary to first examine its working principles, as illustrated in Figure 3.

The white wall separating the clean room from the gray room is visible at the front. Next to it is the control panel, positioned beside two automatic load locks, each capable of holding sixteen 8-inch substrates. Behind these load locks lies the vacuum transfer chamber, equipped with a handler, an aligner for precise substrate positioning, and a flipper. This flipper allows substrates to be turned for backside coating without breaking the vacuum. In the background, the large coating chamber can be seen. It houses a rotating substrate table with a capacity for sixteen 8-inch substrates, as shown in the picture on the right. The sputter sources are mounted on the chamber, with the system supporting up to four sources, each equipped with a different target material. The additional plasma source (PSC) in the background is capacitively coupled and operates with various gases, mainly for etching, increasing density, or oxidizing the sputtered layers. In our experiments to coat QNL, we use the two magnetron sputter sources at the front, fitted with a Si-target and a Ta-target. For producing pure $SiO_2$ layers, we use the same Si-target in combination with the PSC source. To understand why our magnetron sputtering system is particularly well-suited for QNL production, it is helpful to first consider the standard process for creating single-layer materials. The system is designed for continuous table rotation during normal coating processes. Initially, the process gas is introduced, and the sputter source is activated with the shutter closed. Once the plasma stabilizes, the shutter opens, and the sputtering material is evenly deposited onto all substrates as the table rotates.

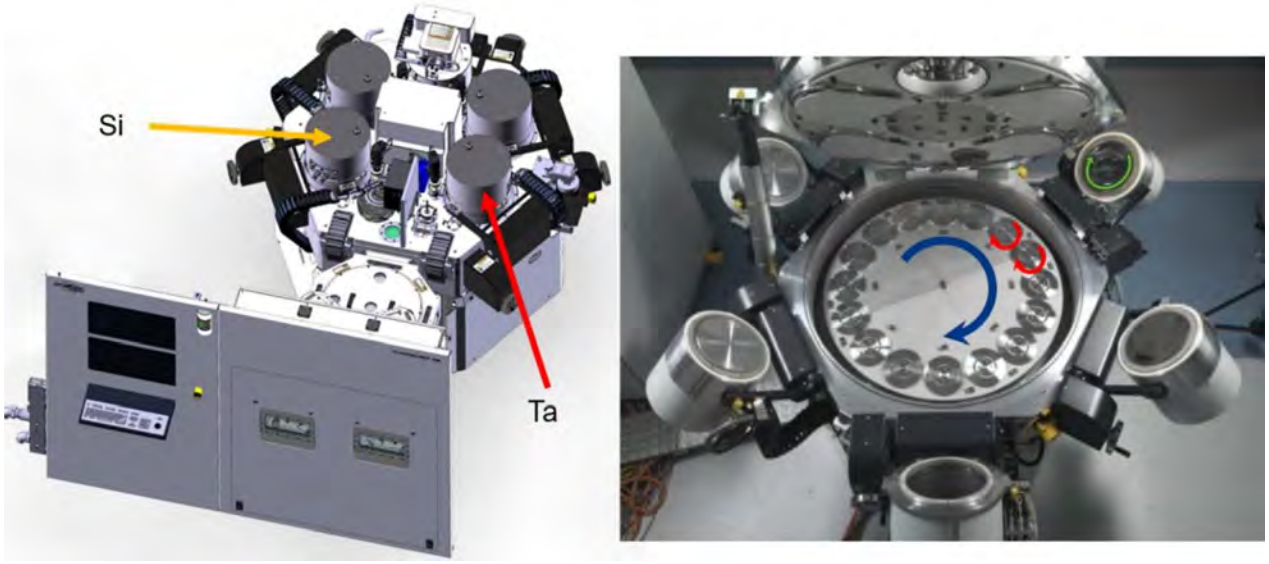


**Figure 3.** Schematically drawn the tool with the sputter and plasma sources on top of it facing downwards on the table (left side). The opened tool with the rotating substrate table and the sources folded away (right side).

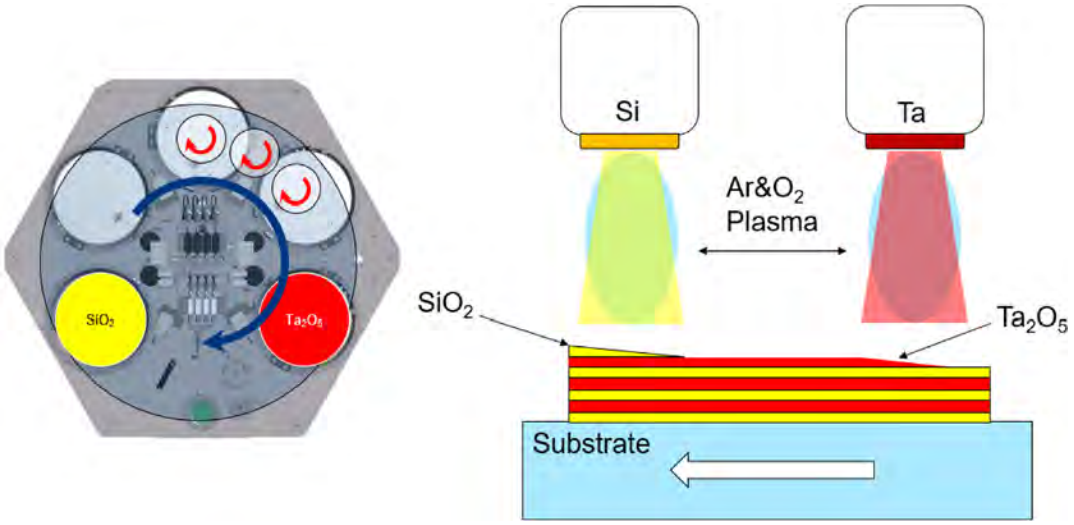


**Figure 4.** The diagram shows the process for producing QNL schematically. Due to the continuous process, a high rate and also a very stable behavior can be achieved.

Each rotation allows the layer to grow incrementally as the substrates pass under the source. The growth rate of this layer can be controlled either through calculations based on known rates or via optical monitoring, here the Evatec GSM1102 is used with both monochromatic and broadband monitoring algorithms. For QNL production, where two different materials are required, we operate two sources simultaneously. This setup necessitates stabilizing the system to prevent process drift. By doing so, we can deposit one layer of $SiO_2$ and one of $Ta_2O_5$ with each table rotation, see Figure 4. The ratio between the two materials is adjusted by modifying the power supplied to the respective sputter sources. Additionally, the layer pair thickness can be fine-tuned by altering the rotation speed of the table; faster rotations yield thinner layers which amplifies the impact on the band gap. The ability to maintain a continuous process while depositing material from both sources simultaneously eliminates interruptions for alternating layers. This approach not only achieves a significantly higher deposition rate but also ensures a stable and consistent process. As a result, we can reliably produce uniform individual layers. This efficiency makes the production of QNL highly cost-effective, enabling its use as a standalone material in complex coating designs.

## 2.3 Material properties

We tested a variety of processes with different material ratios. All samples were coated for a duration of 900 s each, regardless of their deposition rate. For some selected

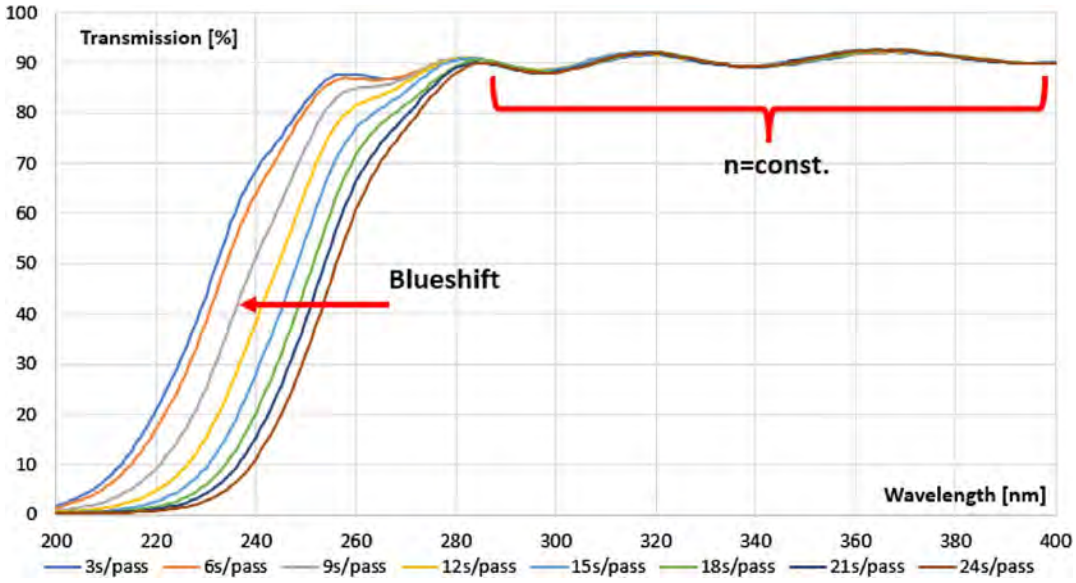


**Figure 5.** With the same source settings but different table rotation speed, a shift in absorption can be seen, while the refractive index and deposition rate stays constant.

combinations, we kept the process settings constant and only adjusted the table rotation speed, which is specified in seconds per rotation. This approach keeps the mixing ratio of the QNL within a set constant, but the thickness of the individual layers is altered. The lower the rotation time, the faster the table rotates, and the thinner the individual layers become. The transmission spectra of such a series are shown in Figure 5.

In the higher wavelength range, it can be observed that the measured spectra overlap, indicating that they must have the same refractive index as well as the same rate. In the lower wavelength range, the absorption edge shifts to shorter wavelengths for faster rotation speeds and correspondingly thinner individual layer thicknesses. Some of the layers were analyzed using HAADF STEM measurements. One of these layers is shown in Figure 6. This specific sample was coated with a table rotation speed of 6 s per pass for half an hour, resulting in 300 individual laminates and a total thickness of ~536 nm. Since we know the number of table rotations during the coating process and can determine via photospectrometry the thickness of the QNL stack, we are able to easily calculate the thickness of a single laminate pair. To calculate the thickness of each material within a laminate pair, we use the formula mentioned at the beginning. By knowing the refractive indices of the individual materials as well as from the overall block, it is possible to determine the volume fraction factor "f", which allows us to calculate the average laminate thickness of both $SiO_2$ and $Ta_2O_5$. The ability to analyze these layers using STEM HAADF image allowed us to additionally verify this formula. The average calculated thickness for $SiO_2$ was found to be 1.35 nm, and for $Ta_2O_5$ it was 2.18 nm, while the STEM measurements showed an average thickness of $SiO_2 = 1.39$ nm and $Ta_2O_5 = 2.12$ nm, respectively, which shows a high level of agreement. A line scan is shown in Figure 7.

From the transmission and reflection spectra, the band gap of the layers was calculated using a Tauc plot. By using the software OptiChar, the refractive indices, extinction coefficients and physical thickness can be determined across a wide wavelength range from the transmission and reflection spectra. From the total thickness and the measured refractive index, the individual layer thickness of the $Ta_2O_5$ laminates can be calculated using the presented formula for mixing refractive indices, since the number of table rotations during the 900 s coating time is known. The calculated band gaps are plotted against the $Ta_2O_5$ laminate thicknesses in Figure 8.

The different colors represent different process settings and thus different mixing ratios. Points of the same color correspond to different rotation speeds and, accordingly, different $Ta_2O_5$ thicknesses. All samples were annealed in ambient atmosphere at 450 °C for 1 h to reduce potential defects. The refractive indices of the samples are also plotted against the $Ta_2O_5$ laminate thickness in Figure 9.

## 3 Results

As described in the previous section, the refractive indices and extinction coefficients were determined for all coated samples. This made it possible to select QNL settings with desired values for multilayer systems and create designs using OptiLayer, an optical interference design software. For the first filter, we chose a setting that provides a significant difference in the absorption edge compared to pure $Ta_2O_5$, while still maintaining a relatively high refractive index of $n \approx 1.8$ (QNL5), to design a short pass filter. We built a design with a transmission region in the UV range up to a transition range from 320 to 340 nm and a high reflection part from 340 to 380 nm. The transition edge was intentionally chosen to be close to the absorption edge

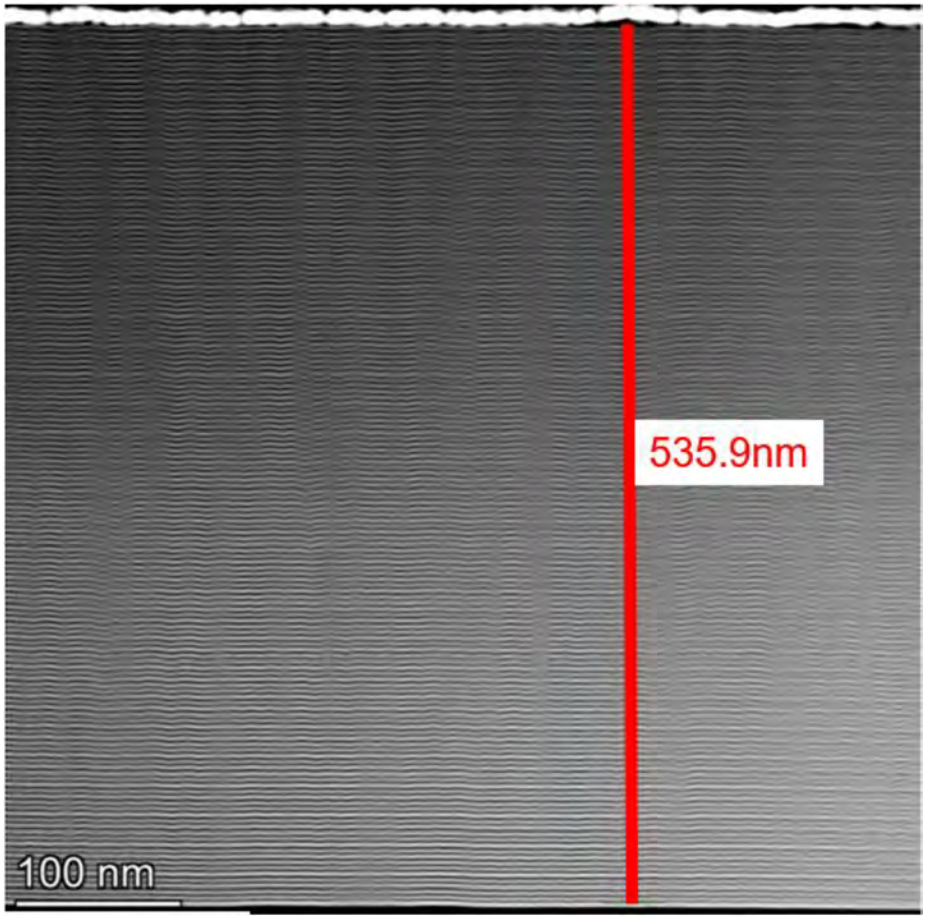


**Figure 6.** High-angle annular dark-field scanning transmission electron microscopy image of a QNL cross-section which took 30 min of deposition time with rotating table at 6 s/pass. Measured at EMPA using a Titan Themis 200 G3.

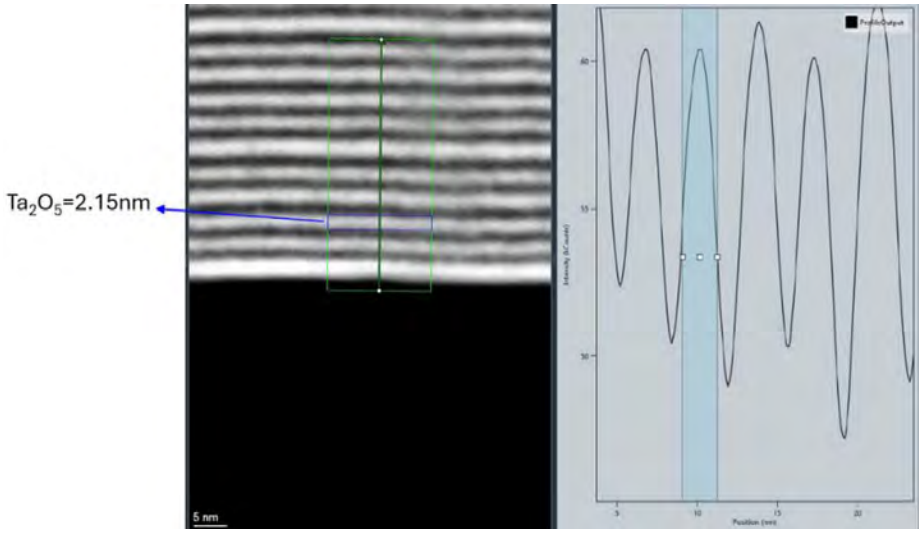


**Figure 7.** STEM HAADF image with a line scan for intensity shows a high level of agreement with the calculated thicknesses.

of pure $Ta_2O_5$ to show the difference. The design was created in two variants: a classic one using $Ta_2O_5$ as the high refractive index material and $SiO_2$ as the low-refractive-index material, consisting of a total of 40 layers. The same analogue design with 40 layers was also created using the selected QNL setting to replace $Ta_2O_5$ as high refractive material, with slight adjustments. This design consists of 20 layers of $SiO_2$ and 20 layers of QNLs, arranged

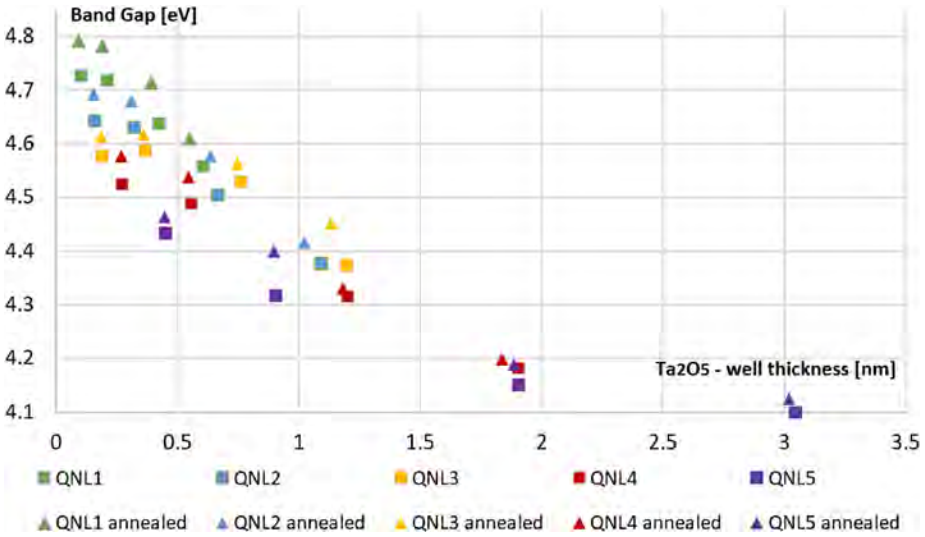


**Figure 8.** This figure shows the bandgap for the used sample sets compared to the thickness of the $Ta_2O_5$ laminates. Samples were measured directly after coating and after annealing.

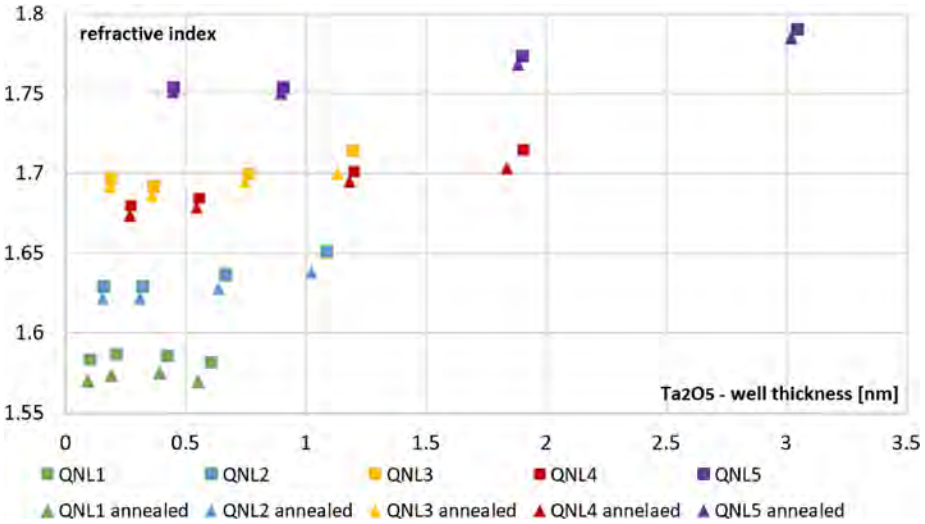


**Figure 9.** The refractive index at 550 nm compared to the thickness of the $Ta_2O_5$ laminates for the same samples as in Figure 8. Samples were measured directly after coating and after annealing.

alternately. Each QNL layer consists of a multiple of laminate pairs made of $Ta_2O_5$ and $SiO_2$. The thickness of the individual $SiO_2$ and $Ta_2O_5$ laminates was calculated as $SiO_2 = 1.36$ nm and $Ta_2O_5 = 1.00$ nm, resulting in a pair thickness of 2.36 nm. Each of the 20 QNL blocks in this optimized design has its own thickness, ranging from 47 nm to 60 nm, which results in a total QNL thickness of 1016 nm and thus approximately 430 laminate pairs within the design. These two designs were then coated using optical monitoring and subsequently measured with a spectrophotometer.

In Figure 10, the shortpass filter using QNL as the high-refractive-index material is shown in blue, while the one with $Ta_2O_5$ is shown in red. The transmission spectra are illustrated with solid lines for both, and it can be seen that the design with QNL allows for a larger transparent range in the UV region until absorption (dotted line) prevents further use. This curve clearly shows that the chosen mixture is usable for an additional 20 nm into the shorter wavelength range. However, in the dashed reflection spectra, it is also evident that due to the lower refractive index, the width of the mirror region is significantly narrower compared to the $Ta_2O_5$ based design.

As another experiment, a QNL mixture with a very low refractive index of $n \approx 1.6$ (QNL1) was chosen. This allowed for the creation of a very deep absorption edge. Using this, it became possible to design an antireflection coating with 6 layers at 266 nm. A quartz glass was coated on both sides with the design and measured using a photo spectrometer, as shown in Figure 11.

The spectrum is shown in blue, with the solid line once again representing the transmission in this case. It can be

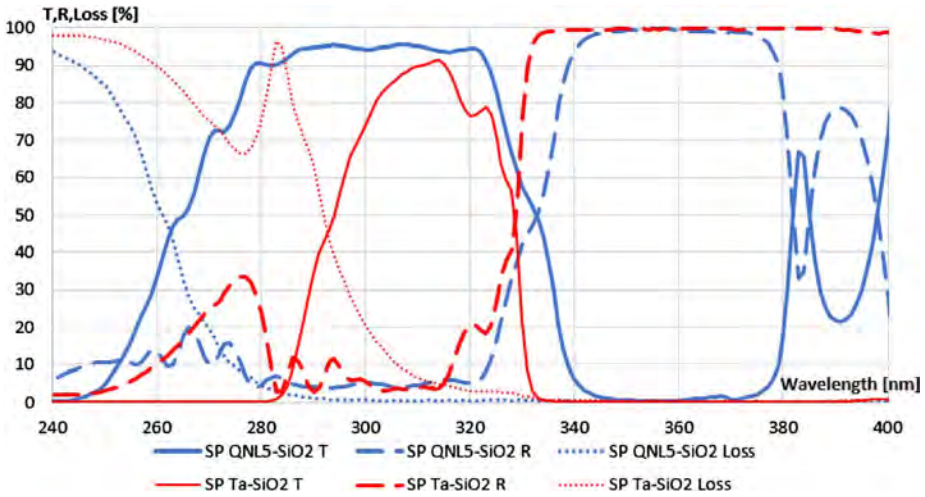


**Figure 10.** The shortpass with QNL (blue) and the shortpass with $Ta_2O_5$ (red). The solid line shows the transmission, the dashed the reflection and the dotted the loss. Both designs have a total of 40 layers.

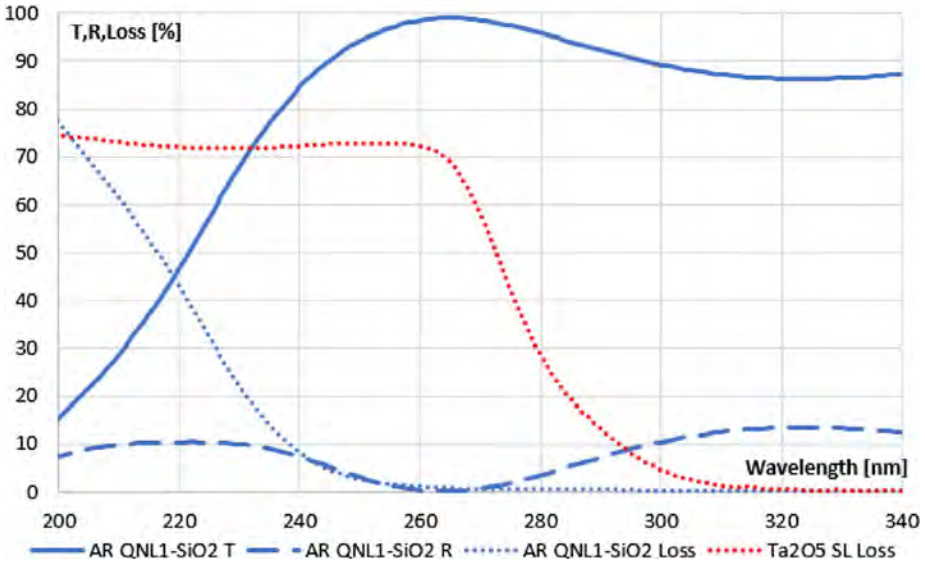


**Figure 11.** A double-side anti-reflective coating. The blue solid line indicates the transmission, the dashed the reflection and the dotted the absorption spectrum. The dotted red line shows the absorption spectrum of a $Ta_2O_5$ single layer.

seen that it reaches a value of over 99% at 266 nm. The dashed line represents the reflection, which is 0.2% at 266 nm, and the dotted line represents the absorption. Based on the red dashed line, which shows the absorption of $Ta_2O_5$, it can be observed that this antireflection coating is practically free of absorption at 266 nm, whereas $Ta_2O_5$ would already absorb 70% of the incoming light at this wavelength, making it unusable for this application.

## 4 Discussion

In this work, we were able to demonstrate that we are capable of producing QNL with high rates and very stable properties using the Clusterline 200 BPM coating tool from Evatec through a process we developed. We subsequently coated, measured, and evaluated a variety of these QNLs with different refractive indices and band gaps. TEM measurements allowed us to confirm the structure. We then used two different QNLs to coat two designs that we considered suitable. In both processes the layers were terminated using optical broadband monitoring. The first design represents a short pass system consisting of 40 layers. Since we also produced a comparable design using $Ta_2O_5$, we were able to compare the two spectra. It is evident that, due to the lower absorption edge of the QNL, a larger transmission range exceeding 90% is achieved compared to the $Ta_2O_5$ design. The absorption of $Ta_2O_5$ typically starts to grow significantly at the edge around 310 nm. With the chosen QNL mixture, this edge was successfully shifted by 20 nm into the shorter wavelength range. However, it can also be observed that, due to the mixing behavior of the

QNL and the resulting lower refractive of $n = 1.8$ instead of $n = 2.1$, the width of the high reflection region is narrower. The second design describes an antireflection coating that was coated on both sides of a quartz glass. For this design, which consists of a total of 6 layers on each side, a QNL setting with a refractive index of $n = 1.6$ was used. This also shifted the absorption edge by about 60 nm, resulting in a significantly larger usable range. This allows us to significantly expand the application range of $Ta_2O_5$ by structuring it with $SiO_2$ as laminates into a range that would normally not be achievable with $Ta_2O_5$ as bulk material in a system at all.

## Funding

This work is funded by Innosuisse, the Swiss agency for innovation promotion in the project 110.023 IP-ENG "QUINTESSENCE – Quantized nanolaminates as industrial magnetron sputtering process".

## Conflicts of interest

There is no conflict of interests.

## Data availability statement

Data underlying the results presented in this paper are not publicly available at this time but may be obtained from the authors upon reasonable request.

## Author contribution statement

Conceptualization: Manuel Bärtschi, Stephan Waldner, Silvia Schwyn Thoeny, Xavier Maeder, Vivek Devulapalli, Fabian Steger, Thomas Frei.
Optical designs: Manuel Bärtschi.
Process development: Manuel Bärtschi, Fabian Steger.
Monitoring strategy: Stephan Waldner, Thomas Frei, Manuel Bärtschi.
Measurements: Manuel Bärtschi, Xavier Maeder, Vivek Devulapalli, Fabian Steger.
Software: Thomas Frei, Manuel Bärtschi.
Analysis: Manuel Bärtschi.
Visualization: Manuel Baertschi, Silvia Schwyn Thöny.
Writing: Manuel Bärtschi.
Review: Stephan Waldner, Silvia Schwyn Thöny, Xavier Maeder.

## References

1 Willemsen T, Geerke P, Jupé M, Gallais L, Ristau D, in *Proceedings of SPIE Laser Damage Conference, Boulder*, edited by G.J. Exarhos, V.E. Gruzdev, J.A. Menapace, D Ristau, M.J. Soileau (SPIE, Bellingham, 2016), p. 10014. https://doi.org/10.1117/12.2244828.
2 Steinecke M, Badorreck H, Jupé M, Willemsen T, Hao L, Jensen L, Ristau D, Quantizing nanolaminates as versatile materials for optical interference coatings, *Appl. Opt.* **59**, 236 (2020). https://doi.org/10.1364/AO.379131.
3 Jupé M, Willemsen T, Liu H, Steinecke M, Jensen L, Ristau D, *Manufacturing of Quantized Nanolaminates (paper TB.4)* (Optica Publishing Group, 2019). https://doi.org/10.1364/OIC.2019.TB.4.
4 Schwyn Thoeny S, Baertschi M, Baselgia M, Batzer M, *Process to deposit quantized nano layers by magnetron sputtering, WO2024/056313A1 (Patent)* (World Intellectual Property Organization: International Application Published under the Patent Cooperation Treaty, 2024).
5 Schwyn Thoeny S, Baertschi M, Batzer M, Baselgia M, Waldner S, Steinecke M, Badorreck H, Wienke A, Jupé M, Magnetron sputter deposition of $Ta_2O_5$-$SiO_2$ quantized nanolaminates, *Opt. Express* **31**, 15825 (2023). https://doi.org/10.1364/OE.487892.
6 Feldman A, in Proceedings Modeling of Optical Thin Films, San Diego (1988), p. 0821. https://doi.org/10.1117/12.941850.

## 12.3 Magnetron Sputter Deposition of Amorphous Silicon-SiO2 quantized Nanolaminates

While we coated the first $Ta_2O_5/SiO_2$-QNL layers and saw that the principle works, we came up with a second attempt to coat QNL with a much higher difference in refractive index and a modified experimental setup. We started simultaneously on the neighboring magnetron sputter device the coating of $\alpha Si/SiO_2$-QNL. Amorphous silicon ($\alpha Si$) has a much higher refractive index of $n_{\alpha Si} \approx 4$ at $1000\,nm$, which would have a significantly higher potential for a possible band gap shift relative to the high refractive index material [47].
The paper starts with again a short explanation about how to understand quantized nanolaminates based on[42],[75] and [44].
The setup uses the same magnetron sputter deposition type of tool but with a different setup for the process. To coat $\alpha Si/SiO_2$-QNL we used only one sputter source with a silicon target. Although the process uses only argon as the sputter plasma, it coats amorphous silicon without oxygen while the table is continuously turning. An additional capacitive coupled etching source is operated with a small amount of oxygen. So, oxygen ions are accelerated towards the passing $\alpha Si$ layer and oxidize the top silicon molecules, creating a $SiO_2$ layer on top of the amorphous silicon. This way again without interrupting the process, with every rotation a pair of high- and low refractive index materials are coated, creating the QNL system.
One has to be careful with interpreting the coating setup as it differs in the behavior compared to the $Ta_2O_5$ version. With $Ta_2O_5/SiO_2$ the ratio and therefore the refractive index can be directed directly by the sputter rate of the two materials which is in a limited range depending proportional to the generator power. The thickness of the layers, on the other hand, is directly proportional to the table rotation time, leading to an easy to handle system. The $\alpha Si/SiO_2$ process is slightly more complicated as the ratio depends on the sputter rate of the amorphous silicon but also the penetration depth and the amount of oxygen available at the etch source. This also means that the thickness control depends not only on the rotation time of the table but also on the penetration depth of the ions and the amount of oxygen. This leads to the problem that it is not as easy to coat a series of samples with the same ratio but different layer thicknesses because the processes could be different and needs to be adapted. Furthermore, because there could still be loose oxygen in or between the layers, which could lead to slow diffusion, the samples were annealed for an hour at $500\,°C$, which also leads to reduced loss in the absorption region in the amorphous silicon layers.
As first experiments, we coated a series of $\alpha Si/SiO_2$-QNL stacks where we varied only the table rotation speed. With this brief experiment, we could show that the faster the table rotates, the lower the absorption edge, similar to the insight in [46]. However, as previously mentioned, this is not directly traceable back to a quantization effect, since we also showed that the refractive index changes significantly with different table rotation times.
This is because the degree of oxidation as mentioned is dependent on the penetration depth of the ions. This view is also supported by the fact that the calculated thicknesses of the combined layer pairs are linear to the table rotation time.
To find out which portion of the shift in the absorption edge can be attributed to a quantization effect, we coated three layers with the same thickness ratio of the two materials. After measuring the coated layers with the photo spectrometer we calculated the refraction and extinction coefficients of one of them and used it to simulate the spectra with the thicknesses of the other two and compared it with the measured spectra. In this way we could show that we got a discrepancy of roughly $50\,nm$ in the absorption edge of the predicted and coated transmission spectrum from the $2.3\,nm$ to the $0.5\,nm$ layer pair thickness, which points to an additional effect.
We also calculated the Tauc-plots that lead to the same conclusion of a shift in the band gap of $> 50nm$.
With the help of EMPA we could also take TEM pictures of the coated layer stacks and verify not just the thickness calculation but also the fact that the materials form sharp and uniform transition zones.
In the end, we designed and coated a 16 layer design of $\alpha Si/SiO_2$ as high index material and $SiO_2$ as low index material, which blocks the whole visible range but has a high transmission in the NIR range. Although a design with only $\alpha Si$ would have a high absorption up to $900\,nm$, a comparable design with $TiO_2$ would be much thinner and would not be able to block the whole visible part of the spectrum.
With this demonstration, we were able to demonstrate the great advantage of $\alpha Si$-QNL compared to

classical materials under specific conditions, especially if one assumes that only one type of sputter material is required and a very inexpensive one, too.

### Contribution

Since the work on these experiments was carried out in part parallel with the work of [46], I was only partially included everywhere. I assisted with the process engineering and measurements, participated in discussions about the calculations, analysis, and in the end interpretation of the results.

ADVANCED PHOTONICS RESEARCH
www.adpr-journal.com

# Magnetron Sputter Deposition of Amorphous Silicon–$SiO_2$ Quantized Nanolaminates

*Silvia Schwyn Thöny,* Manuel Bärtschi, Marietta Batzer, Manuel Baselgia, Raphael Gmünder, Amit Sharma, Tijmen Vermeij, Xavier Maeder, and Stephan Waldner*

**Quantization effects in nanolaminate structures of oxide materials are proposed and experimentally demonstrated only recently. Herein, the material combination of amorphous silicon and $SiO_2$ deposited by magnetron sputtering is investigated and it is shown that the quantization effect can be observed indeed. Transmission electron microscopy characterization gives evidence of continuous layers of amorphous silicon and $SiO_2$ with well-defined interfaces. The deposition process is described and the tunability of the refractive index and the bandgap energy is demonstrated. By doing so, the advantages of this novel material over classical optical materials are shown and feasibility is proved. As an example, a longpass optical interference filter with edge at 720 nm is deposited using quantized nanolaminates as the high and $SiO_2$ as the low refractive index material. This filter can be deposited successfully with close match to the design. It shows a blocking range throughout the visible spectrum whereas a comparable filter based on $SiO_2$–$TiO_2$ only blocks 500–700 nm.**

## 1. Introduction

Optical interference coatings such as antireflection, mirror or filter coatings are based on stacks of materials with at least two different refractive indices, *n*. The interference effect is stronger if the difference in refractive index between materials is larger. Hence, a stack design based on materials with a larger difference in refractive index requires a smaller number of individual layers and thus less overall thickness to fulfill the same specification as a design based on materials with a smaller difference. In addition to the refractive index, the materials have to fulfill other requirements, among those being transparent with negligible losses in the wavelength range of interest.

However, in dielectric materials the refractive index and absorption edge are linked.[1] Materials with high refractive index have their absorption edge at a long wavelength, while low refractive index materials have the absorption edge at a short wavelength. $TiO_2$ is the dielectric material with the highest refractive index, which is transparent in the visible range (VIS) of the spectrum starting to transmit at ≈400 nm. Having a material at disposition with a higher refractive index while being transparent in the VIS would be of broad practical relevance because it would allow interference designs with a lower number of layers and reduced overall thickness. As will be shown in this article, the deposition rate of the nanolaminates exceeds the one of $TiO_2$. Both reduced thickness and high deposition rate are expected to result in increased productivity of the coating systems and reduced manufacturing cost.

Apart from the fabrication of nanolaminates, one approach to decouple the refractive index from bulk material properties is glancing angle deposition,[2,3] in which a columnar film structure is formed, which reduces the effective refractive index. Thus, interference effects will occur between bulk-like layers and layers with columnar structure of one and the same material. This opens up interesting effects such as plate polarizers or higher laser damage resistance due to the absence of interfaces between different materials.

A comparable approach are the self-organizing structures formed by ion etching of organic films as described by refs. [4,5]. Again, the effective refractive index of the layer is reduced by etching, which introduces localized and unlocalized porous structures.[6] This effect is beneficial, if the layer is used as the outermost layer in an antireflection design. As for glancing angle deposition, the drawback of the self-organizing layers is the increased sensitivity to environmental conditions.

A more recent concept to overcome the connection between the two characteristics is quantized nanolaminates (QNLs), which were first reported by Willemsen, Jupé et al. in 2016[7] and investigated in more detail in refs. [8,9]. In this concept, thin

S. S. Thöny, M. Batzer, M. Baselgia, R. Gmünder, S. Waldner
Evatec AG
Hauptstrasse 1a, 9477 Trübbach, Switzerland
E-mail: silvia.schwyn-thoeny@evatecnet.com
M. Bärtschi
RhySearch
Werdenbergstrasse 4, 9471 Buchs, Switzerland
A. Sharma, T. Vermeij, X. Maeder
Laboratory for Mechanics of Materials and Nanostructures
Empa, 3602 Thun, Switzerland
The ORCID identification number(s) for the author(s) of this article can be found under https://doi.org/10.1002/adpr.202400057.



**DOI: 10.1002/adpr.202400057**

layers of high and low refractive index with a thickness in the nanometer range or below are stacked. The limited structure size leads to a change of the energy gap, which can be adjusted by the physical thickness of the materials, whereas the thickness ratio of the materials determines the effective refractive index of the QNL. Similar effects are observed in multiquantum well structures of crystalline material. However, Willemsen et al.[10] have shown in their investigations that the crystalline structure is by no means the precondition for the occurrence of quantum effects, but that they can also be observed in amorphous dielectric materials.

In optical interference coatings, the decoupling of bandgap and refractive index potentially offers the advantage of using the QNL material combination instead of using a specific material. As an example, in the UV range the bandgap of $Ta_2O_5$ can be pushed toward shorter wavelength and can thus replace the use of $HfO_2$. This is desirable because hafnium targets are expensive and because $HfO_2$ has a tendency to form polycrystalline films with grain boundaries which can cause losses by straylight. First demonstrations of this approach are given in refs. [7–9].

The article by Henning et al.[11] explains that the combination of amorphous silicon (aSi) and $SiO_2$ has the potential to be transparent even in the visible wavelength range with an effective refractive index higher than 2.7. In a recent article,[12] Kreuzer et al. show results of magnetron sputtered aSi/$SiO_2$ nanolaminates using cylindrical targets with varying aSi layer thicknesses and compositions. A shift in bandgap is observed. However, Kreuzer et al. state that this shift is approximately one order of magnitude smaller than expected.

It is thus the scope of this article to investigate a wide parameter field for the deposition of nanolaminates of aSi–$SiO_2$ by magnetron sputtering from a planar target and to demonstrate the potential of optical interference coatings using the nanolaminate as high index material.

Nanolaminates showing the quantization effect were demonstrated experimentally for dielectrics such as $SiO_2$ combined with $Ta_2O_5$, $HfO_2$, or $Al_2O_3$, but not for aSi–$SiO_2$. The deposition methods reported are atomic layer deposition (ALD), ion beam sputtering (IBS),[7–9] and magnetron sputtering.[12,13] Although ALD and IBS lead to good results, they do have drawbacks with regard to volume production, whereas magnetron sputtering was demonstrated on a volume production machine with deposition rates comparable to standard values.

As reported in ref. [13], the turntable configuration of the Evatec CLUSTERLINE 200 BPM magnetron sputter system is ideally suited for the deposition of QNL because both materials, $SiO_2$ and $Ta_2O_5$, can be deposited in one table rotation. We will show in this article how the process for the material combination aSi and $SiO_2$ is implemented in this magnetron sputter deposition system. This time the sputter source is used for the deposition of aSi, whereas the $SiO_2$ is formed when passing a plasma source operated with oxygen that generates reactive atomic oxygen neutrals and ions. Again, the turntable exposes the growing film sequentially to both sources. A series of experiments was conducted, in which the thicknesses of individual layers in the nanolaminate was varied by changing the speed of the table rotation. With these experiments we will demonstrate that the quantum effect is observed as predicted in ref. [12]. Furthermore, the structure of the aSi/$SiO_2$ QNL is analyzed by transmission electron microscopy (TEM). We will then take these results and show that a longpass filter blocking the vis and transmitting from 700 nm onward can be realized with just 16 layers combining $SiO_2$ and QNL based on aSi–$SiO_2$.

## 2. Theory

As mentioned in the introduction, in standard dielectric materials the refractive index and the energy of the absorption gap are fundamentally linked.[1] Quantized nanolaminates proposed in refs. [7–9], however, allow to set the refractive index and the absorption edge independently within the limits given by the bulk properties of the high and low index material.

The theory of the quantized nanolaminates is detailed in the publications[7–9] and summarized hereafter for the sake of clarity. First of all, a brief look at the electronic material properties is necessary. As already mentioned, optical coatings mostly produce amorphous or polycrystalline materials whose band structure is not clearly defined; nevertheless, an energy gap between quasi-free ground states and higher conduction states is present. Thus, the bandgap itself can be regarded as a depletion zone of states and the densities between bound and free states are so low that they can be neglected. Thus, the potential well, which is necessary for the quantization, is clearly defined.

The electron mobility can be limited in the growth direction if two materials with high and low bandgap are combined in a thin periodic structure. In this case, the low index material will act as a barrier, whereas the high index material acts as the quantum well, as illustrated in **Figure 1**. As this is a simple potential consideration, even nonclosed atomic layers can lead to a suitable periodic potential.

The thickness of the quantum well will determine the shift in bandgap, whereas the thickness ratio of high-to-low bandgap material will determine the refractive index. Thus, the novel concept of so-called QNLs allows for independent adjustment of the optical bandgap and the refractive index. To give an idea of the thicknesses required, we turn to data published for $SiO_2$–$Ta_2O_5$ in ref. [13], which shows that the quantum well layer should be much smaller than 2 nm to achieve a shift, which is of practical use.

## 3. Experimental Section

The quantized nanolaminates were deposited using a Clusterline 200 BPM magnetron sputter deposition system manufactured

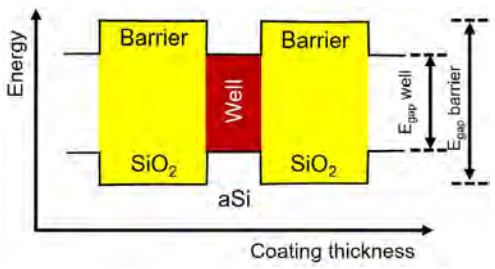


**Figure 1.** Periodic structure of high and low bandgap areas, which limit the electron mobility.

by Evatec, which was discussed in detail in refs. [14–16]. For the sake of clarity, we will summarize the main parts of the system as well as the mode of operation in this Experimental Section. As shown in **Figure 2**a, the system uses a sputter down configuration with a maximum of four magnetron sputter sources denoted with (1). For the deposition of aSi–$SiO_2$ QNL, one sputter source was equipped with a silicon target with the purpose to deposit an aSi layer. The $SiO_2$ layer is formed by the plasma source (PSC) (2), where the aSi film partially gets oxidized by the oxygen plasma. The plasma source is a RF-driven capacitively coupled discharge, where oxygen as operating gas is partially dissociated and ionized. The schematic tool configuration is shown in Figure 2b.

When depositing the longpass filter consisting of aSi–$SiO_2$ QNL as the high refractive index material and $SiO_2$ for the low refractive index material, a second sputter station equipped with a silicon target was used to reactively deposit the low index $SiO_2$ layers.

The turntable configuration is perfectly suited for the deposition of QNL. With the continuous table rotation substrates pass repeatedly beneath the active sources, thereby exposing the substrates to both the sputter and the plasma source with each rotation. The total thickness deposited in one turn is determined by the rotation speed of the table, a parameter which can easily be varied in a wide range, and the deposition rate. The thickness ratio of the aSi and $SiO_2$ materials is determined by the sputter and the plasma source power, which can be adjusted individually. Further deposition parameters, which influence the deposition rate and material properties are the gas flows of argon and oxygen. Deposition rates for QNL layers tend to be as high as those for single aSi because the active source is run at standard conditions.

This deposition system has a capacity of 15 substrates of diameter 200 mm. Substrate loading and unloading is executed automatically through a vacuum transfer module and load-lock. The system is also equipped with broad band and monochromatic optical monitoring.[17]

The samples were deposited on double side polished fused silica substrates. These were characterized by spectrophotometry in transmission $T$ and reflection $R$ both at an angle of 8° on the exact same spot on the sample by using a PhotonRT photospectrometer by EssentOptics.

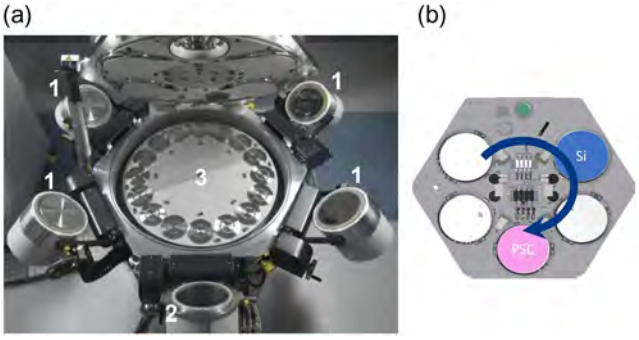


**Figure 2.** a) Evatec Clusterline BPM magnetron sputter system opened to maintenance position: sputter sources (1), plasma source (2), and turn table (3). b) Schematic of sputter process for the QNL layers of aSi–$SiO_2$.

The effective refractive index $n_{\text{eff}}$ and the extinction coefficient $k$ in the transparent range of the coating were determined using OptiChar by Optilayer. The models used were normal dispersion for $n$ and UV–vis mode for the extinction coefficient $k$. This evaluation also allows us to determine the physical thickness $d$ of the nanolaminate stack.

The same commonly high accuracy methodology is used to determine the properties of the standard dielectrics, in our case $SiO_2$ and aSi. Their optical constants serve as a reliable input for a rather simple, but robust evaluation procedure based on the concept of Wiener bounds limit.[18,19] In mixed component systems, the refractive index can be modeled by applying the effective medium theory.[20] The effective refractive index of the resulting metamaterial $n_{\text{eff}}$ is determined by the volumetric fraction $f$ of the high refracting material in the QNL

$$n_{\text{eff}}^2(\lambda) = f\, n_{\text{high}}^2(\lambda) + (1-f)\, n_{\text{low}}^2(\lambda) \tag{1}$$

The effective refractive index $n_{\text{eff}}$ is derived from the spectral measurements in $T$ and $R$ as detailed above. The refractive indices of $n_{\text{high}}$ and $n_{\text{low}}$ are determined from aSi and $SiO_2$ single layers. The values used were: aSi $n_{\text{high}} = 3.937$ and $SiO_2$ $n_{\text{low}} = 1.466$, both indices relate to a wavelength of 1000 nm. Equation (1) then allows us to calculate the volume fraction $f$ of the two materials. This simple formula shows that the refractive index of the QNL is always between the values of the high and low refractive index materials and defines the physical refractive index limits of the nanolaminate.

The thickness per table pass can be calculated by dividing the physical thickness $d$ of the nanolaminate stack by the number of passes in the deposition. The thickness of the individual high and low refractive index layers in the QNL can then be calculated by multiplying the total thickness per pass with the volume fraction $f$ of the high index material, respectively (1-f) for the low index material.

The Tauc-plot method[21] was used to determine the optical bandgap based on the optical absorption coefficient calculated from the spectrophotometric measurements in transmission and reflection.

All samples used in this article underwent an annealing step at 500 °C for 1 h in air. These conditions led to the lowest loss values, based on the results of a series of annealing tests involving variations in time and temperature.

The structure of the aSi–$SiO_2$ QNL was characterized by scanning transmission electron microscopy (STEM) imaging using a Themis 200 G3 spherical aberration (probe)-corrected TEM (Thermo Fischer, Waltham, USA), operated at 200 kV. This was performed on thin lamellae of the cross section of the coating, prepared via focused ion-milling (FIB lift-out technique) using a dual beam FIB-SEM Tescan Lyra FEG system (Brno, the Czech Republic). The FIB parameters for the lift-out were 30 kV and 3 nA for the rough cutting and 30 kV and 500 pA for the polishing. The lamella was thinned down to 30 nm using 30 kV with 100 and 50 pA, with a final polishing at 5 kV with 50 pA. Elemental distribution and concentration line profile were acquired using energy-dispersive spectroscopy in STEM mode.

## 4. Results

### 4.1. Quantum Nanolaminate Layers of aSi–$SiO_2$

In a first experiment, the Si sputter source and plasma source were run at 5 and 1 kW, respectively. When the sample passes the sputter source, a film of aSi is deposited. With the table rotation this sample is then translated to pass beneath the plasma source where a part of the previously deposited aSi layer gets oxidized. This sequence is repeated for a defined coating time.

In a first experiment, the table speed was varied from 1.5 to 12 s per pass, resulting in an increasing thickness of the individual nanolaminate layers. The coating time was fixed for this series of four samples and resulted in a nanolaminate stack thickness of ≈180 nm. The number of individual nanolaminate layers varies from 300 to 38 corresponding to 1.5–12 s/pass. In **Figure 3**, the curves of the spectrophotometric measurements in transmission of the 4 runs reveal three characteristics of the layers: first, the wavelength of the absorption edge, second, the losses in the transparent wavelength range, and third, the refractive index of the layers.

First, the absorption edge of this series of deposition runs shifts toward shorter wavelength the faster the table speed. The absorption edge of the sample with 1.5 s/pass lies at the shortest wavelength, whereas 12 s/pass results in the longest wavelength with a difference of ≈280 nm between the samples at a fixed transmission of 75%. For comparison, the black dashed line indicates the onset of transmission of a regular aSi layer.

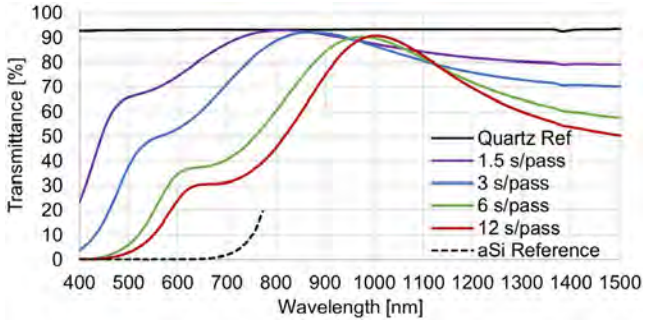


**Figure 3.** Transmittance spectra of QNL layers with the same power ratio of aSi to PSC, but with table speeds (1.5/3/6/12 s/pass).

Second, the transmission maxima at $\lambda/2$ optical thickness closely touch the solid line of the uncoated quartz indicating low absorption of the QNLs in the longer wavelength range.

Third, the transmission at 1500 nm increases with table speed. This is indicative of a reduction in effective refractive index of the nanolaminates. In the following we will first explain the shift in refractive index and then the shift in the absorption edge.

As explained in the Experimental Section, the effective refractive index $n_{eff}$ and the total layer thickness $d_{tot}$ can be determined from the transmission and reflection measurements in the transparent region. The thickness deposited per table turn can then be obtained by dividing $d_{tot}$ by the number of table-turns. As expected, the thickness deposited per turn is linear with the table speed, as can be seen in **Figure 4**a. However, the individual thicknesses of aSi to $SiO_2$, calculated according to Equation (1), do not increase linearly as can be seen from Figure 4b. In the run with the fastest table speed, an aSi layer of 0.7 nm thickness was deposited, which was subsequently oxidized by the oxygen plasma of the PSC to an $SiO_2$ layer with a thickness of 0.6 nm. For the slowest table speed of 12 s/pass however, the 4.2 nm aSi only gets oxidized to a thickness 1.8 nm $SiO_2$. The decrease in oxidized thickness is expected: the energetic oxygen species generated in the plasma source have a limited penetration depth even if the exposure time is extended. In consequence, thicker layers have a reduced fraction of $SiO_2$, which, in turn, will lead to a higher refractive index of the nanolaminate as can also be seen in Figure 4b on the right axis.

In a next step, we will take a look at the shift of the absorption edge. The strong shift in absorption edge, as shown in Figure 3, can mainly be attributed to the change of the average stoichiometry over the total thickness of the nanolaminate stack as explained above. In order to see whether a quantum effect is present, films with increasing individual nanolaminate thicknesses, but constant thickness ratio of aSi and $SiO_2$ have to be compared. For this to be the case, adjustments had to be made in the process settings such as Si source power and oxygen flow.

An example of such an experiment is shown in **Figure 5**a: runs 1–3 have a very close thickness ratio of aSi:$SiO_2$ of around 0.68, as can be seen from the overlaying minimum transmission value at 1650 nm. Thus, these films have the same refractive index and average composition, but decreasing total thickness per pass of 2.3, 1.1, and 0.5 nm. The transmission measurement of the three runs shows a shift in absorption edge of 57 nm. We will clarify now whether these films are mixtures, and the edge shift is due

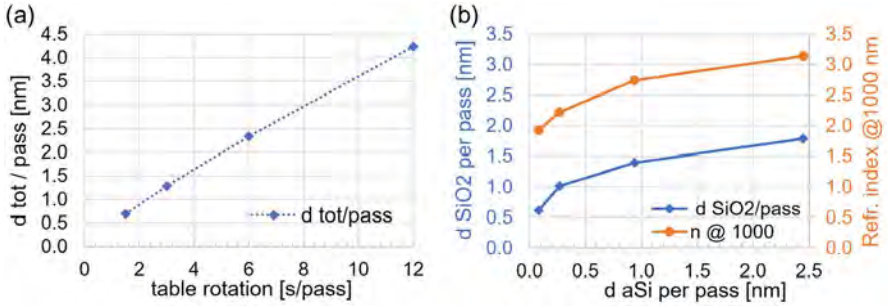


**Figure 4.** a) The total thickness per pass increases linearly with increasing time per pass. b) Lower increase of the $SiO_2$ thickness compared to aSi (left axis) which leads to an increase in refractive index (right axis).

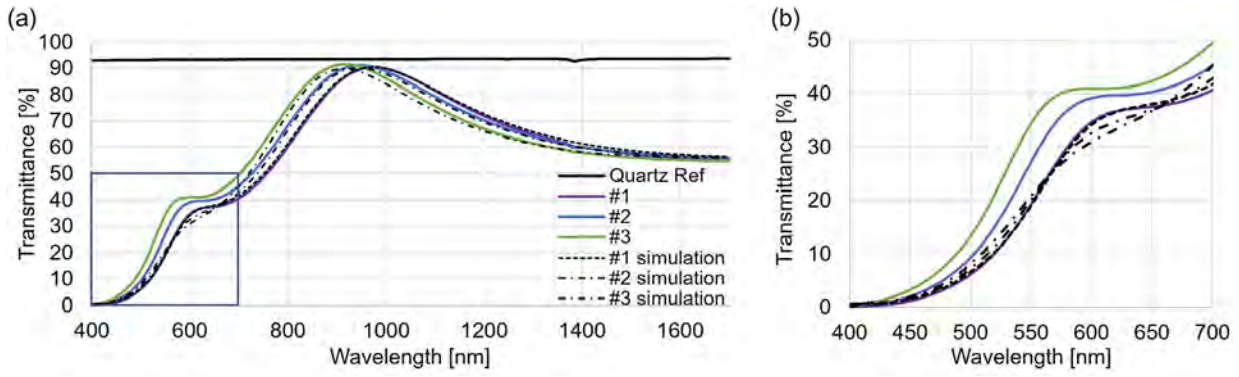


**Figure 5.** a) Shift of absorption edge in transmission of three films with the same thickness ratio of aSi:$SiO_2$ but decreasing individual nanolaminate thickness. b) Inset of the absorption region showing the simulation of the mixture in dashed lines.

to the slightly different stack thickness or whether the shift is due to the quantization effect. To evaluate the first hypothesis the dispersion of the refractive index and extinction coefficient for run 1 is determined. In accordance with the assumption of a mixture, the transmission curves for the 3 thicknesses are simulated, based on the same dispersion values. The three curves shown as dashed lines in Figure 5 overlay at the absorption edge; thus, the effect cannot be explained with mixture materials. Hence, the edge shift of these layers with different nanolaminate thickness, but constant material ratio can be attributed to the quantization effect as explained in the theory section.

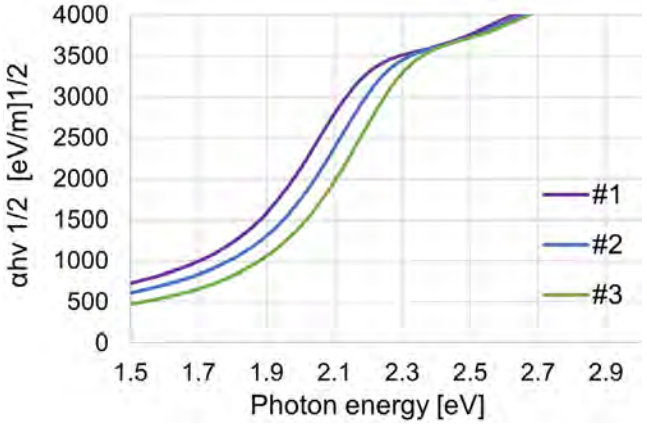


**Figure 6.** Tauc plot of samples 1–3 showing the shift in bandgap energy.

The final confirmation of quantization is seen in the shift of the bandgap energy in **Figure 6**, which was determined from the Tauc plot as described in ref. [21]. The gap energy increases with the decreasing aSi well thickness of samples 1–3 by 0.14 eV, which corresponds to a shift of 58 nm in wavelength. This result determined on three different nanolaminates with the same composition and refractive index confirms that the quantization effect can be observed in the material system aSi–$SiO_2$ deposited by magnetron sputtering.

As mentioned in the Experimental Section, all samples shown so far were annealed at 500 °C in air ambient. **Figure 7**a shows the losses (100%–*T*–*R*) of samples 1–3 before and after annealing. Two effects can be observed: a faster decay of losses in the transmission region and a shift of the absorption edge toward shorter wavelength for samples with annealing. The relative edge shift between samples is very similar in pre- and postannealed samples as can be seen in Figure 7b, confirming that the nanolaminate structure and quantization effect are preserved upon annealing. It is worth noting, that for the present samples an increased shift of the gap energy is observed the thinner the barrier. However, for even thinner barriers tunneling is expected to set in and hence the gap shift will reduce.

Figure 7b shows that the refractive index among the samples is in a very narrow band but shows a reduction of ≈0.04 after annealing. This indicates that the annealing effect is independent of the thickness of individual aSi and $SiO_2$ layers. The refractive index after annealing remains high at $n \approx 2.75$ ($\lambda = 1000$ nm), which implicates that if oxidation is the origin of the reduction

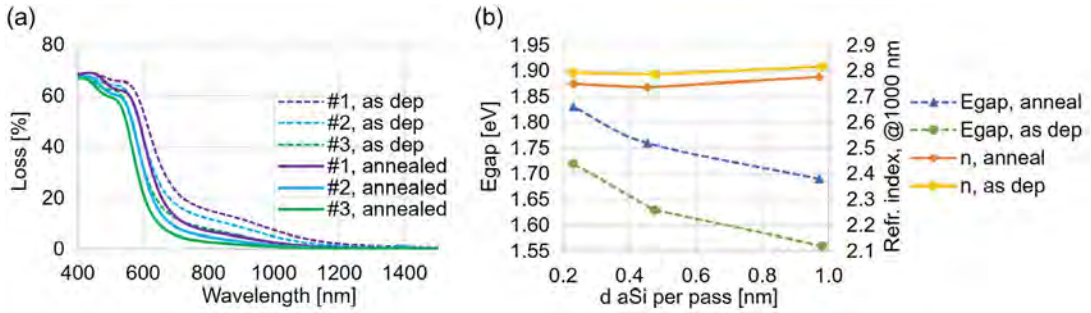


**Figure 7.** a) Losses decrease for the samples after annealing. b) Refractive index and gap energy for samples before and after annealing.

of the index, the effect is small (a few percent in thickness) and precludes a substantial oxidation of aSi layers to $SiO_2$. To clarify the nature of the changes, dedicated TEM analysis will be conducted to get insight into the effect of annealing.

Subsequently, experiments were performed varying different deposition parameters. **Figure 8** shows the dependence of the gap energy and the refractive index with oxygen flow in the plasma source for a series of runs with table speed of 1.5 s/pass. With an increasing availability of oxygen in the plasma, the $SiO_2$ nanolayer thickness increases and thus the refractive index decreases while the gap energy, in turn, increases. The full evaluation as well as additional experiments to push the QNL effect further will be the scope of future work.

### 4.2. TEM Characterization

A STEM high-angle annular dark-field (HAADF) image of the entire cross section of an aSi–$SiO_2$ QNL deposited on fused silica is shown in **Figure 9**, with an increase of the magnification in the figure inset. This is the sample shown in Figure 3 deposited with 6 s/pass. The coating has a total thickness of 179.5 nm with 75 bilayers. The layering contrast is coming from the slight difference in density between the aSi and $SiO_2$ layers, the bright layers being the $SiO_2$. The STEM images show that the layers are continuous with a sharp and very well-defined interface between the aSi and the $SiO_2$ layers. The mean thickness of the aSi and $SiO_2$ layers is 0.95 and 1.52 nm, respectively. These values are in good agreement with the thicknesses calculated from the optical measurements being 0.9 and 1.45 nm with a total thickness of 175.5 nm. An additional periodicity in layer thickness is seen in the STEM images and is in the focus of further investigations.

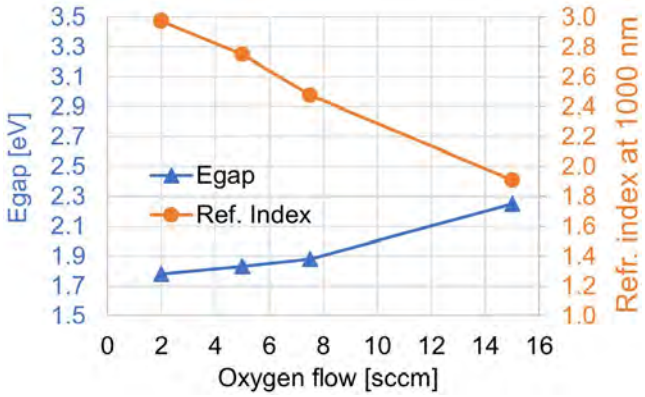


**Figure 8.** An increase of the oxygen flow in the PSC leads to a decrease in refractive index and an increase in $E_{gap}$.

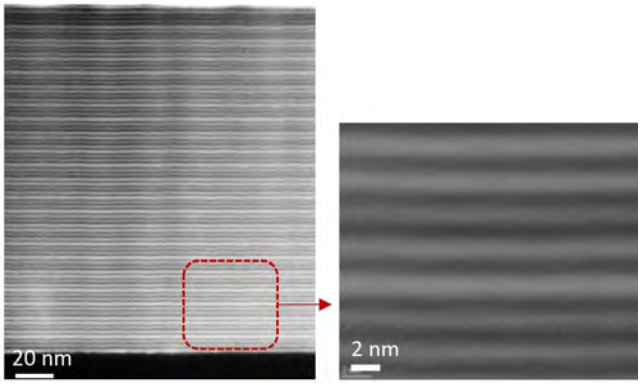


**Figure 9.** STEM HAADF image of the entire cross section of an aSi–$SiO_2$ QNL. The figure inset shows the details of the nanolaminates.

### 4.3. Longpass Filter

As shown in the previous section, QNL can be manufactured with a wide range of refractive indices and gap energies. The nanolaminate of run #3 from Section 4.1 was chosen as the high and $SiO_2$ as low refractive index material to deposit a longpass filter. As described in the Experimental Section, the QNL was deposited using the aSi sputter source in combination with the plasma source, whereas the $SiO_2$ layers were deposited from the additional sputter source. A design was chosen with 16 layers of $\lambda/4$ optical thickness with some of the outer layers being adjusted to provide an edge formed curve. Material #3 has a refractive index of 3.18 and 2.75 at wavelength 550 and 1000 nm, respectively, and $E_{gap}$ of 1.83 eV. In this case, a high index layer with optical thickness of $\lambda/4$ at 600 nm has a physical thickness of 49 nm and consists of a total of 180 alternating layers of aSi and $SiO_2$. Thanks to the turn table configuration of the BPM magnetron sputter deposition system, the deposition rate of the nanolaminate is as high as for a standard aSi layer.

**Figure 10** shows the measured spectrum of the longpass filter. It confirms that this filter indeed blocks the entire visible part of the spectrum and transmits the near-infrared (NIR) part. For reference, the analogous design using standard aSi as high index material will suffer from high losses in the wavelength region of 700–900 nm and only reach full transparency beyond 1000 nm; this is due to the absorption edge at higher wavelength.

In situ broadband optical monitoring in reflection in a wavelength range of 380–980 nm was used to monitor the coating thickness. It turned out that the reflection signal of the QNL developed completely regular, exactly as a layer with the corresponding effective refractive index would evolve. We can therefore conclude that optical monitoring is perfectly suited for controlling the thickness in film stacks with QNLs.

For comparison, the same type of filter was coated based on the standard material combination $SiO_2$–$TiO_2$ also using 16

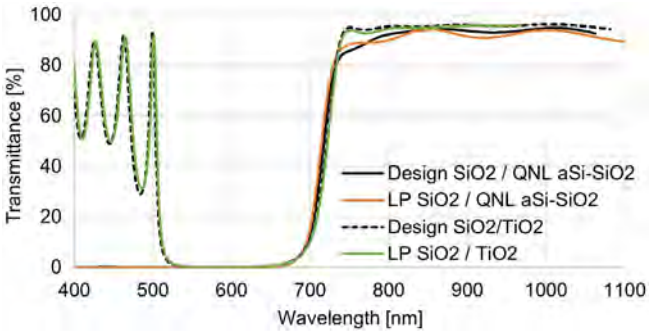


**Figure 10.** Transmittance of a longpass filter based on $SiO_2$/QNL aSi–$SiO_2$ and on $SiO_2$–$TiO_2$ for comparison.

layers, based on the same design principle as the nanolaminate filter. In Figure 10, it becomes immediately apparent that the standard design does only block half of the visible range, whereas the QNL design blocks the entire range. Of course, it is possible to reach full blocking with an $SiO_2$–$TiO_2$ design, however at the expense of double the number of layers.

The standard coating has a total thickness of 1.4 μm as compared to 1 μm for the QNL–$SiO_2$ design. Furthermore, the deposition rate of the QNL is about double the rate of $TiO_2$. Both reduced thickness and increased deposition rate result in a cut of the deposition time by a factor of 2. Thus, this comparison shows the large potential of the new nanolaminate material to significantly boost productivity and reduce manufacturing cost.

## 5. Conclusion

As demonstrated in this article, magnetron sputtering using a deposition tool with turntable configuration is ideally suited to depositing quantum nanolaminate layers. The individual layers of the nanolaminate stack are deposited sequentially, the aSi when passing under the silicon source and the $SiO_2$ by oxidation of the top part of the aSi layer when passing the plasma source. This sequence is repeated with every rotation of the turntable. The setting of the table rotation speed allows to select the total thickness of aSi and $SiO_2$ per turn, whereas the power setting of the sputter and plasma sources allows to set the thickness ratio of aSi and $SiO_2$. We demonstrated individual layers with a few tenth of nm and a wide range of aSi volumetric fractions $f$ of 0.1–0.75.

The single layers show a large shift in the absorption edge. The analysis of the data revealed two mechanisms causing the shift. As a first effect, a change in composition leads to a shift of the absorption edge to shorter wavelength the higher the $SiO_2$ fraction in the film. This is an effect, which is well known. The second effect, however, caused by quantization, is demonstrated using aSi–$SiO_2$ QNL with the same average composition: they show a shift in absorption edge when the thickness of the aSi barrier layer decreases while the refractive index is constant. This is in accordance with theory, as described in Section 2.

The TEM analysis confirms that continuous layers with sharp and well-defined interfaces are present in the QNL.

In a next step, QNL layers were used as the high index material in an optical interference filter. We demonstrated that the turntable configuration of the sputter system leads to a viable manufacturing process for this longpass filter blocking the visible part of the spectrum while transmitting the NIR. From a technical standpoint, the deposition of these filters runs like a standard process with the difference that in the QNL layer two sources are powered. Furthermore, optical monitoring can also be used without any adaption.

The longpass filter coating was in good agreement with the design and showed good transmission in the wavelength range above 700 nm, thus confirming the precise and reproducible deposition in the sub-nm range. As a comparison, a standard $SiO_2$/$TiO_2$ longpass filter was also deposited. This showed that with the same number of layers the blocking range was much narrower than for the QNL design. For a standard filter with the same characteristic as the QNL filter, double the number of layers would be required. This clearly shows that the concept of QNL indeed opens up a wide field for novel applications with significant improvements in productivity.

## Acknowledgements

The authors thank Innosuisse—Swiss Innovation Agency for funding Project 110.023 IP-ENG.

## Conflict of Interest

The authors declare no conflict of interest.

## Data Availability Statement

The data that support the findings of this study are available from the corresponding author upon reasonable request.

## Keywords

bandgap, low-loss coating, magnetron sputtering, meta materials, optical thin films, quantized nanolaminates

Received: April 4, 2024
Revised: June 13, 2024
Published online: July 22, 2024

[1] H. Finkenrath, *Infrared Phys.* **1988**, *28*, 327.
[2] T. Tolenis, L. Grineviciute, L. Smalakys, M. Ščiuka, R. Drazdys, L. Mažule, R. Buzelis, A. Melninkaitis, *Sci. Rep.* **2017**, *7*, 10898.
[3] L. Grineviciute, M. Andrulevicus, A. Melninkaitis, R. Buzelis, A. Selskis, A. Lazauskas, T. Tolenis, *Phys. Status Solidi A* **2017**, *214*, 1700764.
[4] U. Schulz, *Appl. Opt.* **2006**, *45*, 1608.
[5] U. Schulz, F. Rickelt, P. Munzert, N. Kaiser, *Opt. Mater. Express* **2014**, *4*, 568.
[6] H. Badorreck, M. Steinecke, L. Jensen, D. Ristau, M. Jupé, J. Müller, R. Tonneau, P. Moskovkin, S. Lucas, A. Pflug, L. Grinevičiūtė, A. Selskis, T. Tolenis, *Opt. Express* **2019**, *27*, 22209.
[7] T. Willemsen, P. Geerke, M. Jupe, L. Gallais, D. Ristau, *Proc. SPIE* **2016**, *10014*, 100140C.
[8] M. Jupé, T. Willemsen, H. Liu, M. Steinecke, L. Jensen, D. Ristau, in *Optical Interference Coatings Conf.*, Santa Ana Pueblo, New Mexico, USA **2019**.
[9] M. Steinecke, H. Badorreck, M. Jupé, T. Willemsen, L. Hao, L. Jensen, D. Ristau, *Appl. Opt.* **2020**, *59*, A236.
[10] T. Willemsen, M. Jupé, M. Gyamfi, S. Schlichting, D. Ristau, *Opt. Express* **2017**, *25*, 31948.
[11] P. Henning, M. Jupé, S. Bruns, T. Melzig, M. Steinecke, A. Wienke, M. Vergoehl, in *Optical Interference Coatings*, **2019**.
[12] K. Kreuzer, P. Henning, M. Vergoehl, S. Bruns, T. Melzig, C. Patzig, R. Feder, *Appl. Opt.* **2024**, *63*, 1641.
[13] S. S. Thöny, M. Bärtschi, M. Batzer, M. Baselgia, S. Waldner, M. Steinecke, H. Badorreck, A. Wienke, M. Jupé, *Opt. Express* **2023**, *31*, 15825.
[14] S. S. Thöny, M. Chesaux, S. Gees, A. Frigg, in *Optical Interference Coatings Conf.*, Tucson, Arizona, USA **2016**.

[15] M. Chesaux, S. S. Thöny, S. Gees, A. Frigg, in *Optical Interference Coatings Conf.*, Tucson, Arizona, USA **2016**.
[16] S. S. Thöny, S. Gees, E. Schüngel, in *Optical Interference Coatings Conf.*, Santa Ana Pueblo, New Mexico, USA **2019**.
[17] S. Waldner, J. Buchholz, R. Benz, in *Optical Interference Coatings Conf.*, Santa Ana Pueblo, New Mexico, USA **2019**.
[18] C. Franke, O. Stenzel, S. Wilbrandt, J. Wolf, N. Kaiser, A. Tünnermann, *Appl. Opt.* **2015**, *54*, 2362.
[19] R. Jansson, H. Arwin, *Opt. Commun.* **1994**, *106*, 133.
[20] A. Feldman, *Model. Opt. Thin Films* **1988**, *821*, 129.
[21] B. D. Viezbicke, S. Patel, B. E. Davis, D. P. Birnie, *Phys. Status Solidi B* **2015**, *252*, 1700.

## 12.4 Nanoindentation on Ta2O5 SiO2 QNL

As this paper has not been published yet, only the submitted version has been taken into account.
During the project, EMPA performed nanoindentation tests on a series of samples, all of which had the same material ratio and total thickness but different layer pair thicknesses.
This is interesting because there are a large number of material hardness tests for nanolaminate structures, but most of them are crystalline/amorphous or metal/metal, and the fact that we were able to measure both amorphous/amorphous and oxide/oxide very regularly and in any pair thickness was new [74].
All coated samples have a 50:50 volume ratio of $Ta_2O_5 : SiO_2$, and also a total thickness of $1\mu m$, the pair thicknesses vary between 2, 4, 10, 20, 40, ,200 and $334nm$. In addition, pure $Ta_2O_5$ and $SiO_2$ films with the same thickness were coated and measured as reference.
Using a Berkovich tip and an indentation depth of $300nm$ showed for the $Ta_2O_5$ layer a pile of material around the dent which was expected due to the ductile response of the material [78], while the pure $SiO_2$ film showed a brittle fracture in the corners of the dent. While samples with thinner pairs showed more ductile behavior like $Ta_2O_5$, the thicker samples showed more brittle behavior like $SiO_2$. With higher ductility, the crack building resistance also increased, which is correlated with higher interface density, suppressing crack formation.
The $SiO_2$ film showed the highest hardness, whereas the laminates showed a decreasing behavior as the pairs are thinner. The unexpected thing is that all coated laminates have a lower hardness than the combined material according to the rule that mixing with metal laminates should have [79], [80].
TEM images of the cross-section with the underlying SI wafer as substrate were taken of each sample. It has been shown that vertically shear bands form beneath the dents and they are further apart each other, the thicker the laminate pairs are.
In an image of a shear band in the sample $SiO_2$, it is shown that it continues through the whole film to the substrate below.
An interesting finding is that crystalline silicon oxide has formed in the shear band of the previously amorphous film material, whereas amorphous silicon has formed in the previously crystalline substrate.
By comparing the shear band images of the samples with the thickness of the pair 4 and $40nm$, it could be shown that for the thinner probe, each interface can stop the growth of a shear band and also distribute the force in multiple deformation pathways leading to higher plasticity. The measurement also shows that the most deformed regions are completely ripped. For the thicker pairs with lower interface density, no rupture is shown in the shear bands but chemical mixing. The different behavior indicates a different deformation mode.
The density measurements on the $20nm$ pair showed that the densification spread in all directions during the indentation tests and was not limited to a vertical shear band, as was the case with the $SiO_2$ sample.
The main finding from the work is that the many layers increase plasticity and toughness, as they distribute the force more widely and allow for slight deformation.

### Contribution

My contribution is largely limited to process development and ultimately also to the coating of all mentioned samples. In addition, I participated in discussions about the experimental plan, results, and slightly in the interpretation of the results.

Interface mediated softening and deformation mechanics in amorphous/ amorphous nanolaminates

Vivek Devulapalli[1 *], Fedor F. Klimashin[1], Manuel Bärtschi[2], Stephan Waldner[3], Silvia Schwyn Thöny[3], Johann Michler[1], Xavier Maeder[1 *]

[1] EMPA, Laboratory for Mechanics of Materials & Nanostructures, Feuerwerkstrasse 39, 3602 Thun, Switzerland

[2] RhySearch, Institute for optical coatings and characterization, Werdenbergstrasse 4, 9470, Switzerland

[3] Evatec Ltd., Hauptstrasse 1a, 9477 Truebbach, Switzerland

*Corresponding authors' email: vivek.devulapalli@empa.ch, xavier.maeder@empa.ch

**Abstract**

The mechanical behaviour of amorphous-amorphous $Ta_2O_5/SiO_2$ nanolaminates with bilayer thicknesses ranging from 2 nm to 334 nm was investigated through nanoindentation testing and post-deformation microstructural analysis. Whilst monolithic $SiO_2$ exhibits catastrophic failure through single dominant shear bands extending into the silicon substrate, multilayer architectures demonstrate fundamentally different deformation mechanisms. Hardness decreases systematically with decreasing bilayer thickness, from 7.7 GPa at 167 nm to 5.5 GPa at 2 nm spacing, contrasting with crystalline systems that exhibit Hall-Petch strengthening. Cross-sectional transmission electron microscopy reveals that fine bilayer spacings promote closely spaced vertical shear bands with uniform layer compression, while coarser spacings show fewer, widely spaced shear bands with chemical intermixing. Scanning electron diffraction mapping demonstrates significant densification beneath indents, with deformation confined within the multilayer structure rather than extending to the substrate. The high interface density in fine multilayers facilitates strain accommodation that prevents catastrophic failure typical of monolithic amorphous material.

**Main manuscript**

Monolithic amorphous alloys, while possessing exceptional strength and hardness, are severely limited by their propensity for highly localised shear band formation at room temperature, leading to catastrophic brittle failure that restricts their practical engineering applications [1,2]. However, when confined to nanoscale dimensions or constrained within multilayered architectures, these materials can exhibit remarkable plasticity, fundamentally altering their deformation behaviour [3–7]. This discovery has led to intensive research into amorphous-amorphous nanolaminates (A/ANLs), multilayered structures comprising alternating amorphous layers with differing compositions, which have demonstrated enhanced mechanical properties enabling applications across diverse fields, including structural engineering, microelectronics, optoelectronics, and biomedical devices [8–13].

While interfaces in crystalline-amorphous multilayers are well-established as barriers to shear band propagation [7,14], the role of interfaces in A/ANLs remains contentious. Studies report conflicting interlayer thickness-dependent behaviour: some demonstrate strengthening with decreasing bilayer spacing due to interface obstruction of shear bands [10,11,13], while others show thickness-independent properties [15,16,8]. For example, experimental studies on ZrCu/ZrCuAl metallic glass based nanolaminates showed shear bands blocked by interfaces due to significant chemical intermixing [13]. In contrast, nanoindentation of CuNb-based and CuTa/CoZrNb systems demonstrated hardness values equivalent to rule-of-mixtures predictions regardless of bilayer period, suggesting interfaces offer no resistance to shear band propagation [16]. These contradictory findings suggest that the fundamental mechanisms governing interface-mediated deformation in A/ANLs are poorly understood, particularly regarding whether interfaces act as strengthening or weakening elements.

While metallic A/ANLs have been extensively studied, oxide-based systems where different bonding characteristics may lead to behaviour distinct from metallic systems have received considerably less

attention. Oxide-based A/ANLs, such as $Ta_2O_5/SiO_2$ systems, are of particular interest for antireflective coating applications due to their excellent optical properties and environmental stability. Varying the bilayer thickness in such nanolaminates alters their optical band gap through quantum confinement effects, which is essential for tuning their antireflective properties [17,18]. Understanding how bilayer thickness simultaneously affects both the band gap tuning and mechanical deformation mechanisms is therefore essential for developing robust optical coatings that maintain structural integrity during service.

This investigation addresses these knowledge gaps by systematically examining the relationship between bilayer thickness and mechanical response in $Ta_2O_5/SiO_2$ nanolaminates through nanoindentation testing. By examining bilayer thicknesses ranging from a few layers to highly multilayered systems, we aim to elucidate the fundamental deformation mechanisms governing mechanical behaviour in oxide A/ANLs.

All films were deposited in Clusterline 200 BPM magnetron sputtering system (Evatec AG, Switzerland) using reactive magnetron sputtering with identical process parameters, varying only the substrate rotation speed. Silicon and tantalum targets were operated at 4 kW and 7 kW pulsed DC power, respectively. The process parameters consisted of 75 sccm Ar distributed to both targets, with $O_2$ flow regulated via plasma emission monitoring to maintain a total chamber pressure of $3.15\times10^{-3}$ mbar. The resulting deposition rate was 0.766 nm/s. The rotating substrate table enabled continuous bilayer deposition, with thickness ratios controlled by power adjustment and overall bilayer thickness tuned by rotation speed. Pure $SiO_2$ layers were produced using the Si target with a capacitively coupled plasma source operating with oxygen. Seven multilayer systems, each 1μm thick, with bilayer thicknesses of 2 nm, 4 nm, 10 nm, 20 nm, 40 nm, 200 nm, and 334 nm were deposited on single crystal Si substrates, along with two monolithic reference films. In all multilayer systems, the first layer deposited on the substrate was $Ta_2O_5$, while the last layer was $SiO_2$.

Nanoindentation was performed using quasi-continuous stiffness measurement (ZwickRoell) with a Berkovich tip (Synton-MDP Ltd., Switzerland) under 300 mN maximum load. Depth-resolved hardness and elastic modulus profiles were obtained following Oliver and Pharr analysis [19] at 0.05 $s^{-1}$ strain rate and 45 Hz frequency. For hardness measurements, nine indentations per sample with >20 μm spacing ensured statistical reliability. Additional deeper indents were made using cube corner to study the crack growth behaviour, as discussed subsequently. Cross-sectional transmission electron microscopy (TEM) specimens were prepared using Tescan Lyra focused ion beam (FIB) with 30 kV $Ga^+$ ions followed by 5 kV cleaning. TEM analysis (Thermo Fischer Titan Themis 200) included bright-field, dark-field, and high-resolution imaging to characterise multilayer structure and interface quality. Scanning precession electron diffraction (SPED) was performed in the same TEM using a NanoMEGAS DigiSTAR system with a 2 nm step size to generate 4D-STEM data.

Fig. 1 presents SEM micrographs of nanoindents on all specimens, revealing the varied deformation behaviour of each film. An indentation depth of 300 nm was applied to the 1 μm thick films, which exceeds the conventional 10% film thickness criterion [20,21]. This depth was intentionally selected to examine the deformation behaviour, with the understanding that the substrate is expected to contribute to the measured hardness. Fig. 1a shows pronounced pile-up around the indents in amorphous $Ta_2O_5$, without evidence of radial or lateral cracking. The observed pile-up suggests that deformation proceeds predominantly by shear flow, consistent with the reported ductile response of amorphous $Ta_2O_5$ [22–24]. It must be noted that the pile-up is likely promoted by the mechanical mismatch between the relatively soft amorphous $Ta_2O_5$ film and the stiff, hard single-crystal Si substrate. Conversely, the monolithic $SiO_2$ film (Fig. 1h) demonstrated brittle fracture with well-defined radial cracks emanating from the indentation vertices, reflecting its low fracture toughness. The sink-in observed in $SiO_2$ indent, contrasting with the pile-up behaviour exhibited by all other films, indicates densification occurring beneath the indenter, as discussed in detail below.

Multilayers with finer bilayer spacings (4-40 nm; Fig. 1b-e) showed markedly enhanced plastic deformation capability and superior crack growth resistance compared to the monolithic constituents. These configurations exhibited significant material flow and minimal radial cracking, attributed to high plasticity facilitating stress redistribution. As bilayer spacing increased to 200-334 nm (Fig. 1f-g), the deformation behaviour transitioned towards that of brittle $SiO_2$, with localised chipping and incipient crack formation. This degradation correlates with reduced interface density, which diminishes interface-mediated toughening mechanisms.

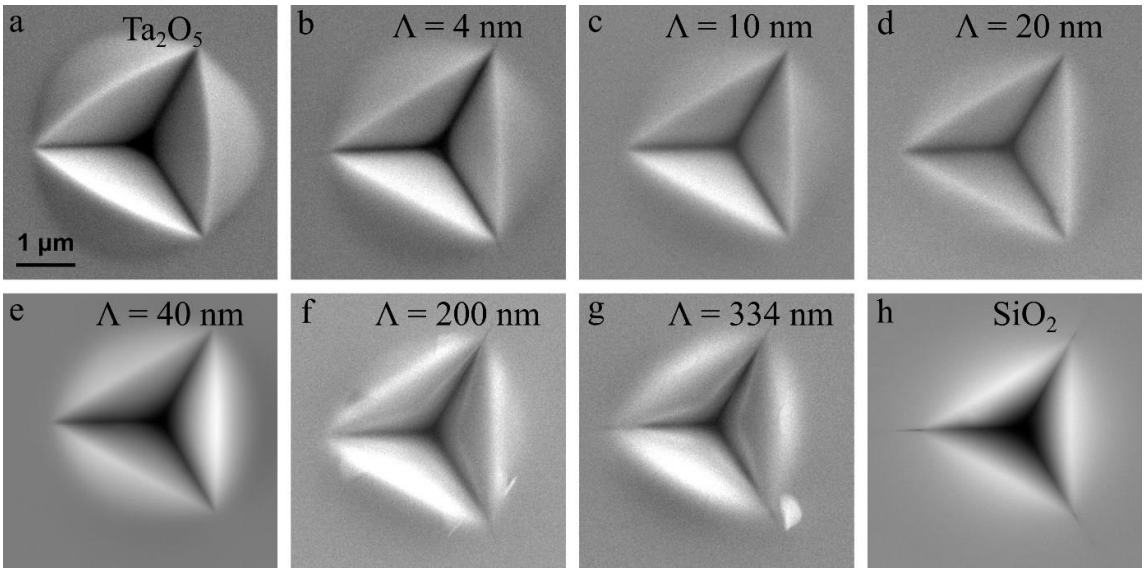


Fig. 1: SEM micrographs of 35 mN nanoindentation impressions on $Ta_2O_5/SiO_2$ multilayers with varying bilayer architectures. (a, h) Monolithic $Ta_2O_5$ and $SiO_2$ films exhibit significant pile-up and radial cracking, respectively. (b-g) Multilayers with bilayer spacings of 4 nm, 10 nm, 20 nm, 40 nm, 200 nm, and 334 nm demonstrate a gradual shift from pile-up towards chipping and cracking.

Although pile-up can cause hardness values to be overestimated [21,25], our focus is on comparing materials and understanding their deformation mechanisms from microscopy. Since pile-up is more pronounced in the softer films, any overestimation mainly affects these materials. Therefore, the hardness trends shown in Fig. 2 remain reliable and may even be stronger when considering this effect. Furthermore, to assess the films' resistance to fracture under severe contact loading, we deliberately made indents of depths exceeding the film thickness, $h/t > 1$. Fig. S1 shows the remarkable crack resistance offered by the 10, 20 and 40 nm bilayer thickness films in contrast to the thicker and monolithic films that crack. To elucidate the deformation mechanisms in detail and explain the observed exceptional plasticity, cross-sectional specimens were prepared from the indentations using FIB lift-out techniques for subsequent S/TEM investigation.

Fig. 2 presents the hardness values for multilayers with bilayer thicknesses ranging from 2 nm to 334 nm, alongside the monolithic films. The monolithic $SiO_2$ film exhibits the highest hardness values at approximately 9.4 GPa, substantially exceeding all multilayer configurations. However, as was evident from the SEM images of the indents, the introduction of a multilayer architecture alters their mechanical response. The multilayer with 334 nm bilayer thickness exhibits hardness values closely matching those predicted by the rule of mixtures, indicating minimal interface effects at large layer thicknesses. Hardness decreases systematically with bilayer thickness, dropping from approximately 7.7 GPa at 167 nm to 5.5 GPa at 2 nm bilayer spacing. This behaviour contrasts markedly with crystalline multilayer systems, which exhibit increased strength with additional interfaces [26,27]. The increased number of interfaces reduce the resistance to initial plastic yielding while preventing the runaway failure typically associated with monolithic amorphous systems. The insets in Fig. 2 show STEM cross-sectional images beneath an indentation, revealing vertical shear bands with an inter-band spacing of 12 ± 3 nm in the 4

nm bilayer film, demonstrating the distributed nature of strain accommodation. The 40 nm bilayer film exhibits wider shear band spacing of 60 ± 10 nm accompanied by enhanced interlayer mixing.

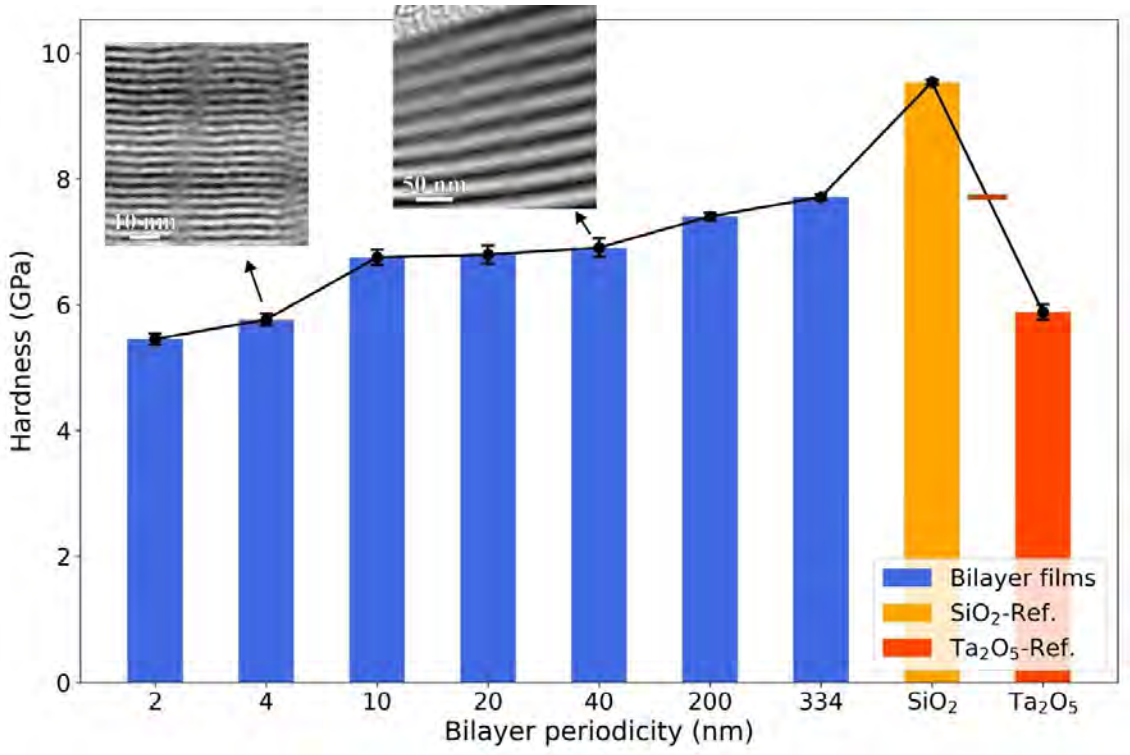


Fig. 2: Hardness of bilayer films as a function of individual layer thickness. Reference values for monolithic $SiO_2$ and $Ta_2O_5$ films and the rule of mixtures prediction are shown for comparison. The insets show STEM cross-sectional images revealing shear bands and interlayer mixing that accommodate deformation.

The BF TEM image of the cross-section of a nanoindent in the monolithic $SiO_2$ film, shown in Fig. 3, to understand the deformation mechanisms in the absence of periodic interfaces. We observe that a single shear band propagates through the entire film thickness extending into the underlying silicon substrate. The shear band in $SiO_2$ has a darker contrast in the bright field image due to its densification. The increase in density of $SiO_2$ within the shear band in the amorphous region is mapped in Fig. S2 using SPED. The map shows the first moment of radial intensity profiles of individual diffraction patterns. The localised deformation demonstrates the characteristic failure mode of silica under nanoindentation, where a single dominant shear band propagates through the entire film thickness. The most notable finding is the crystalline-to-amorphous phase transformation observed in the single-crystal silicon substrate within the region of shear band-substrate interaction. Diffraction patterns in Fig. 3 confirm that directly beneath the indent the deformed substrate (yellow circle) is amorphous. The undeformed (blue circle) regions away from the shear-band-substrate interaction zone retain their single crystalline nature. Similar deformation induced amorphization of Si has been reported earlier [28,29].

On the other hand, the bright region within the shear band is due to its crystallization. HRTEM imaging of the bright region reveals 2 – 5 nm sized small grains, indicative of deformation-induced crystallisation. This phenomenon has been previously observed in metallic glasses subjected to severe plastic deformation. Chen et al. demonstrated that such localised shear bands in aluminium-based amorphous alloys form due to local atomic rearrangements in the region of high plastic strain [30]. Similarly, Kim et al. showed that the primary mechanism for crystallization inside shear bands is flow dilatation - the expansion of atomic structure during deformation that creates conditions similar to the glass transition temperature and dramatically enhances atomic diffusional mobility. This enhanced

mobility allows atoms to diffuse rapidly enough to form nanocrystallites, without requiring significant temperature rise or other external factors [31]. Our oxide system exhibits analogous behaviour, while confirming that densification is the prominent deformation mechanisms in low density $SiO_2$ [32–34].

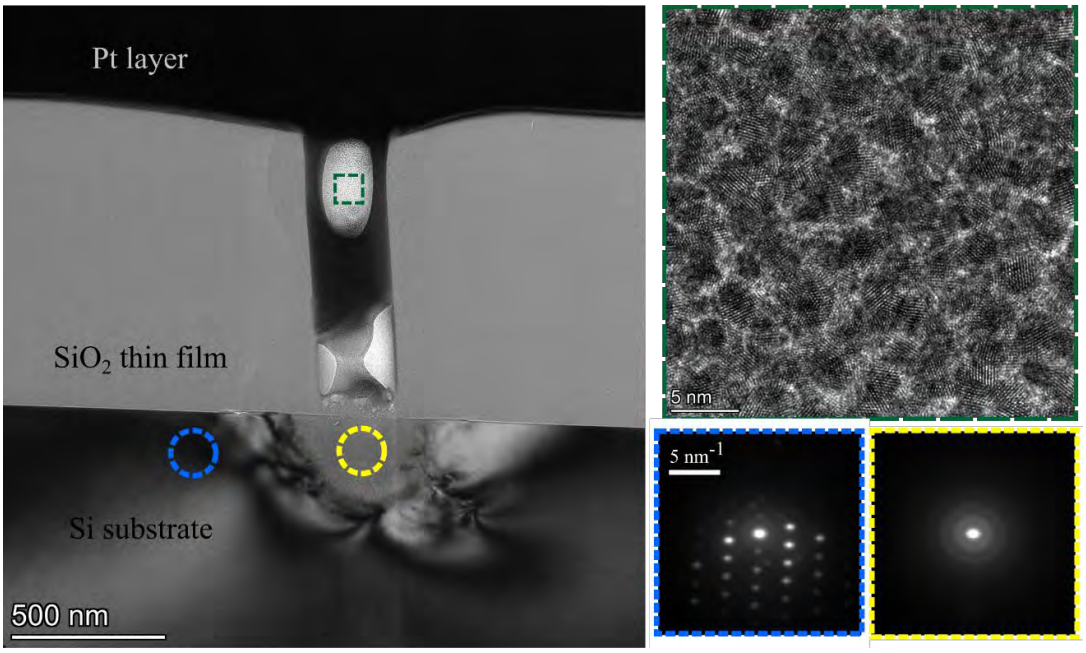


Fig. 3: Deformation-induced crystallisation in the amorphous $SiO_2$ thin film and amorphization in the substrate beneath the indentation. The HRTEM image reveals nanocrystallites ranging from 3-5 nm in size within the bright regions of the bright field image, located directly beneath the indenter impression. Selected area diffraction patterns from the substrate indicate that shear band propagation induces local amorphisation in the crystalline silicon substrate.

In the 4 nm bilayer spacing multilayer (Fig. 4a-g), closely spaced vertical shear bands are observed, with the interlayer spacing decreasing from the original 4 nm to approximately 2.4 nm in the most heavily deformed regions beneath the indent. This uniform compression across all layers effectively distributes the applied strain across multiple deformation pathways. Each interface represents a potential nucleation site for new shear bands while simultaneously impeding the growth of existing ones, leading to enhanced plasticity through interface-mediated deformation mechanisms. Fig. S3 reveals more example images used to measure the spacing between these vertical shear bands. They demonstrate how layer continuity is disrupted due to shear band propagation, with complete severance of individual layers in the most deformed regions.

In contrast, the 40 nm bilayer spacing film (Fig. 4h-m) exhibits fewer and more widely spaced shear bands. The interlayer spacing under the indent is uniformly reduced from 40 nm to approximately 20 nm, demonstrating similar compressive behaviour but with reduced interface density. EDS elemental mapping reveals localised chemical intermixing between Ta and Si layers in the deformed regions. Notably, whilst the 4 nm system shows complete layer discontinuity, the 40 nm bilayer thickness film exhibits only chemical intermixing without any breaking of the layer architecture, indicating a fundamentally different deformation mode. The intensity line profiles across the deformed and undeformed regions clearly distinguish the compositional variations resulting from plastic flow. Crucially, neither multilayer system shows deformation extending to the substrate level, demonstrating the protective effect of the laminated architecture and the confinement of plastic deformation within the multilayer structure. Additionally, the undeformed regions (Fig. 3f and l) demonstrate excellent interfacial quality in the as-deposited film. The individual layer thicknesses exhibit uniformity throughout, while the interlayer interfaces are well-defined and sharp.

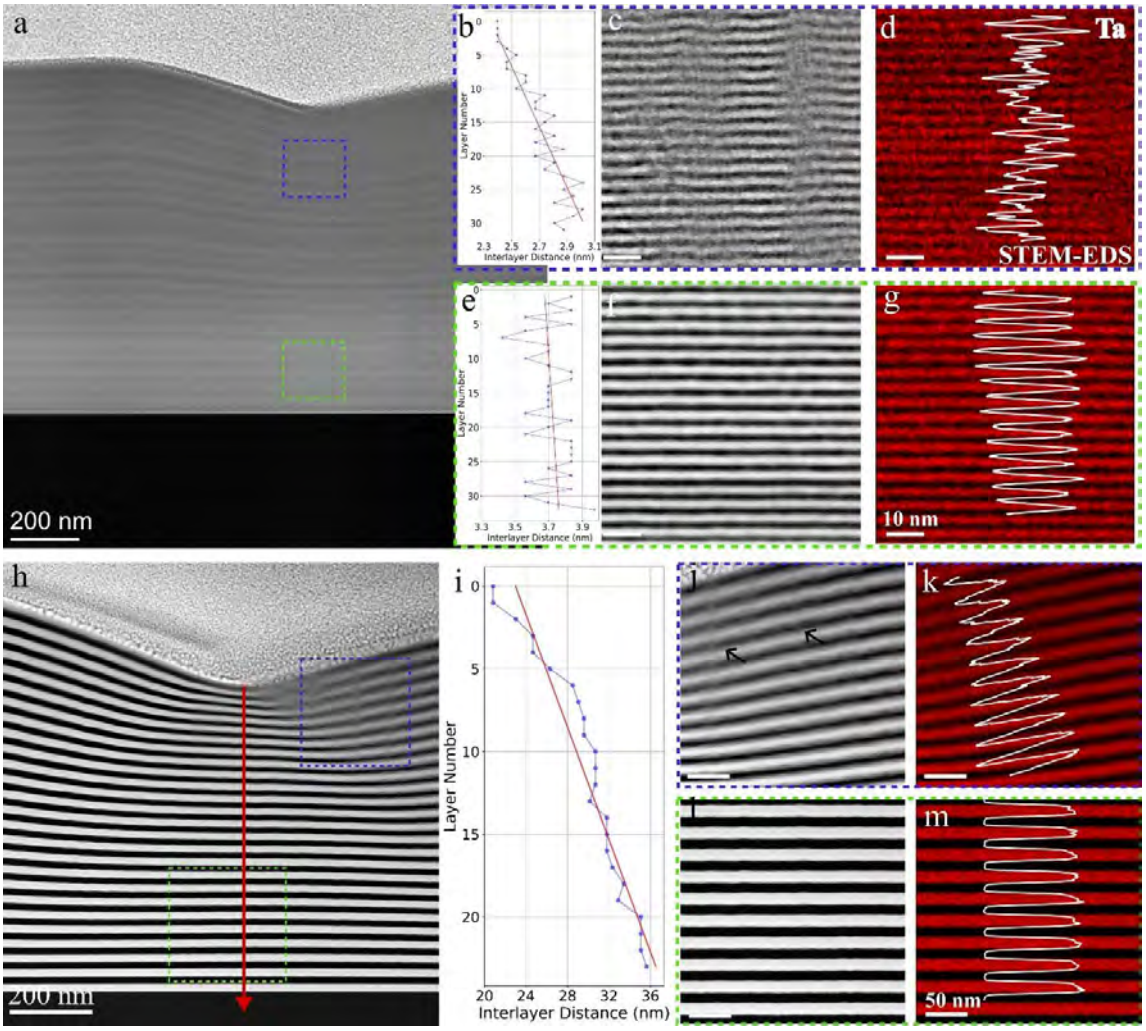


Fig. 4: Cross-sectional microstructural characterisation of Ta/Si multilayers beneath the indentation region. (a) Low-magnification HAADF-STEM overview image showing the indented surface region with selected areas (blue and green dashed boxes) for higher magnification analysis. (b) Changes in the bilayer spacing under the indent for the 4 nm film. (c, d) High-magnification HAADF-STEM image and corresponding Ta EDS elemental map of the region directly beneath the indent in the 4 nm film. (e) The bilayer spacing further away from the indent in the 4 nm film appears to be preserved nearly as in the parent film. (f, g) HAADF-STEM images and EDS maps of the region away from the indent. (h) Low-magnification HAADF-STEM overview of the 40 nm bilayer spacing film after indentation, showing the deformed region. (i) Interlayer distance variation profile. (j, k) High-magnification HAADF-STEM image with arrows pointing at the vertical shear bands and corresponding Ta EDS map of the deformed region. (l, m) Undeformed region of the 40 nm film. The scale bars represent 10 nm for high-magnification images of the 4 nm bilayer spacing film, and 50 nm for of the 40 nm bilayer spacing film.

Fig. 5 reveals with pronounced structural heterogeneity throughout the indented region. With a 2 nm resolution, SPED was used to measure the densification beneath the indenter in the 40 nm bilayer spacing film as a representative example. Virtual dark field imaging reveals localised disruption of the nanolaminates while confirming their continuity in the highest density region immediately below the indentation. The diffraction patterns from undeformed and deformed regions exhibit markedly different characteristics. While the undeformed material displays the typical broad, diffuse ring characteristic of an amorphous structure, the deformed region beneath the indent shows a well-defined ring indicating increased density. The normalised radial intensity profiles (Fig. 5e) quantify this difference, with the

deformed region exhibiting a pronounced peak at approximately 3 $nm^{-1}$ that is absent in the undeformed material.

The density map reveals that the highest density values (red regions) are concentrated immediately beneath the indent centre, with density gradually decreasing with distance from the deformation zone. The same was also noted in Fig. 4 by measuring the change in bilayer spacing under the indent, with layer thickness showing a continuous gradient from the point of maximum deformation to the undeformed film near the substrate. The map also captures the intrinsic density difference between the constituent materials in the as-deposited film, with $SiO_2$ exhibiting characteristically lower density compared to $Ta_2O_5$. The densification process appears to occur gradually across the deformed volume rather than being concentrated in discrete shear band that accommodates all the deformation as seen in Fig. S2, suggesting that the multilayer structure enables efficient stress transfer between layers. The combination of shear band multiplication and layer densification provides complementary pathways for strain accommodation.

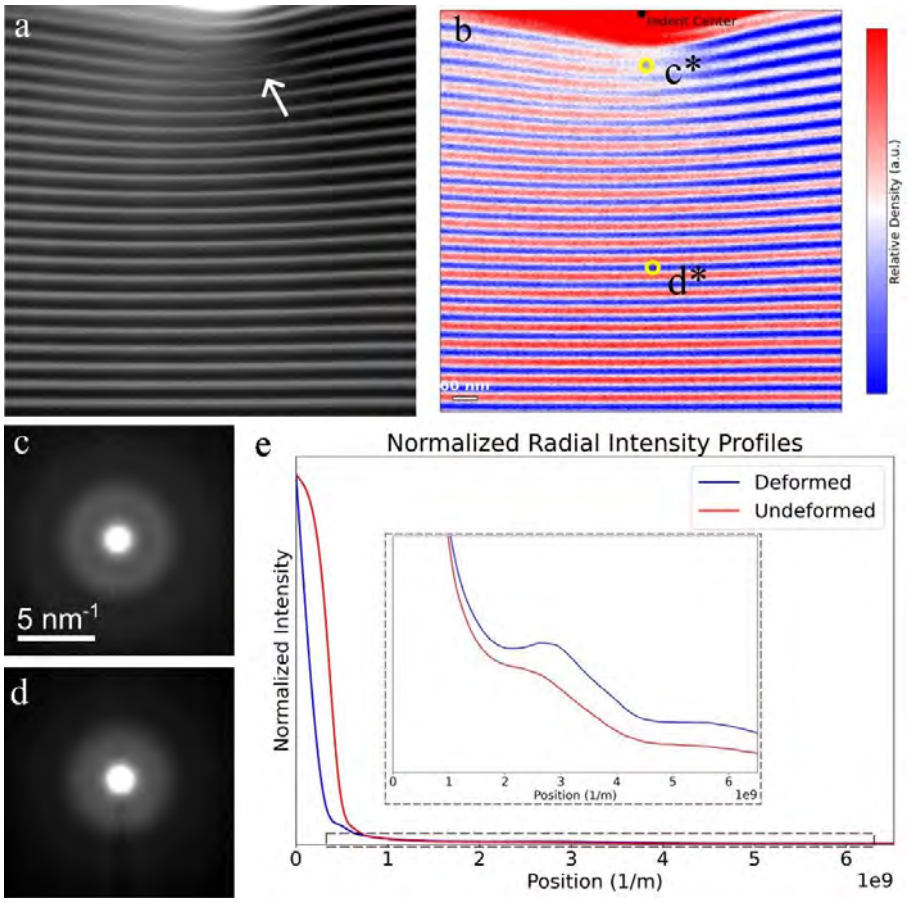


Fig. 5: Diffraction-based density mapping of an indented amorphous film. a) Virtual dark field image of the indented 20 nm bilayer spacing film obtained using the SPED data with an arrow pointed at the disregistery in the nanolaminates. b) Spatial map of relative density calculated from the first moment of radial diffraction profiles, revealing significantly higher density immediately beneath the indent. Diffraction patterns from c) deformed and d) undeformed regions beneath the indent, as indicated in the density map. e) Normalised radial intensity profiles showing the emergence of a peak at 3 $nm^{-1}$ in the deformed region.

A key finding of the present work is that multilayer architecture improves the plasticity and toughness by making the deformation more homogenous. The propagation of shear bands in amorphous materials is fundamentally dependent on the availability of free volume, which provides the necessary atomic

mobility for shear transformation zone activation. Interfaces generally possess excess free volume that can contribute to additional sites for shear band nucleation [35]. However, when individual layers are under a critical thickness, the formation and propagation of mature, localised shear bands can be suppressed. Instead, multiple smaller, "embryonic" shear transformation zones or distributed plastic events occur, leading to a more uniform macroscopic shear flow [28,36,37]. This deformation mechanism transition from highly inhomogeneous flow to relatively more homogeneous deformation. This has been reported both using simulations and experimentally and in both metallic and oxide-based A/ANLs [3,8,10,35,37–39]. For example, the deformation homogenisation effect was demonstrated through molecular dynamics (MD) simulations on $Mg_{80}Al_{20}/Mg_{20}Al_{80}$ A/ANLs, where strain delocalisation was observed as layer thickness decreased below a critical size [39]. Similar enhanced plasticity was reported experimentally using nanoindentation and micropillar compression in Zr/La based A/ANLs [3].

In all reported previous studies, a Hall-Petch-like strengthening with increasing number of interfaces was reported. The conventional understanding suggests that adding interfaces should enhance the strength of a material, as shear bands serve as the primary carriers of plasticity, and blocking their propagation can strengthen the material. For example, Kuan et al. showed that in ZrCuTi/ PdCuSi system, the propagation of shear bands is arrested due to significant elastic force at the interfaces resulting in increased strength [8]. More recently, Poltronieri et al., pointed out that the enhanced strength in their CuZr-based A/ANLs was due to the local chemical variation at the interface [13]. However, we demonstrate that hardness in A/ANLs systematically decreases with increasing number of interfaces.

The intrinsic mechanical properties of the constituent materials provide crucial insight into our findings. $Ta_2O_5$ is inherently ductile. During nanoindentation, $Ta_2O_5$ films characteristically display significant pile-up around indents. In stark contrast, $SiO_2$ exhibits brittle behaviour characterised by densification under mechanical stress (up to 20% volume change) during indentation [32,40]. When these materials are combined to form nanolaminates, their deformation behaviour is modified. The films with 2 or 4 nm bilayer spacing show markedly little pile-up or sink-in. The film shows plasticity due to densification, chemical intermixing and co-deformation due to homogenous shear banding. This behaviour parallels observations in $Al_2O_3/Ta_2O_5$ nanolaminates, where the presence of harder $Al_2O_3$ layers reduced pile-up from approximately 7 nm in pure $Ta_2O_5$ to around 4 nm in the nanolaminates [24]. The observed reduction indicates that the presence of $SiO_2$ layers constrains the flow behaviour of $Ta_2O_5$, preventing the unrestricted plastic deformation characteristic of the monolithic ductile material. On the contrary, localized shear banding of $Ta_2O_5$ prevents the catastrophic failure of $SiO_2$. In our $Ta_2O_5/SiO_2$ films, the interfaces serve as both shear band nucleation sites and barriers to their propagation, creating a complex interplay between strengthening and softening mechanisms that ultimately governs the overall mechanical response.

In conclusion, $Ta_2O_5/SiO_2$ nanolaminates exhibit interface-controlled deformation mechanisms that fundamentally differ from crystalline multilayer systems. The interfaces nucleate and multiply shear bands, promote densification, and confine deformation. The oxide A/ANLs represent a distinct class of materials where interfaces enhance toughness by softening, unlike crystalline or metallic A/ANLs.

References


[1] M. Chen, Annual Review of Materials Research 38 (2008) 445–469.
[2] J.H. Perepezko, S.D. Imhoff, M.-W. Chen, J.-Q. Wang, S. Gonzalez, Proceedings of the National Academy of Sciences 111 (2014) 3938–3942.
[3] P. Sharma, K. Yubuta, H. Kimura, A. Inoue, Phys. Rev. B 80 (2009) 024106.
[4] D. Jang, J.R. Greer, Nature Mater 9 (2010) 215–219.
[5] D.Z. Chen, X.W. Gu, Q. An, W.A. Goddard III, J.R. Greer, Applied Physics Letters 106 (2015) 061903.
[6] Y. Wang, J. Li, A.V. Hamza, T.W. Barbee, PNAS 104 (2007) 11155–11160.

[7] C. Brandl, T.C. Germann, A. Misra, Acta Materialia 61 (2013) 3600–3611.
[8] S.Y. Kuan, H.S. Chou, M.C. Liu, X.H. Du, J.C. Huang, Intermetallics 18 (2010) 2453–2457.
[9] J. Ma, K.C. Chan, L. Xia, S.H. Chen, F.F. Wu, W.H. Li, W.H. Wang, Materials Science and Engineering: A 587 (2013) 240–243.
[10] D. Hua, W. Ye, Q. Jia, Q. Zhou, Q. Xia, J. Shi, Y. Deng, H. Wang, Applied Surface Science 511 (2020) 145545.
[11] Z.Q. Chen, M.C. Li, J.S. Cao, F.C. Li, S.W. Guo, B.A. Sun, H.B. Ke, W.H. Wang, Journal of Materials Science & Technology 99 (2022) 178–183.
[12] Q. Zhou, Y. Du, Y. Ren, W. Kuang, W. Han, H. Wang, P. Huang, F. Wang, J. Wang, Journal of Alloys and Compounds 776 (2019) 447–459.
[13] C. Poltronieri, A. Brognara, C. Jung, F. Challali, P. Djemia, G. Dehm, J.P. Best, M. Ghidelli, Scripta Materialia 259 (2025) 116571.
[14] J. Wang, R.G. Hoagland, A. Misra, Scripta Materialia 60 (2009) 1067–1072.
[15] J.B. Vella, A.B. Mann, H. Kung, C.L. Chien, T.P. Weihs, R.C. Cammarata, Journal of Materials Research 19 (2004) 1840–1848.
[16] R.L. Zong, S.P. Wen, F. Lv, F. Zeng, Y. Gao, F. Pan, Surface and Coatings Technology 202 (2008) 4242–4247.
[17] A.A. Chaaya, R. Viter, I. Baleviciute, M. Bechelany, A. Ramanavicius, Z. Gertnere, D. Erts, V. Smyntyna, P. Miele, J. Phys. Chem. C 118 (2014) 3811–3819.
[18] M. Bärtschi, S. Waldner, S.S. Thöny, X. Maeder, F. Steger, T. Frei, V. Devulapalli, J. Eur. Opt. Society-Rapid Publ. 21 (2025) 24.
[19] W.C. Oliver, G.M. Pharr, Journal of Materials Research 7 (1992) 1564–1583.
[20] M.F. Doerner, W.D. Nix, Journal of Materials Research 1 (1986) 601–609.
[21] N. Moharrami, S.J. Bull, Thin Solid Films 572 (2014) 189–199.
[22] S.F. Bubar, D.A. Vermilyea, J. Electrochem. Soc. 113 (1966) 892.
[23] H. Rizkalla, S.T. Wellinghoff, J Mater Sci 19 (1984) 3895–3907.
[24] H.-M. Piirsoo, T. Jõgiaas, P. Ritslaid, K. Kukli, A. Tamm, Coatings 12 (2022) 404.
[25] G. Alcalá, P. Skeldon, G.E. Thompson, A.B. Mann, H. Habazaki, K. Shimizu, Nanotechnology 13 (2002) 451.
[26] A. Misra, J.P. Hirth, R.G. Hoagland, Acta Materialia 53 (2005) 4817–4824.
[27] R.G. Hoagland, R.J. Kurtz, C.H. Henager, Scripta Materialia 50 (2004) 775–779.
[28] Y.-C. Wang, W. Zhang, L.-Y. Wang, Z. Zhuang, E. Ma, J. Li, Z.-W. Shan, NPG Asia Mater 8 (2016) e291–e291.
[29] Y. He, L. Zhong, F. Fan, C. Wang, T. Zhu, S.X. Mao, Nature Nanotech 11 (2016) 866–871.
[30] H. Chen, Y. He, G.J. Shiflet, S.J. Poon, Nature 367 (1994) 541–543.
[31] J.-J. Kim, Y. Choi, S. Suresh, A.S. Argon, Science 295 (2002) 654–657.
[32] A. Perriot, D. Vandembroucq, E. Barthel, V. Martinez, L. Grosvalet, Ch. Martinet, B. Champagnon, Journal of the American Ceramic Society 89 (2006) 596–601.
[33] G. Kermouche, E. Barthel, D. Vandembroucq, Ph. Dubujet, Acta Materialia 56 (2008) 3222–3228.
[34] K.R. Gadelrab, F.A. Bonilla, M. Chiesa, Journal of Non-Crystalline Solids 358 (2012) 392–398.
[35] K. Dai, C. Zhang, W. Lu, J. Li, Nanomaterials 14 (2024) 546.
[36] S. Adibi, Z.-D. Sha, P.S. Branicio, S.P. Joshi, Z.-S. Liu, Y.-W. Zhang, Appl. Phys. Lett. 103 (2013) 211905.
[37] J. Li, L. Dai, J. Li, Materials Chemistry and Physics 331 (2025) 130197.
[38] S. Liu, Q. Cao, D. Zhang, J.-Z. Jiang, Advanced Engineering Materials 21 (2019) 1900046.
[39] X. Zhou, C. Chen, International Journal of Plasticity 80 (2016) 75–85.
[40] T. Rouxel, H. Ji, J.P. Guin, F. Augereau, B. Rufflé, J. Appl. Phys. 107 (2010) 094903.

Supp. Figures

# References


[1] Wolfgang Demtröder. *Experimentalphysik 2: Elektrizität und Optik*. Springer, 5th edition, 2009.

[2] Wolfgang Demtröder. *Experimentalphysik 3: Atome, Moleküle und Festkörper*. Springer, 4th edition, 2010.

[3] Martin Dressel and George Grüner. *Electrodynamics of Solids: Optical Properties of Electrons in Matter*. Cambridge University Press, 2002.

[4] Rixchard Feynman. *The Feynman Lectures on Physics Volume 1*. Adison Wesley, 1964.

[5] Olaf Stenzel. *Optical Coatings - Material aspects in Theory and Practics*. Springer, 2014.

[6] Daniel Franta, David Nečas, Ivan Ohlídal, and Angelo Giglia. Optical characterization of SiO2 thin films using universal dispersion model over wide spectral range. In Christophe Gorecki, Anand Krishna Asundi, and Wolfgang Osten, editors, *Optical Micro- and Nanometrology VI*, volume 9890, page 989014. International Society for Optics and Photonics, SPIE, 2016.

[7] D. Franta, D. Nečas, and I. Ohlídal. A. Giglia. Refractive index of SiO2. https://refractiveindex.info/database/data/main/SiO2/nk/Franta-25C.yml Access on 12.10.2025.

[8] Eugene Hecht. *Optik*. Oldenbourg, 5th edition, 2002.

[9] Steven J. Byrnes. Multilayer optical calculations, 2020.

[10] Leandro N. Acquaroli. Matrix method for thin film optics. *Arxiv*, 2018.

[11] H.Angus Macleod. *Thin Film Otpical Filters*. CRC Press, 5th edition, 2018.

[12] UAB EssentOptics Europe. *Photon RT Universal Scanning Spectrophotometer*. Essent Optics, 2022.

[13] Grazia Giuseppina Politano and Carlo Versace. Spectroscopic ellipsometry: Advancements, applications and future prospects in optical characterization. *Spectroscopy Journal*, 1(3):163–181, 2023.

[14] J.A. Woolam. Optical constants. https://www.jawoollam.com/resources/ellipsometry-tutorial/optical-constants access on 21.10.2025.

[15] O Stenzel, S Wilbrandt, M Schürmann, N Kaiser, H Ehlers, M Mende, D Ristau, S Bruns, M Vergöhl, M Stolze, M Held, H Niederwald, T Koch, W Riggers, P Burdack, G Mark, R Schäfer, S Mewes, M Bischoff, M Arntzen, F Eisenkrämer, M Lappschies, S Jakobs, S Koch, and B Baumgarten. Tailored nanocomposite coatings for optics. In *Optical Interference Coatings*, page MD2. Optica Publishing Group, 2010.

[16] Dhananjay Patel, Dhruv Shah, James Hilfiker, and Matthew Linford. A tutorial on spectroscopic ellipsometry (se), 5. using the tauc-lorentz and cody-lorentz models to describe the absorption features of amorphous silicon (a-si). *Vacuum,Technology and Coating*, 20:34, 09 2019.

[17] Emilio Márquez, Juan J. Ruíz-Pérez, Manuel Ballester, Almudena P. Márquez, Eduardo Blanco, Dorian Minkov, Susana M. Fernández Ruano, and Elias Saugar. Optical characterization of h-free a-si layers grown by rf-magnetron sputtering by inverse synthesis using matlab: Tauc–lorentz–urbach parameterization. *Coatings*, 11(11), 2021.

[18] Jens Als-Nielsen. *Elements of Modern X-Ray Physics*, volume 55. Wiley, 01 2002.

[19] Andreas Biermanns. *LaborKurs - Röntgenreflektometrie zur Untersuchung von Oberflächen und dünnen Schichtsystemen*. Uni Siegen, 04 2008.

[20] Maher Ahmed Maria Rosa Ardigo and Aurélien Besnard. Stoney formula: Investigation of curvature measurements by optical profilometer. *HAL open science*, 2014.

[21] Leibniz-Institut für Phonoische Technologien. *Experimenteller Demonstrator für direkte Absorptions-messungen bei den Wellenlängen 532nm und 1070nm*, 05 2022.

[22] Puja Kadkhoda, Wjatscheslaw Sakiew, Stefan Günster, and Detlev Ristau. Fast total scattering facility for 2d inspection of optical and functional surfaces. *Proceedings of SPIE - The International Society for Optical Engineering*, 7389, 06 2009.

[23] L.Jensen and Richard Quaderer. *Construction of a Total Scatterometer for Optics Industry and Fundamental Research according to ISO 13696 : 2002*, 03 2019.

[24] (NAFuO) Normenausschuss Feinmechanik und Optik. *ISO Norm 13696:2002 - Bestimmung von Streustrahlung, hervorgerufen durch optische Komponenten*, 2002.

[25] Philipp Döring. *Laser und Laseranlagen - Prüfverfahren für die laserinduzierte Zerstörschwelle*, 2011.

[26] C. W. Carr, H. B. Radousky, and S. G. Demos. Wavelength dependence of laser-induced damage: Determining the damage initiation mechanisms. *Phys. Rev. Lett.*, 91:127402, Sep 2003.

[27] Detlev Risteau. *Laser-Induced Damage in Optical Materials*. CRC Press, 2015.

[28] B. C. Stuart, M. D. Feit, S. Herman, A. M. Rubenchik, B. W. Shore, and M. D. Perry. Nanosecond-to-femtosecond laser-induced breakdown in dielectrics. *Phys. Rev. B*, 53:1749–1761, Jan 1996.

[29] Colin M. Harthcock, Raluca A. Negres, Gintarė Batavičiūtė, and Andrius Melninkaitis. Femtosecond 1030-nm mirror thin film damage competition. In Christopher Wren Carr, Detlev Ristau, Carmen S. Menoni, and Michael D. Thomas, editors, *Laser-Induced Damage in Optical Materials 2024*, volume 13190, page 131900C. International Society for Optics and Photonics, SPIE, 2024.

[30] L.A. Giannuzzi and F.A. Stevie. A review of focused ion beam milling techniques for tem specimen preparation. *Micron*, 30(3):197–204, 1999.

[31] Gerhard Dehm, James M. Howe, and Josef Zweck. *In-situ Electron Microscopy Applications in Physics, Chemistry and Materials Science*. Wiley-VCH, Weinheim, 2012.

[32] Marc De Graef. *Introduction to Conventional Transmission Electron Microscopy*. Cambridge University Press, 2003.

[33] Hamish L. Fraser, David W. McComb, and Robert E.A. Williams. 12 - transmission electron microscopy for physical metallurgists. In David E. Laughlin and Kazuhiro Hono, editors, *Physical Metallurgy (Fifth Edition)*, pages 1143–1226. Elsevier, Oxford, fifth edition edition, 2014.

[34] Manuel Scimeca, Simone Bischetti, Harpreet Kaur Lamsira, Rita Bonfiglio, and Elena Bonanno. Energy dispersive x-ray (edx) microanalysis: A powerful tool in biomedical research and diagnosis. *European Journal of Histochemistry*, 62(1), Mar. 2018.

[35] K. Watanabe. *Theory for HAADF-STEM and its Image Simulation*, chapter Chapter 5, pages 179–216. Imperial College Press, 2014.

[36] Caroline S. Gorham and David E. Laughlin. On the formation of solid states beyond perfect crystals: Quasicrystals, geometrically-frustrated crystals and glasses. *Arxiv*, 2019.

[37] Xiang-Yuan Cui, Simon P. Ringer, Gang Wang, and Z. H. Stachurski. What should the density of amorphous solids be? *The Journal of Chemical Physics*, 151(19):194506, 11 2019.

[38] K. Wieczerzak, A. Sharma, C. Hain, and J. Michler. Crystalline or amorphous? a critical evaluation of phenomenological phase selection rules. *Materials and Design*, 230:111994, 2023.

[39] Grégory Abadias, Eric Chason, Jozef Keckes, Marco Sebastiani, Gregory B. Thompson, Etienne Barthel, Gary L. Doll, Conal E. Murray, Chris H. Stoessel, and Ludvik Martinu. Review article: Stress in thin films and coatings: Current status, challenges, and prospects. *Journal of Vacuum Science & Technology A*, 36(2):020801, 03 2018.

[40] Stephan Waldner, Jürgen Buchholz, and Rico Benz. Hybrid mode optical monitoring – monochromatic and broadband algorithms in the same coating process. In *Optical Interference Coatings Conference (OIC) 2019*, page WA.9. Optica Publishing Group, 2019.

[41] Stephan Waldner and Jürgen Buchholz. Versatile optical monitoring system with both broadband and monochromatic algorithms. In *Optical Interference Coatings 2016*, page WC.5. Optica Publishing Group, 2016.

[42] T. Willemsen, P. Geerke, M. Jupé, L. Gallais, and D. Ristau. Electronic quantization in dielectric nanolaminates. In Greg J. Exarhos, Vitaly E. Gruzdev, Joseph A. Menapace, Detlev Ristau, and MJ Soileau, editors, *Laser-Induced Damage in Optical Materials 2016*, volume 10014, page 100140C. International Society for Optics and Photonics, SPIE, 2016.

[43] Zhores I Alferov, Herbert Kroemer, and Jack S Kilby. Advanced information on the nobel prize in physics 2000. *the nobel price foundation*, 2000.

[44] Morten Steinecke, Holger Badorreck, Marco Jupé, Thomas Willemsen, Hao Liu, Lars Jensen, and Detlev Ristau. Quantizing nanolaminates as versatile materials for optical interference coatings. *Applied Optics*, 59:A236–A241, 02 2020.

[45] Thomas Willemsen, Marco Jupé, Laurent Gallais, Dominic Tetzlaff, and Detlev Ristau. Tunable optical properties of amorphous tantala layers in a quantizing structure. *Opt. Lett.*, 42(21):4502–4505, Nov 2017.

[46] S. Schwyn Thöny, M. Bärtschi, M. Batzer, M. Baselgia, S. Waldner, M. Steinecke, H. Badorreck, A. Wienke, and M. Jupé. Magnetron sputter deposition of ta2o5-sio2 quantized nanolaminates. *Opt. Express*, 31(10):15825–15835, May 2023.

[47] Silvia Schwyn Thöny, Manuel Bärtschi, Marietta Batzer, Manuel Baselgia, Raphael Gmünder, Amit Sharma, Tijmen Vermeij, Xavier Maeder, and Stephan Waldner. Magnetron sputter deposition of amorphous silicon–sio2 quantized nanolaminates. *Advanced Photonics Research*, 5(12):2400057, 2024.

[48] Albert Feldman. Modeling Refractive Index In Mixed Component Systems. In Michael Ray Jacobson, editor, *Modeling of Optical Thin Films*, volume 0821, pages 129 – 132. International Society for Optics and Photonics, SPIE, 1988.

[49] Sebastian Paschel, Cassian Bergmann, Holger Badorreck, Morten Steinecke, Andreas Wienke, Detlev Ristau, and Marco Jupé. Theoretical and experimental analysis of the stability of quantizing nanolaminates. *Opt. Express*, 33(12):26241–26256, Jun 2025.

[50] Alex Valavanis Paul Harrison. *Quantum Wells, Wires and Dots*. Wiley, 4th edition, 2005.

[51] Thomas Willemsen. *Funktionale Schichten für den Ultrakurzpuls Bereich*. PhD thesis, Gottfried Wilhelm Leibniz Universität Hannover, 2018.

[52] Charles Kittel. *Introduction to Solid State Physics*. Wiley, 8th edition, 2005.

[53] Koichi Shimakawa, Jai Singh, and S.K. O'Leary. *Optical Properties of Disordered Condensed Matter*, chapter 3, pages 67–81. John Wiley & Sons, Ltd, 2019.

[54] R. C. Rai. Analysis of the urbach tails in absorption spectra of undoped zno thin films. *Journal of Applied Physics*, 113(15):153508, 04 2013.

[55] B. Sadigh, P. Erhart, D. Åberg, A. Trave, E. Schwegler, and J. Bude. First-principles calculations of the urbach tail in the optical absorption spectra of silica glass. *Phys. Rev. Lett.*, 106:027401, Jan 2011.

[56] D. L. Wood and J. Tauc. Weak absorption tails in amorphous semiconductors. *Phys. Rev. B*, 5:3144–3151, Apr 1972.

[57] J. Tauc. *Optical Properties of Amorphous Semiconductors*, pages 159–220. Springer US, Boston, MA, 1974.

[58] Julian Klein, Laura Kampermann, Benjamin Mockenhaupt, Malte Behrens, Jennifer Strunk, and Gerd Bacher. Limitations of the tauc plot method. *Advanced Functional Materials*, 33(47):2304523, 2023.

[59] Michael Stuckelberger, Rémi Biron, Nicolas Wyrsch, Franz-Josef Haug, and Christophe Ballif. Review: Progress in solar cells from hydrogenated amorphous silicon. *Renewable and Sustainable Energy Reviews*, 76:1497–1523, 2017.

[60] Brian D. Viezbicke, Shane Patel, Benjamin E. Davis, and Dunbar P. Birnie III. Evaluation of the tauc method for optical absorption edge determination: Zno thin films as a model system. *physica status solidi (b)*, 252(8):1700–1710, 2015.

[61] Tahsin Faraz, Harm C. M. Knoops, Marcel A. Verheijen, Cristian A. A. van Helvoirt, Saurabh Karwal, Akhil Sharma, Vivek Beladiya, Adriana Szeghalmi, Dennis M. Hausmann, Jon Henri, Mariadriana Creatore, and Wilhelmus M. M. Kessels. Tuning material properties of oxides and nitrides by substrate biasing during plasma-enhanced atomic layer deposition on planar and 3d substrate topographies. *ACS Applied Materials & Interfaces*, 10(15):13158–13180, 2018. PMID: 29554799.

[62] Manuel Bärtschi, Stephan Waldner, Silvia Schwyn Thöny, Xavier Maeder, Fabian Steger, Thomas Frei, and Vivek Devulapalli. UV coatings using Ta2O5-SiO2 quantized nanolaminates. *Journal of the European Optical Society-Rapid Publications*, 21(1):24, 2025.

[63] Thomas Willemsen, Marco Jupé, Laurent Gallais, Dominic Tetzlaff, and Detlev Ristau. Tunable optical properties of amorphous tantala layers in a quantizing structure. *Opt. Lett.*, 42(21):4502–4505, Nov 2017.

[64] Thomas Willemsen, Marco Jupé, Mark Gyamfi, Sebastian Schlichting, and Detlev Ristau. Enhancement of the damage resistance of ultra-fast optics by novel design approaches. *Opt. Express*, 25(25):31948–31959, Dec 2017.

[65] Neil W. Ashcroft and N.David Mermin. *Solid State physics*. Cengage, 1976.

[66] Yuanan Zhao, Yingjian Wang, Hui Gong, Jianda Shao, and Zhengxiu Fan. Annealing effects on structure and laser-induced damage threshold of ta2o5/sio2 dielectric mirrors. *Applied Surface Science*, 210(3):353–358, 2003.

[67] Treffers Ernst and Tobias Bredl. A toast to laser glass cutting. *PhotonicsViews*, 17(5):34–37, 2020.

[68] Produit, Thomas, Walch, Pierre, Herkommer, Clemens, Mostajabi, Amirhossein, Moret, Michel, Andral, Ugo, Sunjerga, Antonio, Azadifar, Mohammad, André, Yves-Bernard, Mahieu, Benoît, Haas, Walter, Esmiller, Bruno, Fournier, Gilles, Krötz, Peter, Metzger, Thomas, Michel, Knut, Mysyrowicz, André, Rubinstein, Marcos, Rachidi, Farhad, Kasparian, Jérôme, Wolf, Jean-Pierre, and Houard, Aurélien. The laser lightning rod project. *Eur. Phys. J. Appl. Phys.*, 93(1):10504, 2021.

[69] Marie C. Cheynet, Simone Pokrant, Frans D. Tichelaar, and Jean-Luc Rouvière. Crystal structure and band gap determination of HfO2 thin films. *Journal of Applied Physics*, 101(5):054101, 03 2007.

[70] M.F. Al-Kuhaili. Optical properties of hafnium oxide thin films and their application in energy-efficient windows. *Optical Materials*, 27(3):383–387, 2004.

[71] Sebastian Paschel, Cassian Bergmann, Holger Badorreck, Morten Steinecke, Andreas Wienke, Detlev Ristau, and Marco Jupé. Theoretical and experimental analysis of the stability of quantizing nanolaminates. *Opt. Express*, 33(12):26241–26256, Jun 2025.

[72] M.W. Prairie and R.M. Kolbas. A general derivation of the density of states function for quantum wells and superlattices. *Superlattices and Microstructures*, 7(4):269–277, 1990.

[73] Olaf Stenzel and Steffen Wilbrandt. Theoretical aspects of thin film optical spectra: Underlying models, model restrictions and inadequacies, algorithms, and challenges. *Applied Sciences*, 15(4), 2025.

[74] Vivek Devulapalli, Fedor F. Klimashin, Manuel Bärtschi, Stephan Waldner, Silvia Schwyn Thöny, Johann Michler, and Xavier Maeder. Interface mediated softening and deformation mechanics in amorphous/amorphous nanolaminates. *Scripta Materialia*, 2025.

[75] M. Jupé, T. Willemsen, H. Liu, M. Steinecke, L. Jensen, and D. Ristau. Manufacturing of quantized nanolaminates. In *Optical Interference Coatings Conference (OIC) 2019*, page TB.4. Optica Publishing Group, 2019.

[76] Holger Badorreck, Morten Steinecke, Lars Jensen, Detlev Ristau, Marco Jupé, Jérôme Müller, Romain Tonneau, Pavel Moskovkin, Stephane Lucas, Andreas Pflug, Lina Grinevičiūtė, Algirdas Selskis, and Tomas Tolenis. Correlation of structural and optical properties using virtual materials analysis. *Opt. Express*, 27(16):22209–22225, Aug 2019.

[77] Tomas Tolenis, Lina Grinevičiūtė, Rytis Buzelis, Linas Smalakys, Egidijus Pupka, Simas Melnikas, Algirdas Selskis, Ramutis Drazdys, and Andrius Melninkaitis. Sculptured anti-reflection coatings for high power lasers. *Opt. Mater. Express*, 7(4):1249–1258, Apr 2017.

[78] S. F. Bubar and D. A. Vermilyea. Deformation of anodic oxide films. *Journal of The Electrochemical Society*, 113(9):892, sep 1966.

[79] A. Misra, J.P. Hirth, and R.G. Hoagland. Length-scale-dependent deformation mechanisms in incoherent metallic multilayered composites. *Acta Materialia*, 53(18):4817–4824, 2005.

[80] R.G. Hoagland, R.J. Kurtz, and C.H. Henager. Slip resistance of interfaces and the strength of metallic multilayer composites. *Scripta Materialia*, 50(6):775–779, 2004. Viewpoint Set No 34. Deformation and stability of nanoscale metallic multilayers.

[81] Horst Frank and Phrood anf Anony. Electromagnetic spectrum -de. https://commons.wikimedia.org/wiki/File:Electromagnetic_spectrum_-de_c.svg Access on: 12.10.2025.

[82] Cdang. Loi de bragg, 2004. https://commons.wikimedia.org/wiki/File/Loi_de_bragg.png Access on: 08.10.2025.

[83] Sandro Knauß. Schema magnetonsputtern. wikimedia.org/wiki/File:Schema_Magnetonsputtern.svg access on 12.10.2025.

# List of Figures

# Declaration

In this work, I used the large language model software DeepL and ChatGPT 4-5.1 to partially translate and correct texts. Further, the grammar was checked and partially corrected using Overleaf's built in language tool "Writefull". Unless otherwise stated, the texts were originally written by me. Unless otherwise stated, the figures have also been created by me. If I was inspired by an existing figure, the source is noted in the list of figures. If I took the figure from a source, this is mentioned in the caption. To the best of my knowledge and belief, I cited and indicated all sources and significant input.

unine
Université de Neuchâtel

# Déclaration sur l'honneur*

Par la présente, j'affirme avoir pris connaissance des documents d'information et de prévention du plagiat émis par l'Université de Neuchâtel et m'être renseigné-e correctement sur les techniques de citation.

J'atteste par ailleurs que le travail rendu est le fruit de ma réflexion personnelle et a été rédigé de manière autonome.

**Je certifie que toute formulation, idée, recherche, raisonnement, analyse ou autre création empruntée à un tiers est correctement et consciencieusement mentionnée comme telle**, de manière claire et transparente, de sorte que la source en soit immédiatement reconnaissable, dans le respect des droits d'auteur et des techniques de citations.

**Je suis conscient-e que le fait de ne pas citer une source ou de ne pas la citer clairement, correctement et complètement est constitutif de plagiat.**

Je prends note que le plagiat est considéré comme une faute grave au sein de l'Université. J'ai pris connaissance des risques de sanctions administratives et disciplinaires encourues en cas de plagiat (pouvant aller jusqu'au renvoi de l'université).

Je suis informé-e qu'en cas de plagiat, le dossier sera automatiquement transmis au rectorat.

Au vu de ce qui précède, **je déclare sur l'honneur ne pas avoir eu recours au plagiat ou à toute autre forme de fraude.**

**Nom : Bärtschi** **Prénom : Manuel Ilias**

**Cursus : Doctorat en Physique** **Faculté d'inscription : Faculté des sciences**

**Lieu et date : Buchs SG, Novembre 2025** **Signature :** M. Bärtschi

**Ce formulaire doit être dûment rempli par tout étudiant ou toute étudiante rédigeant un travail substantiel (notamment un mémoire de bachelor ou de master) ou une thèse de doctorat. Il doit accompagner chaque travail remis au professeur ou à la professeure.**

* Formulaire largement inspiré de la Directive de la direction 0.3 bis, intitulée Formulaire Code de déontologie en matière d'emprunts, de citations et d'exploitation de sources diverses, de l'Université de Lausanne, du 23 avril 2007 et adapté aux besoins de l'Université de Neuchâtel.

**Rectorat. Fbg de l'Hôpital 41, 2000 Neuchâtel, tél. +41 32 718 10 20, messagerie.rectorat@unine.ch**